

University of Kentucky

UKnowledge

Theses and Dissertations--Physics and
Astronomy

Physics and Astronomy

2012

A systematic study of transport, magnetic and thermal properties of layered iridates

Oleksandr B. Korneta

University of Kentucky, korneta@pa.uky.edu

[Right click to open a feedback form in a new tab to let us know how this document benefits you.](#)

Recommended Citation

Korneta, Oleksandr B., "A systematic study of transport, magnetic and thermal properties of layered iridates" (2012). *Theses and Dissertations--Physics and Astronomy*. 2.
https://uknowledge.uky.edu/physastron_etds/2

This Doctoral Dissertation is brought to you for free and open access by the Physics and Astronomy at UKnowledge. It has been accepted for inclusion in Theses and Dissertations--Physics and Astronomy by an authorized administrator of UKnowledge. For more information, please contact UKnowledge@lsv.uky.edu.

STUDENT AGREEMENT:

I represent that my thesis or dissertation and abstract are my original work. Proper attribution has been given to all outside sources. I understand that I am solely responsible for obtaining any needed copyright permissions. I have obtained and attached hereto needed written permission statements(s) from the owner(s) of each third-party copyrighted matter to be included in my work, allowing electronic distribution (if such use is not permitted by the fair use doctrine).

I hereby grant to The University of Kentucky and its agents the non-exclusive license to archive and make accessible my work in whole or in part in all forms of media, now or hereafter known. I agree that the document mentioned above may be made available immediately for worldwide access unless a preapproved embargo applies.

I retain all other ownership rights to the copyright of my work. I also retain the right to use in future works (such as articles or books) all or part of my work. I understand that I am free to register the copyright to my work.

REVIEW, APPROVAL AND ACCEPTANCE

The document mentioned above has been reviewed and accepted by the student's advisor, on behalf of the advisory committee, and by the Director of Graduate Studies (DGS), on behalf of the program; we verify that this is the final, approved version of the student's dissertation including all changes required by the advisory committee. The undersigned agree to abide by the statements above.

Oleksandr B. Korneta, Student

Dr. Gang Cao, Major Professor

Dr. Tim Gorringer, Director of Graduate Studies

A SYSTEMATIC STUDY OF TRANSPORT, MAGNETIC AND THERMAL
PROPERTIES OF LAYERED IRIDATES

DISSERTATION

A dissertation submitted in partial
fulfillment of the requirements for
the degree of Doctor of Philosophy
in the College of Arts and Sciences
at the University of Kentucky

By
Oleksandr Korneta
Lexington, Kentucky

Director: Dr. Gang Cao, Professor of Physics
Lexington, Kentucky 2012

Copyright© Oleksandr Korneta 2012

ABSTRACT OF DISSERTATION

A SYSTEMATIC STUDY OF TRANSPORT, MAGNETIC AND THERMAL PROPERTIES OF LAYERED IRIDATES

A unique feature of the $5d$ -iridates is that the spin-orbit interaction (SOI) and Coulomb interactions U are of comparable strength and therefore compete vigorously. The relative strength of these interactions stabilizes new exotic ground states that provide a fertile ground for studying new physics. SOI is proportional to Z^4 (Z is the atomic number), and it is now recognized that strong SOI can drive novel narrow-gap insulating states in heavy transition metal oxides such as iridates. Indeed, strong SOI necessarily introduces strong lattice degrees of freedom that become critical to new physics in the iridates. This dissertation thoroughly examines a wide array of newly observed novel phenomena induced by adjusting the relative strengths of U and SOI interactions via slight chemical doping and application of hydrostatic pressure in the layered iridates, particularly, BaIrO_3 and Sr_2IrO_4 .

KEYWORDS: spin-orbit interaction, Mott insulator, iridates, magnetism, pressure

Author's signature: Oleksandr Korneta

Date: August 22, 2012

A SYSTEMATIC STUDY OF TRANSPORT, MAGNETIC AND THERMAL
PROPERTIES OF LAYERED IRIDATES

By
Oleksandr Korneta

Director of Dissertation: Gang Cao

Director of Graduate Studies: Tim Gorringer

Date: August 22, 2012

ACKNOWLEDGMENTS

Looking back at the years spent pursuing my doctoral study, I am surprised at and very grateful for all I have received throughout this time. It has certainly shaped me both as a person and as a scientist, and has led me where I am now. All these years of Ph.D. study are full of such gifts. I owe a considerable debt of gratitude to all those who allowed me to stay centered and rediscover what is important, and why I am doing what I am doing. I would like to express my heart-felt appreciation to my research advisor Prof. Gang Cao for his educational and financial support, guidance of my research direction and giving me the freedom to explore throughout the time it took me to complete this work. The extensive research facilities I had at my disposal in our laboratory and at the Center of Advanced Materials established by him, were invaluable for my future career. His diligent working attitude will always inspire and encourage me during my future professional development. I also want to thank Prof. Joseph Brill, Prof. Joseph Straley and Prof. Arthur Cammers for serving as my Ph.D. advisory committee members all these years. Their immense professional support, constructive criticism, valuable suggestions and thorough corrections to my dissertation are extremely appreciated. I also feel grateful to my former supervisor Dr. Yuri Sushko who initially led me into the field of experimental condensed matter physics when I first joined this department at the University of Kentucky. Many thanks should also go to previous, visiting and present members of our research group: Tongfei Qi, Min Ge, Vinobalan Durairaj, Shaline Chikara, Alec Sim and Wenhui Song for their help and friendship. I wish to acknowledge the help I received from the technical staff in the machine, electronics and vacuum shops of our department who lent their helping hands whenever I was in need, whether it was to maintain and troubleshoot our existing instruments and probes or to design new ones. I am also

thankful to all the people in Physics main office for handling all the paperwork. I especially thank Carol Cotrill, Eva Ellis and Diane Riddell for being extremely helpful in all administrative matters related to my work, and for their personal support. In addition to the technical and instrumental assistance above, I received equally important assistance from family and friends. Special thanks are due to my wife Iryna, who has sacrificed a lot and supported me in every possible way. I must thank my parents for their support and patience over the years I have spent away from home working towards my degree. I should not fail to acknowledge the funding agencies, helping us turn our initial ideas into final results. I wish to thank the Graduate School of the University of Kentucky and The Huffaker Family Fund for the numerous travel grants I have received, which enabled me to present my research findings at various physics conferences.

TABLE OF CONTENTS

Acknowledgments	iii
Table of Contents	v
List of Figures	vii
List of Tables	x
Chapter 1 INTRODUCTION	1
1.1 Transition metal oxides	1
1.2 Ruddlesden-Popper series	2
1.3 The case of $5d$ oxides	8
1.4 Structure of the thesis	11
Chapter 2 THEORETICAL CONCEPTS	12
2.1 Magnetism	12
2.1.1 Hund's rules	13
2.1.2 Crystal field environment	14
2.1.3 Jahn-Teller Effect	16
2.1.4 Spin-orbit coupling	17
2.2 Exchange interactions	19
2.2.1 Direct exchange	19
2.2.2 Superexchange	22
2.2.3 Indirect exchange in metals	26
2.2.4 Anisotropic exchange interaction	27
2.3 Itinerant electron magnetism	28
2.4 Pressure effect on magnetic ordering	30
2.4.1 Pressure effect on superexchange	30
2.4.2 Pressure effect on double exchange	33
2.4.3 Pressure effect on RKKY-type magnetic ordering	34
2.4.4 Anisotropic exchange under pressure	35
2.4.5 Pressure effect on itinerant magnetism	35
2.5 Metal-Insulator transitions	37
2.5.1 Disorder induced MIT	38
2.5.2 Slater insulator	39
2.5.3 Mott insulator	40
2.5.4 Pressure induced metal-insulator transition	42
Chapter 3 EXPERIMENTAL TECHNIQUES	45
3.1 Material synthesis	45
3.1.1 The importance of the single crystals	45

3.1.2	Single crystals growth by flux method	47
3.1.3	Oxygen depletion	51
3.2	Structural analysis of materials	53
3.2.1	Powder X-ray diffraction	53
3.2.2	Single crystal X-ray diffraction	56
3.2.3	Energy-dispersive X-ray spectroscopy	58
3.3	Thermogravimetric analysis	61
3.4	Magnetic properties measurements	65
3.5	Transport properties measurements	69
3.5.1	Electrical resistivity	69
3.5.2	Current-Voltage characteristics measurements	71
3.6	Heat capacity measurements	71
3.7	Thermoelectric power measurements	74
3.8	Measurements under pressure	76
Chapter 4	TUNING THE GROUND STATE OF BaIrO_3 VIA PRESSURE AND CHEMICAL DOPING	81
4.1	Introduction	81
4.2	Underlying physical properties of BaIrO_3	83
4.3	Crystal structure of BaIrO_3	85
4.4	Structural changes in Gd-doped BaIrO_3	86
4.5	Chemical substitution effect on magnetic properties	87
4.6	Transport properties	91
4.7	Pressure effect studies	95
4.8	Summary	101
Chapter 5	TRANSPORT AND THERMODYNAMIC PROPERTIES OF SPIN- ORBIT INDUCED MOTT INSULATOR Sr_2IrO_4	103
5.1	Introduction	103
5.2	Crystal structure and basic properties	107
5.3	Oxygen depleted Sr_2IrO_4	108
5.4	Magnetic properties of $\text{Sr}_2\text{IrO}_{4-\delta}$	112
5.5	Non-Ohmic behavior of $\text{Sr}_2\text{IrO}_{4-\delta}$	113
5.6	Summary	117
Chapter 6	CONCLUDING REMARKS AND OUTLOOK	119
	Bibliography	123
	Vita	143

LIST OF FIGURES

1.1	Schematic crystal structure of four representatives of the Ruddlesden-Popper series.	3
1.2	Temperature dependence of resistivity and magnetization for members of layered perovskite family $(\text{La,Sr})_{n+1}\text{Mn}_n\text{O}_{3n+1}$	6
1.3	A qualitative phase diagram of the Ruddlesden-Popper series for Ca- and Sr-based ruthenates.	7
1.4	Schematic energy diagrams illustrating the splitting of $5d$ bands.	10
2.1	Illustration of angular distribution of the d -orbitals.	14
2.2	Splitting of the electronic d -orbitals due to the crystal field in octahedral and tetrahedral environment	15
2.3	The illustration of the Jahn-Teller effect.	16
2.4	Hierarchy of exchange coupling.	19
2.5	Schematic illustration of the symmetry relations between various d and p orbitals	20
2.6	Illustration of the in-line and orthogonal orientation of cation-anion-cation chain	23
2.7	Formation of the negative (a) and positive (b) bonds at admixture of excited states with the ground state.	24
2.8	The illustration of a superexchange interaction between the magnetic ions in an orthogonal coordination case.	25
2.9	A functional dependence describing the real space magnetization of electron gas by a localized magnetic moment.	26
2.10	Illustration of the Dzyaloshinsky-Moriya interaction.	28
2.11	Density of states showing spontaneous splitting of energy bands without an applied magnetic field.	29
2.12	The density of states (DOS) of electrons in a solid as a function of the local Coulomb.	38
2.13	Schematic illustration of the upper and lower Hubbard bands in Mott insulator as a function of reciprocal interatomic distance.	41
2.14	Schematic phase diagram based on Hubbard model.	43
3.1	Modern classification of crystal growth techniques.	46
3.2	Pseudo-binary phase diagram showing means for achieving crystallization from fluxed melts.	48
3.3	SEM images and powder XRD pattern of the single crystals of Sr_2IrO_4 , grown using flux technique.	50
3.4	SEM images and powder XRD pattern of the single crystals of BaIrO_3 , grown using flux technique.	51
3.5	Illustration of the fulfillment of the Bragg's equation.	54

3.6	Schematic diagram of Bragg-Brentano diffraction geometry in $\theta - 2\theta$ configuration.	55
3.7	Schematics of the classical four-circle goniometer used in single-crystal X-ray diffractometers.	57
3.8	Diffraction pattern obtained with a Kappa CCD diffractometer	58
3.9	Moseley's relation between λ and Z for the characteristic X-ray lines. . .	59
3.10	EDX spectrum of single crystal Eu doped BaIrO ₃ studied in this work. .	60
3.11	Thermogravimetric analyzer block diagram	61
3.12	The original and differentiated form of thermogravimetric analysis data. .	63
3.13	Schematics of TGA measuring cell.	64
3.14	Schematics of SQUID magnetometer with longitudinal pickup coils	65
3.15	Illustration of DC-SQUID and V vs Φ/Φ_0 for constant bias current I	66
3.16	rf-SQUID inductively coupled to a parallel LC tank circuit.	67
3.17	Schematic cross-section of the MPMS [®]	68
3.18	Equivalent circuit of four-point probe setup for resistivity measurements. .	69
3.19	The change of temperature as a function of time due to a pulse of heat applied to a sample.	72
3.20	Illustration of Two-Tau model for sample and sample holder and schematic drawing of microcalorimeter sample holder design.	73
3.21	Block diagram of the measurement system of thermoelectric properties measurements apparatus and schematic diagram of TEP apparatus sample stage.	75
3.22	Cutaway view of the hydrostatic piston-cylinder type clamp pressure cell. .	77
3.23	Photograph of the hydrostatic piston-cylinder type clamp pressure cell. .	79
4.1	The temperature dependence of the resistivity, magnetization and inverse susceptibility for stoichiometric BaIrO ₃	84
4.2	Polyhedral representation of the crystal structure of BaIrO ₃	86
4.3	The temperature dependence of the magnetization $M(T)$, $1/\Delta\chi$ and specific heat $C(T)$ of Gd-doped BaIrO ₃	88
4.4	The low-temperature dependence of heat capacity $C(T)$, magnetization $M_{ab}(T)$, magnetic contribution to specific heat $\Delta C_M(T)$ and magnetic entropy removal S_M for Ba _{1-x} Gd _x IrO ₃	89
4.5	The low-temperature dependence for Ba _{1-x} Gd _x IrO ₃ of $C(T)/T$ vs T^2 for $x = 0$ and $x = 0.04$ at various magnetic fields H up to 9 T.	90
4.6	The c -axis magnetization data M_C for Ba _{1-x} R _x IrO ₃ Gd($x = 0.04$) and other rare earth doping as indicated.	91
4.7	The temperature dependence of (a) $\rho_{ab}(T)$ (left scale for $x = 0.06$ and 0.07), (b) Seebeck coefficient $S_{ab}(T)$ for Gd-doped BaIrO ₃	92
4.8	The temperature dependence of $\rho_C(T)$ and $M_c(T)$ for Ba _{1-x} Eu _x IrO ₃ $x = 0$ and $x = 0.02, 0.04$	94
4.9	The c -axis resistivity $\rho_C(T)$ for Ba _{1-x} Gd _x IrO ₃ ($x = 0.04$) under a hydrostatic pressure up to 12.1 kbar.	96
4.10	The c -axis resistivity $\rho_C(T)$ for Ba _{1-x} Eu _x IrO ₃ ($x = 0.04$) under a hydrostatic pressure up to 12.1 kbar.	97

4.11	Pressure dependence of T_C for BaIrO_3 and $\text{Ba}_{0.96}\text{Eu}_{0.04}\text{IrO}_3$	98
4.12	The $T - x$ and $T - P$ phase diagrams for $\text{Ba}_{1-x}\text{Gd}_x\text{IrO}_3$	100
5.1	Schematic energy diagrams for the $5d^5$ (t_5^2) configuration.	104
5.2	Temperature dependence of (a) a - and c -axis resistivity ρ_a , ρ_c and (b) magnetization c -axis and ab -plane M_a , M_c for Sr_2IrO_4	105
5.3	Polyhedral representation of the crystal structure of Sr_2IrO_4	108
5.4	Temperature dependence of ρ_a for several representative values of δ in $\text{Sr}_2\text{IrO}_{4-\delta}$	110
5.5	Temperature dependence of a - and c -axis resistivities and thermoelectric power for $\delta = 0.04$ in $\text{Sr}_2\text{IrO}_{4-\delta}$	111
5.6	Temperature dependence of resistivity $\rho(T)$ fit for variable range hopping (VRH) relation.	112
5.7	Temperature dependence of ab -plane and c -axis magnetization M_a , M_c for $\text{Sr}_2\text{IrO}_{4-\delta}$	113
5.8	Temperature dependence of c -axis resistivity ρ_c at several representative values of excitation current I for $\text{Sr}_2\text{IrO}_{4-\delta}$ ($\delta = 0.04$).	114
5.9	Normalized I-V curves for Sr_2IrO_4 ($\delta = 0.04$) at several representative temperatures.	115
5.10	Temperature dependence of (a) c -axis resistivity of $\text{Sr}_2\text{IrO}_{4-\delta}$ ($\delta = 0.04$) at various current density (b) threshold potentials E_T	116

LIST OF TABLES

4.1	Lattice parameters, Ir1-O2-Ir3 bond length and bond angles at 295 K and 90 K for BaIrO ₃	85
4.2	Lattice parameters, Ir1-O2-Ir3 bond length and bond angle at 295 K and 90 K for Ba _{0.96} Gd _{0.04} IrO ₃	87
5.1	Lattice parameters, Ir1-O2-Ir1 bond length and bond angle for Sr ₂ IrO _{4-δ}	107
6.1	A list of studied single crystal iridates of various crystal structure and their respective properties.	120

Chapter 1 INTRODUCTION

1.1 Transition metal oxides

The extraordinary range of properties of transition metal oxides (TMO) makes them worthy of special attention [1] for the last several decades. Some of the properties like magnetism and colors of naturally occurring minerals and gemstones were known since ancient times. The others, like high-temperature superconductivity, have been discovered only recently. The unique nature of the outer d -electrons is clearly at the core of the unusual properties of TMO. Because of progressive filling of d -orbitals and the fact that the valence electrons of these transition metals can be present in more than one shell, the number of various oxidation states can be realized in the compounds and the metal-oxygen bond can vary anywhere from nearly ionic to metallic. Hence, the variety of electronic properties of TMO ranges from insulating to metallic and even superconducting behavior. The electrical resistivity in known oxides spans within the astonishing range of 10^{-5} $\Omega\cdot\text{cm}$ (in metallic oxides like LaNiO_3) to 10^{20} $\Omega\cdot\text{cm}$ (in highly insulating compounds like BaTiO_3). The same applies to their magnetic properties, where the diverse states from Pauli paramagnetism to long-range ordering of local magnetic moments are found, and the properties span anywhere from ferromagnetism (for instance CrO_2) to antiferromagnetism (NiO). Because of the small overlap between d and p orbitals the oxides formed by d -block elements also have narrow electronic bands. This distinguishes them from other metallic compounds, covalent semiconductors and ionic insulators, since in such narrow bands case the electronic correlations play an important role. There are oxides (including the ones some discussed in this work) the properties of which can traverse with change of temperature, magnetic field, external pressure or composition. Naturally, those materials receive the most attention from researchers. The studies of the high-temperature superconductivity (HTSC) in cuprates [2], a colossal magnetoresistance (CMR) in manganites [3] and an unconventional spin-triplet superconductivity and orbital ordered states in ruthenates [4] unveiled the novel physics that had been challenging the fundamentals of our understanding of materials.

Besides providing an excellent case study in solid state physics and a gateway to understanding inorganic solids, this fascinating class of materials is progressing towards practical potential in the real world, where these phenomena can be used for technological applications. These oxidized transition metals have been used in technology for a long time for their versatile optical properties. In the more recent past however, the transition metal oxides with complex lattice structures have been opening new broadways for technological applications, including low-loss energy delivery and quantum computing using superconducting compounds, ultra high-density magnetic data storage thanks to CMR materials, new types of data recording devices using multiferroic compounds, applications in spintronics for TMOs with spin-valve effect and potentially novel current-controlled state switching devices based on iri-

dates. A detailed discussion includes many more examples of the application [5, 6] but is beyond the scope of this thesis. It is obvious though, that the contribution to technological advancements is one of the major factors driving the studies of the exciting physics of transition metal oxides.

1.2 Ruddlesden-Popper series

Transition metal oxides possessing many types of complex structure have been characterized in recent years. Besides well known perovskites, spinels and pyrochlores some low-dimensional structures as well as new three-dimensional mixed frameworks have been intensively studied. Nevertheless, the perovskite-type crystal structure is the building block of many transition metal oxide families and has been of great interest for the past decades due to intensive studies of cuprates, manganites, nickelates, ruthenates, titanates and more recently — iridates. First described for $\text{Sr}_{n+1}\text{Ti}_n\text{O}_{3n+1}$ by Ruddlesden and Popper [7], a series of structural phases was derived from the perovskite structure and is called a *layered perovskite structure*. This series can be described by a general formula $A_{n+1}B_nO_{3n+1}$, where A and B both represent cations, while O represents an anion (oxygen in more specific case), and n denotes the number of layers of octahedra in the perovskite-like stack. An alternative notation of the formula unit is $AO(ABO_3)_n$, illustrating the fact that n perovskite layers are stacked between rock-salt $A-O$ layers along the crystallographic c -axis [8]. In these compounds the n sheets of metallic $B-O$ layer form an insulated building block, separated by $A-O$ layers as shown on a reference tetragonal structure in figure 1.1. The A cations are characterized by cuboctahedral anionic coordination with the coordination number 12 and are included into the perovskite-like stack. The B cations are located inside the anionic octahedra. A progression of n from 1 to infinity corresponds to change of dimensionality of the compounds, with the three-dimensional character increasing with increasing n , and there are known existing stoichiometric compounds with $n = 1, 2, 3, 4$ and $n = \infty$. This makes the Ruddlesden-Popper (RP) series an almost perfect model for many different derived structures because of its high susceptibility to alterations by introduction of doping elements, which proved to be a fertile ground for condensed matter physics and material science research.

The nature and size of the cations on the sites A and B significantly influence the structure and properties of the layered compounds from R-P series. The size of the A -site ion affects the cell parameters and the overall structure of these compounds by increasing the inter-layer distance and respectively elongating the c -axis when the ionic size increases. It is generally expected that c -axis is affected more prominently by the size of A -site ion than the a -axis, therefore ionic substitution to this site leads to drastic changes in physical properties associated with inter-layer coupling. Since, the $B-O$ interactions occur predominantly within the plane, the size of a cation at site B is expected to affect a -axis parameter much more strongly. Another factor influencing the behavior of the compounds in these phases is the Jahn–Teller effect (discussed in section 2.1.3), which naturally manifests itself due to octahedral anion environment of the B ion. An example is a high-spin Fe^{+4} ion in $t_{2g}^4e_g^1$ electronic state,

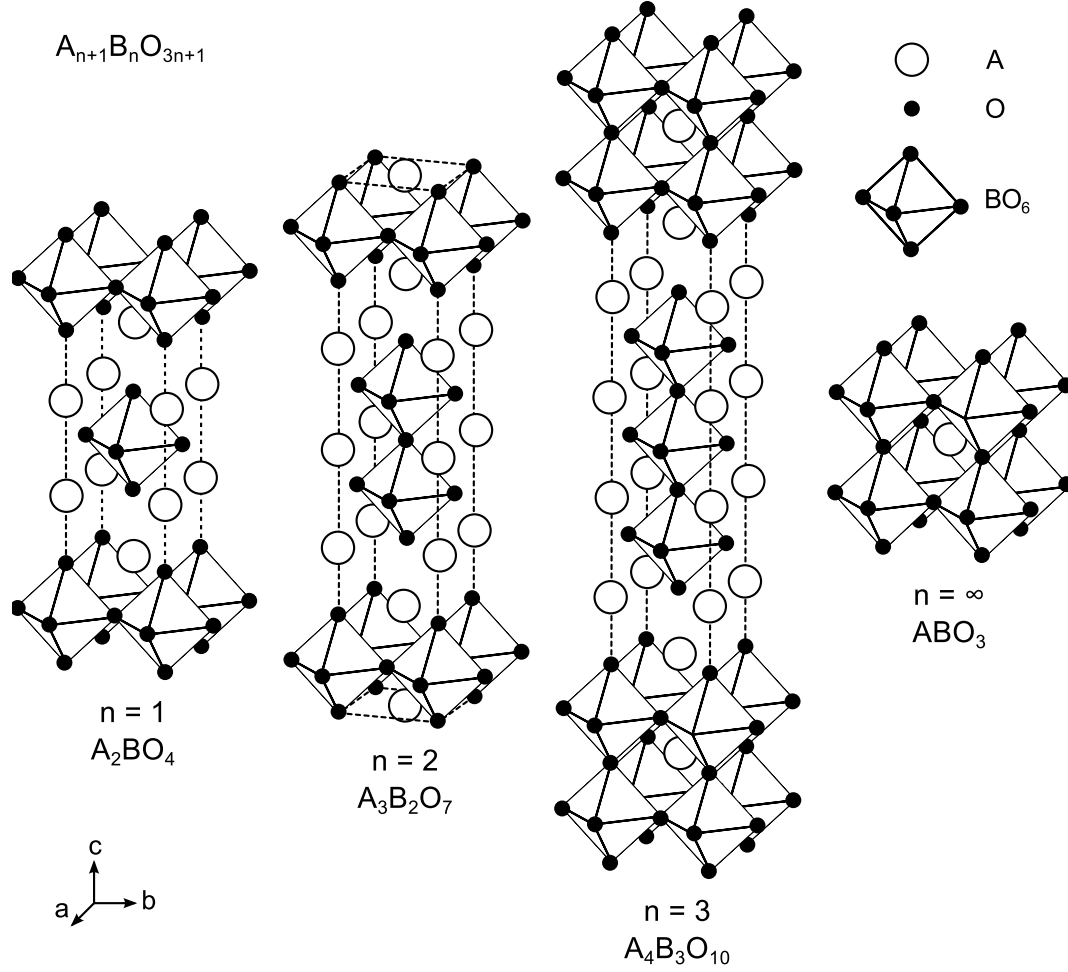


Figure 1.1: Schematic crystal structure of four representatives of the Ruddlesden-Popper series. Dash lines indicate the boundaries of the unit cell. Models produced using VESTA 3 software [9].

which is known to undergo a Jahn–Teller distortion, thus affecting the structural electronic and magnetic properties of compounds [10]. Needless to say, the highly symmetric structures similar to tetrahedral $I4/mmm$ for $n = 1$ (figure 1.1) are formed by a rather narrow range of ionic combinations, while most of the real structures form with significant distortions of the crystal lattice. Obviously, there should be a reasonable limit over which the ionic size can change while maintaining the stability of the overall crystal structure. The formation of an end member of the R-P series — simple perovskite ($n = \infty$) is governed by a *perovskite tolerance factor* t derived by Goldschmidt [11]

$$t = \frac{r_A + r_O}{\sqrt{2}(r_B + r_O)} \quad (1.1)$$

where the r_A , r_B and r_O are respective ionic radii. The criterion provides a reliable

guide when the perovskite-related structures may be expected and has been in use for over a half of century. The compositions with tolerance factors within the range from 0.75 to 1.0 adopt cubic perovskite structure, with $t = 1$ providing the geometrically ideal ratio of $A - O$ and $B - O$ bond lengths. The perovskite structure does allow a rather large degree of mismatch between the equilibrium bonds length though. Small deviations below unity subject the $A - O$ bond to tensile stress and $B - O$ bond to compressive stress, which are relieved by cooperative twisting and tilting distortions of the BO_6 octahedra. The $B - O - B$ bond angle is reduced below 180° in this case, in order to accommodate smaller A -site cations. This also can involve a shift of the A cation position. If the tolerance factor t takes a value greater than unity, the character of the stress reverses — the $B - O$ bond is under tensile stress now, and $A - O$ bond is under compressive stress. As turns out, no cooperative rotations of the corner-shared BO_6 octahedra can relax these stresses and accommodate larger A cations. Instead, hexagonal perovskite structures are adopted, where the columns of face-shared octahedra are formed in order to expand the A -cation sites. This is happening at the expense of the $B - B$ electrostatic Madelung energy across the shared face of the octahedra. These face-shared $B - O - B$ linkages have bond angles of approximately 90° , which can lead to dramatic changes in super-exchange interactions compared with apex-sharing [12]. Gradual change of the tolerance factor leads to a formation of polytypes of hexagonal perovskites with various ratio of face-sharing to corner-sharing octahedra. In the ultimate case the structure consist of one-dimensional columns along c -axis when all the octahedra share faces, as realized in $BaNiO_3$ (2H polytype) [13]. These polytypes are labeled by the number of the BO_6 layers in the unit cell and a letter symmetry tag — R standing for *rhombohedral*, H for *hexagonal*. The complete sequence includes polytypes 3C, 6H, 4H, 9R and 2H as the tolerance factor t increases over unity. The $B - O$ bond length (or ionic radius of B) can be also adjusted by changing the mean oxidation state, either by A -site doping or through the introduction of anion vacancies (oxygen non-stoichiometry) [14]. Also, considering different compressibilities of $A - O$ and $B - O$ bonds, various polytypes can be generated under high pressure. In particular as discussed in following chapters, a significant difference of ionic radii between Ba and Ir leading to extreme value of the tolerance factor is the main cause of the complex crystal structure of $BaIrO_3$ — one of the subjects of this work [15]. Besides the ambient temperature low pressure phase (9R polytype), the successful synthesis of several other high pressure polytypes has been reported [16]. This structure (described in details in section 4.3) is a combination of corner-sharing and face-sharing octahedra, joined into clusters, which are also twisted and buckled in attempt to accommodate large Ba ions.

Several research groups have recently investigated the stability of various structural types of another end member of the R-P series with $n = 1$, using the Goldschmidt tolerance factor t as a criterion. Specifically for A_2BO_4 phase a new tolerance factor on the basis of geometrical matching between the bond distances has

been formulated by B.-H. Chen [17].

$$t_f = \frac{3\sqrt{2}r_O + 2\sqrt{6}(r_A + r_O)}{9(r_B + r_O)} \quad (1.2)$$

Here the notation is equivalent to the one used earlier (expression 1.1). With the ideal value $t = 1$ as in conventional Goldschmidt tolerance factor, the new expression has been proven to successfully work in numerous cases, clearly separating various phases and predicting possible range of existence of stable structures formed by various chemical elements [18]. Thanks to a high interest to the compounds of this series, the vast amount of structural data has been produced over decades, allowing Beznosikov and Aleksandrov [19] to derive a dependence of the lattice parameters on ionic radii of A and B and to determine the allowable ranges of phases formation for higher value of n in their work. It has been found that the probability of existence of the phases with $n = 1, 2, 3$ is almost equal, which means that no formation of a one-layer structure can be predicted for particular combination of ions, if no multilayer structures ($n \rightarrow \infty$) have been successfully synthesized by the time. Correspondingly, the formation of the compounds with $n = 3$ is the most probable for the compositions where the compounds with $n = 1$ and $n = 2$ are known to exist. Worth noting, that even though the authors predicted the synthesis of R-P structures for simple ABO composition with $n > 3$ as hardly probable, the successful synthesis of $\text{Ba}_7\text{Ir}_6\text{O}_{19}$ ($n = 6$) has already been reported [20]. The deviation of t_f from unity also correlates with rotational distortion of the IrO_6 octahedra in the crystal unit cell of Sr_2IrO_4 — the essential factor determining the transport properties in this compound (see section 5.2).

Initially, an evolution of properties of R-P compounds as a function of the number of perovskite layers has been observed on $3d$ based transition metal oxides (see figure 1.2). Particularly, in manganite compounds demonstrating colossal magnetoresistance the temperature dependence of resistivity $\rho(T)$ demonstrated drastically different behavior for the end members of the R-P series [3]. Namely, the compounds are insulating for a single-layer configuration ($n = 1$) and metallic for $n = \infty$. For a multilayer configuration the intermediate behavior is observed where the material is insulating above a critical temperature and metallic below as in the case of $(\text{La}, \text{Sr})_{n+1}\text{Mn}_n\text{O}_{3n+1}$.

In the past several decades $3d$ transition metal oxides have been extensively studied for their extraordinary properties. However, in the last decade the focus has shifted towards the $4d$ electron materials. These are characterized by spatially more extended orbitals, which results in stronger hybridization of neighboring $4d$ and $\text{O } 2p$ orbitals. Likewise, the ground states of R-P series of $4d$ -based oxides are critically linked to the number of layers and structural distortions. The observed physical properties of any member of the series depend sensitively on its structural parameters and a change in dimension through increase or decrease of the number of $B-O$ octahedral layers is promptly reflected in its ground state. This is nicely illustrated on the rich

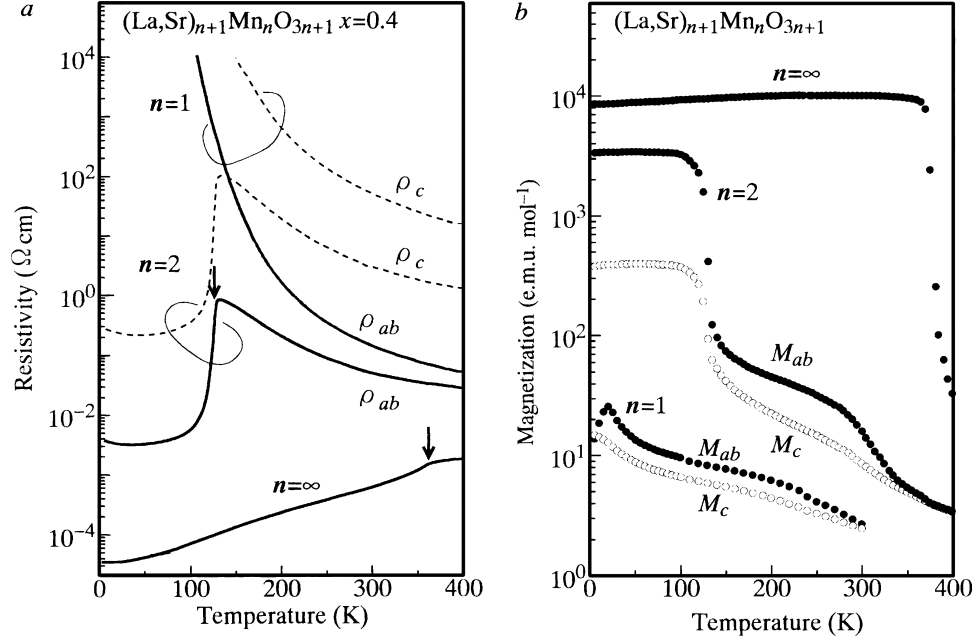


Figure 1.2: Temperature dependence of resistivity (a) and magnetization (b) for members of layered perovskite family $(\text{La,Sr})_{n+1}\text{Mn}_n\text{O}_{3n+1}$, demonstrating a systematic evolution of properties as a function of number of MnO_2 layers. Courtesy of Y. Moritomo [21].

phase diagram for Ca and Sr ruthenates depicted in the figure 1.3. The very narrow bands in $\text{Ca}_{n+1}\text{Ru}_n\text{O}_{3n+1}$ compounds tend to localize the electrons, and therefore the members of the family are at the verge of a metal-nonmetal transition, prone to anti-ferromagnetism. As the dimensionality of the structure increases with n an itinerant flavor develops, the materials start demonstrating a metallic behavior and magnetic interactions are suppressed. On the other hand the $\text{Sr}_{n+1}\text{Ru}_n\text{O}_{3n+1}$ compounds have electronic bands wide enough to exhibit itinerancy and therefore are metallic with a tendency to ferromagnetism (superconducting Sr_2RuO_4 being an exception). As the number of layers increases the ferromagnetic coupling between spins is enhanced in this system. Notable, even though these two systems are isostructural and isoelectronic, the trends for the ordering temperatures are found to be drastically different as the number of perovskite layers n varies.

Although $4d$ -electron based ruthenates still draw a lot of attention, the $5d$ -based compounds is a further departure from well studied $3d$ -electron transition metal oxides. These compounds have even more spatially extended orbitals which leads to a larger bandwidth, therefore we expect weak electron correlation effects and conventional metallic behavior. However, comparable energy scales of the reduced Coulomb interaction, large crystal field and strong spin-orbit interaction promote a vigorous competition between the electronic orders, realizing electronic and magnetic phases in Ir- and Os-based materials that are never previously observed for $3d$ and $4d$

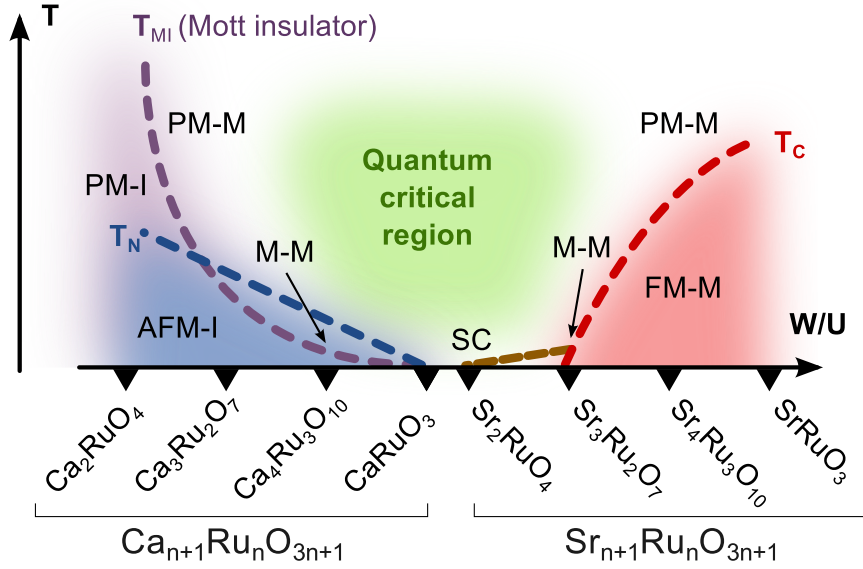


Figure 1.3: A qualitative phase diagram (temperature T vs. bandwidth W/U) of the Ruddlesden-Popper series for Ca- and Sr-based ruthenates. As illustrated, physical properties can be systematically tuned by altering the number of Ru-O layers (n), and the ground state can be readily changed by changing the cation. Here PM stands for paramagnet, FM – ferromagnet, AFM – antiferromagnet, SC – superconductor, M and I are metal and insulator respectively [22].

transition metal oxides. Similarly to their $3d$ and $4d$ counterparts, the iridates of the Ruddlesden-Popper series $\text{Sr}_{n+1}\text{Ir}_n\text{O}_{3n+1}$ also display a systematic evolution of electronic properties as a function of the number of IrO_2 layers n . The single-layer compound Sr_2IrO_4 is a weak ferromagnetic insulator exhibiting a giant magnetodielectric effect [23], but as n increases the electronic structure progresses toward a metallic ground state, as evidenced by the softening of the charge gap in $\text{Sr}_3\text{Ir}_2\text{O}_7$ ($n = 2$). However even the latter compound remains an insulating weak ferromagnet, demonstrating complicated crossovers in its magnetic behavior [24]. A stable three-layer compound ($n = 3$) so far has been reported to form only at high pressure (about 3.5 GPa), therefore it is not well studied yet [25]. For an end member with ($n = \infty$) a correlated metallic ground state with non-Fermi-liquid behavior is found in SrIrO_3 [26]. In case of $\text{Ba}_{n+1}\text{Ir}_n\text{O}_{3n+1}$ the tolerance factor is rather large ($t \approx 1.051$, as calculated from the ionic radii), therefore BaIrO_3 ($n = \infty$) cannot adopt a high symmetry tetrahedral structure at ambient conditions, but crystallizes into a monoclinic structure with the space group $C2/m$ instead [27]. It is the first known ferromagnetic insulator containing a $5d$ transition metal cation in a ternary oxide, with the Curie temperature $T_C \approx 183$ K, where the ferromagnetic moment is not produced from canting [28]. The high tolerance factor is the reason another end member compound of the same series ($n = 1$) cannot form at ambient pressure, although recently a successful synthesis of polycrystalline samples has been reported

under high pressure of 6 GPa [29]. Recently synthesized compound Ba_2IrO_4 has been found to be isostructural to the Sr-based compound, although without the rotational distortions of the crystal lattice. It has properties of a Mott insulator with antiferromagnetic ground state and very low magnetic moment. The compound also demonstrates an unconventional transport behavior under a high applied pressure and is suspected to be in the vicinity of a marginal quantum critical point (MQCP) [30]. Thus one can see that the $5d$ systems tentatively do follow the general trend of R-P series and indeed become less localized as n increases, because of enhanced inter-layer coupling. However the insulating state and the weak ferromagnetism are totally unexpected ground states in these compounds. It is this unexpected behavior that has prompted the extensive studies of the iridates.

1.3 The case of $5d$ oxides

Identifying the hierarchy of energy scales associated with multiple interacting degrees of freedom is the starting point for understanding the physical properties of transition-metal oxides. As mentioned in previous section, some of the most striking phenomena in solids, such as high-temperature superconductivity and colossal magnetoresistance were found in transition-metal systems involving $3d$ orbitals. These phenomena are closely related to the strong electron-electron correlation, which originates from the on-site Coulomb repulsion between the $3d$ -orbitals electrons. The well localized orbitals in these TMOs yield strongly correlated, narrow bands with a large on-site Coulomb repulsion U and a small bandwidth W . When $W \ll U$, the Coulomb interaction, as the largest energy scale, suppresses the charge motion and the material is found as a Mott insulator (see section 2.5.3), which allows description of the low-energy physics in terms of the remaining spin and orbital degrees of freedom. In case of $W \gtrsim U$, a metal-insulator transition (MIT) occurs, and the system becomes metallic. This also allowed us to understand rather well the magnetism in $3d$ TMOs within the framework of Goodenough–Kanamori–Anderson (see section 2.2), assuming the conservation of spin angular momentum in the virtual charge fluctuations. As predicted, most of the stoichiometric $3d$ TMOs are indeed antiferromagnetic Mott insulators [31]. For a while, relatively low attention was paid to the class of oxides based on $4d$ transition metals. Their orbitals are spatially more extended compared with the $3d$ counterparts, and the on-site Coulomb repulsion is lower, therefore the electron correlation effects were expected to be insignificant. It was found, however, that due to the same extended nature the $4d$ orbitals hybridize more strongly with neighboring orbitals (e.g. oxygen $2p$ orbitals), have relatively larger charge-transfer energy Δ_{pd} and much larger crystal field splitting energy $10Dq$ — all contributing to the numerous intriguing properties of these compounds, such as non-Fermi liquid behavior and spin-triplet superconductivity [32].

Further down the periodic table (Ir, Os, Re, Hf, Pt) the electronic orbitals of $5d$ TMOs are even more extended than in their $4d$ counterparts. The on-site repulsion is reduced to a mere 1–3 eV comparing to 2–10 eV for $3d$ electrons, therefore the Coulomb interactions are expected to play a considerably smaller role. Moreover, the

extended nature of the orbitals leads to significant overlap of the nearest-neighbor ions, resulting in a broad bandwidth W . It was commonly expected that these oxides are more metallic and less magnetic than their $3d$ and $4d$ counterparts, since the Stoner criterion in these conditions favors a metallic, paramagnetic state (see section 2.3). In fact, this is indeed the case in the nearly-ferromagnetic correlated metal SrIrO_3 . However this compound is rather an exception out of the entire class than a rule, since in marked contrast, most of other studied $5d$ TMOs, including iridates, are magnetic insulators e.g. BaIrO_3 , Sr_2IrO_4 , $\text{Sr}_3\text{Ir}_2\text{O}_7$, $\text{Ca}_5\text{Ir}_3\text{O}_{12}$, and Ca_4IrO_6 . Now it has been realized that because of the spatially more extended orbitals in $5d$ systems a regime of vigorous intermediate correlation appears. As the charge on the atomic nucleus (Z) increases, spin-orbit coupling between the nucleus and the electrons increases as $\propto Z^4$, and inherently spin and orbital degrees of freedom become strongly entangled. The energy scale of spin-orbit coupling (λ_{SO}) in $5d$ oxides is estimated to be 0.1–1 eV — significantly higher comparing to 0.01 ÷ 0.1 eV in $3d$ oxides. Because it is now comparable to the on-site Coulomb repulsion energy (≈ 0.6 eV) it is no longer considered a perturbative parameter. In fact, this additional interaction already competes with other energy scales such as the crystal field and the hopping amplitude, and it is capable of modifying the electronic structure of materials resulting in a localized state very different from those in conventional insulators. For example, as was predicted and verified on Sr_2IrO_4 [33, 34], a large spin-orbit interaction splits the $5d$ -band into a fully filled $J_{\text{eff}} = 3/2$ and half-filled $J_{\text{eff}} = 1/2$ bands, where the Fermi level resides in the latter. The bandwidth of the half-filled band is so narrow that even the greatly reduced Coulomb interaction U is strong enough to open an insulating gap, as illustrated on figure 1.4. This leads to a novel spin-orbit interaction induced Mott state, and defines a completely new class of materials supporting this state. The underlying physics here is not a simple extension of the physics of $3d$ transition metal oxides to a reduced U regime, but presumes a new paradigm to understand its mechanisms. This is still a largely unexplored domain, but as it attracts more attention of the researchers the tantalizing new phenomena have already been glimpsed.

In case of materials with anomalous, novel electronic states like the highly insulating state in Sr_2IrO_4 , disturbing the ground state with various perturbations allows to test its robustness and infer the conclusion about the possible mechanisms responsible for these states. One of the approaches is dilute doping with impurities. Considering the competing energies, a decision is made whether we want to tune the spin-orbit coupling or crystal field in the material, or perhaps perform a charge carrier doping — the ionic substitution needs to be done on respective ionic sites and with a choice of appropriate elements. Introducing oxygen vacancies in Sr_2IrO_4 is one of the approaches, acting in two directions at once. First effect of oxygen depletion results in electron doping in the insulating state. According to LDA+SO+U band-structure calculations additional electrons will occupy states in four symmetric pockets located near the M points of the basal plane of the Brillouin zone. Each pocket has an estimated filling of 2 % of the Brillouin zone for $\delta = 0.04$ [35]. The situation appears analogous to doping oxygen vacancies in strongly correlated $(\text{La}_{1-x}\text{Sr}_x)_2\text{CuO}_{4-\delta}$ (where the pockets of similar shape arise at the same positions in the Brillouin zone) and $\text{La}_2\text{CuO}_{4-\delta}$,

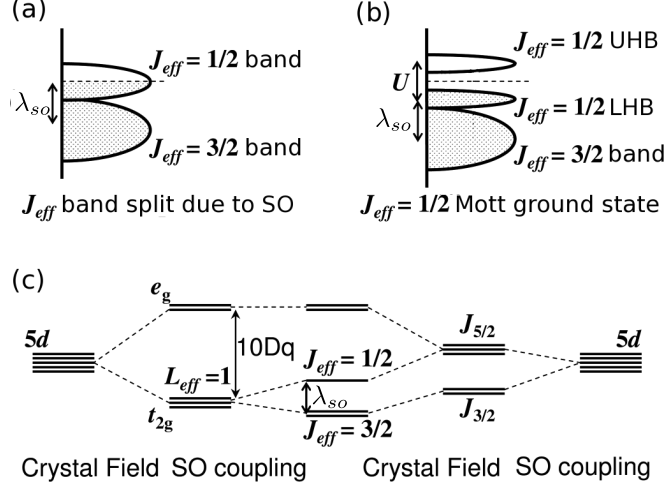


Figure 1.4: Schematic energy diagrams for the $5d^5 t_{2g}^5$ configuration illustrating the removal of orbital degeneracy and bands splitting (a) with spin-orbit coupling λ_{SO} but no Coulomb repulsion U , (b) with λ_{SO} and U , (c) $5d$ -level splittings by the crystal field $10Dq$ and spin-orbit coupling λ_{SO} . Adopted from [33].

which at a time resulted in the appearance of superconducting phase [36]. The fundamental difference is the type of carriers, since in case of cuprates the added carriers were holes. Another effect from the oxygen depletion is a structural disorder, which has its own consequences discussed in the last chapter.

Similarly, the case of BaIrO_3 is no less intriguing. Despite a semiconductor-like behavior of this compound, its low-temperature insulating state is not simple semiconducting, but is thought to be the consequence of a complex ground state with three order parameters — charge density wave (CDW), spin density wave (SDW) and magnetization [37, 38]. The band-structure calculations for this material show a presence of a sharp peak in the density of states (DOS) near the Fermi level, suggesting that the system is in fact on a verge of metallic state, and the insulating behavior of this compound originates from weak localization of the carriers due to disorder in the complex crystal structure [39]. The motivation for doping the BaIrO_3 with rare-earth ions, which have smaller ionic size than Ba, is a further development of the previous successful work [40] to relax the crystal structure in anticipation of recovering the metallic behavior of this compound. The measurements under high hydrostatic pressure follow double purpose in this work. First of all, pressure is a sensitive tool to probe the magnetic states and which could provide the information about the type of magnetic ordering (see section 2.4), especially in a material so sensitive to structural distortions like BaIrO_3 . The second goal is to probe the robustness of the new electronic ground state which resulting from dilute impurity doping, in order to better understand the physics responsible for the change of behavior.

1.4 Structure of the thesis

In this thesis, I discuss the physical properties of some of the representatives of iridium-based oxides family. As a result of strong correlations between the charge carriers and strong spin-orbit interaction these compounds exhibit rather unconventional transport properties. In particular, the materials exhibit anomalous insulating properties where they are expected to be metallic. In attempt to recover the metallic state and probe its robustness we used chemical doping, induced post-growth oxygen deficiency and application of high external hydrostatic pressure.

The thesis consists of five chapters. A brief introduction to strongly correlated transition metal oxides, Ruddlesden-Popper series and our motivation for studying iridates is given in Chapter 1. A theoretical background covering the important concepts of magnetism, spin-orbit coupling and metal-insulator transitions closely related to this study is included in Chapter 2. This should prepare the reader to the following discussion of the real physical properties of studied compounds. The concise description of the experimental techniques available in our lab and used in this work for characterization of the properties is presented in Chapter 3. These include magnetization, electrical transport and thermodynamic properties measurements, as well as the studies under an applied high hydrostatic pressure. The justification of the need for single crystals and brief introduction to growth techniques used for synthesis of the studied compounds as well as their structural characterization are also included in this chapter. Chapters 4 and 5 cover the experimental results and discussion part of the thesis. In this part of the thesis I report the unconventional physical phenomena observed in iridate-based compounds. In Chapter 6 I present the inferences from the experimental observations that lead to some important conclusions drawn from the results. This chapter also outlines some prospects for follow-up research.

Chapter 2 THEORETICAL CONCEPTS

2.1 Magnetism

Most of the solids are considered "non-magnetic", which presumes that these materials develop a magnetic moment only due to applied external magnetic field. Typically these effects are weak and disappear once the magnetic field is removed. In a simplistic picture, the magnetic field acts on the moving charges (i.e. electric current), and the magnetic effects in solids can be roughly understood as a consequence of the presence of these charges whether in form of bound to atoms or free electrons. For instance, an electron possesses a spin, which is an elementary magnetic moment interacting with external field. In addition, the bound charges exhibit an orbital momentum, which is contributing another microscopic source of current, also reacting to external field, either reinforcing it (paramagnetism) or fighting it (diamagnetism). The effect of each individual magnetic moment is small if it remains "independent", while the case of collective behavior (a result of mutual interaction of individual magnetic moments) is producing much stronger and robust magnetism. Some of the sources of such interaction are discussed further in this chapter. In the case when the interaction between the charge carriers can be neglected, the magnetism due to electrons is described by Dirac equation, which governs the relativistic quantum dynamics of an electron in a static field (electric field $\mathbf{E} = -\nabla\phi$ and magnetic field $\mathbf{B} = \nabla \times \mathbf{A}$) [41]. In the non-relativistic limit (electron's speeds in a solid are orders of magnitude lower than speed of light c , except for core electrons of heavy elements) one can write the Dirac Hamiltonian in the form

$$\hat{H} = \hat{H}_0 + \hat{H}_S + \hat{H}_{SO} + V(r) \quad (2.1)$$

distinguishing four contributing Hamiltonian terms. \hat{H}_0 is a Hamiltonian of a spinless orbiting particle in a magnetic field. \hat{H}_S is a spin Hamiltonian, \hat{H}_{SO} is the contribution from spin-orbit coupling and $V(r)$ is an electrostatic potential. The Hamiltonian of a spinless particle is also perturbed in magnetic field giving rise to two additional terms.

$$\Delta\hat{H}_0 = \hat{H}_L + \hat{H}_D \quad (2.2)$$

The first term \hat{H}_L is the angular momentum contribution. Usually being dominant, it is known as the paramagnetic term — a positive magnetic susceptibility of an atom in applied magnetic field. The second term is due to diamagnetic moment — a weak negative contribution opposing the applied field. All these terms and their contribution are discussed in great details in common literature [42], whereas I will focus on the important outcomes applicable to this study.

2.1.1 Hund's rules

In the atomic shell model the possible states for an electron are determined by a set of quantum numbers n, l, m_l, m_s , which are known as principle, orbital, orbital magnetic and spin magnetic quantum number respectively. The Pauli exclusion principle states that each quantum state can be occupied by one electron. As long as spin-orbit coupling is not dominant (true for all but very heavy ions) the good quantum numbers are the total orbital and total spin angular momentum for given subshell l :

$$L = \sum m_l \text{ and } S = \sum m_s \quad (2.3)$$

In a typical atom, which has more than one electron, most of these fill up the lower-energy shells, producing both L and S equal to zero. However, there may be partially unfilled higher-energy shells. Thus the total electronic angular momentum of the atom $J = L + S$ will be determined by those outermost shells producing one of $(2L + 1)(2S + 1)$ possible values. These different combinations will cost different amounts of energy, because the choice of spin angular momentum affects the spatial part of the electron wave function, and the orbital momentum affects how the electron travels around the nucleus. The optimal value should allow the electrons to well avoid each other thus minimizing the Coulomb repulsion energy. This is the origin of the semiempirical Hund's rules – a set of principles summarizing the distribution of the electrons among the states of the partially filled shells [43]:

1. The states are occupied to maximize S , means maximum electrons have theirs spins aligned. Electrons with parallel spins avoid each other which reduces the Coulomb repulsion. Hence the ground state of an incomplete shell in a free atom is that of a maximum spin.
2. The states are occupied to maximize the value of L , which means the subshells with maximum $|l|$ are preferential.
3. The total angular momentum J is obtained by combining L and S depending on the level the shell is filled:
 - less than half filled subshell, $J = |L - S|$
 - more than half full subshell, $J = |L + S|$
 - $L = 0$ and $J = S$ if the subshell is exactly half-full

The 3rd rule is an attempt to minimize the spin-orbit energy and is only applicable in the circumstances when that energy is significant over the other energies such as crystal field energy, which will be discussed later. In overall, the Hund's rules help to predict the ground state of an isolated atom by allowing to deduce the effective magnetic moment, but these rules do not tell much about the excited states.

2.1.2 Crystal field environment

In order to understand the interaction of the magnetic ion with its environment it is necessary to consider the shapes of atomic orbitals. Among the first three orbitals s , p and d , only s possesses spherical symmetry, while the others have pronounced angular dependence (figure 2.1). We are going to focus mostly on d -orbital since it plays an essential role in many transition metal compounds.

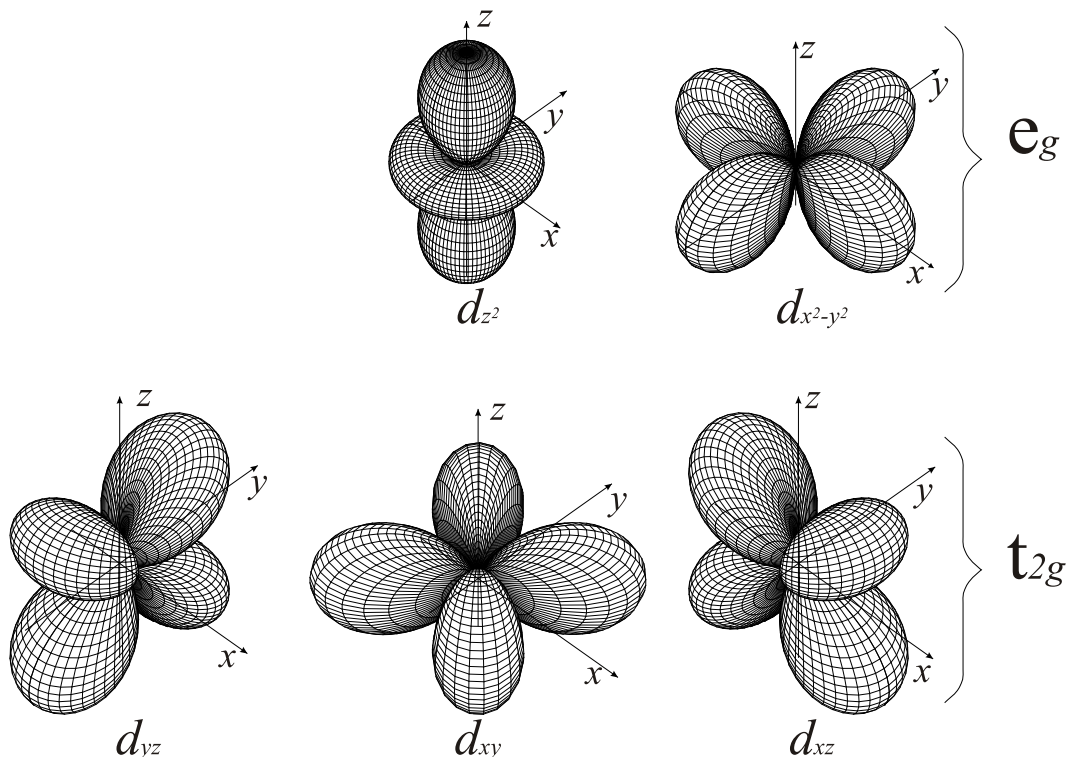


Figure 2.1: Illustration of angular distribution of the d -orbitals.

The d -orbitals fall into two classes, the t_{2g} orbitals (pointing between the x , y and z axes) and e_g orbitals (pointing along the axes of coordinates in Cartesian frame). In the case of the free atom, the d -orbitals will all be energetically degenerate, since the external environment can be approximated as spherically symmetric. However, the energy levels of the atom in a crystal environment will be modified by the field due to neighboring atoms. It is said, that the atom is affected by the *crystal field*. The size and nature of the crystal field depends crucially on the symmetry of the local environment. In oxides the environment is the arrangement of the O^{2-} ions surrounding the transition metal atom. The most common among all the cases are octahedral and tetrahedral environments (figure 2.2), the latter can be conveniently described considering the alternate corners of a cube.

In the case of octahedral coordination, a cation containing some d -electrons is placed in the center of the octahedron, surrounded by 6 anions (oxygen - in oxides, halogen group elements in other compounds). This situation leads to segregation

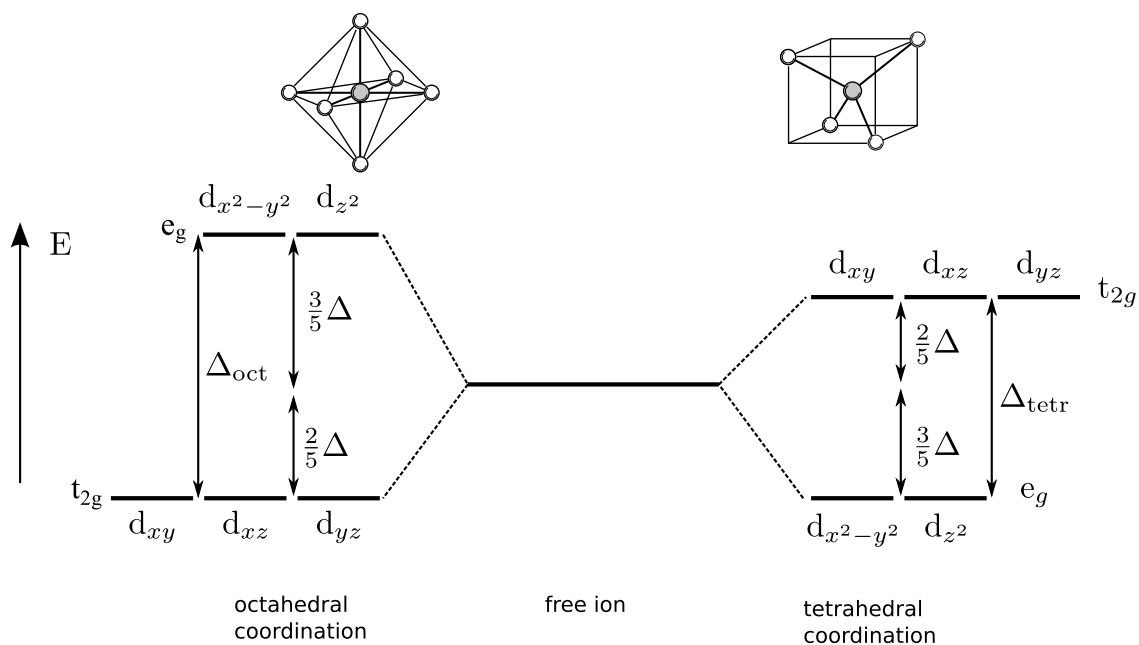


Figure 2.2: Splitting of the electronic d -orbitals due to the crystal field in octahedral and tetrahedral environment

of the negative charge in 6 discrete points in space. This treatment is according to crystal field theory, while the ligand field theory considers the overlap of electron orbitals, which is a more advanced approach. The total electronic energy of all five d -orbitals remains the same, but the degeneracy is removed. Namely, the two-fold e_g levels (with orbitals strongly overlapping with the neighboring p -orbitals of the oxygen anions) are raised in energy and the three-fold t_{2g} levels (pointing in directions between the ions) are lowered in energy (see the left side of figure 2.2). Phenomenologically, wave functions pointing toward O^{2-} ions have higher energy in comparison with those pointing between them. The exact value of splitting strongly depends on configuration of the crystal field. In some other configurations the picture might be the opposite to the one occurring in octahedral coordination. A tetragonal environment is a good example here (figure 2.2, right panel), where the e_g orbitals now have little overlap with the anions orbitals, and have lower energy. In the same time, the three-fold t_{2g} orbitals are pointing along the lines connecting cation-anion and are raised in energy due to significant amount of overlap. Since the degeneracy of the d -orbitals is removed, it would be obvious to expect the filling of these orbitals to start from low-energy sites and continue to higher-energy. In reality the filling arrangement depends on the competition of crystal field energy with the Coulomb repulsion described in form of Hund's rules above. There are two distinct cases here. Weak-field case: the crystal field energy is lower than the pairing energy, every orbital is occupied before any double-occupancy occurs. In the strong-field case the electrons will double occupy all the low-energy orbitals before occupying higher-energy sites, since the crystal field energy is high enough.

2.1.3 Jahn-Teller Effect

The crystal field environment described by highly symmetric octahedral or tetrahedral environments is not always the case. Various factors such as alternative valency, point-like defects of crystal structure and external uniaxial pressure applied to a solid may lead to additional distortion of the environment. Because each orbital has different anisotropy of the wave function, it is coupled to the displacement of the atoms surrounding the transition-metal ion. The levels-splitting picture becomes substantially more complicated, because now the e_g and t_{2g} group of orbitals may also become nondegenerate (see figure 2.3). For example, when the two apical atoms move away from the ion, the energy of d_{z^2} becomes lower than that of $d_{x^2-y^2}$ and the degeneracy is lifted. Exact opposite of this happens when the octahedra is distorted by a compression along the z -axis — the d_{xy} level of the t_{2g} and $d_{x^2-y^2}$ of the e_g become lower in energy scale than the respective z counterparts.

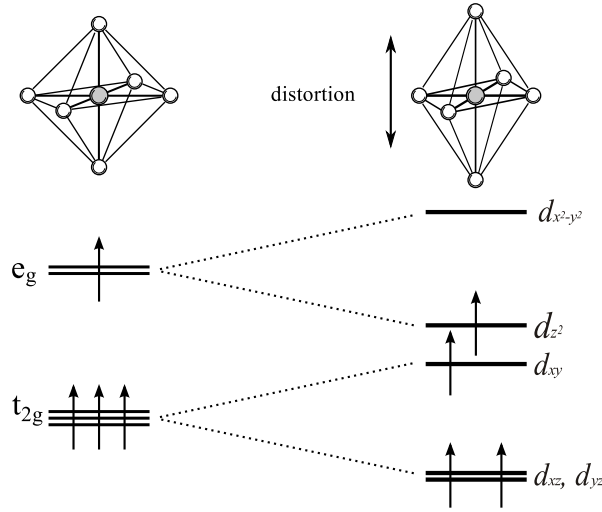


Figure 2.3: The illustration of the Jahn-Teller effect on example of Mn^{3+} ($3d^4$). The distortion of an octahedral complex leads to splitting of the t_{2g} and e_g levels. The energy saving comes from the lowering of the single-occupied e_g level. The energy gain from the lowering of the d_{xz} and d_{yz} is balanced by the raising of the d_{xy} level. Courtesy of [42].

Depending on the population of the electronic levels of a particular ion this can give a significant electronic energy savings. In some cases this reduction of energy can balance the elastic energy of distortion so it becomes energetically favorable for the octahedral complex to distort. Such a phenomenon of the spontaneous distortion of the crystal structure is known as the *Jahn-Teller effect*. By conventional classification several types of this effect are distinguished [44]. Static Jahn-Teller effect: spontaneously occurred distortion is fixed on a particular axis of an octahedron and is permanently present in a crystal. Dynamic Jahn-Teller effect: originates from the special coupling to vibrational modes and low frequency electronic motion. The dis-

tortion occurs along different axes depending on temperature and may involve rapid hopping of the distortion from site to site (for materials involving ions with mixed valency). Cooperative Jahn-Teller distortion: spontaneous transition throughout the crystal at certain temperature. Because the Jahn-Teller effect occurs due to lattice-orbital coupling only, it is independent of spin and spin ordering temperatures, and the cooperative distortion may exhibit a thermal hysteresis [45].

2.1.4 Spin-orbit coupling

The spin-orbit interaction is another well-known phenomenon that causes a lifting of degeneracy of one-electron energy levels in atoms of solids. It is an important degree of freedom in transition metal oxide compounds, affecting the metal-insulator transitions and other properties such as high-temperature superconductivity and colossal magnetoresistance. In a nutshell it is the effect the electron's magnetic dipole moment experiences from the magnetic field generated by the electron's orbit around the nucleus.

In the electron's instantaneous rest frame the nucleus with a charge Ze orbiting around it creates a magnetic field of a magnitude

$$B = \frac{\mu_0 I}{2r} \quad (2.4)$$

where $I = Ze/T$ is effective current from the charge orbiting with a period T in a hydrogen-like atom. On the other hand the orbital angular momentum of the electron (in the nucleus rest frame) is $L = rmv = 2\pi mr^2/T$ and points in the same direction as B . Hence, using $c = 1/\sqrt{\epsilon_0\mu_0}$ the expression 2.4 becomes

$$\mathbf{B} = \frac{1}{4\pi\epsilon_0} \frac{Ze}{mc^2 r^3} \mathbf{L} \quad (2.5)$$

This magnetic field interacts with the spin of the electron to create additional term in the Hamiltonian

$$\hat{H}_{SO} = -\frac{1}{2} \mathbf{m} \cdot \mathbf{B} \quad (2.6)$$

where the factor $\frac{1}{2}$ is the relativistic kinematic correction, known as Thomas precession, which takes care of the fact that the rest frame of electron in which the analysis started is not an inertial system [46]. Using the magnetic moment of the electron $\mathbf{m} = -(e/m)\mathbf{S}$ and the expression for magnetic field 2.5, one obtains the expression for the spin-orbit interaction:

$$\hat{H}_{SO} = \left(\frac{Ze^2}{8\pi\epsilon_0} \right) \frac{1}{m^2 c^2 r^3} \mathbf{S} \cdot \mathbf{L} \quad (2.7)$$

In the presence of spin-orbit coupling the Hamiltonian does not commute with \mathbf{S} and \mathbf{L} , so the spin and orbital momenta are not separately conserved. However \hat{H}_{SO}

does commute with L^2 , S^2 and the total angular momentum $\mathbf{J} = \mathbf{L} + \mathbf{S}$, all of which are now “good” states to use in perturbation theory. Now

$$\mathbf{L} \cdot \mathbf{S} = \frac{1}{2}(J^2 - L^2 - S^2) \quad (2.8)$$

and therefore the eigenvalues of $\mathbf{L} \cdot \mathbf{S}$ are

$$\frac{\hbar^2}{2}[j(j+1) - l(l+1) - s(s+1)] \quad (2.9)$$

and for electronic states with quantum numbers l and n [42] the expectation value of $1/r^3$ is

$$\left\langle \frac{1}{r^3} \right\rangle = \frac{Z^3}{l(l+1/2)(l+1)n^3a^3} \quad (2.10)$$

Using $s = 1/2$ for electron, the energy splitting due to interaction between the spin and orbital part of electron’s wave function in an atom can be calculated.

$$E_{SO} = \langle \hat{H}_{SO} \rangle = \frac{e^2}{8\pi\epsilon_0} \frac{Z^4}{m^2c^2} \left\{ \frac{(\hbar/2)[j(j+1) - l(l+1) - s(s+1)]}{l(l+1/2)(l+1)n^3a^3} \right\} \quad (2.11)$$

This approximation holds as long as the orbital magnetic field is substantially smaller than external applied field $B_{int} > B_{ext}$. Otherwise, the shift of the energy levels due to Zeeman effect (or the Paschen-Back effect for $B_{ext} \gg B_{int}$) disrupts the SO splitting and dominates [46].

As seen, the value of spin-orbit interaction is proportional to Z_{eff}^4 (the effective atomic number), so it plays a role in the properties of transition metal oxides. In magnetic oxides based on $3d$ transition metal ions, the energy scale of spin-orbit coupling is usually substantially smaller than those of crystal field splitting and on-site Coulomb repulsion U , therefore Hund’s rules (see section 2.1.1) determine the ground state values of L (except when its value is quenched) and S . SO coupling here can be treated as a smaller perturbation, a primal role of which is to give rise to a magnetic anisotropy. Nevertheless, the orbital degree of freedom and its coupling with charge, spin, and lattice dynamics plays a crucial role in understanding the metal-insulator transitions and colossal magnetoresistance properties of manganates [47] and high-temperature superconductivity of cuprates [48]. SO coupling in $4f$ compounds is much larger than the crystal field, so J is completely determined by the sign of spin-orbit interaction. Besides much larger Z_{eff} , the reason for this is also that $4f$ wave functions are very localized and the orbitals are hidden deep below $5p$ and $6s$ shells. As a result, the $4f$ -ions are much less sensitive to crystal potential than their $3d$ counterparts and crystal field is a smaller perturbation in these compounds [49]. The SO splitting and crystal field splitting energies in $4d$ and $5d$ compounds are often comparable which results in complicated interplay of properties and unexpected ground states. Known examples are the highly anisotropic magnetic properties of some ruthenium-based oxides of the Ruddlesden-Popper series [50, 51, 52] and iridates, the subject of this work.

2.2 Exchange interactions

The interpretation of magnetic properties of an insulating solid utilizes two important concepts. The first is that discrete magnetic moments are associated with ions of a solid, and the second is that these microscopic moments interact mutually not only through the ordinary dipole-dipole forces (as these are far too weak) [42], but through quantum-mechanical forces — *exchange interactions*. The exchange forces lie at the core of phenomenon of long-range magnetic order, and depending on the separation and spatial arrangement of the localized magnetic moments these can lead to the variety of magnetic order in solids. A bulk magnetic moment is the net effect of competing influences between the thermal energy tending to randomize the alignment and the ordering influence, where the latter depends on the type of magnetism. As the temperature is reduced, the thermal excitations decrease and spontaneous cooperative magnetic order is established below a certain point. Depending on the context, the quantum-mechanical couplings responsible for cooperative magnetism are described metaphorically in different ways, however they all are a manifestation of the Pauli exclusion principle and the Coulomb interaction (see figure 2.4).

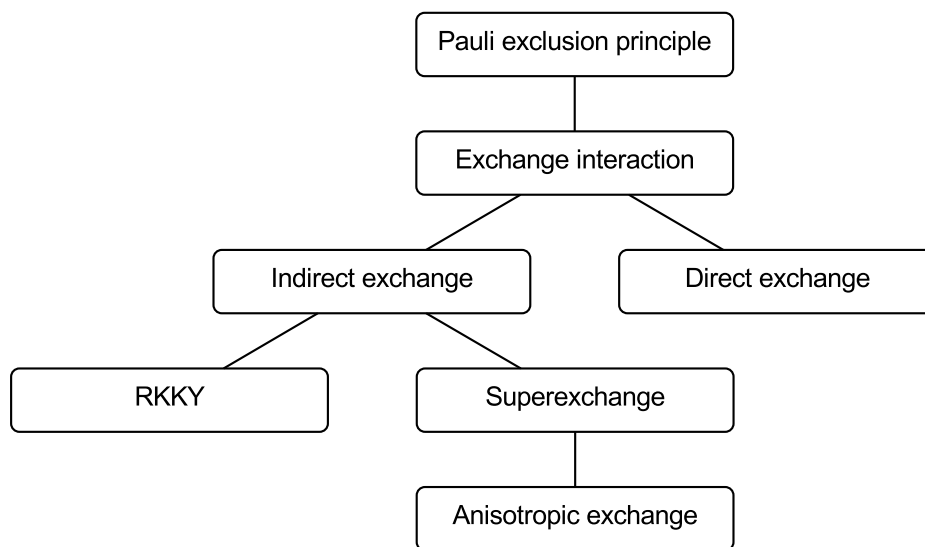


Figure 2.4: Hierarchy of exchange coupling. Pauli exclusion principle is the basis of all exchange forces and the exchange interaction is a metaphorical description of its effect on the Coulomb repulsion. Based on [43].

2.2.1 Direct exchange

In order to produce the long range magnetic order, the magnetic moments of individual ions need to interact with each other. The direct coupling through the chemical bonding between two magnetic atoms that are close enough to have significant overlap of their wave functions is called a *direct exchange* interaction. It originates from

the Coulomb electrostatic interaction and is the result of the energy savings due to distributing the charges further apart. Such direct, through-space interactions are too weak to produce a robust long-range magnetic order, therefore in most of cases some other processes are responsible. Nevertheless, it is advisable to introduce this mechanism for educational purpose before considering more advanced cases.

The energy difference between the singlet ($S=0$) and triple ($S=1$) states of the combined system can be expressed as

$$\Delta E = 2K - 4St \quad (2.12)$$

The first and the second terms are potential and kinetic exchange terms respectively. The potential exchange term $2K$ arises from the Pauli principle (requirement of antisymmetry of the total wave function) and leads to the Hund's rules which results in high-spin ground state of the system of electrons. Thus, the effect of this term is a ferromagnetic alignment. The kinetic exchange term involves the overlap integral S of the two orbitals and the resonance integral t between those. Because the energy difference ΔE becomes negative when the second term increases it leads to stabilization of the system when the spins are opposed (bonding which produces the overlapping of the orbitals becomes more stable). Herein, the kinetic exchange term is antiferromagnetic in sign.

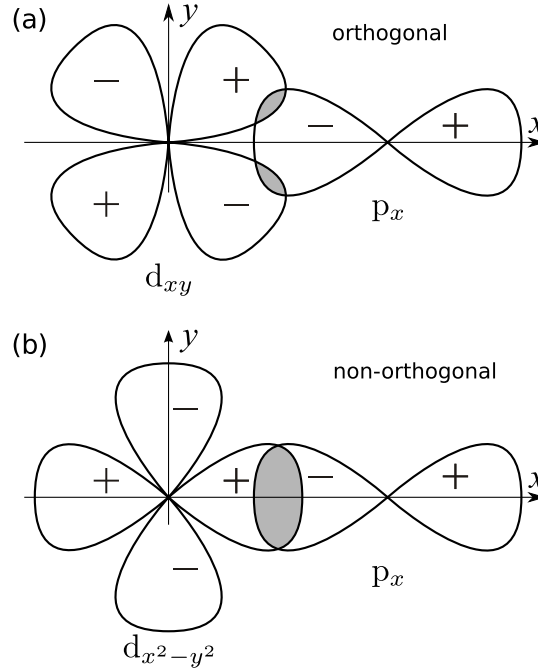


Figure 2.5: Schematic illustration of the symmetry relations between various d and p orbitals [53]

The antiferromagnetic and ferromagnetic types of interaction arise in different circumstances. These different cases are defined by so called *orthogonality rule*, demon-

strated in a diagram 2.5. When the orbitals on different magnetic ions are orthogonal (panel (a) figure 2.5) only the potential exchange term contributes, and ferromagnetic coupling is expected. In case of substantial overlap between the orbitals, the kinetic exchange term dominates and the antiferromagnetic coupling occurs. The simple rule to determine the orthogonality is to flip the whole system about the line joining two ions. If the total sign of the system changes to the opposite (means the signs of the two individual orbitals change differently) the system is considered to be orthogonal, and nonorthogonal if the sign remains the same (panel (b) of figure 2.5). Herein, the mutually orthogonal orbitals always couple ferromagnetically and the nonorthogonal configuration results in antiferromagnetic coupling.

As an alternative explanation of the exchange interaction the Heisenberg model of two electronic states [42] serves very well. The spatial coordinates of the electrons are $\mathbf{r}_1, \mathbf{r}_2$ and the corresponding wave functions $\psi_a(\mathbf{r}_1), \psi_b(\mathbf{r}_2)$. The joint wave function is, obviously, $\psi_a(\mathbf{r}_1)\psi_b(\mathbf{r}_2)$, but it does not obey the particle exchange symmetry, therefore symmetrized and antisymmetrized product states are used later. Writing down the total wave function of the singlet state χ_S ($\mathbf{S} = 0$) and the triplet state χ_T ($\mathbf{S} = 1$) including both spatial and spin parts.

$$\begin{aligned}\Psi_S &= \frac{1}{\sqrt{2}} [\psi_a(\mathbf{r}_1)\psi_b(\mathbf{r}_2) + \psi_a(\mathbf{r}_2)\psi_b(\mathbf{r}_1)] \chi_S \\ \Psi_T &= \frac{1}{\sqrt{2}} [\psi_a(\mathbf{r}_1)\psi_b(\mathbf{r}_2) - \psi_a(\mathbf{r}_2)\psi_b(\mathbf{r}_1)] \chi_T\end{aligned}\quad (2.13)$$

The corresponding energies of the two possible states are

$$\begin{aligned}E_S &= \int \Psi_S^* \hat{H} \Psi_S d\mathbf{r}_1 d\mathbf{r}_2 \\ E_T &= \int \Psi_T^* \hat{H} \Psi_T d\mathbf{r}_1 d\mathbf{r}_2\end{aligned}\quad (2.14)$$

The spin parts of the wave function χ_S, χ_T are assumed to be normalized. Herein, the energy difference between the spin states

$$E_S - E_T = 2 \int \psi_a(\mathbf{r}_1)\psi_b(\mathbf{r}_2) \hat{H} \psi_a(\mathbf{r}_2)\psi_b(\mathbf{r}_1) d\mathbf{r}_1 d\mathbf{r}_2 \quad (2.15)$$

Considering the last equation the exchange integral (or exchange constant), J is defined by

$$J = \frac{E_S - E_T}{2} = \int \psi_a(\mathbf{r}_1)\psi_b(\mathbf{r}_2) \hat{H} \psi_a(\mathbf{r}_2)\psi_b(\mathbf{r}_1) d\mathbf{r}_1 d\mathbf{r}_2 \quad (2.16)$$

This term is used in the spin-dependent part of effective Hamiltonian which accounts for the interactions between nearest-neighbor magnetic moments.

$$\hat{H}^{spin} = -2J\mathbf{S}_1 \cdot \mathbf{S}_2 \quad (2.17)$$

So now one can clearly see the basic principles of direct interaction from the properties of exchange integral J :

$J > 0$, $E_S > E_T$, the energy of the high spin state is favored, which leads to ferromagnetic coupling;

$J < 0$, $E_T > E_S$, the energy of the singlet spin state is lower and therefore favored, thus the antiferromagnetic coupling occurs.

Because this theory describes a magnetic interaction between the localized electrons it would be an adequate model for explaining the magnetic properties of electrically insulating narrow-band ionic and covalent non-molecular solids. However, due to insufficient overlap between the localized neighboring magnetic orbitals, the direct exchange mechanism cannot have a decisive role in controlling the magnetic properties of the TMOs. It is also not applicable for description of the rare-earth based materials with deeply buried f -orbitals. If one considers the $4d$ or $5d$ elements with the spatially extended orbitals then the role of conduction electrons cannot be neglected, and that involves the band structure and is described by completely different models. Historically, the theoretical attempts to estimate the exchange constant on transition metal based compounds using this model, resulted in values far off from the experimentally determined ones [54]. Nevertheless, there have been reports of successful results using this theory to estimate the magnetism associated with unpaired electrons on sp orbitals from defects in semiconductor thin films [55].

2.2.2 Superexchange

As mentioned, the direct exchange is a short-range coupling, and the overlap of the neighboring magnetic ions orbitals is rarely sufficient for this mechanism to work. However, a coupling between two magnetic ions which are too far apart can be also mediated by a non-magnetic ion, which in case of the oxides is oxygen. First suggested by Kramers [56], such indirect exchange interaction is called *superexchange* and originates from admixture of excited states of cations with a ground state of an anion. The excited states are the result of the electron removal from an oxygen ion and placing it on in an empty or half-filled cation orbital [57]. Depending on the mutual configuration and the types of orbitals involved in the process, several models of superexchange are described.

Anderson’s mechanism describes an interaction between the electron on p -shell of the anion and d -shell of the cation. This type of interaction is the strongest when the cation-anion-cation bond is aligned on $\sim 180^\circ$ (see figure 2.6 panels (a) and (b)). The type of the coupling, resulting from such interaction depends both on the sign of J (exchange integral) and the “sign of the bond”. The latter term is a conventional characteristics and is determined by the initial occupancy of the d -orbital of the cation. The sign of the bond is defined by the following rule:

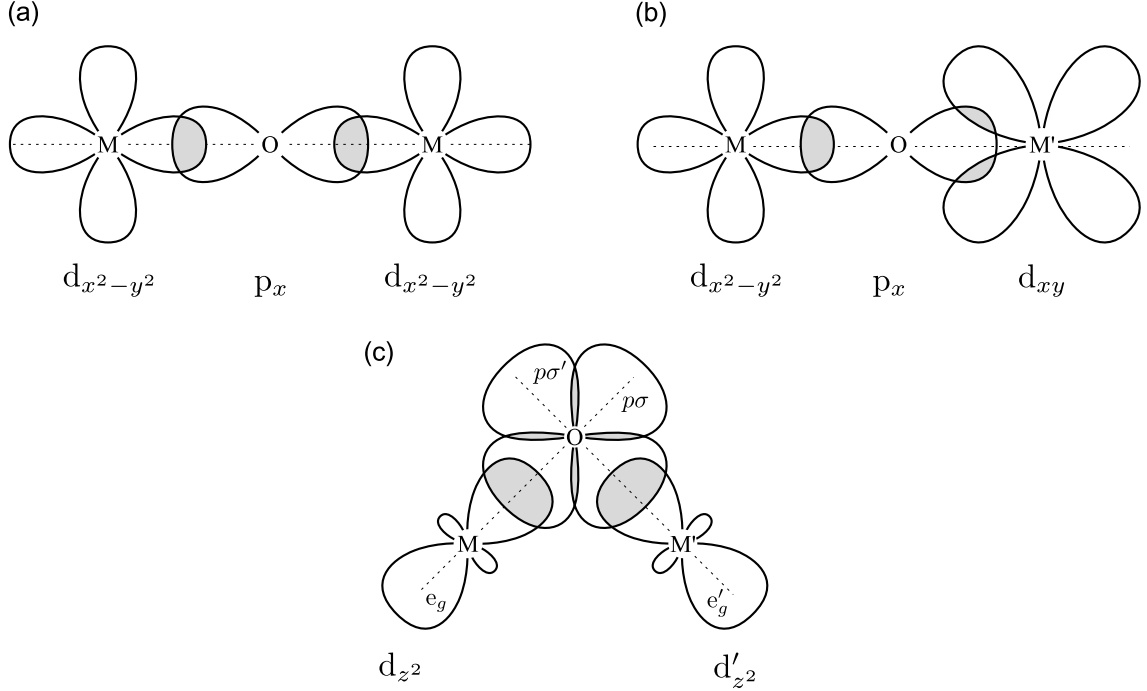


Figure 2.6: Illustration of the in-line and orthogonal orientation of cation-anion-cation chain. Here, 180° case is for (a) same type ions, (b) different type ions and (c) is 90° coordination. M and M' are the ions of different type, thus different d -orbitals take part in interaction.

Negative bond: the cation d -orbital is less than half-filled and the electron transferred from the anion's (p or s) orbital aligns its spin parallel to the spin of all the electrons, which is obvious result from the first Hund's rule, figure 2.7 (a)

Positive bond: the d -orbital is more than half-filled. The transferred electron must align antiparallel to the cation spin because of the Pauli principle, figure 2.7 (b).

Depending on the product of these two factors the superexchange interaction can produce either antiferromagnetic (classical examples: CaMnO_3 , LaCrO_3 , LaFeO_3 , NiO) or much more rarely ferromagnetic interaction (theoretical example is $\text{Ni}^{2+}-\text{O}^{2-}-\text{V}^{2+}$) [53]. As a generalization of this mechanism, the antiferromagnetic interaction is expected between the cations of the same type. If the interaction takes place between the cations with different populations of the d -orbitals (i.e. more-than-half-versus less-than-half-filled) the preferable coupling will be ferromagnetic [53].

Another model is the **Slater's mechanism**, which takes into account the polarization of the electron cloud of the anion through the exchange interaction with the cations. The sign of superexchange interaction here is the product of the signs of two simultaneous polarizations multiplied further by “-” sign, which arises from the Pauli principle within the intervening anion orbital [53]. A variation of this is the **Goodenough's mechanism**, which takes into account the simultaneous partial

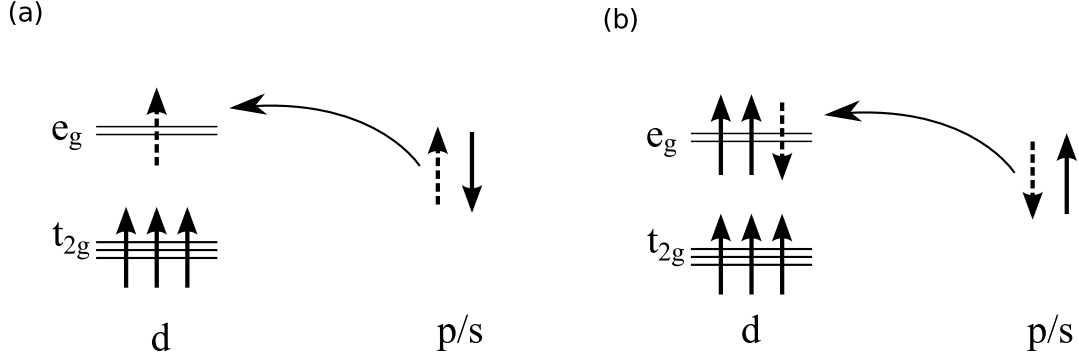


Figure 2.7: Formation of the negative (a) and positive (b) bonds at admixture of excited states with the ground state [57].

bond formation of the anion with the cations on both side. The net sign in this mechanism is the product of the signs of the two simultaneous bonds, multiplied further by “−” sign, which arises from the Pauli principle within the intervening anion orbital (similarly to Slater’s mechanism) [53, 57].

The models described above are also applicable to the 90° interaction between magnetic ions (figure 2.6 (c)), although the situation and resulting coupling is quite different from 180° case. The formation of two partial covalent bonds $p\sigma-d_{z^2}$ and $p\sigma'-d'_{z^2}$ occurs simultaneously [58]. The sign of these is determined by same rule as described in the Anderson’s model. The $p\sigma$ and $p\sigma'$ orbitals interact through direct exchange, and because these orbitals are mutually orthogonal the sign of interaction is positive, therefore they are ferromagnetically coupled. However, contrary to the 180° case, here the antiferromagnetic interaction is expected between a cation with a less-than-half filled d -shell and a cation with more-than-half filled d -shell. Similarly, the superexchange interaction between identical cations through 90° angle, results in the ferromagnetic coupling, quite opposite to 180° case. Thus, using the symmetry relations and electron occupancy of the overlapping atomic orbitals plus the Pauli exclusion principle a set of semi-empirical principles were developed in the 1950s by Goodenough and Kanamori [53, 57, 59], naturally referred nowadays as the *Goodenough-Kanamori rules*. These rules have proven to be highly successful in rationalizing the magnetic properties of a wide range of materials on a qualitative level. However in a number of cases the situation develops beyond these rules for an obvious reason. Among those are the cases when various types of exchange mechanisms compete with one another (i.e. exchange through the second nearest neighbor), when the bond coordination deviates from strict inline or orthogonal case, in case of dynamical electron orbital occupancy, or when a strong *spin-orbit* coupling takes place (see Section 2.1.4).

Double exchange proposed by Zener [60], is essentially a mechanism of superexchange for an extended system, where a magnetic ordering breaks the isolation

of magnetic ions. It takes place only in an environment containing ions of more than one oxidation state (example Mn^{+3} , Mn^{+4}). For example, in case of $\text{La}_{1-x}\text{A}_x\text{MnO}_3$ ($0 \leq x \leq 1$) the e_g electron could hop to the neighboring ion with a vacancy on the same energy level, contributing to electric conductivity. However, if the ions are antiferromagnetically aligned, the hopping is impossible due to the Pauli exclusion principle, figure 2.8 (b). Both donating and receiving ions have to be ferromagnetically aligned for effective hopping, which requires additional amount of energy, figure 2.8 (a). These energy savings come from kinetic energy difference, as a result of electron orbital becoming more spatially extended.

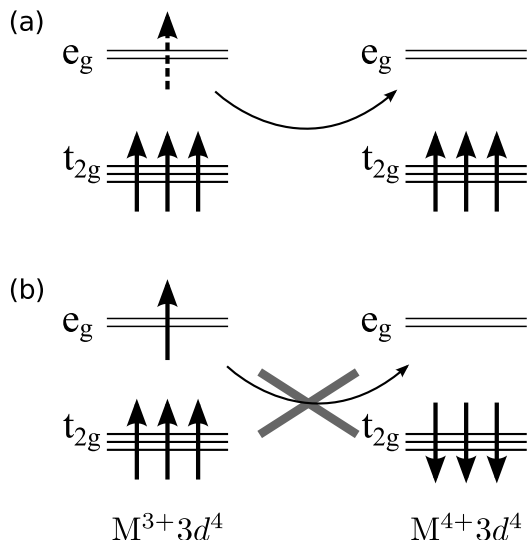


Figure 2.8: Double exchange mechanism gives ferromagnetic coupling between metallic ions with different oxidation states, participating in electron transfer. The single-center exchange interaction favors hopping if (a) neighboring ions are ferromagnetically aligned and prohibits it if (b) neighboring ions are antiferromagnetically aligned [42].

It is worth mentioning, that this mechanism works only if the atoms with different ionizations are randomly distributed throughout the material. If the ions are ordered — the electron hopping is inhibited [57, 61]. The double exchange interaction takes place in a number of oxides, among which are magnetite Fe_3O_4 (the double exchange mechanism was first formulated to explain ferrimagnetic properties of this material [62]) and the compounds from the $\text{La}_{1-x}\text{A}_x\text{MnO}_3$ -family ($0 \leq x \leq 1$, A represents Ca, Sr or Ba). Despite the fact that the electrons have some itineracy here and such interaction mechanism gives rise to high electric conductivity, the band interpretation is not applicable in this case. The reason is that the end compounds from such families of materials, contain the ions of single oxidation state only and are usually magnetic insulators with ferromagnetic order associated with other mechanisms. Only after doping level reaches certain concentration of magnetic ions, the magnetic order switches to double exchange type.

2.2.3 Indirect exchange in metals

The exchange interaction between magnetic ions can be mediated by the itinerant electrons, as has been found in metallic compounds containing localized magnetic moments. This type of interaction is unique because the sign of the exchange integral J oscillates between positive and negative as a function of interionic separation r_{ij} . A localized magnetic moment polarizes the spins of the conduction electrons and couples to the next-neighbor magnetic moments through this polarization. The reason for the oscillatory polarization is that the conduction electrons tend to screen the magnetic moment of the ion by means of their spins. Such mechanism of indirect interaction is named RKKY by the names of its principal investigators — Ruderman, Kittel [63], Kasuya [64], Yoshida [65]. The interaction between local magnetic moments S_i and S_j is given by

$$\hat{H}_{\text{RKKY}} = \sum_{i=0}^n J_{ij} S_i \cdot S_j \quad (2.18)$$

where the exchange constant dependence J_{ij} has the form of

$$J_{ij} = N_F \frac{2k_F |r_i - r_j| \cos 2k_F |r_j| - \sin 2k_F |r_i - r_j|}{(2k_F |r_i - r_j|)^4} \quad (2.19)$$

Here k_F is the Fermi surface wave number and N_F is the density of states at the Fermi level E_F [66, 42]. Thus, assuming a spherical Fermi surface of radius k_F , the magnetization of the electron gas at large distances ($R = |r_i - r_j| \gg k_F^{-1}$) is proportional to $\cos 2k_F R / R^3$ and has an oscillatory character (figure 2.9). Therefore, a coupling between the neighboring magnetic ions can be ferromagnetic or antiferromagnetic, depending on the range R .

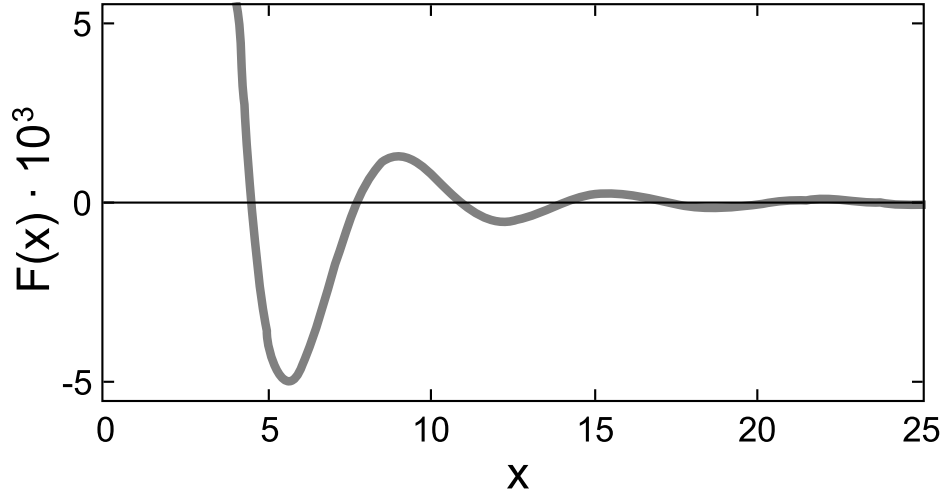


Figure 2.9: A functional dependence describing the real space magnetization of electron gas by a localized magnetic moment.

This type of interaction is used to explain (in some cases partially) the properties of dilute magnetic semiconductors ($\text{Zn}_{1-x}\text{Mn}_x\text{Te}$, $\text{Mn}_x\text{Ge}_{1-x}$) [67, 68, 69]. It is also considered to be mainly responsible for the impurity-impurity interaction in dilute metallic spin-glass alloys, such as Au:Mn , Au:Mn , Au:Fe , Ag:Mn [70, 71, 72]. Typically RKKY is not found in transition metal oxides, although there have been attempts to describe the magnetic interaction between Cu^{2+} spins and p -orbitals of vacancies in superconducting cuprates using this model [73].

2.2.4 Anisotropic exchange interaction

This type of interaction leads to arousal of a weak ferromagnetic component perpendicular to the spin-axis in initially antiferromagnetic material. Initially predicted purely on the ground of symmetry, the Dzyaloshinsky-Moriya (DM) [74, 75, 76] interaction arises from a combined effect of a strong relativistic spin-orbit coupling of the cations and the superexchange interaction. The spin information is being carried between the magnetic ions by the delocalized electrons of superexchange, or by itinerant electrons in RKKY version of DM coupling [77]. The interaction between the DM vector \mathbf{D} (which is proportional to the strength of spin-orbit interaction) and two spins on lattice bond with no inversion center makes the spins cant by a small angle. The additional term that appears in the Hamiltonian at this interaction \hat{H}_{DM} has a form

$$\hat{H}_{DM} = \mathbf{D} \cdot [\mathbf{S}_1 \times \mathbf{S}_2]. \quad (2.20)$$

The form of the interaction is such that it favors the spins \mathbf{S}_1 and \mathbf{S}_2 to be at right angles to the plane perpendicular to the vector \mathbf{D} , in such an orientation to ensure that the energy is negative. The moments \mathbf{S}_1 and \mathbf{S}_2 form separate sublattices with antiferromagnetic alignment, which are equivalent but not exactly antiparallel, resulting in a net magnetic moment. As mentioned above, the crystal symmetry is of particular importance for the anisotropic interaction. For the case of line AB with the midpoint C joining two magnetic cations i and j (see figure 2.10), the following rules describe the direction of \mathbf{D} [44]:

$\mathbf{D} = 0$ if a center of inversion symmetry is located at C .

$\mathbf{D} \perp AB$ if a mirror plane perpendicular to AB passes through C .

$\mathbf{D} \perp$ **mirror plane** if the mirror plane includes AB .

$\mathbf{D} \perp$ **two-fold axis** if the two-fold rotation axis is perpendicular to AB at C .

$\mathbf{D} \parallel AB$ if AB is an n -fold rotation axis ($n \geq 2$).

Simultaneously, \hat{H}_{DM} is opposed by a strong tendency towards ferromagnetic or antiferromagnetic alignment from superexchange interaction, therefore in the typical real life systems the angles are small. However in the systems where the conflict is not strong, the canting angle can be up to $\pi/2$ as was reported for $\beta\text{-MnS}$ [78]. The

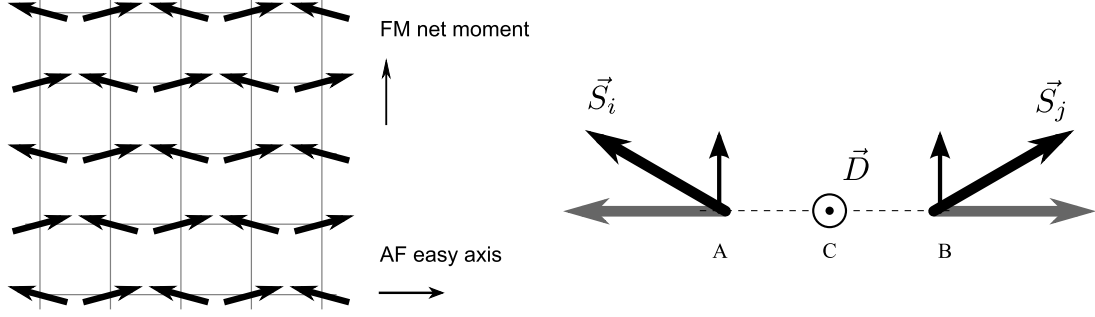


Figure 2.10: Illustration of the spin canting due to the Dzyaloshinsky-Moriya interaction. Weak ferromagnetic (FM) component arises perpendicularly to the spin-axis in initially antiferromagnetic (AF) materials.

classical example of this interaction is a weak ferromagnetic order arising in MnCO_3 , CoCO_3 and $\alpha\text{-Fe}_2\text{O}_3$ compounds [74, 76]. More recently it has been proposed that this interaction also gives rise to a weak ferromagnetism in antiferromagnetic layers of La_2CuO_4 — the parent compound of high-temperature superconductors [79, 80]. DM interaction is considered to be the main motive force behind the most promising multiferroic materials, where noncollinearly coupled magnetic moments through the electron-lattice interaction displace the oxygen cations located between them [81]. In addition, the weak ferromagnetism of Sr_2IrO_4 compound, a subject of this work, has been also ascribed to this mechanism [82].

2.3 Itinerant electron magnetism

In case of metallic d -electron magnetic systems it is not possible to understand the magnetic properties in terms of individual moments coupled by inter-ionic exchange interaction. The conduction electrons are delocalized, can wander freely through the sample and are known as itinerant electrons. The same electrons are responsible for both magnetic moments and exchange interaction through local Coulomb repulsion and kinetic energy. One of the models describing itinerant electron ferromagnetism employs the band theory of solids (the detailed description of which can be found in common literature [83]) and considers the spontaneously-split bands as its origin, known as *band ferromagnetism*. The electrons in this model feel the potential of the other electrons as well as ions, the latter expressed in terms of an average exchange field (molecular field) λM produced by all their neighbors. The electron gas in a metal becomes magnetized by molecular field due to Pauli paramagnetism χ_P [84]. However, as the resulting magnetization in its turn increases the molecular field, at certain conditions such positive feedback mechanism can lead to spontaneous ferromagnetism. Consider an excess of spin-up electrons and the lack of the same number of spin-down electrons due to some reason (no external magnetic field applied). Obviously, only the electrons near the Fermi surface can participate in this process. These electrons will occupy the energy levels up to the value $E_F + \delta E$ with spin-up and $E_F - \delta E$ with

spin-down respectfully as illustrated on figure 2.11.

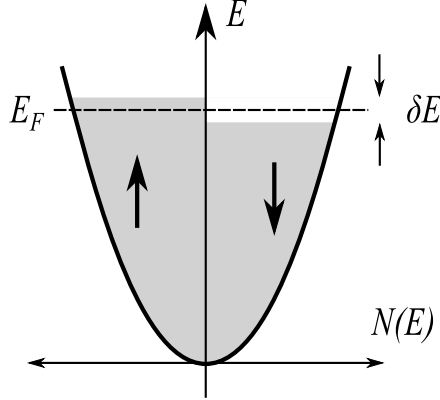


Figure 2.11: Density of states showing spontaneous splitting of energy bands without an applied magnetic field [42].

Thus the number of electrons that flipped their spins up is going to be $N(E_F)\delta E/2$, and they promote their energy by δE . The total kinetic energy change ΔE_{KE} is therefore

$$\Delta E_{KE} = \frac{1}{2}N(E_F)(\delta E)^2 \quad (2.21)$$

This energy demand is balanced by the potential energy reduction due to interaction of the magnetization with molecular field. Consider the number density of up-spins n_\uparrow , down-spins n_\downarrow and corresponding magnetization M , assuming each electron magnetic moment is μ_B .

$$\begin{aligned} n_\uparrow &= \frac{1}{2}(n + N(E_F)\delta E) \\ n_\downarrow &= \frac{1}{2}(n - N(E_F)\delta E) \\ M &= \mu_B(n_\uparrow - n_\downarrow) \end{aligned} \quad (2.22)$$

Herein, the molecular field energy is

$$\Delta E_{PE} = - \int_0^M \mu_0(\lambda M') dM' = -\frac{1}{2}\mu_0\lambda M^2 = -\frac{1}{2}\mu_0\mu_B^2\lambda(n_\uparrow - n_\downarrow)^2 \quad (2.23)$$

Using the expression for Coulomb energy $U = \mu_0\mu_B^2\lambda$, one obtains

$$\Delta E_{PE} = -\frac{1}{2}U(N(E_F)\delta E)^2 \quad (2.24)$$

Summing both terms together yields the total change of energy

$$\Delta E = \Delta E_{PE} + \Delta E_{KE} = -\frac{1}{2}N(E_F)(\delta E)^2(1 - UN(E_F)) \quad (2.25)$$

In order to obtain a spontaneously ordering magnetic system, the energy change needs to be negative, $\Delta E < 0$, which implies

$$UN(E_F) \geq 1 \quad (2.26)$$

The expression 2.26 is known as *Stoner criterion* or sometimes *ferromagnetic instability*. It is clear that such band splitting is favored for large Coulomb exchange interaction energy as well as for large density of states at the Fermi level (high conductivity material). In some materials the Stoner criterion is not satisfied and there no spontaneous ferromagnetism can be achieved, however the susceptibility becomes altered and its value is enhanced compared to the Pauli susceptibility, by a factor $(1 - UN(E_F))^{-1}$. The phenomenon is called Stoner enhancement and is experimentally observed in the metals like Pt and Pd which do not possess spontaneous ferromagnetism but are still treated as a systems on the verge of ordering, since their magnetic susceptibility is significantly enhanced by the large parameter $UN(E_F)$.

2.4 Pressure effect on magnetic ordering

Sensitivity of the collective ordering of magnetic moments to the overlap and charge transfer properties of electronic orbitals through magnetoelastic coupling makes the inter-ionic spacing an important parameter in the study of magnetic and transport properties of transition metal oxides. The dependence of properties on inter-ionic spacing has been experimentally observed in a variety of ways including pressure dependence of magnetic ordering temperature and magnetic susceptibility, thermal expansion measurements, magnetostriction measurements and the chemical pressure effect as a result of ionic substitution. Conveniently, the result of each of these experiments or their combination gives a direct measure of the volume dependence of the magnetic exchange integral [85]. In order to compare the results and generalize the effect on the properties observed in different experiments often the concept of “magnetovolume effect” is used. Since the experimental methods utilized in this study were limited to hydrostatic pressure, the discussion in this section focuses on isotropic “magnetovolume effect” if not mentioned otherwise. The reason for this is that the effect of hydrostatic pressure within reasonable limits is not ordinarily expected to lower the symmetry of a material under study. Therefore it should only change the magnetic ordering temperature (whether it is Curie or Néel temperature) and the magnetic moment, although the change of the latter can be quite different for different crystallographic directions in case of strong magnetic anisotropy.

2.4.1 Pressure effect on superexchange

J.B. Goodenough [86] made the first theoretical prediction about the dependence of the Néel temperature on the inter-ionic distance between the localized moments. The perovskite-like structures were used as a subject of the study, which provided an opportunity to consider 180° cation-anion-cation interactions between the nearest neighbors, while omitting the cation-cation direct interaction term as negligible.

In the localized electron limit, where the superexchange perturbation approach is applicable, his theory gives the following expression for the definition for the Néel temperature [86, 87]:

$$T_N \sim b^2 [U^{-1} + (2\Delta)^{-1}] \quad (2.27)$$

where $b \approx (b^{ca})^2/\Delta$ is metal-metal electron-transfer energy integral (for AMO_3 , Alkali, Metal perovskite), Δ is the anion-cation charge transfer gap (say O-2p and the lowest M-3d) and U is the on-site Coulomb energy. The metal-metal electron-transfer energy integral also contains b^{ca} – an anion-cation back-transfer integral. The first part of the expression 2.27 is the Anderson’s superexchange term [88, 89] and the second involves a two-electron transfer from the anion to each of the interacting cations. This perturbation description for the superexchange spin-spin interaction should break down on the approach to crossover from localized to itinerant electronic behavior. J.B. Goodenough predicted that provided $[U^{-1} + (2\Delta)^{-1}] \approx \text{const}$ the Néel temperature for localized magnetic moments should behave as $dT_N/dr < 0$, where r is inter-ionic distance. In terms of external pressure this expression has a form $dT_N/dP > 0$ [86]. This prediction soon received further experimental support from numerous studies [90, 91, 92], including the ones by D. Bloch, who studied a variation of magnetic ordering temperature T_m with pressure [93]. In his review he collected the data from multiple experiments performed on various magnetic insulating materials, including some oxides (CoO, NiO, MnO), ferrites and garnets¹. The results were expressed in form of a general empirical relationship for the volume dependence of the superexchange integral J .

$$\left(\frac{d \ln J_{i,j}}{d \ln V}\right)_T = a \quad (2.28)$$

Bloch pointed out a tendency toward a value $a \approx 10/3$ for a wide selection of systems. The expression was named a “10/3 Law for the volume dependence of superexchange”. In order to connect the expression directly to external pressure a simple model was developed based on the following assumptions

- the material has a cubic crystal structure;
- ions are restricted in orbital s -states, which allows one to adopt a conventional Heisenberg Hamiltonian and all the volume change effects are considered through the change in exchange integral J_{ij} ;
- the magnetic transition temperature is considered to be a linear function of the exchange constants $T_M = \sum_{i,j} A_{i,j} J_{i,j}$;
- all J_{ij} are assumed to vary equivalently with volume, so there is no i, j dependence in the model.

¹Compounds of the family $5(\text{Fe}_2\text{O}_3)3(\text{RE}_2\text{O}_3)$, where RE is the rare-earth element

All of the above allowed one to do the following transformation.

$$a = \frac{d \ln J_{i,j}}{d \ln V} = \frac{d \ln J_{i,j}}{dp} \bigg/ \frac{1}{V} \frac{dV}{dp} \simeq - \frac{d \ln T_M}{dp} \bigg/ K_T \quad (2.29)$$

where, V is the volume, p is the pressure, K_T is the isothermal compressibility of the material. The expression 2.28 itself was proposed by G.K. White in 1962 [94, 95] as a volume dependence of the spin interaction energy

$$\gamma_m = - \frac{d \ln E_m}{d \ln V} \quad (2.30)$$

γ_m was named a "magnetic Grüneisen constant" by analogy to the Grüneisen constant of lattice vibrational energies [96]. Along with γ_m G.K. White defined γ_e — an electric Grüneisen constant

$$\gamma_e = \frac{d \ln C_e}{d \ln V} \quad (2.31)$$

which represents dependence of the density of states at the Fermi surface (the electronic heat capacity [94]) on volume and becomes useful in discussion of the dependence of itinerant magnetic moments ordering on pressure. The typical values of this constant for some transition metals were determined later [97]. The magnetic Grüneisen constant is applicable to the variety of cases where the dependence of exchange interaction on inter-ionic spacing have been experimentally observed, such as static and dynamic magnetoelastic effects and the effects of thermal expansion behavior on the magnetization [98]. The value $\gamma_m = -10/3$, which D. Bloch found to be common for the multiple simple magnetic insulators, represents a dependence of the exchange constant J on inter-ionic separation r as

$$J_{ij} \propto r^{-n}, \text{ where } n \approx 10 \quad (2.32)$$

The negative sign reveals that the decrease of the distance r between the ions enhances the exchange interaction, while the case of $\gamma_m > 0$ would indicate an opposite effect. In the case of the materials where the superexchange interaction is still (fully or partially) responsible for magnetic ordering but the crystal structure is more complicated than simple cubic, it often found that $|\gamma_m| > 10/3$ ($n \approx 13$ was found in GdCl_3 and LaCl_3 [99]), which expresses even stronger dependence of the exchange constant on volume of the unit cell. It is suggested that in such case γ_m is considered to reflect the combination of volume dependence of several exchange parameters, means not only nearest neighbor relationship, but a second nearest-neighbor or even a third nearest neighbor.

K.C. Johnson and A. J. Sievers [98] were the first trying to provide a theoretical rationalization of the Bloch's "10/3 Law" and calculate the γ_m for some real compounds (MnO and MnF_2 in their case). Depending on the orbitals and the bonding considered, the results obtained were either really close to the ones obtained experimentally (matching 10/3 value) or deviate by up to 30%. Similar result was obtained by K. N. Shrivastava et.al. in another attempt to calculate magnetic Grüneisen γ_m [100].

Moreover, according to their model, the dependence $\ln J$ vs $\ln r$ is not always linear, but γ_m itself might be dependent on inter-ionic separation. Therefore the exchange may not be determined by a power law $J \propto r^{-\gamma_m}$ but an exponential law $J \propto e^{-\beta r}$ instead.

It is worth mentioning, that later Zhou and Goodenough have actually conducted a systematic study on a wide series of manganese perovskites AMnO_3 and RMnO_3 (A = alkaline-earth, R = rare-earth), designed to explore an evolution of the Bloch's parameter as the localized to itinerant magnetism transition is approached from localized-electron side [101]. It has been confirmed that $T_N \sim r^{-10} \sim V^{-3.3}$ and $\gamma_m = -3.3$, provided that the values of the on-site electron-electron repulsion U the charge transfer gap Δ remain constant with pressure. In fact, this presumes the constant value of compressibility κ as well. However, as the compound under study approached the crossover to itinerant electron behavior, γ_m was found to deviate from 3.3 and systematically increase ultimately reaching up to 5.6. Later a systematic increase of compressibility with increase of ordering temperature T_N was reported, which breaks an assumption of the constant U and Δ and could lead to a breakdown of the entire model.

2.4.2 Pressure effect on double exchange

Experimentally the application of external pressure in DE compounds leads to an increase of the critical temperature of magnetic phase transition (which coincides with the temperature of metal-insulator transition) [102, 103, 104]. However, in contrast to the superexchange models discussed above, the effect does not depend solely on the inter-atomic distance. The earliest models of pressure effect on DE predicted a dependence of the inter-site interaction (which directly correlates with critical temperature of transition) between the neighboring spins on both exchange integrals J and the bandwidth W . The magnitude of interaction is proportional to bandwidth W in the strong coupling limit ($J \gg W$), but varies as $\propto J$ in the limit ($J \ll W$) [105]. The results is that the pressure coefficient of the critical temperature depends on the magnitude of T_C , which was confirmed by corresponding experiments. Using various approaches, the DE compounds were driven into a weak-coupled region by increasing the hole doping [104], or by increasing ionic radius R_0 using isovalent ionic substitution [106, 107]. In all the approaches the result was a lower sensitivity of T_C to external pressure in the weakly-coupled region. Thus, the T_C dependence on pressure is non-linear and approaches saturation with high pressure [102]. The latter is related to substantial increase of exchange integral J at certain inter-atomic distance, as well as broadening of bandwidth W . Moreover, the increase of carrier concentrations leads to increased W which results in lower $d \ln T_m / dP$ coefficient [104] and the system becomes significantly less pressure sensitive. However, according to published experimental data, even then the pressure dependence of T_c in double-exchange compounds is much stronger than that for superexchange ones, varying within the range $\gamma_m \approx -(7 \div 40)$ versus $\gamma_m \approx -(3 \div 4)$ for superexchange.

2.4.3 Pressure effect on RKKY-type magnetic ordering

The pressure effect on RKKY type of interaction was studied rather well by J. S. Schilling, who had reviewed a large amount of data measured on dilute magnetic alloys [72]. There was a connection established between the effective exchange integral J_{RKKY} and an observable quantity like critical temperature of magnetic ordering T_m . It was shown that for a spin-glass

$$T_m \propto \Delta_c \equiv \left[\overline{\sum_{i \neq j} \varphi_{ij}^2} \right]^{1/2}, \quad (2.33)$$

where Δ_c is the root-mean-square (r.m.s.) interaction strength in the alloy and φ_{ij} is the effective interaction strength between the pair of spins S_i and S_j . The latter one in turn is connected with RKKY exchange constant as

$$\varphi_{ij} \propto N(E_f) J_{\text{RKKY}}^2 \quad (2.34)$$

Thus, the rough pressure dependence of effective exchange interaction is expected to be of the form

$$\frac{d\Delta_c}{dP} \approx \frac{d[N(E_f) J_{\text{RKKY}}^2]}{dP} \quad (2.35)$$

or if we consider the logarithmic volume dependence of magnetic ordering temperature, the expression takes the form

$$\frac{d\ln T_m}{d\ln V} = \frac{d\ln \Delta_c}{d\ln V} \approx \frac{2d\ln J_{\text{RKKY}}}{d\ln V} + \frac{d\ln N(E_f)}{d\ln V}. \quad (2.36)$$

The result was proved to hold generally for magnetic ordering in systems with long-range RKKY-interaction and is not specific for the spin-glass materials only. J. S. Schilling in his review refers to the theoretical models describing the radial RKKY-spin polarization within the free electron framework. According to results of these studies, the volume dependence of the density of states at the Fermi-level is rather weak $d\ln E_f/d\ln V = 2/3$, comparing to such dependence of J_{RKKY} . Later, these results were found to agree well with thermal expansion measurement results on copper (≈ 0.64) and band structure calculations (≈ 0.43). The positive dependence of the density of states is easily explainable from the consideration that the decrease of inter-ionic separation increases the bandwidth, which in turn lowers the density of states at Fermi-level, provided that the concentration of free electrons does not depend on pressure (which is the case most of the times). Thus, from theoretical consideration and the large amount of experimental data gathered, it was concluded that J_{RKKY} has a dominant role in pressure dependence of ordering temperature. The character of this dependence was predicted to be

$$\frac{d\ln T_m}{d\ln V} \approx -(3 \div 5), \quad (2.37)$$

which holds for 3d-impurities in noble metals. This is quite rapid increase of the ordering temperature with pressure corresponding to a dependence of $J_{\text{RKKY}} \propto r^{-15}$ in maximum case — substantially stronger than that for superexchange interaction $J_{SE} \propto r^{-(10 \div 12)}$.

2.4.4 Anisotropic exchange under pressure

The studies of pressure effect on the ordering temperature of classical representative compounds with DM interaction MnCO_3 , CoCO_3 and FeCO_3 have been done by Srivastava [91]. In this case one needs to include an extra term $\mathbf{D} \cdot [\mathbf{S}_1 \times \mathbf{S}_2]$ in the spin Hamiltonian in order to estimate the γ_m . In the simplest case only nearest neighbor interaction was considered with exchange parameter J

$$\gamma_m = \frac{J}{J^2 + D^2} \left[\frac{d \ln J}{d \ln V} + \frac{D}{J} \frac{d \ln D}{d \ln V} \right] \quad (2.38)$$

For some compounds the term D/J is found to be negligible, thus the main shift in ordering temperature is due to change in antiferromagnetic J and the behavior is partially governed by the same principles applicable to superexchange interaction [87]. For such compounds the value of γ_m has been determined to closely match the one pointed by Bloch [93]. Thus in general case the dependence of DM interaction on hydrostatic pressure has a positive sign as the spin-orbit interaction increases with a decrease of inter-ionic distance [108, 109, 110]. However because the DM vector \mathbf{D} is proportional to the strength of spin-orbit interaction which in turn is proportional to Z_{eff}^4 (effective atomic number, see section 2.1.4), the rate of variation was later found to differ significantly from one compound to another.

2.4.5 Pressure effect on itinerant magnetism

One of the earliest successful results of measuring the change of magnetic ordering temperature with pressure on some pure metals and alloys was obtained by L. Patrick in 1954 [111] and revealed a decrease of a ferromagnetic T_C . G.K. White attributed the effect to the value of electronic Grüneisen parameter

$$\gamma_e = 1 + \left(\frac{d \ln N(E_F)}{d \ln V} \right)_T \quad (2.39)$$

the value of which was determined to be within the range $1 \div 3$ [97, 95]. Here, $N(E_F)$ is the density of states at the Fermi level, and the second term in expression 2.39 has appreciable positive value. The positive dependence of magnetic ordering temperature T_M as a function of unit cell parameters of metallic oxides was observed later in multiple experiments, using chemical substitution in perovskites [112] and external hydrostatic pressure [90]. The results have been found consistent with the ones measured later in thermal expansion experiment [113]. D. Bloch and coworkers [114] carried out a systematic study on pressure dependence of T_C in binary transition metal alloys, with a non-magnetic elements as second component, in order to

study a dependence on magnetic moment variation. The observed experimental values for dependence of exchange coupling on volume $d \ln J / d \ln V$ fell within a range from -2.15 to -1.4 , which is substantially weaker dependence than that observed on localized magnetic moment systems. The behavior

$$\frac{dT_C}{dP} < 0 \quad (2.40)$$

is completely opposite to the one observed in materials with localized electron magnetism and J.B. Goodenough tried to develop a theoretical rationale for these experimental results [86]. It has been concluded that in case of a band ferromagnetism the strength of magnetic coupling should decrease with an increase of the bandwidth W , which is a result of increased overlap of electronic orbitals due to applied pressure. This can be understood in the framework of Stoner model of band ferromagnetism (see section 2.3), as the general increase of bandwidth with pressure reduces the effective density of states $N(E_F)$, affecting the Stoner criterion.

$$UN(E_F) \geq 1 \quad (2.41)$$

Since U weakly depends on pressure, the major effect on exchange coupling in the itinerant electron magnetic system comes from dependence of W on interatomic distance. In order to estimate the exact rate of pressure dependence one needs to know the bandwidth variation rate with unit cell volume, thermal expansion coefficient and compressibility of material at given temperature range. The two last are measurable parameters and there are multiple techniques available including crystal structure refinement under pressure and direct thermal expansion measurements. The $W(R)$ dependence for transition metals $sp-d$ bands has been worked out theoretically by Heine [115] using scattering theory with the result $W \propto R^{-5}$, which implies

$$\frac{d \ln W}{d \ln V} = -5/3. \quad (2.42)$$

Based on this relation several attempts were made to develop a model which would allow one to predict the value of dT_C/dP for itinerant ferromagnets, including those by Lang and Ehrenreich [116], Wohlfarth [117] and Edwards [118]. Later it has been realized that the Hartree-Fock theory the models were based on, does not provide a good description of finite temperature magnetism and another theory was proposed by Hasegawa, based on the single-site spin fluctuation (SSF) theory [119]. Still the value of $d \ln J / d \ln V$ varies appreciably for various itinerant magnetic materials and any of the theories fails to explain all the experimental results, therefore individual approach is needed for specific cases.

Thus, the information about the qualitative pressure dependence of ordering temperature in the first approximation allows narrowing the list of possible types of magnetic interaction responsible for the magnetic properties of the studied material. The combination of a quantitative dependence with the structural data and transport measurements allows to determine the strength of magnetic interaction, therefore

greatly contributing to the complete understanding of the properties of given class of materials.

2.5 Metal-Insulator transitions

The subject of the metal-insulator transition has become a very wide and complicated field of research in condensed matter physics after more than sixty years of study [120]. It came to renewed focus in the last two decades, following the discovery of high temperature superconductivity, which triggered an interest of researches on “bad metals” [121, 122]. Remarkably simple theories [96] successfully describe the limiting situations of transport properties of materials. *Localized electron theory* is applicable to the case of weak interatomic interactions and tightly bound electrons. The latter are characterized by a large value of the Coulomb repulsion energy U required to transfer a valence electron from one site to an occupied orbital on the equivalent site, and a small bandwidth W ($U \gg W$). It allows us to understand good insulators. In case of appreciable overlap between orbitals of neighboring atoms, the electrons are shared equally by all the atoms in a solid and the *band theory* of Bloch and Wilson becomes applicable. The relation $U \ll W$ (or $U = 0$ in extreme case, figure 2.12 (a)) allows us to well understand good metals like Au, Ag and other the noble metallic elements. However, these materials with limiting properties are extremely stable, found to be very difficult to manipulate and modify for needs of modern technology, and rarely demonstrate novel and interesting phenomena to explore for science. There is another case, when $U \approx W$, which creates a possibility of *strongly correlated electrons* in solids leading to both localized and itinerant electron behavior (figure 2.12 (b)-(d)). Here both elementary band theory and localized electron theory fail to account for the properties of such materials even qualitatively. Conventional band theory predicts an insulating state when all bands are fully occupied or empty, whereas a metallic state occurs under different conditions. However, in case of strongly correlated electrons, under influence of external pressure, temperature or suitable doping a crystalline solid can be modified into structure when the empty and filled bands cross or overlap, leading to a transition between metallic and insulating behavior. In some cases the crossover is accompanied by the changes of crystal structure or magnetic ordering. Different types of MITs studied in transition metal oxides include [1]:

1. Pressure induced transitions: a change from localized to itinerant behavior of electrons as a result of increased overlap between neighboring atoms due to application of external pressure.
2. Charge-ordering leading to localization of electrons and resulting in insulating state (*Charge Density Waves, Spin Density Waves*).
3. Disorder induced localization of electrons due to change in composition by doping (*Anderson localization*).
4. Temperature induced metal-insulator transitions in magnetic materials.

In all these cases the potential energy components coming from either electron-electron interactions or due to induced disorder (electron-impurity interaction) become comparable to the Fermi energy, and the ground state can undergo a dramatic change, resulting in localization of electrons. The material suddenly starts exhibiting an insulating behavior, even though the band theory does not predict any gaps at the Fermi surface.

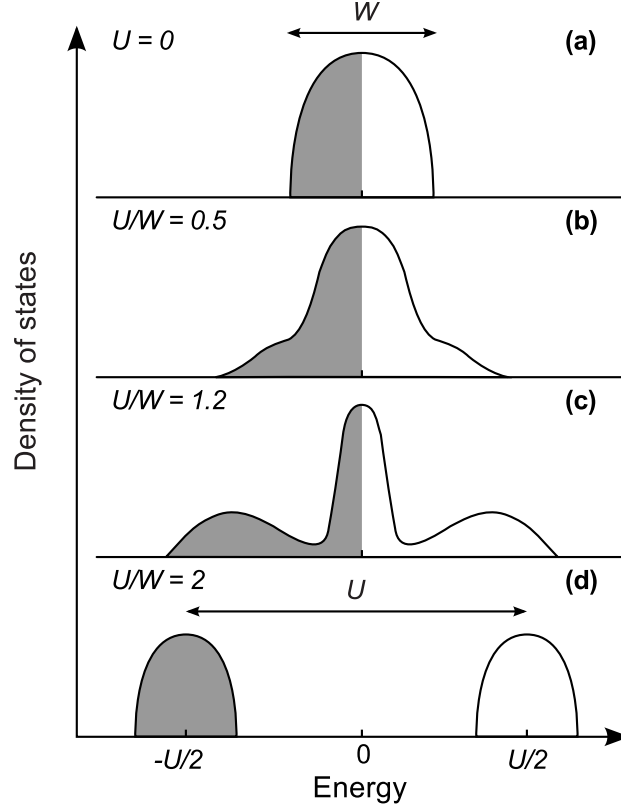


Figure 2.12: The density of states (DOS) of electrons in a solid as a function of the local Coulomb interactions: (a) independent electrons, Fermi level E_F is located in the middle of the band; (b) weakly correlated regime (small U), electrons can be described as quasiparticles with DOS resembling free electrons; (c) strongly correlated metals, the spectrum includes the Hubbard bands originating from local “atomic” excitations and the quasiparticle peak near the Fermi level; (d) sufficiently strong electron interactions cause the quasiparticle peak to vanish. Adopted from [123].

2.5.1 Disorder induced MIT

A small concentration of impurities or defects affects a random scattering of conduction electrons. The typical electrical dependence of resistivity on temperature in metals is a monotonically increasing function

$$\rho(T) \simeq \rho_0 + AT^n \quad (2.43)$$

where both $A > 0$ and n are determined by scattering process, and ρ_0 is determined by elastic scattering on impurities and defects. In ordinary metals a random potential due to impurities is much smaller than the kinetic energy of electrons, thus is treated as a small perturbation. In low carrier density systems (bad metals) the impurity potential becomes comparable or exceeds the Fermi energy and the electrons can be localized by impurities. The process can only have a significant effect below a certain level of thermal activation, thus in the low limit at finite temperature this type of metal-insulator transition has a continuous character. The case when this type of localization manifests itself dramatically was described by Anderson [124]. He realized that the states most susceptible to localization are those at the band edges, because they involve a correlation of electron phase. The localized and delocalized states do not coexist at the same energy but are separated by a barrier called the *mobility edge*. At finite temperature the carriers can hop from one localized state to another due to thermal activation, a phenomenon known as *variable range hopping*. But at $T = 0$ K the conductance at the energy level of localization is zero. The doping of material with carriers shifts the Fermi energy and the system undergoes an Anderson metal-insulator transition [125].

2.5.2 Slater insulator

A material with an odd number of electrons per unit cell is typically predicted to be a metal, according to band theory. However in contrast to expectations, many such materials are experimentally found to be insulating. It turns out that a metal-insulator transition can also be implemented within the band-theory picture in case when a gap in the Fermi surface is opened due to rearrangement of charge or spin density of electrons in the ground state. An important contribution to this subject was made by Slater in his theory of itinerant antiferromagnets [126]. Basing his view on the known features of band and Peierls insulators (an-electron lattice interaction case, with localization via distortion of a periodic 1D lattice found in low-dimensional solids and some charge-transfer organic salts [127]), he realized that the interacting electrons may also generate a periodic modulation of their spatial charge or spin distribution which is stabilized by an electron-electron and not the electron-lattice interactions. The antiferromagnetic ground state often observed in transition metal oxides with insulating properties led Slater to propose an SDW or CDW (the actual terms were introduced by A. W. Overhauser much later [128, 129]) formation as probable origin of such insulating state. In an antiferromagnetic Slater insulator the commensurate AFM order (with every neighboring spin oppositely aligned) occurs at the MIT temperature (T_{MI}), creating an opposite periodic potential on each nearest neighbor. Electrons with same spins tend to avoid each other and therefore their motion is restricted. This creates a gain in potential energy compared to the translationally invariant state, which in turn is balanced by a loss of kinetic energy of electrons. As a result of this process, a doubling of the lattice unit cell occurs in the corresponding band structure picture, which respectively reduces the magnetic Brillouin zone in half. The bands split on the boundaries of the new Brillouin zone because of the periodic potentials, and the energy of the occupied states is lowered.

If the band is half-filled, such splitting causes a gap for charge excitations – the lower band becomes preferentially fully occupied and the upper band is left empty. Thus the system undergoes a transition from itinerant to *Slater insulator* state [127, 130]. Since, the insulating state is viewed as a consequence of band gap opening at the Fermi surface, the mechanism does not require a substantial modification of the band theory picture. These effects are most commonly found in compounds containing the ions in mixed oxidation state (examples: Ti_4O_7 , Fe_3O_4) [131, 132].

2.5.3 Mott insulator

According to Slater [126] the insulating behavior of an antiferromagnetic compound should disappear above the Néel temperature. Remarkably, in most antiferromagnetic transition metal oxides the insulating behavior persists at temperatures substantially higher than any magnetic ordering temperature, ruling out the weak coupling mechanism. This picture was first clarified by Mott and Hubbard, connecting the insulating behavior to a strong Coulomb interaction between the electrons of the same orbital [120, 133]. In his original formulation, Mott’s decisive criterion was an existence of pre-formed local magnetic moments, regardless of whether they are ordered or not (in contrast to the Slater insulator), although later he considered the importance of magnetically ordered state. For a physically instructive explanation of a Mott metal-insulator transition one considers an arrangement of hydrogen atoms (of Bohr radius a_0) on a cubic lattice with L sites and a being a lattice constant [127]. The number of electrons $N = L$ provides the half-filling of the states. In order to transfer an electron between the spatially separated sites one needs to overcome the Hubbard U – the difference between ionization energy and electron affinity $U = I - A$. It is assumed that the electrons hop (tunnel) between the neighboring atoms with probability t , thus they can be mobile only if their kinetic energy ($E_k \sim t$) is high enough to overcome U , otherwise a gap opens in single particle excitation spectrum. The size of the gap is $E_g \simeq U - W$, where $W = 2Zt$ is the bandwidth. Here Z is the lattice coordination number (number of nearest neighbors) and t depends on the ratio a/a_0 . One can see that for a large distance between the atoms when $a \gg a_0$ the overlap between atomic orbital is small, which leads to $W \ll U$. For $W \gg U$ a single half filled band is predicted with a gapless energy-excitation spectrum – the system is a paramagnetic metal. Respectively, for the intermediate values near $U_C \approx W$, a metal-insulator transition is expected. The charge excitations with energy U and the spectrum for the removal of a charge from a half-filled electron system together form an Upper Hubbard band (UHB) and Lower Hubbard band (LHB), respectively (figure 2.13). However, these bands are a consequence of electron correlation and do not represent single-electron states, therefore Mott MIT should not be confused with the result of simple band crossing.

It is obvious that the description above does not consider the spin degree of freedom, thus neglecting the possibility of an ordering of magnetic moments. However even for $U \gg W$ the tunneling of the electrons to neighboring sites is allowed, thus magnetic exchange interactions cannot be ignored. Because of half filling, in

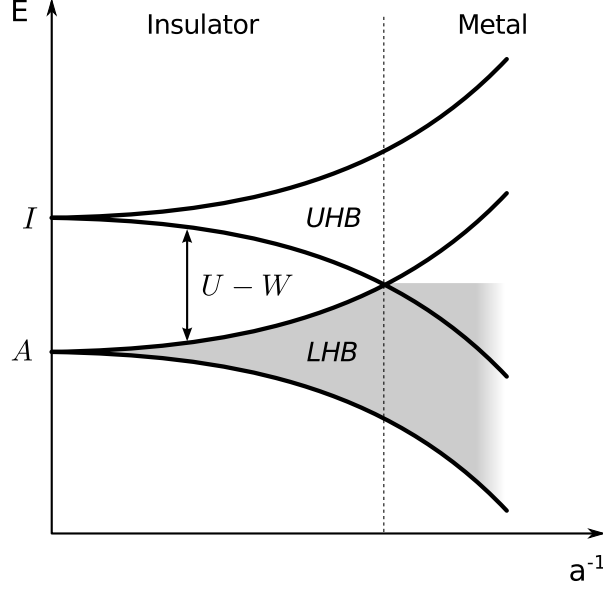


Figure 2.13: Schematic illustration of the upper and lower Hubbard bands in Mott insulator as a function of reciprocal interatomic distance. At $a \ll a_0$ we have $W = 0$ and the isolated ions are separated by $U = I - A$. As the bandwidth increases the gap $U - W$ decreases until the bands overlap and material becomes a metal. Adopted from [134].

the insulating ground state each lattice site is single occupied with a spin 1/2 electron, behaving as a local magnetic moment. The superexchange interaction between the moments $J \sim t^2/U$ determines the antiferromagnetic ordering temperature T_N . However, the charge excitation (E_g) and spin excitation (J) energy scales are well separated. The insulating behavior is not caused by magnetic ordering and will persist way above $T_N \ll T_{MI}$. For small interactions near $U_C \approx W$, the Mott-Hubbard gap is absent, but as long as $U > 0$ the electronic correlations lead to preformed magnetic moments. Again, the moments may be subject to a long range order, and at the ordering temperature T_N the material goes from a correlated paramagnetic metal into an antiferromagnetic Mott-Heisenberg insulating state. It is worth noting, that according to Mott the magnitude of the local magnetic moments does not change much at the Néel temperature. As mentioned above, this provides a contrasting characteristic to distinguish the Mott-Heisenberg insulator from Slater insulator (see section 2.5.2). As known, in the latter not only the long range order, but also the local magnetic moments are absent above T_N .

Approximately a half of the known binary compounds (including many oxides of transition metals) predicted to be metallic by the band theory, are in fact insulating. The transport properties of many of these (including NiO studied by Mott in his pioneering work [120]) can be explained invoking the MIT theory described above. Recently, a new class of 5d Mott insulators was discovered in iridates, such

as Sr_2IrO_4 [33, 135, 34] and Na_2IrO_3 [136, 137], where the strong spin-orbit interaction (SO, see section 2.1.4) plays a crucial role in stabilizing an insulating state. Because of the spatially extended orbitals, the Coulomb interaction between $5d$ -electrons is $U \sim 2$ eV — much smaller than that of $3d$ electrons in conventional Mott insulators and is sufficient to open a gap. On the other hand, the spin-orbit interaction in iridates ($\lambda \simeq 0.5$ eV) is much larger than that in $3d$ systems and splits the t_{2g}^5 states of the $5d^5$ -shell into a half-filled $J_{\text{eff}} = 1/2$ and fully-occupied $J_{\text{eff}} = 3/2$ states. As a result, the narrow half-filled $J_{\text{eff}} = 1/2$ band tends to undergo Mott transition even at relatively weak Coulomb interactions U .

2.5.4 Pressure induced metal-insulator transition

Common criteria of a metal-insulator transition for a wide range of physical models can be described by an expression

$$a^* n^{1/3} \geq D \quad (2.44)$$

where n is the electron density, D – constant, and a^* is a radius of a hydrogenic type orbital — characteristic length scale.

$$a^* = (m/m^*)\epsilon a_0 \quad (2.45)$$

which depends on effective mass m^* , dielectric properties of the medium ϵ and Bohr radius a_0 [134]. For a band insulator the best empirical estimation over a wide range of simple elements and complex systems produces $D \approx 0.26$ [138, 139]. The data stretches over 3 orders of magnitude of effective radius a^* and physically asserts that anything becomes metallic when compressed enough. Thus, conceptually the simplest kind of metal-insulator transition in an ordered solid would be one due to a band crossing resulting in an overlap at the Fermi energy. If the energy gap between the valence and conduction bands can be closed under pressure — the transition from insulator to metal can occur. In practice a real system exhibiting such transition under pressure remains yet to be found. An application of high external pressure to classical semiconductors like Si or Ge leads to a structural transition which in turn causes the MIT [140, 141] and therefore does not fit the criteria. The cases where metal-insulator transition happens without the change of crystal structure are of much higher interest. A good example would be provided by the divalent metals Ca, Sr and Yb [142, 143]. However, these cases are even more unique — the continuous transition proceeds from metallic state to an insulating as the applied pressure increases. Even though the bandwidth increases under pressure in these materials, contrary to all the expectations the band gap increases as well. The behavior has been attributed to a formation of a hybridization gap at the Fermi level E_F as a result of increased mixing of $4f$ and $5d$ shells [144]. Similar distinct behavior under pressure has been observed on Li, although this material passes through a series of structural transitions before turning into a semiconductor under a pressure of nearly 80 GPa [145]. These materials represent just a handful of cases with such out of ordinary transport properties behavior under pressure. For most other cases the application of pressure leads to the

enhancement of metallicity, as expected due to increase of degree of orbital overlap between the neighboring atoms.

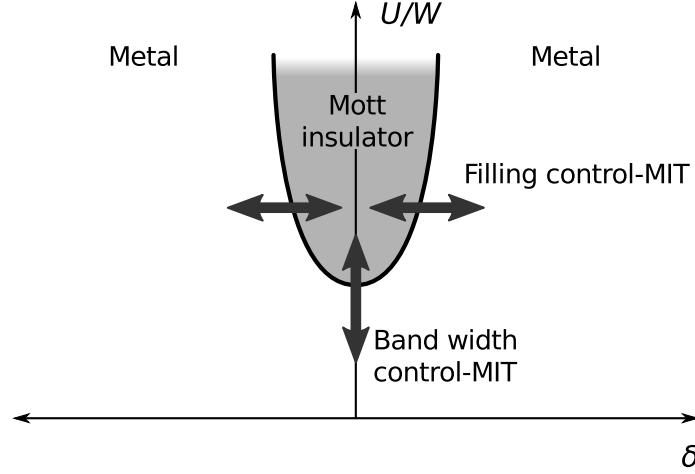


Figure 2.14: Schematic phase diagram based on Hubbard model in the coordinates of the correlation U/W and the deviation from the integer filling δ . Two routes for the metal-insulator transition are indicated: filling control (through possible carrier doping) and band width control (change of interatomic distance through pressure). Adopted from [31].

A Mott transition between the magnetic insulating state and the metallic state occurs with decrease of U/W ratio, as demonstrated on figure 2.14. From our rough formulation of the model in the section 2.5.3 one can see that there are at least two distinct routes to the Mott insulator when approaching the point from metallic side. The carrier number can be affected by electron- or holes-doping, and the control of bandwidth through the change of interatomic spacing can be implemented by application of external pressure, or chemical pressure (isovalent doping by elements of different various ionic radii) [31]. The potential problem with pressure effect is that a transition from Mott insulator state to metallic one occurs at a critical lattice constant, when the Coulomb interactions are weak enough to raise a large free carrier concentration. However, in modern pressure experiments the change of the lattice constant is limited to a few percent, therefore the desired effect should only be achievable in the close vicinity to MIT. Nevertheless, the experimentally observed drastic changes of resistivity as a result of pressure-induced Mott transitions have been reported for numerous transition metal oxides. Perhaps the most celebrated example is V_2O_3 , where the application of pressure slightly reduces the lattice constant and the metallic state is preferred. Moreover, the apparent equivalence between doping and external pressure in this compound was demonstrated by doping the structure with titanium (Ti) or chromium (Cr). The doping leads to respective decrease and increase of the lattice parameters, resulting in corresponding effect on the metal-insulator transition [146, 147]. Another classical example is Fe_2O_3 [148, 149] which also undergoes a metal-insulator transition under pressure, despite substantially wider insulating gap.

However, it is worth mentioning that NiO, the large band gap material used by Mott as a prototype in his pioneering work [120], has not yet been found experimentally to undergo a metal-insulator transition under hydrostatic pressure up to 147 GPa [150]. Considering materials more closely related to this work, the collapse of Mott-like insulating state under pressure has been reported on complex ruthenium-based oxides from Ruddlesden-Popper series $\text{Ca}_{n+1}\text{Ru}_n\text{O}_{3n+1}$ ($n = 1, 2$) [151, 152]. Recently a pressure-induced metal-insulator transition has been reported on spin-orbit driven Mott insulator Ba_2IrO_4 [30]. Even though the material is a high-pressure synthesized phase isostructural to Sr_2IrO_4 (a subject of this work), no metal-insulator transition has been detected on the latter compound under external pressure up to 40 GPa [153].

Chapter 3 EXPERIMENTAL TECHNIQUES

3.1 Material synthesis

3.1.1 The importance of the single crystals

What are single crystals? An ideal concept of a crystal is an infinite array of atoms following a particular periodical spatial arrangement in all three dimensions. The periods of the arrangement (or crystal lattice), which usually constitutes a relatively small number (on the order of 10) of interatomic distances, are called *lattice parameters* and define a size of the smallest repeating unit of the lattice called a *unit cell*. For inorganic materials the lattice parameters range from about 0.25 nm to 3.5 nm. Lattice spacings for organic materials involving macromolecules can be much larger, reaching up to hundreds of nanometers. Real crystals are featuring the same long range order and symmetry, however due to finite dimensions the surface sometimes has detectable effects on the properties in these solids. The real crystals also have crystal lattice defects such as vacancies and interstitial atoms (point like defects), the concentration of which depends on the temperature, growth and post-growth conditions and is thermodynamically predictable in many cases. Crystals also contain impurity atoms and linear defects (dislocations), which due to an electrical activity and surrounding stresses can develop a degradation process in the crystal up to unacceptable condition. The single crystal materials are typically considered in comparison with randomly arranged materials, such as polycrystalline (long-range order exists only within limited volume grains) and amorphous ones (no long-range order). In research on the intrinsic physical properties of novel materials (which includes this study), the samples in the form of the single crystals are strongly preferred due to a number of advantages. (1) The transition metal oxides, the primary focus of this work, possess strongly anisotropic magnetic and transport properties, which are the result of difference of the long range order in various directions. These properties can only be reliably measured and described using single crystal samples. A polycrystalline sample consists of a numerous disoriented crystallites and prevents any meaningful measurements of anisotropy of the bulk properties and an amorphous material does not possess long range order of any kind. (2) Grain boundaries are inevitable characteristics of polycrystalline material. The intergranular space is often the precipitation of three-dimensional defects (dislocation arrays), discrete inclusions of the second phase and a segregation of impurity atoms. All of these factors lead to trapping and additional scattering of charge carriers, interfering with most transport measurements. In addition, much higher surface to bulk ratio and porosity of the polycrystalline materials often completely exclude certain types of measurements from a study. (3) Nonuniform internal structure leads to large internal stresses in polycrystalline materials, which in case of a strong thermal expansion anisotropy (most of our measurements are performed at various temperatures) can lead to cracking of the sample. In addition to all of the above, a generally higher level of purity

is obtained in single crystals, and in case of dilute doping the detailed structural characterization simply cannot be performed on something other than a high-quality single crystal. This makes the synthesis of single crystals a matter of considerable importance for a condensed matter scientist. In the same time a crystal growth procedure is a difficult task in general and is even more so for novel materials, due to many control parameters involved, and high time demands because of low growth rate.

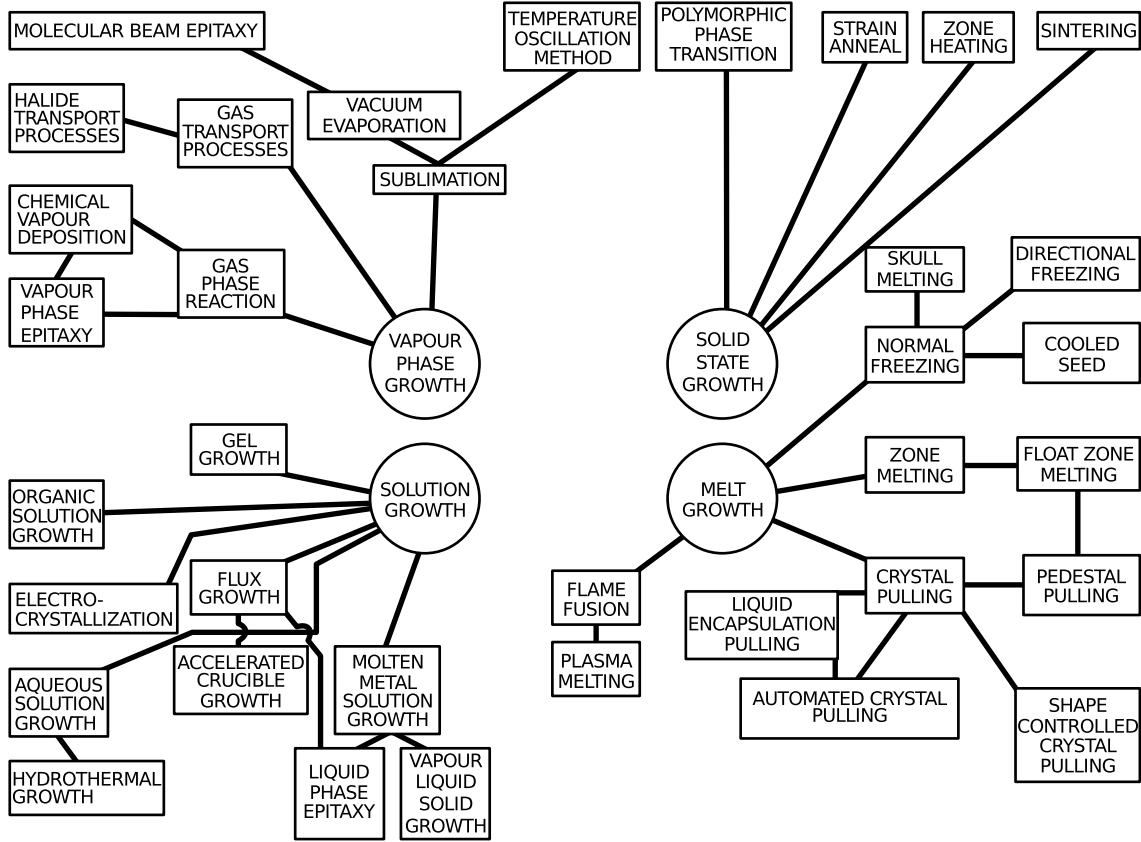


Figure 3.1: Modern classification of crystal growth techniques. Courtesy of [154].

Crystal growth is involved with the control of a phase change, which defines the classification of those multiple crystal growth techniques developed in modern science (see figure 3.1). Considering the phase adjacent to the growth phase the whole variety is conventionally divided into four categories [154]:

- Solid growth. Processes involving Solid–Solid phase transition. Used for limited number of cases where a crystal structure change occurs between the room temperature and melting point.
- Melt growth. The most straightforward techniques of normal or directional cooling. Solid–Liquid–Solid processes are also related into this category.

- Vapor growth. Processes include the growth from a gaseous phase as well as sublimation.
- Solution growth. Crystal growth from solvents, which for high temperature processes uses a molten metal or salt called the *flux*.

Many of the methods are nowadays implemented on the industrial scale of materials production, while others are used mainly for small scale synthesis in laboratory research. For crystal growth in our lab we are using a floating zone method and a flux method of crystal growth. The latter is being primarily used for samples synthesis in this study, which determines the further discussion in this section.

3.1.2 Single crystals growth by flux method

The *Flux method* is commonly used to describe the growth of crystals from molten salts or pure metals solvents at high temperatures. The solvent is referred to as the flux because it allows one to perform the synthesis well below the melting temperature of the solute phase, which is the main advantage of this method over growth from the pure melt. The lower melting point often produces a material with fewer defects and much less thermal strain. This and the fact that molten flux often getters impurities, allows better quality crystals to be grown by this than any other method. The flux method works equally well for the congruently and incongruently melting compounds and typically does not suffer from problems of high vapor pressure of one of the constituents. In addition to the list of advantages, the technique can be implemented with the simplest set of equipment in a rather modest laboratory, which lowers a threshold for the newcomers to the field.

The flux growth method is of very wide applicability, since in principle it is possible to find a solvent for any material. However, the choice of flux remains the most crucial point in this technique, since with every new material it turns out that very little work has been done to date, concerning the solubility of the solute at high temperatures. In the ideal, case the flux needs to possess the following list of properties:

- moderate solubility of the precursor materials in the flux, with appreciable positive temperature coefficient of solubility;
- no stable phases formation between the flux and solute below the growth temperature;
- low viscosity, low melting point and low volatility of the flux at the highest growth temperature;
- compatibility of liquid flux with materials of the crucible and compatibility of flux vapors with materials of the furnace.

In reality, no flux fulfills all of these requirements equally well, therefore the priorities are defined and a compromise is always necessary. At least one more parameter can

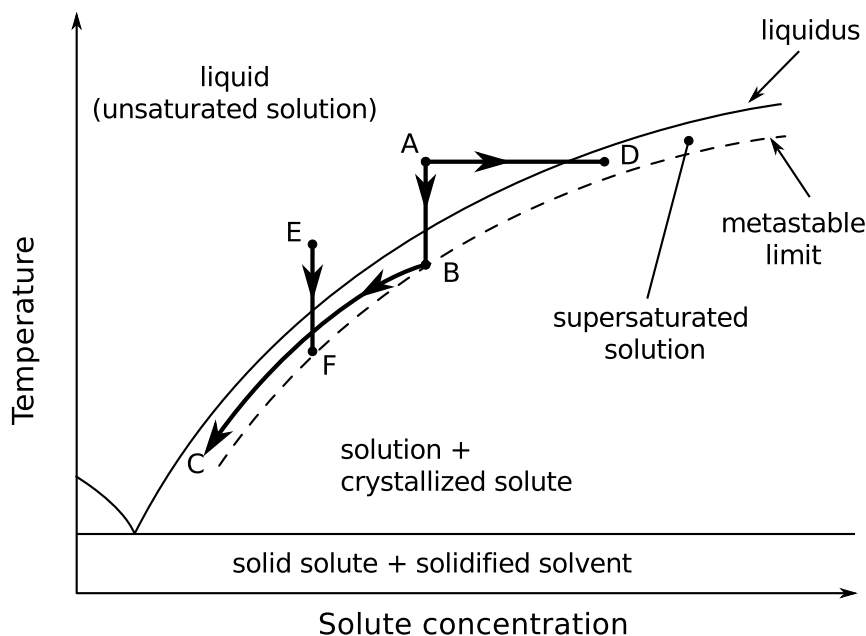


Figure 3.2: Pseudo-binary phase diagram showing means for achieving crystallization from fluxed melts by: ABC – slow cooling, AD – evaporation, EF – temperature gradient transport [154].

be varied in this equation — several crucible materials for high temperature growth are available, allowing a little flexibility. However, the other affected factors could be the type of the crystals, their size and quality. In the process of choosing a flux material the published binary phase diagrams are used as a reference [155, 156]. A thorough examination of available literature is performed for fluxes which might have been successfully used for the growth of similar compounds.

In crystal growth from solution, the most important equilibrium consideration is solubility. The equilibrium itself is defined by a *liquidus* line on a binary phase diagram. (see figure 3.2) and is described by a reaction



where A is the process of solution of a solid. The region above the line represents an unsaturated solution, containing less than the equilibrium concentration of solute. The regions just below the liquidus line are supersaturated. The supersaturated solutions are not stable and will deposit solute spontaneously or *nucleate*, either in the solution or on the walls of the crucible. As soon as the centers of nucleation appear in the solution the excess solute will start depositing on those centers until the concentration falls to the equilibrium. The driving force for crystallization comes from the free energy difference ΔG of the atoms as a result of bonds formation. However, the free energy of the cluster is increased by the surface tension energy, which is significantly competing against the reduction of the total energy while the cluster is small.

Thus in order to initiate and maintain the growth of a crystal the system needs to be kept in the metastable region of the phase diagram to produce the critical size of the nucleation clusters and to maintain necessary high concentration of the solute. This can be achieved by several methods illustrated on the figure 3.2, of which the most widely used one is a slow cooling (indicated by the path ABC on the diagram), however in reality all three effect may be present simultaneously. The solution stabilized at point A can be cooled to a point B , located within the metastable region, where the spontaneous nucleation occurs. The continued slow cooling along the path BC is accompanied by crystal growth and reduction of the solute concentration in the solution. In the case of AD path, the solvent is being evaporated at constant temperature and the nucleation occurs at point D . The advantage of growing the crystals at constant temperature is a more homogeneous composition through the bulk, since the concentration of the solute remains constant during the whole time of the growth. The disadvantage is obvious – intensive evaporation is absorbed by the furnace internal insulation material. In order to implement the path EF the temperature gradient (typically 5° to 50° C) is maintained through the bulk of the fluxed melt and the constituents are transported by convection. While having limited application, this method is useful because it allows growing the single crystals under flux by the floating zone method in so called *traveling solvent floating zone technique* [157]. Prior to executing the program, the temperature of the solution needs to be kept for prolonged time (12 to 24 hours) at the point well above the liquidus line for given solvent concentration, in order to ensure the complete dissolution of the solute (so called, soaking). This is of high importance, as any undissolved particles will act as nucleation centers when the crystallization occurs. This unwanted nucleation is very harmful when the goal is to grow the high-quality crystals of larger size.

Single crystals of Sr_2IrO_4 for this study were grown using self-flux techniques from an off-stoichiometric quantities of IrO_2 or Ir metal, SrCO_3 , and SrCl_2 [24]. The ground mixtures of powders were melted at 1470° C in partially capped platinum (Pt) crucibles. The soaking phase of the synthesis lasted for > 20 hours and was followed by a slow cooling at 2° C/h to reach 1400° C. From this point the crucible is brought to room temperature through a rapid cooling at a rate of $\sim 100^\circ$ C. The produces single crystals of Sr_2IrO_4 tend to be of plate-like shape with an average size of $1 \times 1 \times 0.5 \text{ mm}^3$ (figure 3.3 (a) and (b)). The crystals possess well distinguishable crystallographic features with the c -axis along the shortest dimension, and are well susceptible to cleavage along ab -plane, exposing a high-quality monoatomic surface, see panel (b) of figure 3.3. Energy dispersive X-ray (EDX, see section 3.2.3) studies were carried out in order to confirm the 2:1 ratio of Sr to Ir and the uniformness of stoichiometric distribution. The correct obtained phase has been also confirmed from powder X-ray diffraction pattern on produced single crystals (figure 3.3 (c)).

The BaIrO_3 samples were also synthesized by the flux method at relatively low temperatures (1280° C) from the off-stoichiometric quantities of IrO_2 and BaCO_3 , using BaCl_2 as a flux agent [158]. The soaking phase of the synthesis is followed by a slow cooling at 3° C/h. The doping by rare-earth elements was implemented

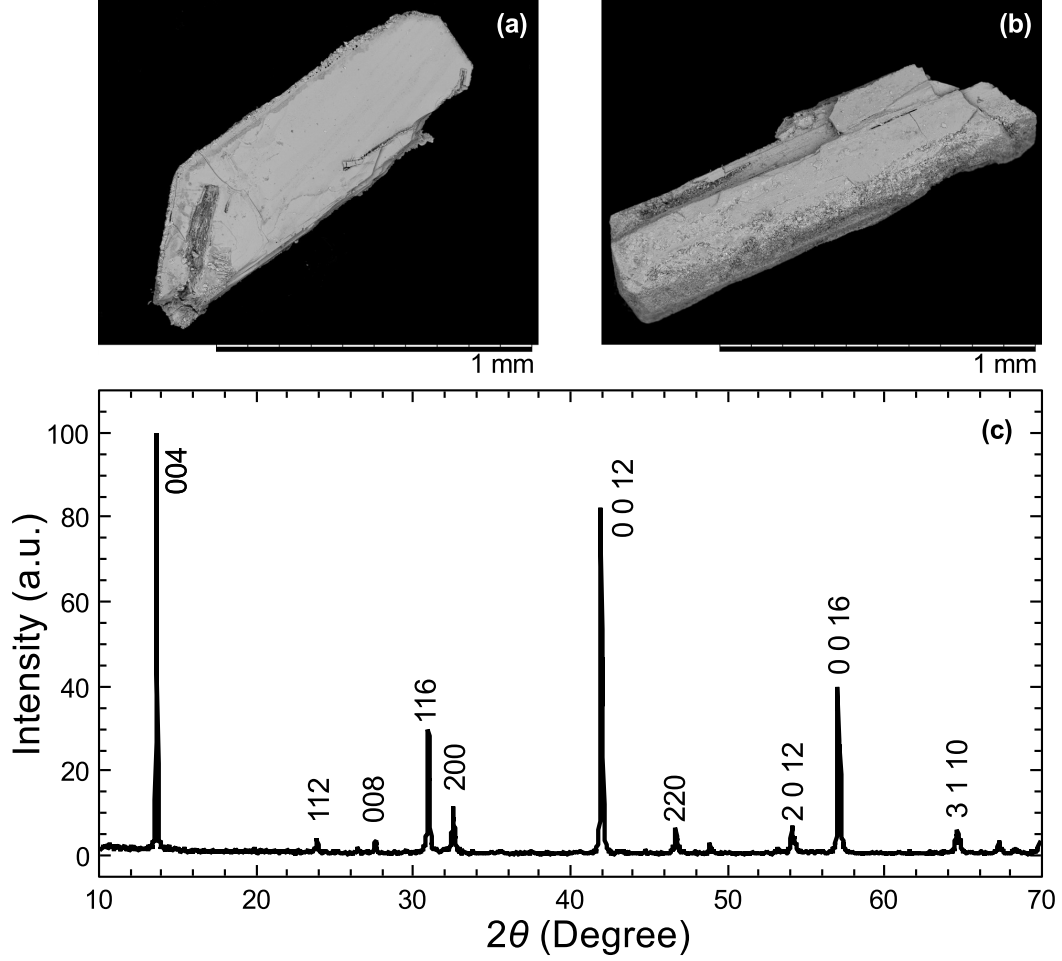


Figure 3.3: Samples of Sr_2IrO_4 grown using flux technique. (a) and (b) Scanning electron microimages of the single crystals of the compound. Here c -axis is pointing out of the plane of the page. Fresh-cleaved regions of the crystal are visible on the panel (b). (c) Powder X-ray diffraction pattern of ground single crystals.

by introducing the corresponding oxides into the mix (Eu_2O_3 , Gd_2O_3 , etc.). The synthesized crystals have a distinctive hexagonal shape with the c -axis pointing out of the plane of the hexagon (see figure 3.4 (a) and (b)). The average size of the crystals was found to be $1 \times 0.5 \times 0.5 \text{ mm}^3$. The correct phase was initially confirmed using powder X-ray diffraction (panel (c) of the figure 3.4) followed by detailed single-crystal X-ray measurements at various temperatures. The latter provides the information about the fine changes of the crystal structure (lattice parameters, bond length and angles) and allows to assess the uniformity of stoichiometric distribution of doping elements (sharpness of the peaks). The (EDX) measurements on multiple samples were used to determine the specific doping content.

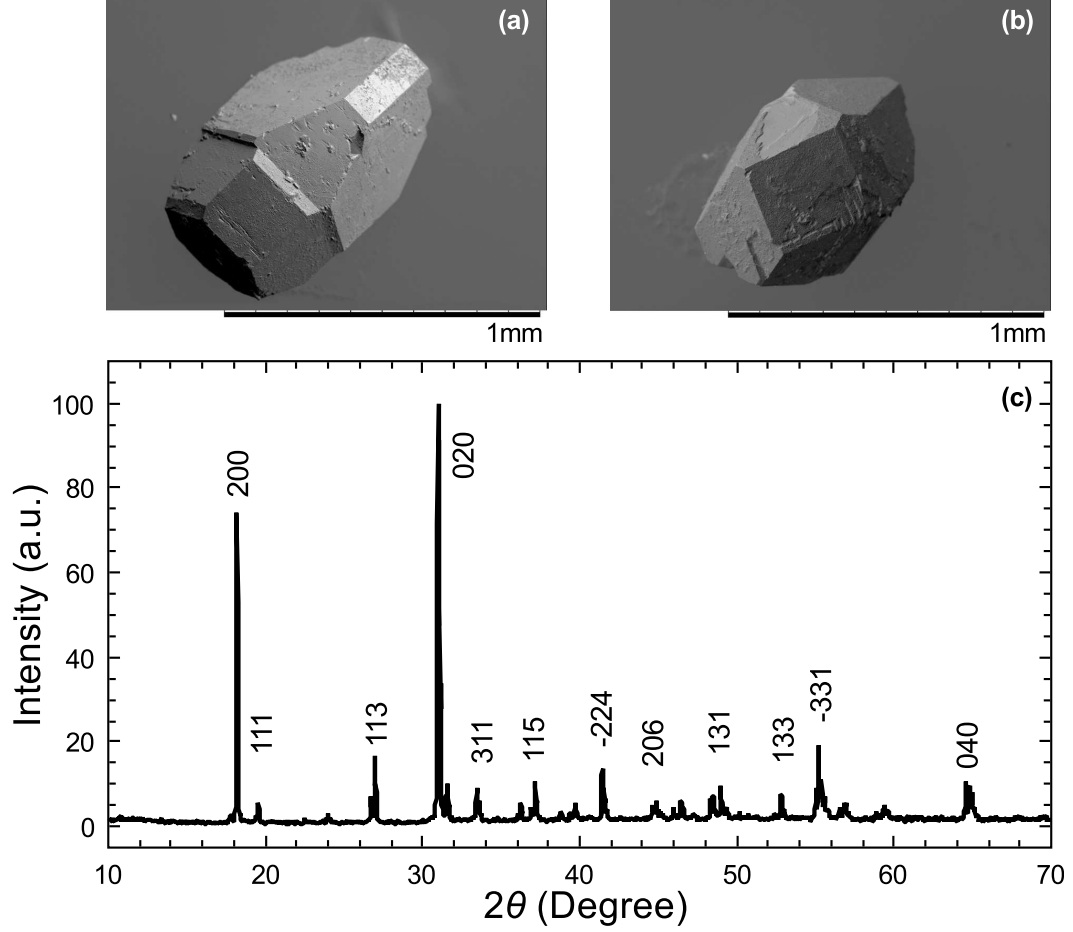


Figure 3.4: BaIrO₃ samples grown using flux technique. (a) and (b) scanning electron microimage of the individual single crystals. Hexagonal *ab*-plane of the crystal is clearly visible in the bottom-left corner. (c) Powder X-ray diffraction profile of the compound. The peak width comparable to the resolution of the scan indicates the high quality of the single crystals.

3.1.3 Oxygen depletion

The formation of ordered anionic vacancies in the host lattices of layer-structured materials can lead to new mixed frameworks, in which the cations sometimes are able to adopt several coordinations and to exhibit mixed valence states. The good illustration of novel, exciting physical properties emerging on materials with induced oxygen deficiency have been observed on close packed ABO₃ perovskites and layered cuprates [1]. The ionic vacancies can be formed during the crystal synthesis stage by modifying the growth condition such as pressure, atmosphere or cooling rate of the samples. Another approach is to introduce the vacancies into a stoichiometric as-grown sample. The advantage of the latter is a possibility to better control the stoichiometry deficiency due to fewer parameters involved, and the fact that the

procedure is performed on the fabricated samples with known initial properties. However, the method may not be applicable to wide range of materials. Regardless of the method utilized, the process has probabilistic character and is rather time consuming. Moreover, the techniques are highly destructive to the samples during the trial period, before definitive relations between the conditions of treatment and the resulting change in physical properties are established.

Unlike the high-temperature superconducting cuprate single crystals that require a complex post-annealing sequence and a long diffusion time (e.g. days or even weeks) to alter the physical properties [159], single-crystal samples of the layered iridates demonstrate significant structural alterations and radical changes in bulk transport and magnetic properties after mere ten hours of post-growth annealing. The method utilized in this work involved heating as-grown stoichiometric single crystals in vacuum by enclosing them in an evacuated and sealed quartz tube. Depending on the number and the size of the samples selected, the tubes of external diameter 10 mm to 22 mm have been used for this treatment. The tube evacuation was performed using a rotary pump, achieving the maximum pressure of ~ 30 mTorr at room temperature. The heat treatment was performed in a high-temperature box furnace or tube furnace. In general case the heating program consisted of rapid ($130^{\circ}\text{C} - 150^{\circ}\text{C}$) heating to a dwell temperature, followed by very slow cooling ($30^{\circ}\text{C} - 50^{\circ}\text{C}$) with a mere several hours period of stable temperature in between. The maximum temperature and the delay time were established empirically and are found to play the key role in the entire procedure to achieve the repeatable results.

Determining the oxygen deficiency δ is a difficult task, as there are not many known experimental techniques for inorganic compounds which would provide reliable quantitative data, applicable for small quantities of single crystal sample. Typically, the methods like Inert Gas Fusion (IGF) analysis require sample quantities from 100 to 300 mg of weight in order to determine the oxygen content with accuracy of 1 ppm [160]. One of the methods is to deduce the approximate deficiency from the structural refinement of single crystal X-ray diffraction data (see section 3.2.2), tracking the unit cell distortion relative to the structure of stoichiometric sample. Another method accessible for us is a thermogravimetric analysis (see TGA in section 3.3), which we utilized for this particular work. The single crystals of amount large enough to comply with TGA specifications were subjected to a temperature program earlier established by us experimentally. The resulting weight change was totally attributed to the oxygen loss, allowing us to determine the corresponding δ . Provided enough sample weight, the result is quite reliable, although this method only yields relative data and would not allow us to assess the absolute oxygen content of the stoichiometric sample.

3.2 Structural analysis of materials

3.2.1 Powder X-ray diffraction

The physical properties of solid materials are strongly linked to their structural parameters, therefore knowledge of the crystal structure of a studied compound is an essential aspect in condensed matter physics. In a crystalline material a unit cell is the basic repeating entity that defines the crystal lattice and characterizes a long range order. The periodic arrangement of atoms forms the families of parallel atomic planes, which are used to define directions and distances in the crystal. Since the discovery of X-rays in 1895 and the first application in crystallography in 1912, the X-ray diffraction (XRD) has grown and matured into a separate discipline with many different experimental techniques. Nowadays the XRD is the most common non-destructive method used to study the crystal structure of solids, suitable for characterizing a wide range of materials including metals, minerals, polymers and thin films. The elaborate discussion on the subject can be found elsewhere [161, 162], therefore here I will only describe the basic principles underlying the technique. Depending on the photon energy and the nature of the sample, the X-rays interact with the matter in many different ways, resulting in secondary X-ray (florescence) or electron emission (Auger process). The coherent (or elastic) scattering is the form of interaction one can use to access the structural information of solids. At low energies, the wavelength of the X-ray photon is comparable to interatomic distances, thus the radiation scattered from a periodic array of atoms is subject to interference with itself. Most of the incident photon beam is therefore eliminated through destructive interference, however at certain incident angles the geometry satisfies the *Bragg's law*

$$n\lambda = 2d_{hkl}\sin(\theta) \quad (3.2)$$

resulting in constructive interference or diffraction (figure 3.5). Here λ is the wavelength of the characteristic X-ray beam, θ – incidence angle (Bragg's angle), d_{hkl} – the interplanar distance between the atomic planes defined by respective Miller indices (hkl) [162]. Considering that the wavelength of the radiation source is typically fixed, each family of atomic planes will produce a diffraction only at certain angles determined by the interplane spacing. The amplitude of the diffracted X-ray is detected and recorded in the form of a count rate as a function of the angle 2θ (defined as the angle between the incident and diffracted beam), producing a series of peaks known as a *diffraction pattern*. For a particular interplanar spacing the d_{hkl} is written as

$$\frac{1}{d^2} = \frac{1}{V^2} \sum_{i=h,k,l} \sum_{j=h,k,l} C_{ij}ij. \quad (3.3)$$

where the volume of the unit cell V and the constants C_{ij} are determined by the crystal lattice parameters a, b, c and lattice angles α, β, γ [163]. For example, in the

case of a simple cubic lattice with $a = b = c$ and $\alpha = \beta = \gamma = 0$ the expression 3.3 reduces down to

$$\frac{1}{d^2} = \frac{(h^2 + k^2 + l^2)}{a^2} \quad (3.4)$$

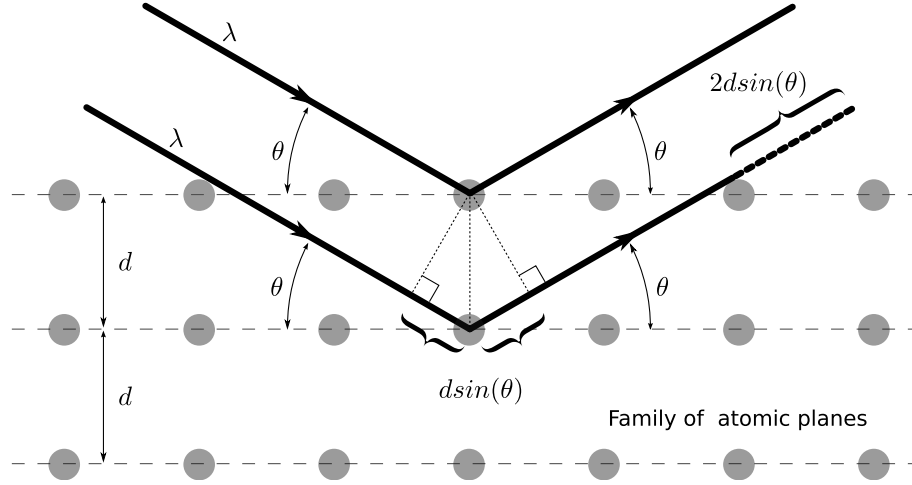


Figure 3.5: Illustration of the fulfillment of the Bragg's equation. If the difference in path length $2d\sin(\theta)$ between the beams reflected from a particular family of parallel atomic planes equals to an integral number of wavelengths $n\lambda$ — it results in constructive interference.

The intensity of the diffracted beam also carries useful information. It is determined by several factors and in general form is described by the following expression [163]

$$I = k|F^2| \left[\frac{1 + \cos^2 2\alpha \cos^2 2\theta}{\sin^2 \theta \cos \theta (1 + \cos^2 3\alpha)} \right] P \cdot A(\theta) \cdot e^{-2B \sin^2 \theta / \lambda^2} \quad (3.5)$$

Here k is just a scaling factor, $|F^2|$ is a structure factor followed by a complex Lorentz polarization factor, which is determined by geometry of the diffractometer. P is the multiplicity of the diffracting plane — the number of planes that belong to the particular family. The term $A(\theta)$ is the absorption correction parameter, determined by the sample and its geometry. The exponent term is a temperature factor, accounting for reduction of coherence due to thermal vibrations. The most interesting parameter here is the structure factor $|F^2|$, accounting for spatial distribution of the atoms, and the atomic scattering factor. The latter is proportional to the atomic number in periodic table, because the X-rays interact differently with the electronic clouds of different types of atoms. Thus, for sufficiently different atoms the XRD method can also provide an information about the atomic occupancy of a particular atomic sites.

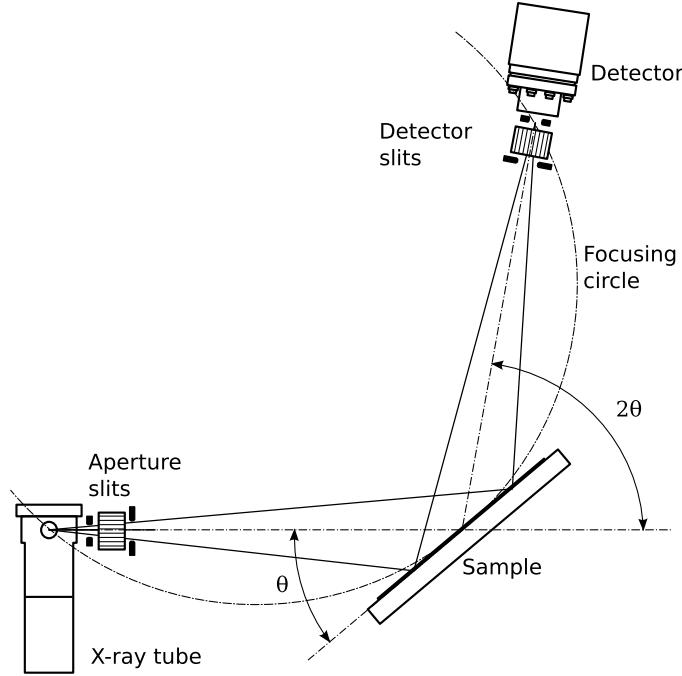


Figure 3.6: Schematic diagram of Bragg-Brentano diffraction geometry in $\theta - 2\theta$ configuration, utilized in most of modern powder X-ray diffractometers. Adopted from [164].

An array of atoms acts like a three-dimensional diffraction grating, therefore a single crystal sample in a diffractometer would produce only one family of peaks on the diffraction pattern if θ is varied within one plane. Obviously this information is not sufficient for reliable identification of the crystal structure. The sample would need to be rotated in space in order to produce enough information required for characterization. This approach is implemented in single-crystal X-ray diffractometer using either 3- or 4-circle goniometers (see section 3.2.2), where one is systematically changing 4 angles (χ , ϕ , Ω and 2θ) that define the relationship between the crystal lattice, the incident ray and detector. The data collected in these measurements allows one to solve the structure of crystalline material and determine the complete set of atomic coordinates in the unit cell. The bond lengths and bond angles, so important for our studies, are directly related to the atomic positions.

Another approach is to perform the measurements on a polycrystalline sample or a single crystal which has been ground into powder. Due to the random orientation of the crystallites of such sample, for every set of atomic planes there will be a small percentage of those that are properly oriented for constructive interference, producing all possible diffraction peaks for the given crystal structure. This is the basis of *Powder XRD* method, which presumes a statistically relevant number of crystallites for every set of diffraction planes. The samples for this type of measurements come in the form of powder, sintered pellets, coatings on substrates or even manufactured

parts of appropriate size. The goniometer used for this method is significantly less complex than the one used for single crystal XRD. There are many different geometries and conditions for these types of measurements, however in most cases a sample is placed on a stationary holder made of a polymer or a zero background holder (ZBH, single crystal silicon or silicon oxide cut along a non-diffracting plane). Most commercial XRD instruments employ the Bragg-Brentano parafocusing geometry [162], which provides both high resolution and high intensity of a diffracted beam (see figure 3.6). The X-ray source and detector are mounted on the different goniometer arms, rotating around the common axis passing through the sample holder plane, which in turn is orthogonal to the plane formed by the incident and diffracted beams. Since the powder XRD method captures only a small amount of relevant information (intersecting through Debye cones of diffraction) it is rarely suitable for solving the crystal structure of the unknown material. However, the produced diffraction pattern is equivalent to a fingerprint of a material, thus the compounds are identified by comparing the diffraction data against a database of currently known materials. This method also allows one to assess such parameters as the grain size (using Scherrer’s formula [162, 165], and preferred orientation of atomic planes in polycrystalline or powder solid samples.

For powder XRD studies in our lab we are using a Scintag X1 diffractometer equipped with Cu $K\alpha$ X-ray source ($\lambda = 1.5418 \text{ \AA}$) and the liquid-N₂ cooled germanium solid state detector element [164]. The instrument features a horizontal goniometer in $\theta - 2\theta$ configuration. In this design the X-ray source is stationary and the variation in the incident angle of the X-ray beam is achieved by rotation of the sample, which is moving around the same axis as the detector. The motion of the detector is mechanically coupled with the motion of the sample holder such that its rotational speed is doubled (figure 3.6). The sample is a piece of polycrystalline pellet or a single crystal ground into a fine powder using an agate mortar and pestle. The powdery sample in form of an ethanol-based paste is smeared in the center of a single crystal quartz plate, which serves as a zero-background sample holder. Phase identification from the recorder scan is performed using a database from the International Centre for Diffraction Data (ICDD) [166].

3.2.2 Single crystal X-ray diffraction

To determine the detailed structure of novel materials the powder XRD technique is not sufficient, thus single crystal X-ray diffraction is used. Thanks to a special goniometer (figure 3.7) and a large area detector, a single crystal X-ray diffractometer allows one to collect enough data to perform a complete structural refinement. Our research group has access to several single crystal X-ray diffractometers hosted in the X-Ray Facility at Department of Chemistry, University of Kentucky. The specific measurements for this work were obtained on Kappa CCD diffractometer manufactured by Nonius (Delft, The Netherlands) using the $K\alpha$ of Mo-based X-ray source. The Kappa-type goniometer is a 3-circle stage where, unlike in classic 4-circle goniometer, no χ -angle rotation is possible, but another angle κ is introduced, rotating

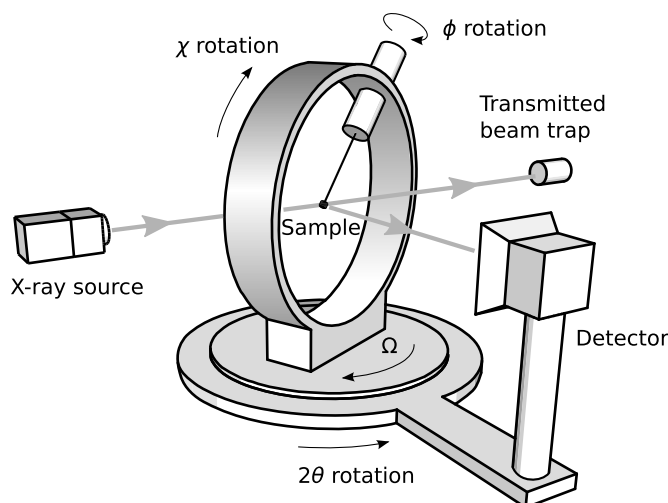


Figure 3.7: Schematic of the classical four-circle goniometer used in single-crystal X-ray diffractometers. ϕ – the angle of rotation of the crystal about the axis of goniometric head; χ – the angle of inclination of the ϕ -axis; Ω – the angle of rotation of the crystal with respect to the principal axis of the goniometer; 2θ – the angle of the rotation of the detector.

the sample about an axis at $\approx 50^\circ$ to Ω -axis. When the κ -angle is zero, the Ω and ϕ axes coincide. The instrument is equipped with a temperature control option, capable of maintaining a stable local environment around the measured sample during the data collection within a range of temperatures from 90 K up to 400 K, using a constant, low-velocity flow of cold nitrogen gas over the crystal. The accuracy of temperature stabilization depends on temperature setpoint and varies from 0.5 K for sub-ambient temperatures to ~ 4 K near the highest boundary of the range.

In a routine experimental procedure, a piece of a single crystal is selected as a sample, preferably of regular geometry. The average size of the samples is kept within the range of 50 – 100 μm depending on the chemical composition of the compound, in order to find a balance between diffraction intensity of X-rays and its absorption within the bulk of the crystal. The sample is attached at the end of the quartz fiber by a drop of inert, viscous polyisobutene oil. There is a list of requirements for the oil, among which is a low optical distortion during microscopy, amorphous solidification on cooling and a low scattering power. Paratone[®] 8227 (Exxon) is the product well satisfying the criteria and is traditionally used for crystallography [167, 168]. The glass fiber is mounted to the copper mounting pin which is in turn is secured on a micro-goniometer head. The sample is constantly observed through a macro-lens video camera, and if necessary additional adjustments on the goniometer head are performed to achieve an accurate positioning.

The pattern of X-ray reflections (figure 3.8) is captured by a charge-coupled device (CCD) image sensor. The positions and relative intensities of the reflection spots provide the information necessary for crystal structure refinement. Multiple images

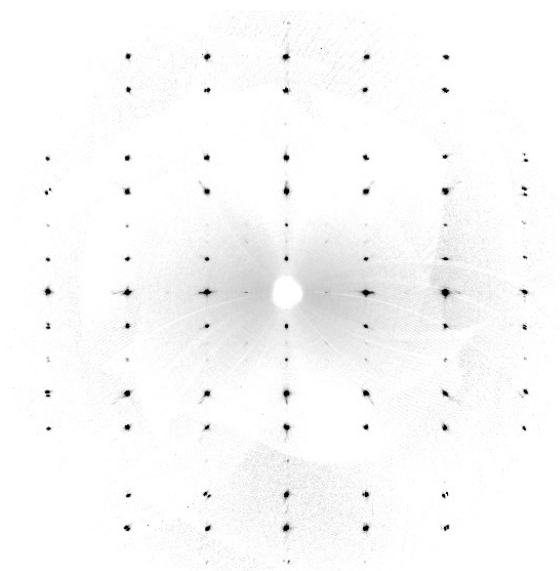


Figure 3.8: Diffraction pattern from Sr_2IrO_4 sample, obtained with a Kappa CCD diffractometer. The pattern has a reciprocal Fourier transform relationship to the actual crystalline lattice in real space therefore each point represents a family of atomic planes.

are recorder while the sample is rotated step by step through the angles χ , κ and Ω . The actual amount of angular rotation needed is determined by symmetry of the crystal unit cell. Combining the X-ray diffraction data with the complementary chemical information, the crystal structure refinement is performed by full-matrix least squares using the SHELX-97 [169] and SADABS (area detector scaling and absorption correction) [170] software packages.

3.2.3 Energy-dispersive X-ray spectroscopy

The chemical characterization and elemental analysis are crucial aspects of experimental condensed matter, especially in research on novel materials. Among the other methods, a technique based on detection of characteristic X-rays was found to provide high resolution and produce reliable data. The use of Energy-Dispersive X-ray detectors (EDX) in combination with Scanning Electron Microscope (SEM) or Transmission Electron Microscope (TEM) creates a powerful instrument for elemental microanalysis of the small samples, which is essential, since new materials are very difficult to produce in large quantities in the form of high quality single crystals. The development of lithium drift silicon (Si(Li)) solid state detectors in 1970s and achievements in quantitative software in 1980s [171] gave a strong momentum to this field of measurements. The X-ray microanalysis had since then matured into a widely-accepted, easy-to-use analytical technique, and EDX detectors are nowadays an option for most commercial SEM and TEM instruments.

The high-energy beam of electrons can interact with a tightly-bound inner shell electron of an atom, ejecting the atomic electron and leaving a vacancy in the shell where it was. Shortly after that the atom relaxes to its ground state, filling the inner shell hole through a limited set of allowed transitions of outer-shell electrons. Since the energy levels of the shells are discrete, the energy difference of a particular transition is a characteristic value and is released in form of a photon of electromagnetic radiation. The photon has a chance to be transmitted to another outer-shell electron ejecting it from the atom (Auger electron) with specific kinetic energy, or it can leave the atom directly. Similarly, the atom can be excited by a beam of X-rays also resulting in emission of characteristic radiation — the experimental method is called X-ray Fluorescence (XRF). The energy and wavelengths of the emitted X-rays are characteristic of the excited atom of particular chemical element. The energy difference between the shells changes significantly even when the atomic number Z changes by one unit. The dependence is expressed in the form of an equation 3.6 called Moseley's relation according to the name of an English physicist who discovered it,

$$\lambda = \frac{B}{(Z - C)^2} \quad (3.6)$$

Here B and C are constants which differ for each family of transitions and λ is the characteristic X-ray wavelength. This relation (see figure 3.9) forms the basis for qualitative analysis, which is a relative identification of chemical elements in the sample under study.

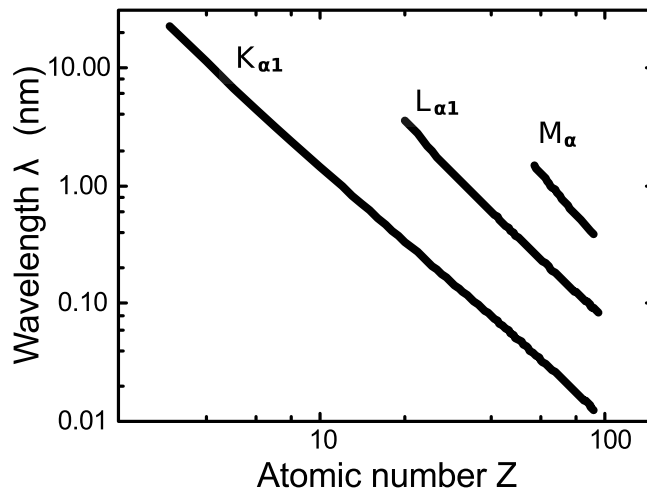


Figure 3.9: Moseley's relation between λ and Z for the $K\alpha_1$, $L\alpha_1$ and $M\alpha$ characteristic X-ray lines [172].

For elements with $Z \geq 11$ the shell structure is sufficiently complex that ionization of the innermost shell leads to a transition from more than one shell, thus the subscript of α, β, γ is used to define the most probable transitions to K, L or M shells in order of observed intensity [172]. The EDX systems are typically either integrated into an

SEM/TEM instruments, or come stand alone as an Electron Probe Micro-Analyzer (EPMA). In the first case the EDX detector is an option with its own data collection and analysis software which can be disengaged when not in use. The older type Si(Li) detectors are liquid nitrogen cooled and extend on a long arm from the chamber to fit a small dewar [172]. A more recent silicon drift (SDD) detectors with an integrated Peltier element are much more compact and do not require a cryogenic liquid cooling, and in the same time these are more sensitive and can operate at substantially higher count rates [173]. The detector produces an electric signal proportional to the energy of an incoming X-ray photon. The data (see figure 3.10) is presented in form of a plot of photon counts as a function of their energy. The generation of the X-rays is a random process and the number of counted photons is nearly always large enough (typical reliable count rate is $R > 600$ cps) that the probable error of the measurements can be assessed by Gaussian distribution. The standard deviation here is $\sigma(\%) = 100/\sqrt{N}$, where total number of counts collected during measurements time t is $N = R \cdot t$. In practice, the energies of the electron orbitals are so sharply defined that the uncertainty of the energy constitutes a small fraction (often $< 0.05\%$) when measured with an appropriate high-resolution detector [174]. This allows one to uniquely identify most of the chemical elements with $Z > 11$, except in the cases of strong overlapping of the peaks, when an alternative technique such as wave dispersion spectroscopy (WDS) has a clear advantage. The lower Z boundary of chemical element detection is determined by the material of the detector window (Be, polymer, etc.).

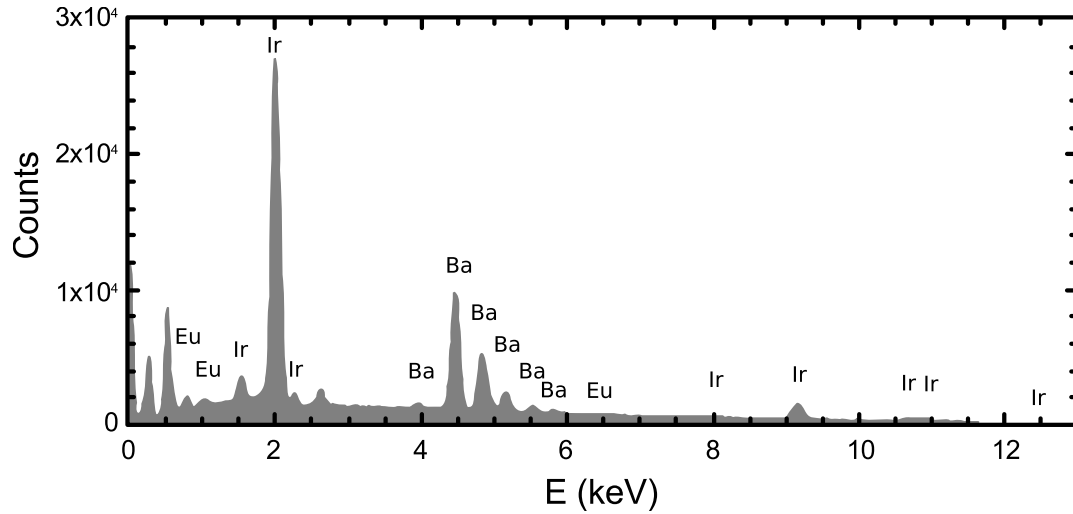


Figure 3.10: EDX spectrum of a single crystal of Eu doped BaIrO₃ studied in this work, with corresponding peaks labeled.

For this work our samples have been analyzed on a commercial SEM instrument Hitachi S3200-N equipped with Si(Li) EDX detector (liquid nitrogen cooled) from EVEX (Princeton, NJ). The ultra thin window (UTW) enables this instrument to detect the chemical elements above carbon ($Z \geq 6$). The typical electron beam

accelerating voltage for these types of measurements is maintained at 20 kV. As the penetration depth of the electron beam at this energy does not exceed several micrometers, the samples (single crystals) are mechanically cracked shortly before mounting on the sample holder in order to expose a fresh surface and avoid surface contamination build-up, which could affect the data. Magnification factor of $300\times$ to $900\times$ allows us to scan a rectangular area of $50\text{ }\mu\text{m} - 100\text{ }\mu\text{m}$ in size. The measurements are performed on 3–4 spots across several single crystals of the same compound to assure the uniformity of doping.

3.3 Thermogravimetric analysis

Historically, thermal analysis is one of the oldest testing methods, utilized extensively even by alchemists with their primitive procedures at the early ages of scientific exploration. The establishment of the industrial revolution in the early XIX century and a need for testing the quality of raw materials and products (testing flour for water or contamination content, coal quality assessment) stimulated a development of various types of thermal analysis and particularly a thermal gravimetric technique to its modern form [175]. Thermogravimetric analyzer (TGA) is the instrument implementing a method of thermal analysis which measures the amount and the rate of change in the weight of material, while it is subjected to a controlled temperature variation.

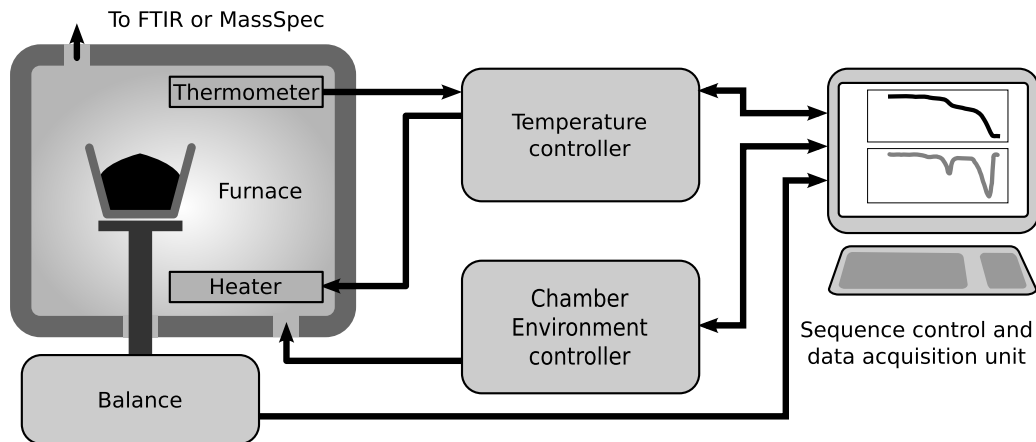


Figure 3.11: Thermogravimetric analyzer block diagram

Conceptually the design of thermogravimetric instrument is not much different today from that employed in the beginning of the century. The essential components include a sample container (ceramic or metal crucible), a high-temperature furnace and an appropriate balance to monitor the weight of the sample. In addition, the atmospheric control in the furnace can be introduced by flowing various types of gases through the chamber under a controlled rate and pressure, creating an

inert (He, Ar, N₂), oxidizing (O₂) or reducing (H₂) environment. A modern thermogravimetric instrument brought much improved accuracy, precision, sensitivity and automation to the table (figure 3.11). Since the analysis relies on a high degree of precision in three measurements: weight, temperature, and temperature change, the automated temperature control and high-speed data acquisition allow substantially higher resolution and speed of the measurements, enabling us study the fine structure of materials during phase transformation [176]. Often a mass spectrometer (MS) or a Fourier-transform infrared spectrometer (FTIR) is connected to a gas outlet of a TGA instrument for continuous, online identification and analysis of the evolving volatile products during transformation of a sample.

The TGA instruments available commercially differ depending on the types of furnace and balance design. In the instrument with the vertical tube furnace the balance can be located either above or below the furnace. In such configuration a sample crucible is either suspended in a mass pan (some instruments by PerkinElmer and TA Instruments) or installed on a platform at the end of an extended vertical balance arm (Netzsch Instruments). The design of such a system involves a special approach to a furnace in order to prevent the convection currents from affecting the sample pan, resulting in mass-signal “noise”. In the case when a balance is located above the furnace, the condensation of the volatile substances leaving the sample could potentially affect the balance elements. An alternative to this approach is a horizontal orientation of the tube furnace, where the sample is located on the crucible at the end of a horizontal beam attached to an extended balance arm projected into the furnace (Mettler Toledo and some models from TA Instruments). Such design eliminates the condensation and heat current issues, however is complicated by a need for a movable furnace to allow sample installation. In addition, the thermal expansion of the beam could affect the weight reading, therefore this type of configuration requires special balance design, to compensate for this effect.

The main data from the thermogravimetric measurements is the weight change of the specimen as a function of temperature or time. If the instrument is equipped with additional sensor measuring the temperature of the furnace, the magnitude and sign of the heat flow to the sample is also recorded. If the design permits, a TGA instrument can be equipped with a special sample platform, accommodating two crucibles and individual thermal sensors, one of which is either empty or filled with a reference material (alumina, silicon carbide are appropriate for solid samples). This enables differential scanning calorimetry (DSC) measurements, which is essentially high-temperature heat capacity, allowing to study phase transitions, melting and solidification behavior of various compounds [177]. The typical temperature program for TGA is a linear scan, although other types of temperature dependence are applicable and often provided by controlling software (functional dependence, dwelling at target temperature). The raw data collected from a TGA measurement is weight loss as a function of temperature and time. Optionally (if the hardware configuration permits), the heat flow information is recorded. Depending on the type of processes studies, the data requires a transformation before results may be interpreted. For

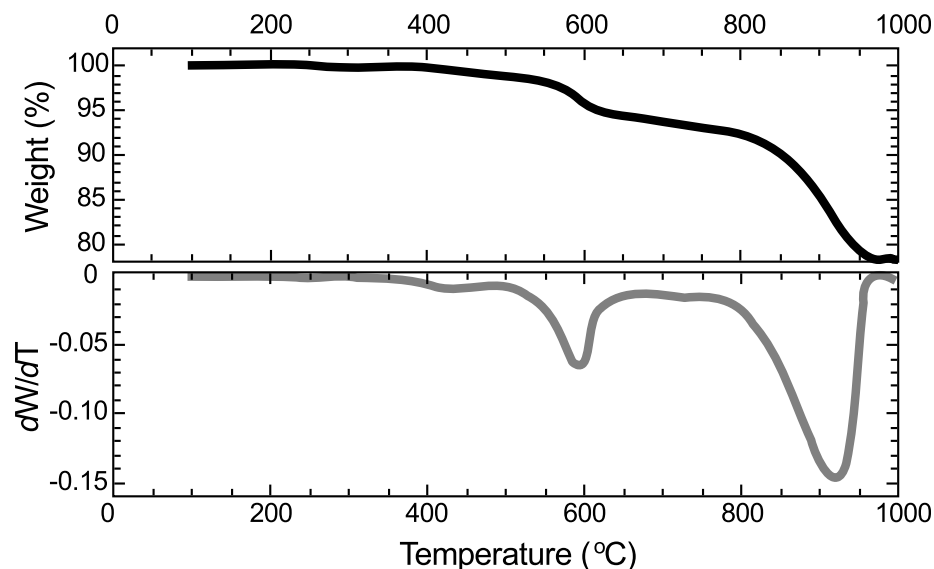


Figure 3.12: The original and differentiated form of thermogravimetric analysis (TGA) data for NaIrKO raw pellet.

trivial weight loss measurements a first derivative of the curve is very informative, allowing one to uniquely identify the thermal events. A precise amount of lost material is determined by consequent integration of the peaks of the first derivative curve, see plot in figure 3.12. Examples of thermal events and processes that can be determined by TGA/DSC include adsorption and desorption of gases and moisture [178], quantitative content analysis through thermal decomposition, kinetics of decomposition [179], the studies of thermal stability of materials [180], pseudopolymorphism of pharmaceutical substances [181], oxidation and oxidation stability [182]. In our lab a TGA is routinely used to study sintering, oxidation or reduction of synthesized compounds and their precursors as well as estimation of stoichiometry correction and oxygen deficiency.

All the TGA measurements for this work have been performed on a commercial instrument TGA/DSC 1 manufactured by Mettler-Toledo (Schwerzenbach, Switzerland). The design of the system features a horizontal furnace cell (see figure 3.13), which helps to minimize possible turbulence due to thermal buoyancy. The system is equipped with a furnace type SF 1100 capable of heating a crucible to a maximum temperature 1100 °C and control it with an accuracy up to 0.25 K. Thanks to a small heated volume and active cooling (water based coolant) the maximum temperature change rate constitutes 250 K/min and 20 K/min for heating and cooling respectively [183]. The gastight cell can be evacuated or purged with a defined gas, providing a controllable atmosphere. A 4-channel programmable gas flow controller manages both protective (balance unit) and reactive gas (furnace cell) simultaneously. The flow rate level is controlled with an accuracy of at least 4 mL/min and a maximum allowed flow 200 mL/min [184]. The high-precision balance can measure

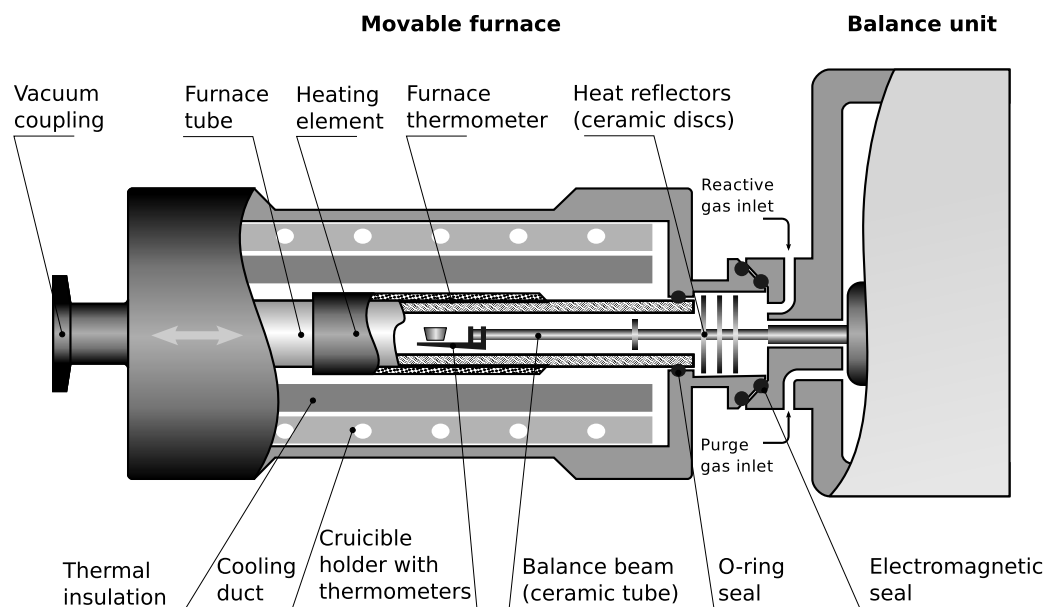


Figure 3.13: Schematics of a measuring cell of the thermogravimetric analyzer with horizontal furnace configuration.

weight change of the samples of maximum weight 1 gram with a resolution of $1 \mu\text{g}$. The parallel guided design of the balance ensures that the no change in position of the sample on a support beam influences the weight measurements. Thus, a thermal expansion of the balance arm or changes of the position of a sample (for instance in case of hyperactive decomposition or melting) should have a minimal effect on the results of the measurements. Several Pt-thermocouples are used to measure the temperatures of the furnace and the sample, allowing to assess the heat flow change (magnitude and direction) in order to trace possible transformations of the sample not accompanied by a change of mass. The maximum sampling rate of 10 data points per second for this system provides high-resolution data for analysis.

A typical sample is a piece of pressed polycrystalline pellet or a powder from ground single crystals. A platinum (Pt) crucible of a maximum volume 70 mL is used to contain the sample on the balance arm. The initial weight of the sample is determined using a built-in balance of TGA/DSC 1 and cross-checked by an external high-precision balance. Every time, prior to the measurements the background data of an empty crucible is recorded according to a sequence identical to the one of the planned experiment (including the gas reactive gas type and flow rate). This data is a parameter of the experiment and is subtracted from the actual measurements in online mode. The usual initial step of the sequence is 30 minutes of fire-off at 100°C in order to avoid the effect of the water evaporation on further experimental data. In case of significant weight loss at this stage, the new weight of the sample is considered a base for further analysis.

3.4 Magnetic properties measurements

The flux magnetometry method is a good solution to study the magnetic properties of bulk materials. It is implemented in numerous commercially available setups, one of which we are using in our lab. MPMS XL from Quantum Design is a modern, advanced, high-sensitivity SQUID magnetometer, very well suited for our research needs. Schematically the MPMS[®] detection system is illustrated in figure 3.14.

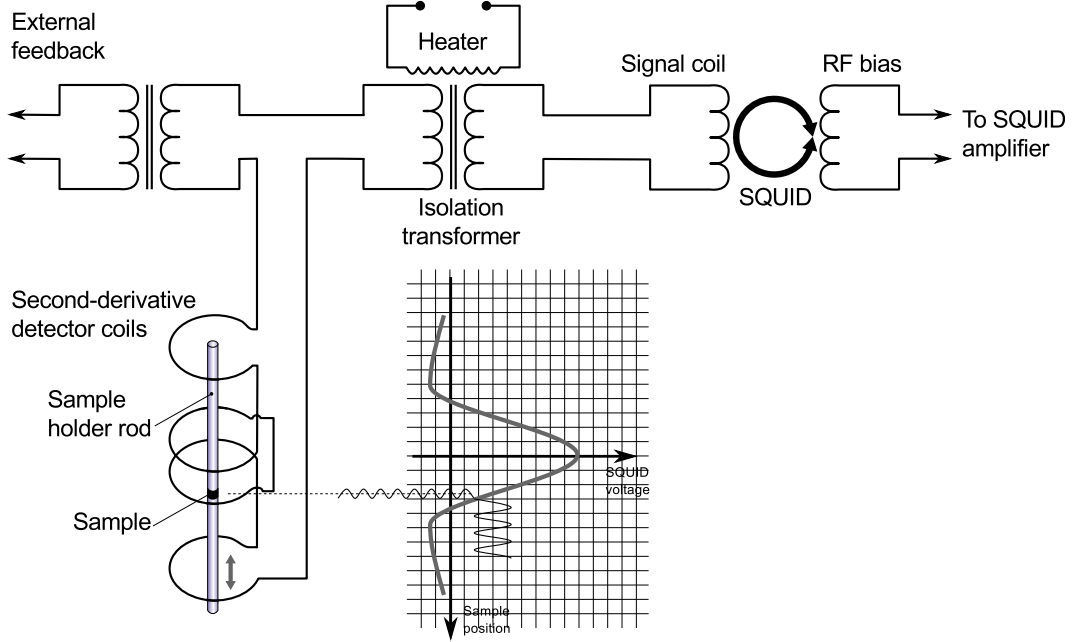


Figure 3.14: Schematics of SQUID magnetometer with longitudinal pickup coils [185].

It consists of the sensing coils, a radio frequency interference (RFI) shielded superconducting transformer and a SQUID sensor. The set of pick-up coils detects a flux change due to a moving sample. These coils are configured as highly-balanced second-derivative contour, designed to reject the uniform field of the external superconducting magnet and the magnetic background of the sample holder. The detected signal is proportional to magnetic moment of the sample which is magnetized by the external magnetic field produced by a superconducting magnet. The coilset is inductively coupled to the SQUID sensor through a superconducting RFI isolation transformer, which allows the system to operate in an electromagnetically noisy environment without experiencing flux jumps during the measurements. The RFI transformer is equipped with a heater, designed to drive both sides of the transformer out of the superconducting state to normal, in order to quench any persistent current in the SQUID circuit. The heater sequence is executed during all magnet charging procedures and at the beginning of sample measurements [185].

The core of the magnetometer sensing circuit responsible for its high sensitivity is a Superconducting QUantum Interference Device — SQUID. It uses one of the

Josephson effects as a basic principle of its operation — the properties of phase coherence of the Cooper pairs, tunneling across the insulating barrier (Josephson junction) between two superconductors. In *DC Josephson effects* the tunneling of the Cooper pairs through the insulating layer gives rise to a supercurrent proportional to phase difference even in the absence of the voltage difference.

$$J = J_0 \sin(\varphi_1 - \varphi_2) \quad (3.7)$$

In case of the *AC Josephson effect* the voltage V_{DC} across the junction is fixed, the phase will vary linearly with time, and the current will oscillate with amplitude I_c and frequency $\frac{2e}{h}U_{DC}$. Here the *Josephson constant* $2e/h$ is an inverse of the *magnetic flux quantum*.

$$\Phi_0 = \frac{h}{2e} = 2.067833636 \times 10^{-15} T \cdot m^2 \quad (3.8)$$

In this mode the Josephson junction acts as a perfect voltage-to-frequency converter [186, 187]. These days there are multiple SQUID designs, utilizing both DC and AC Josephson effects, each of them having its respective advantages and drawbacks. The dc-SQUID uses two or more Josephson junctions in parallel loops to increase a resolution as illustrated on the figure 3.15.

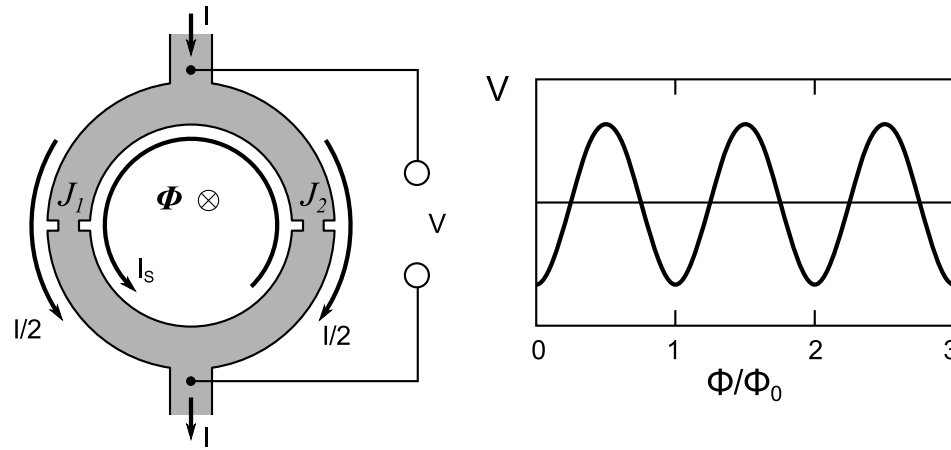


Figure 3.15: Illustration of DC-SQUID and $V(\Phi/\Phi_0)$ for constant bias current I . Here I_s – screening current, V – voltage across SQUID, Φ – external magnetic flux, Φ_0 – magnetic flux quantum.

When there is no external magnetic field the injected current splits symmetrically into the branches. Since the whole device is in the superconducting mode the amplitude of the current can be increased up to $0.5I_c$ — a half of a critical electric current of the weak link. The application of an external magnetic field will lead to appearance of a screening current I_s , trying to zero the total magnetic flux. Due to a quantization of magnetic flux in a superconducting material, the magnitude and direction of I_s will depend on the ratio Φ/Φ_0 , trying to complement the total flux Φ .

to an integral number of flux quanta Φ_0 . As soon as the total current through any of the links exceeds the I_c the superconducting ring becomes resistive, developing a voltage difference. When the magnetic flux is continuously increased the voltage across the SQUID becomes a periodic function of the flux, with the period equal to a flux quantum Φ_0 .

$$\Delta V = \left(\frac{R}{L} \right) \Delta \Phi \quad (3.9)$$

where R and L are the resistance and self-inductance of the SQUID's ring, respectively [188, 189].

The rf-SQUID functionality is based on the AC Josephson effect and uses only one weak link. This is the type of device utilized in the MPMS from Quantum Design for its measurement circuit [190]. It is less expensive and easier to produce in smaller numbers, although it is also less sensitive than dc-SQUID described above. In this device a magnetic flux enclosed by the ring is the sum of the applied flux and the flux LI due to self inductance of the ring L .

$$\Phi = \Phi_{ext} + LI \quad (3.10)$$

The external flux includes Φ_a – flux to be measured and a radio-frequency flux from the inductively coupled coil of the external LC-circuit (tank circuit), as illustrated in figure 3.16. Depending on Φ_a the effective inductance of the tank circuit changes, since the device operates in the resistive mode, thus changing its resonant frequency. These losses in the device appear as voltage across a load resistor and are a periodic function of Φ_a with a period Φ_0 . The voltage variation is directly related to the flux variation. Hence, the setup only measures the variations in the flux or field gradient.

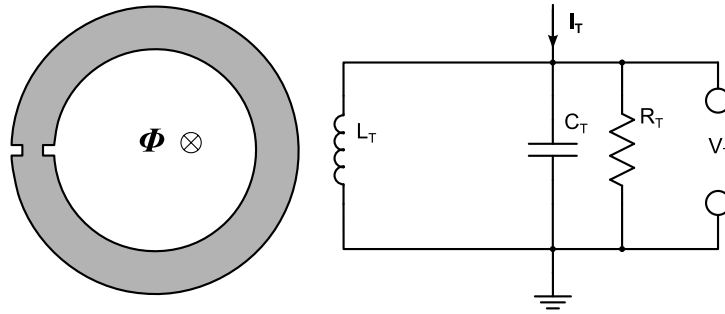


Figure 3.16: rf-SQUID inductively coupled to a parallel LC tank circuit [186]. The output signal is measured as a voltage V_T across the load resistor R_T

The sample chamber of the MPMS[®] is located inside the bore of the superconducting magnet, which is submerged in liquid helium bath, as illustrated in figure 3.17. The temperature conditions of the sample space are controlled by flow of the liquid helium around the sample chamber and a set of built-in heaters and thermometers. All this hardware allows us to measure the magnetic properties of solid or powder-like

samples as function of temperature from 1.7 K up to 400 K, or as a function of magnetic field up to ∓ 7 Tesla [185]. The temperature range can be extended up to 800 K using an optional high-temperature insert. During the measurement a low-pressure helium atmosphere is maintained in the sample space, however a custom gas from an external tank also can be used.

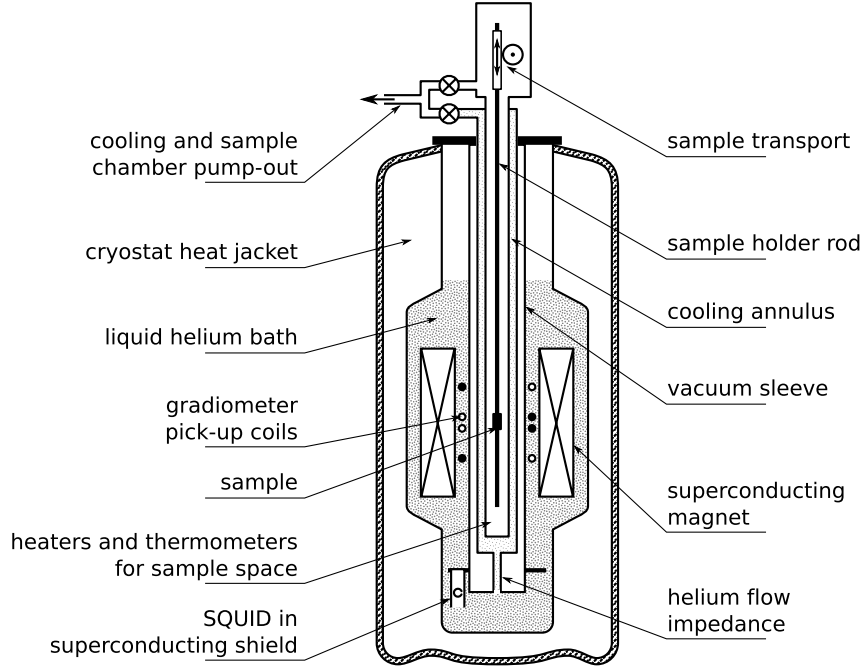


Figure 3.17: Schematic cross-section of the MPMS[®] [190, 191, 185].

In the routine procedure, we first determine the amount of the material, (a single crystal or a piece of a polycrystalline pellet) by weighting the sample in an electronic high-precision balance (accurate to $10\ \mu\text{g}$). The sample needs to be mounted on a non-magnetic uniform rod, about 12 cm long to assure the cancellation of the magnetic background while passing through the pickup coils. In the case of single crystals the sample is mounted on a straight quartz (SiO_2 is weakly diamagnetic [192]) rod about 1 mm in diameter with a small amount of thermoconducting varnish VGE-7031 [193]. Since all the compounds under study are highly anisotropic, additional attention is paid to the orientation of the samples with regard to the magnetic field. In the case of polycrystalline pellets the sample is packaged inside a gelatin capsule which is secured in the middle of a long, clear plastic (polypropylene) drinking straw [185]. The sample quartz rod or straw is attached to the end of the MPMS drive rod to be inserted into the sample chamber. To provide the dipole response expected by the software fitting algorithm, the sample is centered within the pickup coils prior to beginning of the measurement sequence.

3.5 Transport properties measurements

3.5.1 Electrical resistivity

Electrical resistivity is one of the characteristics providing an insight into the charge transport properties of materials. In our studies we are using both AC- and DC-current resistivity measurement techniques in 4-wire configurations.

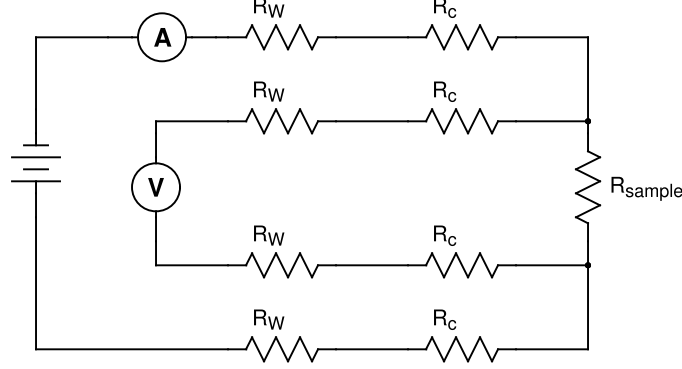


Figure 3.18: Equivalent circuit of four-point probe setup for resistivity measurements. Here R_W is connecting wire resistance, R_C – contact resistance of the leads/sample interface.

When studying the temperature and magnetic field dependence of electrical resistivity one has to deal with a problem of remote location of the measured sample and measuring instruments. The sample holder is usually made to position the sample in the most temperature stable region of the cryostat (for sub-ambient temperature study) or furnace (for high-temperature measurements). The measurement equipment needs to be installed at a safe distance to avoid potential interference from the high magnetic field. The consequence of this is the increase of the length of connecting wires, the resistance of which becomes dominant in the measured signal. Another issue to deal with is the contact resistance of the sensing leads attached to the sample. Typically this one is lower than the resistance of the sample under study and therefore can be neglected. However, in case of variable temperature conditions the contact resistance can dominate and obscure the resistive effects in the sample itself (for instance in superconductors below T_C). These effects cannot be treated as systematic error and have to be accounted by other means. The four-wire technique (also known as Kelvin method) allows us to overcome most of the named problems. It requires using both current and voltage meters and two pair of separate contact wires to connect the instrument to the tested sample. Each wire is individually connected to the surface of the sample, which allows us to account for the contact resistance as illustrated in the equivalent circuit diagram, figure 3.18. The contour forms a series loop, therefore the electric current is the same in all points. The potential difference is measured only across the sample, thus the ratio of voltmeter indication to applied current value yields the resistance of the sample according to Ohm's law. The input

impedance of the voltmeter is sufficiently high that its wires carry minuscule current. One can see that the wire leads and contacts resistance is thus excluded from measurements. The resistivity of the material is assessed using the measured resistance value (R) and geometry of the sample (A , L).

$$\rho = \frac{R \cdot A}{L} \quad (3.11)$$

The leads configuration is important for four-wire measurements. Typically the pair of voltage leads is located between the current supplying leads, which are attached to the edges of the sample. The potential drop should be measured on the section of the sample where electric field lines are relatively straight, which is achieved either by inline placing of all four leads, or very small separation (comparing to the size of the sample) between the voltage leads. Due to several factors like geometry of a sample space and the need for high-quality single crystals the dimensions of studied samples are often less than 1 mm. The separation between the voltage sensing leads often does not exceed several hundred μm , and the area of the electrical lead contact needs to be minimized in order to avoid shunting the large surface of the sample. The contact resistance in the point of attachment in some cases is several times higher than that of the sample itself. This leads to significantly high current density and may cause the local resistive heating of the sample, substantially changing its temperature and rendering the measured data meaningless. In order to avoid this effect, the excitation current is kept at lowest possible level producing reasonable signal/noise ratio. The power source is exploited in current stabilization mode in order to avoid unintentional current level changes due to change of resistance of the sample. Special care must be taken about the contact resistance to minimize it by preparing the surface of the samples appropriately and selecting the leads bonding compound according to experimental conditions and type of material under study. The typical compounds used in our labs for electrical leads attachment include two-component solid silver-filled epoxy EPO-TEK[®] H20E from Epoxy Technology Inc. [194] and carbon paint Dotite XC-12 from Fujikura Kasei Co. [195]. Gold wire of diameter 0.001" is used to form an electrical contact between the sample and sensing leads. The samples are mounted to a sample holder using highly thermoconducting adhesives such as phenolic butvar varnish VGE-7031 by General Electric [193] (for temperature range 1.7K to 550K) or aluminum nitride ceramic adhesive Ceramabond[™] 865 from Aremco Products Inc. [196] (for high-temperature measurements up to 900K). The sample holder is maintained in the helium atmosphere inside a cryostat at pressure of few Torr in order to provide efficient heat exchange and temperature stabilization. If the design of a cryostat allows it, the holder is directly interfaced with a heater and cooling chuck.

We are using LR-700 resistivity bridge from Linear Research Inc. for AC-resistivity measurements, which allow us to resolve the resistance from nano Ohm range up to 2 M Ω [197]. It operates at a fixed frequency of 16 Hz and can utilize very low excitation current in the nanoampere range, thus minimizing the dissipated power and self heating of a sample under test. Because of the fixed frequency at which the LR-700 operates, there is a need in certain cases to verify the data by DC resistivity method,

to avoid the contribution of the reactance of the circuit. A nanovoltmeter and a current source (we are using the Model 2182 Nanovoltmeter and the Model 2400 Source Meter or the Model 6220 Current Source at different measurement stations) from Keithley Instruments are utilized in our lab for DC-resistivity measurements. In order to avoid the error due to thermal EMF in the voltmeter test leads [165], the pair of instrument was configured to utilize Delta measurement technique. The square wave output of the current source produces an excitation signal oscillating three times between I_{max} and $-I_{max}$ per single data point of R . The resulting average resistance is calculated according to formula 3.12, where V_n is the voltmeter output measured at each peak current value I_{max} [198].

$$\langle R \rangle = \frac{(V_1 - 2V_2 + V_3)}{4I_{max}} \quad (3.12)$$

A broad range of temperatures can be covered in our lab while measuring resistivity properties of materials. A custom transport measurements probe for the standard QD MPMS[®] cryostat serves for sub-ambient temperature range 1.7K-400K and external applied magnetic field up to 7 Tesla [185]. The Displex pneumatic closed cycle cryocooler (DE202) from Advanced Research Systems (Macungie, Pennsylvania), equipped with high-temperature interface, covers the range of temperatures from 10K to 800K [199], and in our research is used primarily for high-temperature measurements.

3.5.2 Current-Voltage characteristics measurements

The relationship between the direct current (DC) through a sample versus voltage across it is called a current voltage characteristics or $I - V$ curve. The data can help to illustrate the transport properties of materials and is especially valuable if a non-linear behavior is observed. The measurements are usually performed by sweeping or stepping up a potential difference across the sample under test and measuring the current through it at each step. The same measurement can be done in current stabilization mode by stepping up the electric current and measuring voltage drop across the sample. The technique is more applicable for our case of variable temperature measurements, since the four-point probe setup is needed in order to eliminate the contribution of sensing leads and contact resistance. In our case, the experimental setup is virtually the same as for resistivity measurements (see Section 3.5.1), using the same set of instruments and sensing leads configuration, except that a separate software program is used to drive the current source and the voltmeter. The current is ramped in discrete steps with adjustable increment, various starting and finishing current values (zero, maximum positive or negative current) can be specified.

3.6 Heat capacity measurements

The data from heat capacity measurement can provide valuable information about the electronic, lattice and sometimes magnetic states of our materials. Measurements taken well below the Debye temperature of a specific compound directly probe the

electronic energy levels, and therefore make a nice addition to our data from other types of measurements helping to understand the specific behavior. For our research we are using the heat capacity option to the Quantum Design PPMS[®] to measure heat capacity at constant pressure. With the help of this system, we can perform the measurements within the temperature range $1.8 < T < 400\text{K}$ and in applied magnetic field up to 9 Tesla [200]. The sample holder can accommodate the weight within the range from 1 mg to 200 mg, which perfectly suits the majority of our samples.

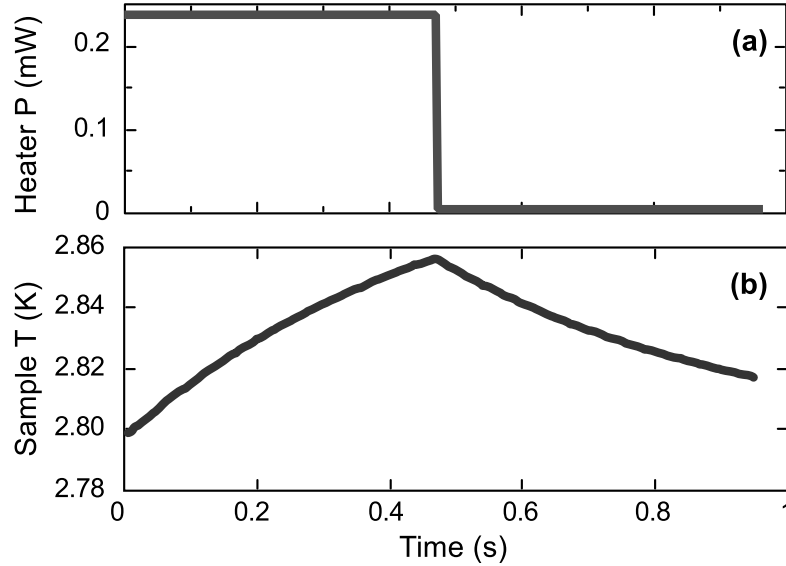


Figure 3.19: The change of sample temperature in a microcalorimeter as a function of time (b) due to a pulse of heat applied (a). The warming and cooling stages of the process of approximately equal duration are clearly distinguishable.

As with other similar techniques for measuring heat capacity, the relaxation technique used here involves a supply and removal of controlled amount of heat, while monitoring the resulting temperature change of the sample. The heat is supplied at a constant power for a fixed time and the following cooling period has the same duration, see figure 3.19. The environment in the sample space is maintained at high vacuum ($\sim 9 \times 10^{-6}$ Torr) by a liquid helium sorption pump, so the thermal conductance between the sample platform and the thermal bath is dominated by the conductance of the metal wires (sample platform support), as illustrated in figure 3.20 (b). This reproducible heat link gives large enough relaxation time-constant to allow the sample and the platform to achieve sufficient thermal equilibrium for reliable measurements. After each heating-cooling measurement cycle, the temperature response of the system is fitted by two-tau model, simulating the effect of heat flowing between the sample platform and the sample [201, 200]. The model accounts for both the thermal relaxation of the sample platform to the bath temperature and the relaxation between the platform and the sample itself. The equations 3.13 express the two-tau model.

$$\begin{aligned}
c_p \frac{dT_p}{dt} &= P(t) - \lambda_g(T_p(t) - T_s(t)) - \lambda_w(T_p(t) - T_0(t)) \\
c_s \frac{dT_s}{dt} &= -\lambda_g(T_s(t) - T_p(t))
\end{aligned}
\tag{3.13}$$

Here c_p and c_s are heat capacities of the platform and the sample respectively, λ_g is the thermal conductivity between the two due to the grease. The respective temperatures of the platform and the sample are given by $T_p(t)$ and T_s . The term λ_w is the thermal conductance of the wires supporting the platform. The same results are also used to compare to the solution to the simple model expressed by equation 3.14, which assumes an ideal thermal contact between the sample and the platform [200]. Under some circumstances the fit to the two-tau model does not converge, which might occur when the sample is perfectly attached to the platforms (very rarely), when connection of the sample is very poor, when the thermal conductance of the sample is poor, or when the weight of the sample is very small compared to the platform (occurs most often).

$$c_{tot} \frac{dT_s}{dt} = P(t) - \lambda_w(T_s(t) - T_0(t)) \tag{3.14}$$

In this case the software falls back to the simple model in order to overcome the fitting difficulties and the platform-sample coupling coefficient is reported to be 100 %. The advantages of relaxation method for heat capacity measurements are the ability to measure rather small samples (down to 1 mg) and the simplicity of sample mounting. The drawbacks are the difficulty of result interpretation if the measurements conditions are not ideal and the fitting algorithm fails.

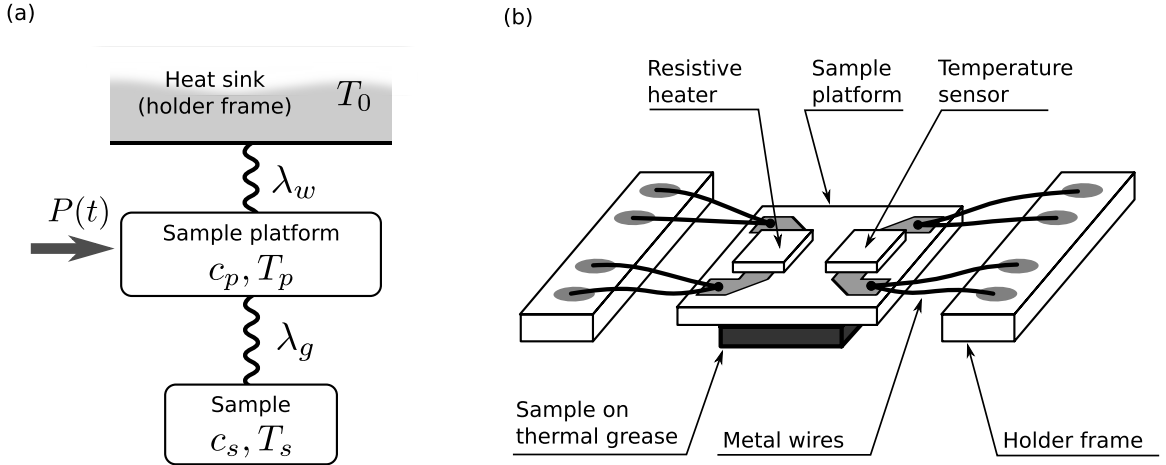


Figure 3.20: (a) Illustration of Two-Tau model for sample and sample holder; (b) schematic drawing of microcalorimeter sample holder design.

In the routine procedure one first needs to measure the addenda to assess the heat capacity of the system without the sample. It involves applying a certain amount of thermal conducting grease to the surface of the sample platform of the clean puck. We are using vacuum grease Apiezon type N [202] for measurements within the sub-ambient temperature range and Apiezon type H [203] for the temperatures up to 400 K. The amount of grease to be applied is determined by the size and weight of the sample (due to the bulk nature of measurements one can install several pieces simultaneously in order to achieve the desired overall weight), so the reliable thermal contact and adhesion can be achieved without the need to disturb the amount of grease when installing the sample for actual measurements. Special attention is paid to the wires supporting the sample platform. In order to avoid mechanical disturbance, the mounting procedure is performed with the puck installed in a special mounting station which secures the sample platform by a suction force from a vacuum pump. Maximum precautions are taken to avoid spreading the grease over the edge of the sample platform, and onto the wires as this can change the thermal conductivity between the platform and the puck frame, and render the calibration data unusable. For a regular and maintenance cleaning of the puck, the toluene solution is used as degreaser, according to a recommendation by manufacturer [200].

3.7 Thermoelectric power measurements

The thermoelectric power (TEP) effect is an observed gradient of electrochemical potential across a sample in response to a temperature gradient. The constant of proportionality α between the voltage and temperature gradient causing it, is the Seebeck coefficient and is defined as $\Delta V/\Delta T$ as $\Delta T \rightarrow 0$. The TEP coefficient is related to the entropy transported per charge carrier $\alpha \sim -S^*/e$, and can be expressed for metallic materials as

$$\alpha = \frac{k}{e} \left[\frac{\pi^2}{3} \right] \left[\frac{kT}{E_F} \right] \quad (3.15)$$

and for intrinsic semiconductors and insulators as

$$\alpha = \pm \frac{k}{e} \left[\frac{S^*}{k} - \frac{E_F}{kT} \right] \quad (3.16)$$

where E_F is the Fermi energy relative to the appropriate band edge and S^* is the entropy transported by charge carriers [1, p. 245]. The thermoelectric effect is used in thermocouples, thermoelectric generators and thermoelectric cooling devices (Peltier effect) [187], thus this type of measurement seems to be more appropriate in research for such materials. However, the measurement of the Seebeck coefficient is also of great value in studies of strongly correlated electron systems, such as this work. As one can see from the expressions 3.15 and 3.16 the value and the sign of the Seebeck coefficient provide the information about the Fermi energy in metallic compounds and the sign of the dominant charge carriers in semiconducting materials respectively. The low-temperature TEP studies under high magnetic field are also

known to provide ample of useful data in studies of strongly correlated electron materials [204, 205, 206].

The thermoelectric properties measurements for this work have been performed using a custom built apparatus (see figure 3.21 (b)) employing dynamic, two-point method. The samples are clamped between two copper pins using small amount of silver paint for improved thermoconductance. The temperature gradient is created using a resistive heater made out of non-inductively wound coils of Manganin wire. The thermoelectric potential is measured using two golden wires attached either to the sample (by silver paint) at the clamping points or to the copper pins (by resistive microwelding method) if the sample size is too small. Type E (chromel-constantan) differential thermocouple is used to measure the temperature gradient across the sample. It is mounted on the copper clamps in direct proximity to the sample sides using thermoconducting varnish VGE-7031 [193]. The clamping posts are mounted to a copper base using electrically insulating, heat conducting cement. The compactness of the whole sample stage allows it to be installed in various cryostats as long as at least 6 electrical feedthrough connections are available. In our case the sample holder was installed in a closed cycle cryocooler with a high-temperature option (model (DE202) from ARS, described earlier in section 3.5.1). The setup needs to be maintained at high vacuum during measurements, the tin-foil enclosure is used as a shield to prevent a parasitic radiative heat contributing to the results.

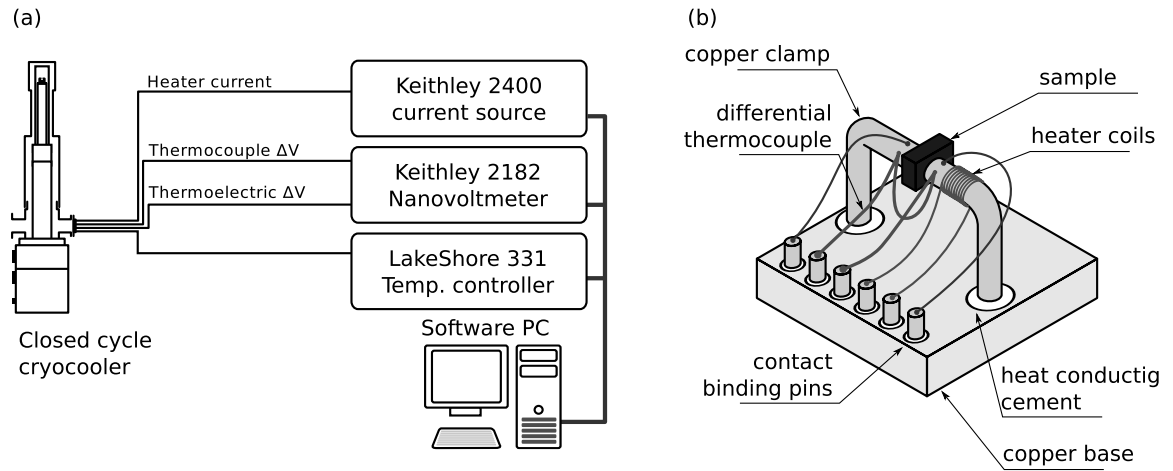


Figure 3.21: (a) Block diagram of the measurement system of thermoelectric properties measurements apparatus and (b) schematic diagram of TEP apparatus sample stage.

The instrumental part (see figure 3.21 (a)) is implemented using several devices from Keithley Instruments. The Model 2400 source meter is used as an oscillating current source to power the pulse heater. The double-channel Model 2182 nanovoltmeter allows us to measure the thermocouple signal and the thermoelectric potential difference simultaneously. The magnitude I and duration τ of generated temperature

gradient ΔT providing the most reliable data is determined empirically depending on material and specific temperature range and can be varied by adjusting the current output and its frequency. The temperature control of the base system is implemented using the Model 331 controller from Lake Shore Cryotronics [207]. The control of the instruments and data acquisition is automated using a computer running custom software developed in LabView environment. The performance and accuracy of the setup has been tested by measuring the constantan wire. This apparatus enables us to reliably measure the thermoelectric properties of samples of various materials within the range of temperatures from 20 K to 650 K.

The sample is typically a fragment of a single crystal of regular shape with two parallel surfaces normal to direction of temperature gradient. The samples are prepared to proper shape and size (1.5 – 0.3 mm) using a micro grinder or a sand paper. Conductive silver paint is applied at the clamping surfaces, however dry clamping is used for temperature range below 100 K, since the thermoconductivity of the paint is found to degrade rapidly in this range of temperature.

3.8 Measurements under pressure

Pressure as a thermodynamic parameter and as a mean of perturbing a symmetry of the system has a unique role in condensed matter physics. Hydrostatic pressure is a clean and controllable way of altering the interatomic spacing or bond angles of a studied material. In our lab we have access to several high-pressure systems manufactured by UNIPRESS (Warsaw, Poland) and EasyLab (Berkshire, United Kingdom) designed for magnetization and electric transport measurements. For this particular study we measured electrical resistivity utilizing a hydrostatic piston-cylinder type, clamp pressure cell LC10 from UNIPRESS (figure 3.22) capable of achieving a maximum pressure 1.3 GPa. The pressure cell is from ~ 130 to 150 mm long in assembled state and is approximately 24 mm in diameter, designed specifically to be used with the QD PPMS type cryostat or any other cryostat with a sample space diameter ≥ 25 mm. The inside diameter of the bore is 6.2 mm, allowing ample space for two samples and a pressure sensor. The minimum depth of the sample space at maximum pressure (maximum piston travel path) remains ~ 30 mm, which we use to install custom made fixtures in order to accommodate the samples in various orientation. The Bridgman type [208] feedthrough of 12 insulated wires allows coupling directly to standard PPMS sample puck, giving an option to monitor pressure sensor *in situ* and measure the Hall-effect or electrical resistance of two samples simultaneously by the 4-probe method. One of the 12 wires is made of constantan alloy (NiCu 45:55) and the rest are insulated copper wires, thus allowing the implementation of an optional type-T thermocouple in order to monitor the temperature inside the pressure cell. The metal body and large size result in quite high heat capacity of the cell, which requires experimentalists to use rather slow temperature ramping rate (typically $0.2 \div 0.3$ K/min) in order maintain thermal balance. Measuring the temperature inside the pressurized medium in close proximity to the sample would allow one to reduce the measurements time. However, the type-T thermocouple is

impractical below ~ 70 K, therefore the constantan wire is more often used as one of the leads for transport measurements in our experiments.

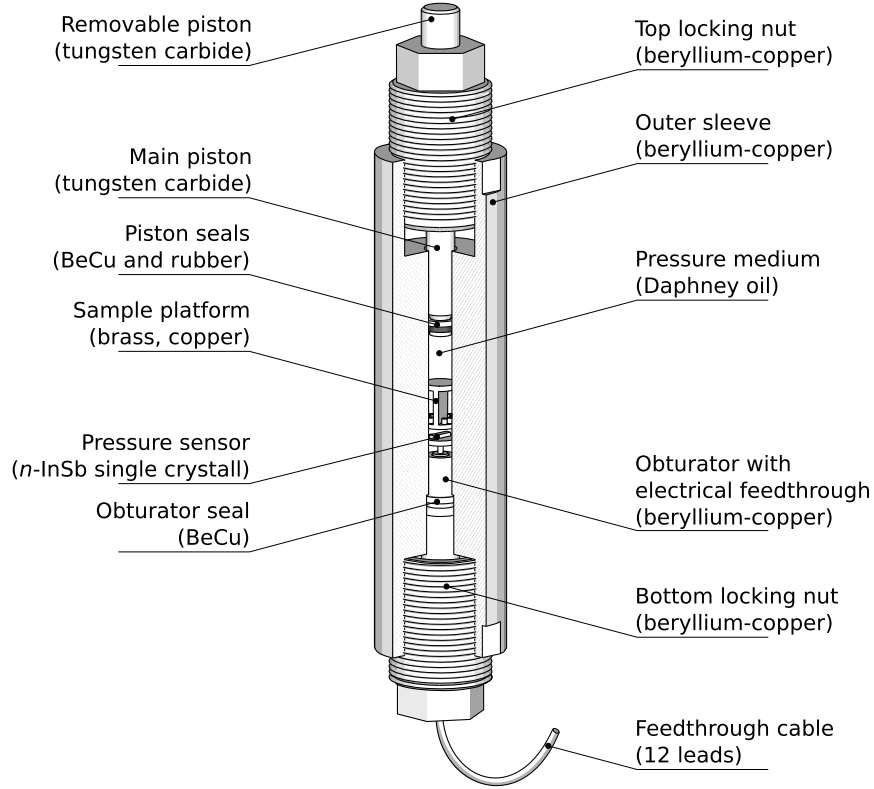


Figure 3.22: Cutaway view of the hydrostatic pressure cell LC10 for resistivity and Hall-effect measurements.

Due to our high interest in the correlation between magnetic and transport properties of novel materials, the measurements in our lab often involve the use of magnetic field, thus the materials used in the construction of the pressure cell are non-magnetic within the operating temperature range ($1.4 \div 400$ K) with highly uniform magnetic moment along the length of the cell [209]. Most of the functional parts of the LC10 pressure cell are made of beryllium-copper (25 BeCu) alloy, with exceptions for the pistons which are made of tungsten carbide alloy (WC).

To monitor a pressure level inside the bore, n -InSb single crystal (commercially available under a name SPG 10 from UNIPRESS) is used as a pressure sensor [210, 211]. This type of semiconductor sensor has a significant advantage over the metal wire coil sensors (i.e. Manganin) due to an order of magnitude higher typical pressure sensitivity, lower sensitivity to deviatoric components of the stress state (stress deviator tensor s_{ij} , which tends to distort the hydrostatic stress tensor) and weak temperature dependence of pressure-resistance characteristics below 300 K [212]. The sensor has been calibrated by the manufacturer of the cell for the pressure range up

to 1.2 GPa and temperature range up to 310 K. The pressure at a given temperature is determined using an empirical equation [213].

$$p(T) = [2.73 + 6.434 \times 10^{-4} \cdot (T - 77.4K)] \cdot \ln\left[\frac{R(p, T)}{R(p_0, T)}\right] \quad (3.17)$$

where T is the current temperature and R is the resistance of the pressure sensor at given conditions. The typical resistance of this type of sensors is below 0.2 Ω , therefore it is necessary to use a four-probe resistance measuring technique for precise pressure control. The nonlinear temperature dependence of the pressure is described by a polynomial dependence with empirical coefficients carrying the terms up to T^5 , thus enabling us to involve necessary corrections for precise determination of pressure within the whole range of operating temperatures. According to the manufacturer of the sensor provided isothermal conditions during pressure change, the maximum error of pressure determination is $\delta P/P < 0.02$.

The choice of pressure transmitting medium for studies under pressure depends on multiple factors, among which is the type of the pressure cell employed (Diamond Anvil Cell, piston-cylinder), the range operating conditions (temperature, pressure) and type of measurements planned (magnetization, transport or optical). In order to provide hydrostatic pressure conditions for the sample in the piston-cylinder clamp type pressure cell special requirements are imposed on the pressure transmitting medium.

- (a) wide temperature range of plasticity;
- (b) low pressure drop on a range from room temperature (295 K) to liquid helium boiling temperature (4.2 K);
- (c) low and continuous pressure drop during the solidification process of pressure medium, without discontinuous phase transitions;
- (d) inert, non-reactive environment to prevent a degradation of the sample, electric leads mounting compound (Ag-based epoxy, carbon paste, In solder) or pressure cell body corrosion.

Traditionally the most popular pressure transmitting media for clamp-type pressure cells were the mixtures of organic solvents, like pentane:isoamyl alcohol [214], pentane:hexane [213], Fluorinert mixtures (trademark for a series of perfluoro-carbon liquids by 3M, St. Paul, MN, USA) [215, 216] or even ethanol:methanol [217] in various proportions. While possessing certain advantages, some of these liquids are very aggressive to the lead mounting compound we are using (carbon paste XC-12 [195]), the other demonstrated abrupt, discontinuous pressure drop during solidification [216]. Another widely used pressure transmitting medium for these type of experiments is the Daphne-7373 oil from Idemitsu (Tokyo, Japan), which we found to be the most suitable for our experiments. The liquid is a mixture of several olefins, developed in 1980 specifically for high hydrostatic pressure experiments on

organic conductors. Depending on the applied pressure, the oil solidifies within the temperature range $170 \div 250$ K [218], with upper limit corresponding to ~ 1.2 GPa, which is our typical maximum operating pressure. It was found that the pressure does not change discontinuously at the solidification temperature, even though dT/dP is slightly discontinuous. The pressure drop in the piston cylinder pressure cell with this type of media on the range from 300 to 4 K was observed ≈ 0.15 GPa, irrespective of the initial applied pressure [218]. The oil does not solidify at room temperature until the pressure of ~ 2.7 GPa [216], which sufficiently overlaps the working pressure range of most BeCu clamp-type pressure cells, including our LC10.

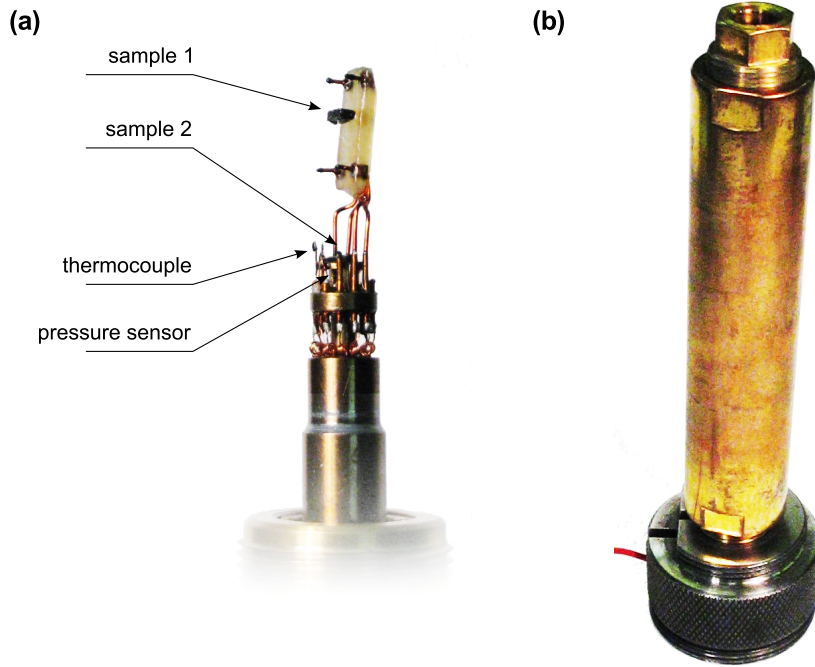


Figure 3.23: Photograph of (a) scaled-up view of the samples mounted on the sample stage in the obturator of pressure cell; (b) general view of assembled pressure cell LC10.

Routinely, the preparation and setup of the experiment takes 2-3 hours. The pressure cell bore and working surfaces of the piston and plug are cleaned repeatedly with acetone and hexanes in order to prevent any loose metal debris from disturbing the piston and plug seals. One-time use sealing O-rings made of BeCu with In-coating are installed on corresponding parts. The samples with electrical leads attached are mounted in the sample space using special fixtures, in case there is a need to secure the sample spatial orientation relative to magnetic field (see figure 3.23). After installation of the obturator, the cell is filled with pressure transmitting medium and the piston is forced inside the bore. The pressurization of the cell is performed using conventional hydraulic press capable of maximum load of at least 4 kN. The pressure cell is installed in a special fixture with protective guard to protect an operator. The

pressure is monitored continuously during the pressurization process, measuring the resistance of the SPG10 pressure gauge using AC-resistivity bridge. It is worth noting that it is recommended to control the temperature of the cell during pressurization for precise measurements [213]. We have found experimentally that the massive metallic structure of the hydraulic press provides a powerful heat sink, sufficiently damping possible thermal fluctuations. Hydrostatic pressure is a non-destructive measurements technique for most inorganic samples (including oxides on which we work), however during the pressure change process there is always a chance of structural damage to the sample or degradation of electrical contacts due to solidification of the pressure medium causing non-compensated strains. In order to stay aware of the condition of the sample and have a chance to interrupt the experiment at an early stage of failure, we also monitor the resistance of any new sample during the pressurization session. After achieving the desired pressure level, the pressure cell is mounted onto the PPMS puck adapter and loaded into the cryostat. The empirical formulas for our specific sensor allow us to establish the pressure at arbitrary temperature within the calibration range as long as initial (ambient pressure) resistance of the sensor at room temperature and 77.4 K is known. However, having a remote access to the pressure sensor while the pressure cell is inside the cryostat we do continue to log the resistance of the sensor to collect an actual pressure information *in situ*.

Chapter 4 TUNING THE GROUND STATE OF BaIrO₃ VIA PRESSURE AND CHEMICAL DOPING

4.1 Introduction

The first attempt to study BaIrO₃ had been made over 50 years ago by R. Ward and coworkers [219, 220] who tried a synthesis and structural characterization of this compound. No detailed crystal structure data was produced at that time, but after several attempts it has been noted that the compound could be isostructural to a well known 9-layer cubic perovskite polytype BaRuO₃ [221]. Chamberland *et al.* have obtained several BaIrO₃ polytypes and later have correctly characterized the low-pressure, room-temperature phase as 9R [15, 27]. Early measurements of magnetic and transport properties of that phase revealed the compound is a weak ferromagnet, ordering near the temperature $T_C \approx 180$ K, and it possesses rather high electrical resistivity. Because of this high ordering temperature and insulator-like properties the initially proposed model described the compound as canted antiferromagnet where the $S = 1/2$ spins are coupled through direct exchange within the Ir₃O₁₂ clusters and through superexchange interaction between the clusters [28]. When 4d and 5d transition metal oxides started to generate significant excitement among researchers due to observations of unexpected orbital ordering [4], localized transport and magnetism [33] in ruthenates and iridate respectively, BaIrO₃ also attracted much attention. Particularly, the observation of a charge-density wave (CDW)¹ simultaneously with formation of weak ferromagnetism at $T_C = 183$ K on a single crystal samples made this material to stand out, because a CDW is clearly expected only for metallic systems which this compound is not [158, 39, 37]. The new model proposed by Cao *et al.* [158] included a band magnetism due to small exchange splitting with an associated CDW below T_C , which places a gap at the Fermi surface and induces a subtle lattice distortion. These arguments were later supported by several independent studies, particularly tight-binding band structure calculations, which showed a sharp peak on the density of states at the Fermi level (N_{E_F}) and partially nested pieces of the Fermi surface [39]. A high N_{E_F} signals that even though the temperature dependence of electrical resistivity in this compound was clearly determined to be a non-metallic, the system is on the verge of a metallic state. The itinerant nature of magnetism was evident from the result of our magnetization measurements under high pressure, which clearly demonstrated a negative value of the pressure coefficient of critical temperature $d \ln T_C / dP \approx -0.12$ kbar⁻¹ [222]. Similar but weaker in magnitude pressure effect on ρ has been reported for polycrystalline BaIrO₃ in pressure measurements up to 10 kbar [223]. The μ SR measurements reported by Brooks *et al.* [38] provided a direct experimental evidences of a small magnetic moment of Ir,

¹The existence of CDW BaIrO₃ is experimentally supported by the non-linear electrical transport properties, the results of optical conductivity and photoemission spectroscopy measurements. However, up to date no attempt of experimental observation of surface superlattice has been reported on this compound.

originating from $5d-2p$ hybridization and a small exchange splitting in the $5d$ bands, and therefore ruled-out the possibility of canted ferromagnetism in a localized spin configuration. This would make BaIrO_3 the first known ferromagnet that contains a $5d$ transition metal cation in a ternary oxide, the magnetic moment of which originates from spin polarization of Ir cations rather than from spin canting. However, Laguna-Marco *et al.* in collaboration with G. Cao's group [224] report the results of the X-ray absorption spectroscopy (XAS) and X-ray magnetic circular dichroism (XMCD) which reveal a presence of a strong spin-orbit coupling in the ground state and the contribution of orbital moment seems to exceed that of spin moment. Therefore, it is argued that the spin-only itinerant description of the Ir $5d$ magnetism in this compound might be incorrect and one should take the orbital contribution into account. The unconventional nature of the ferromagnetic transition in BaIrO_3 is also indicated by the anomalous values of critical exponents γ , β and δ , which define the power-law behavior of such physical quantities as spontaneous magnetization M_S , initial susceptibility χ_0 and critical magnetization isotherm respectively:

$$\begin{aligned}\chi_0^{-1}(T) &\propto \tau^\gamma, \quad \tau > 0, \\ M_S(T) &\propto (-\tau)^\beta, \quad \tau < 0, \\ M &\propto (H)^{1/\delta}, \quad \tau = 0.\end{aligned}\tag{4.1}$$

where H is a magnetic field, and $\tau = (T - T_C)/T_C$ is a reduced temperature, so the expressions 4.1 are defined for a disordered phase, an ordered phase and at T_C respectively. These exponents are important quantities, which do not depend on any detailed properties of a system but determine the universality class of a continuous phase transition according to theoretically predicted values [225]. However the values determined for BaIrO_3 , $\beta \approx 0.82$, $\gamma = 1.03$ and $\delta = 2.20$ do not belong to any universality class reported so far [38, 226]. A high-resolution photoemission study on BaIrO_3 by K. Maiti and coworkers [37] reveals essentially localized electronic states forming a pseudogap at the Fermi energy for $T > T_C$, allowing for a soft gap to open at E_F below T_C with the CDW formation. Apart from everything else, this observation could also explain a semiconductor to insulator transition on transport properties of this compound. In another study, Nakano and Terasaki [227] have used a pulsed current in the measurements of transport properties in order to minimize the Joule-heating effect of the samples. It is worth noting that on their samples of BaIrO_3 they confirmed the giant non-linear conductivity reported earlier, however observed it only near 20 K, which is way below T_C in BaIrO_3 . An interplay between two different bands as the origin of observed nonlinear conduction has been proposed by them, instead of a sliding motion of CDW.

As mentioned earlier, the hexagonal perovskite 9R BaIrO_3 is only one member (a low temperature ambient pressure phase) of the entire series of polytypes which can be formed for this stoichiometry. A successful synthesis of some other members using various temperature regimes and inducing oxygen vacancies has been reported by Chamberland *et al.* [15], although no detailed study of the properties have been carried

out. Recently Cheng *et al.* [16] have identified several new polytypes synthesized under pressure (up to 10 GPa) and explored their properties as a function of corner-, hexagonal-sharing octahedra stacking sequence. They showed that the ground state of BaIrO_3 evolves from a ferromagnetic insulator with $T_C \approx 180$ K in the 9R phase, to a ferromagnetic metal with $T_C \approx 50$ K in the 5H phase and to an exchange-enhanced paramagnetic metal near a quantum critical point (QCP) in the 6H phase. An additional 6M high pressure polytype has been identified by Zhao *et al.* [228] and reported as exchange-enhanced Pauli paramagnet with metallic ground state.

4.2 Underlying physical properties of BaIrO_3

The essential transport and magnetic properties are summarized in the figure 4.1. A quasi one-dimensional nature of this compound is evident from the anisotropy of its transport behavior $\rho(T)$ — more conductive direction is parallel to the crystallographic c -axis, as can be seen on panel (a) of the figure 4.1. Notably, this anisotropy is not that large, compared to those on some other studied iridates like Sr_2IrO_4 [229]. The transition at $T_C \approx 183$ K on resistivity data is abrupt and the steady increase of $\rho_{ab}(T)$ indicates a progressive localization of charge carriers. That transition is accompanied by the onset of ferromagnetism (figure 4.1 panel (b)). It is known from experiments that the transition temperature is unchanged and the resistivity anomaly is not broadened in magnetic fields up to 10 T — a contrast to most ferromagnetic transitions, which are accompanied by short-range magnetic order for temperature $T \geq T_C$. This implies that the ordered magnetic state is driven either by CDW formation or partial Fermi surface gapping, accompanied by subtle lattice distortion [158]. The anisotropy is also observed in magnetic properties of this compound, where the magnetic easy axis is parallel to crystallographic c -axis. The ordered magnetic moment is $\mu_0 \approx 0.03 \mu_B/\text{Ir}$, much lower than expected for spin $S = 1/2$, $^2t_{2g}$ state of Ir^{4+} (5d). In this configuration both d_{xz} and d_{yz} orbitals of iridium ion are degenerate and an excited d_{xy} orbital is half-filled. A low-temperature specific heat measurements (presented later in the chapter on figure 4.3) indicate very low value of electronic specific heat coefficient $\gamma \approx 1 \text{ mJ/mol K}^2$, suggesting very low density of states at the Fermi surface $N(E_F)$.

To our knowledge, no attempt has been made to characterize the properties of the new ground state in a trivalent rare-earth substituted BaIrO_3 at low temperature and high pressure. In this work we first explored the effect of dilute doping and modest hydrostatic pressure on the structural, thermal, magnetic and transport properties of single-crystal $\text{Ba}_{1-x}\text{R}_x\text{IrO}_3$ ($R = \text{Gd}, \text{Eu}$). The rare-earth (RE) doping is found to introduce donor states and induce additional lattice strains in the material. Both of these outcomes have a profound effect on the electronic properties: a metallic state with intriguing magnetic and transport behavior is induced with dilute doping of BaIrO_3 ; under the application of modest hydrostatic pressure ($P \leq 12$ kbar) the metallic state is readily driven back into an insulating-like state, accompanied by a very rapid increase of resistivity. A pressure-induced insulating state has been observed under extremely high pressures (50 to 950 kbar) on a handful of materials

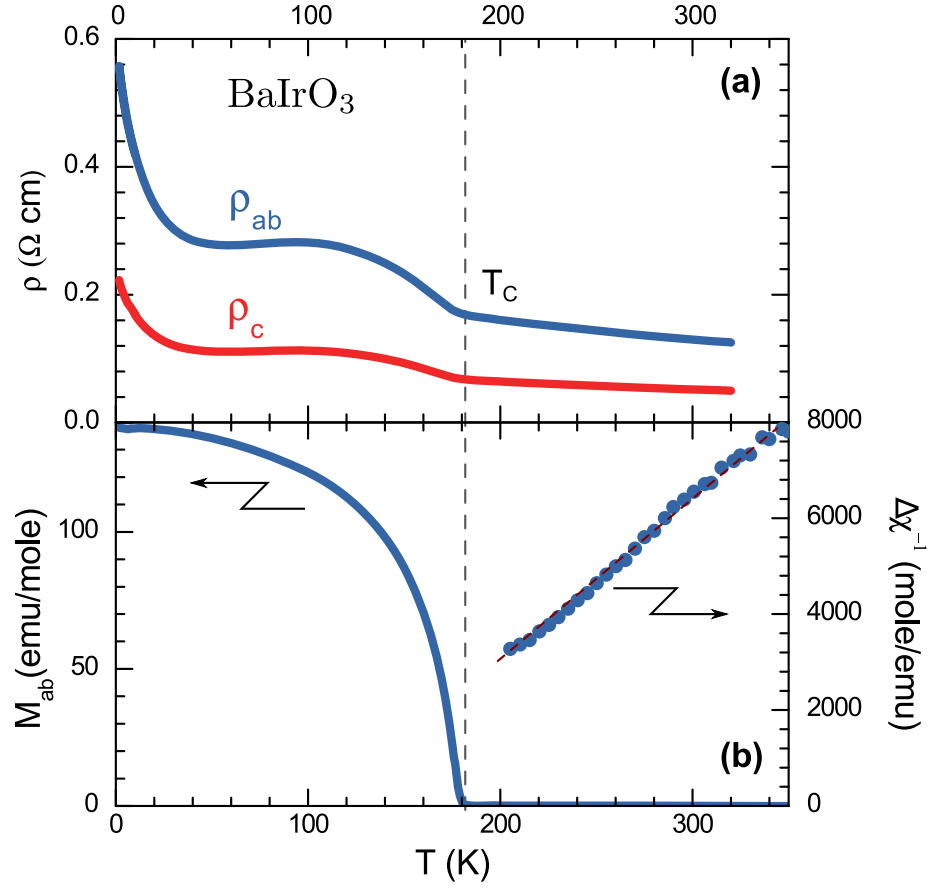


Figure 4.1: The temperature dependence of (a) electrical resistivity $\rho(T)$, (b) magnetization $M(T)$ and inverse susceptibility $1/\Delta\chi$ (right scale, data points and Curie-Weiss fit) for stoichiometric BaIrO_3 .

and never on a $5d$ -based compound, and is shown to be a consequence of unusual electron-lattice interaction in BaIrO_3 .

4.3 Crystal structure of BaIrO_3

Our parent compound is an ambient pressure 9R polytype of the family of materials adopting the ABO_3 perovskite structure [16]. In such phase the crystal structure of BaIrO_3 is characterized by a monoclinic unit cell of space group $C2/m$ with a lattice parameters presented in the table 4.1. It features the Ir_3O_{12} trimers formed by face-sharing IrO_6 octahedra, containing four non-equivalent Ir sites (see figure 4.2 (a)). The trimers are vertex-linked, constituting one-dimensional (1D) chains along the c -axis with a stacking of alternating layers of corner sharing (c) and face sharing (h) IrO_6 octahedra along the sequence $hhchhc$. The framework formed by the chains contains roughly parallel channels accommodating Ba ions. A monoclinic distortion in combination with large ionic radius of Ba ions generates twisting and buckling of the trimers, resulting in a $\sim 12^\circ$ mutual tilt angle (figure 4.2 (b)) [230]. Except for the monoclinic distortion, the BaIrO_3 is isostructural to the well known 9R polytype of BaRuO_3 [28]. As a result of this complex distortion the chains formed out of trimers look zigzag-shaped and produce a two-dimensional layer of corner-shared IrO_6 octahedra in the ab -plane (see figure 4.1 (c)). The 2D layer is formed by octahedra containing only two non-equivalent Ir sites. It is worth mentioning that two crystallographically distinct clusters give rise to slightly different Ir–Ir distances ~ 2.6 Å, although in both cases the interionic separation is shorter than that in Ir metal [231]. The intercluster distances are significantly larger, approaching 4 Å, which allows two types of interactions between iridium ions: direct Ir–Ir bonding for face-sharing and indirect Ir–O–Ir bonding for corner-sharing octahedra. The low crystallographic symmetry and different ratio of direct to indirect linkage between Ir ions in different crystallographic directions form a strong anisotropy of transport properties in this compound, with c -axis being the high conductivity axis and thus the material being a quasi-one-dimensional structure.

Table 4.1: Lattice parameters, Ir1-O2-Ir3 bond length and bond angles at 295 K and 90 K for stoichiometric BaIrO_3 .

Temperature (K)	a (Å)	b (Å)	c (Å)	β (deg)	Ir1-O (Å)	Ir3-O (Å)	Ir-O-Ir (deg)
295 K	10.0180	5.7515	15.1867	103.2920	1.9930	2.0250	163.0
90 K	9.9907	5.7342	15.2359	103.3951	1.9910	2.0240	161.6

The strong temperature dependence of the lattice parameters (see table 4.1) brings significant contribution to the temperature dependence of the electrical transport properties of this material. Though the broadening of the d -bandwidth and metallic behavior are expected due to the presence of direct bonding [62], twisting and buckling of the cluster trimers evidently reduce the bandwidth, because the stoichiometric BaIrO_3 is essentially non-metallic.

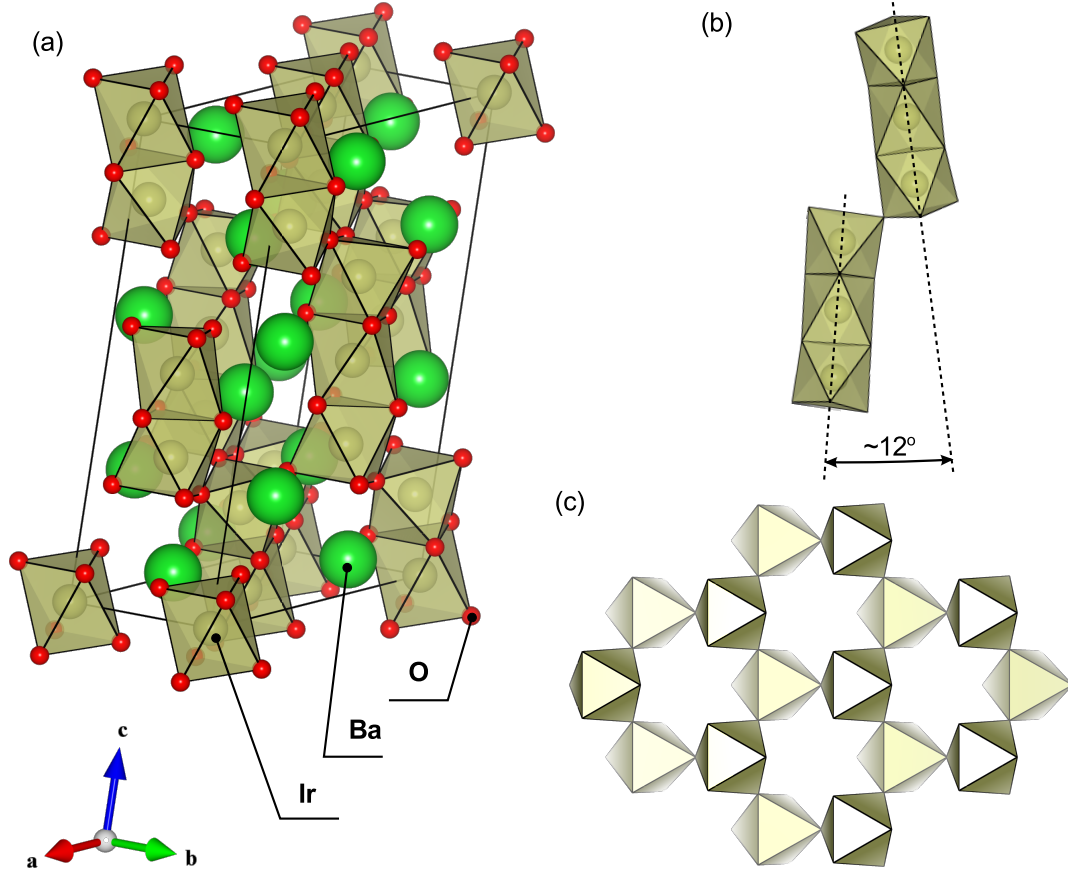


Figure 4.2: Polyhedral representation of the crystal structure of BaIrO₃: (a) crystal structure unit cell; (b) corner-sharing of Ir₃O₁₂ trimers connected using vortices of top and bottom octahedra, the distortion angle of $\sim 12^\circ$ is illustrated; (c) two-dimensional layer of corner-sharing IrO₆ octahedra, upper and lower layer octahedra are indicated. Model produced from original measurements using *VESTA 3* software [9].

4.4 Structural changes in Gd-doped BaIrO₃

A detailed single crystal X-ray diffraction measurement and structural refinement were performed on the flux-method grown samples of Ba_{1-x}Gd_xIrO₃. As determined from the obtained structural data, the dilute trivalent Gd³⁺ substitution (ionic radius $r_{Gd} = 0.94 \text{ \AA}$) for divalent Ba²⁺ (ionic radius $r_{Ba} = 1.35 \text{ \AA}$) introduces important changes to the temperature dependence of the lattice parameters (see table 4.2), which could affect the lattice stability:

1. The It1-O2-Ir3 bond length, that links the corner-sharing IrO₆ octahedra, grows considerably with temperature decrease for $x = 0.04$ but slightly shrinks in the parent compound $x = 0$.
2. The It1-O2-Ir3 bond angle, which reflects the twisting and tilting of the Ir₃O₁₂ trimers, is significantly larger for Gd-doped compound (162.3°) than for parent

compound (161.6°) at low temperature (see table 4.2, 90 K).

3. A substantial changes in temperature dependence of lattice parameters caused by doping lead to c -axis increase by 1.34 % while cooling from 295 to 90 K. In the same time, in pure compound this change constitutes only 0.3 %, even though in both cases the unit cell volume decreases with temperature decrease.

Table 4.2: Lattice parameters and Ir1-O2-Ir3 bond length and bond angle at 295 K and 90 K for $\text{Ba}_{0.96}\text{Gd}_{0.04}\text{IrO}_3$.

Temperature (K)	a (Å)	b (Å)	c (Å)	β (deg)	Ir1-O (Å)	Ir3-O (Å)	Ir-O-Ir (deg)
295 K	9.9978	5.7386	15.0021	103.2200	1.9760	2.0170	163.5
90 K	9.9852	5.7381	15.2028	103.3514	1.9880	2.0230	162.3

Previously reported successful results on single crystals of $\text{Ba}_{1-x}\text{Sr}_x\text{IrO}_3$ demonstrate that a partial metallic state can be recovered at mere $x = 0.12$ substitution of Sr (ionic radius $r_{\text{Sr}} = 1.18$ Å) for Ba [40] with a complete paramagnetic metallic state achieved at $x = 0.23$. Since BaIrO_3 is a rare example of a material that is extremely close to a metal-insulator borderline and is susceptible to lattice contractions, it appears that substitution of a smaller size ion for Ba site should be critical to the behavior of this compound in a wide range of temperatures.

4.5 Chemical substitution effect on magnetic properties

The first pronounced change induced by this doping can be observed on magnetization data $M(T)$ for $\text{Ba}_{1-x}\text{Gd}_x\text{IrO}_3$ on figure 4.3 (a), where the ferromagnetic T_C is being suppressed by gradual increase of doping element from 183 K for $x = 0$ down to 140 K for $x = 0.06$. Using the range of temperatures $200 < T < 350$ K, which is high about the ordering point T_C , we determine a temperature independent contribution to magnetic susceptibility χ_0 from the Curie-Weiss fitting. Extrapolating the plot of inverse temperature dependent magnetic susceptibility $\Delta\chi^{-1} = 1/[\chi(T) - \chi_0]$ we observe a sign change of θ_{CW} from positive to negative, signaling a change of exchange coupling from ferromagnetic (FM) in pure compound to antiferromagnetic (AFM) for $x = 0.04$. The specific heat data $C(T)$ reflects all the magnetic phase transitions as the step-like anomalies near T_C , stronger one for $x = 0$ ($\Delta C \approx 2$ J/mole K, as measured by relaxation method using QD PPMS, however earlier *ac* calorimetry measurements produced even lower value $\Delta C \approx 0.7$ J/mole K [232]) and less noticeable for Gd doped compound (figure 4.3 (b)).

Besides changing the type of magnetic order from FM to AFM the doping with Gd also induces new sharply defined transition visible on magnetization at low temperature. It occurs at $T_{M1} \approx 9$ K and persist to higher concentrations. Although this feature significantly weakens already for doping of $x = 0.06$, it is worth addressing it separately. As seen on figure 4.4 (a) the low-temperature metallic state for $x = 0.04$

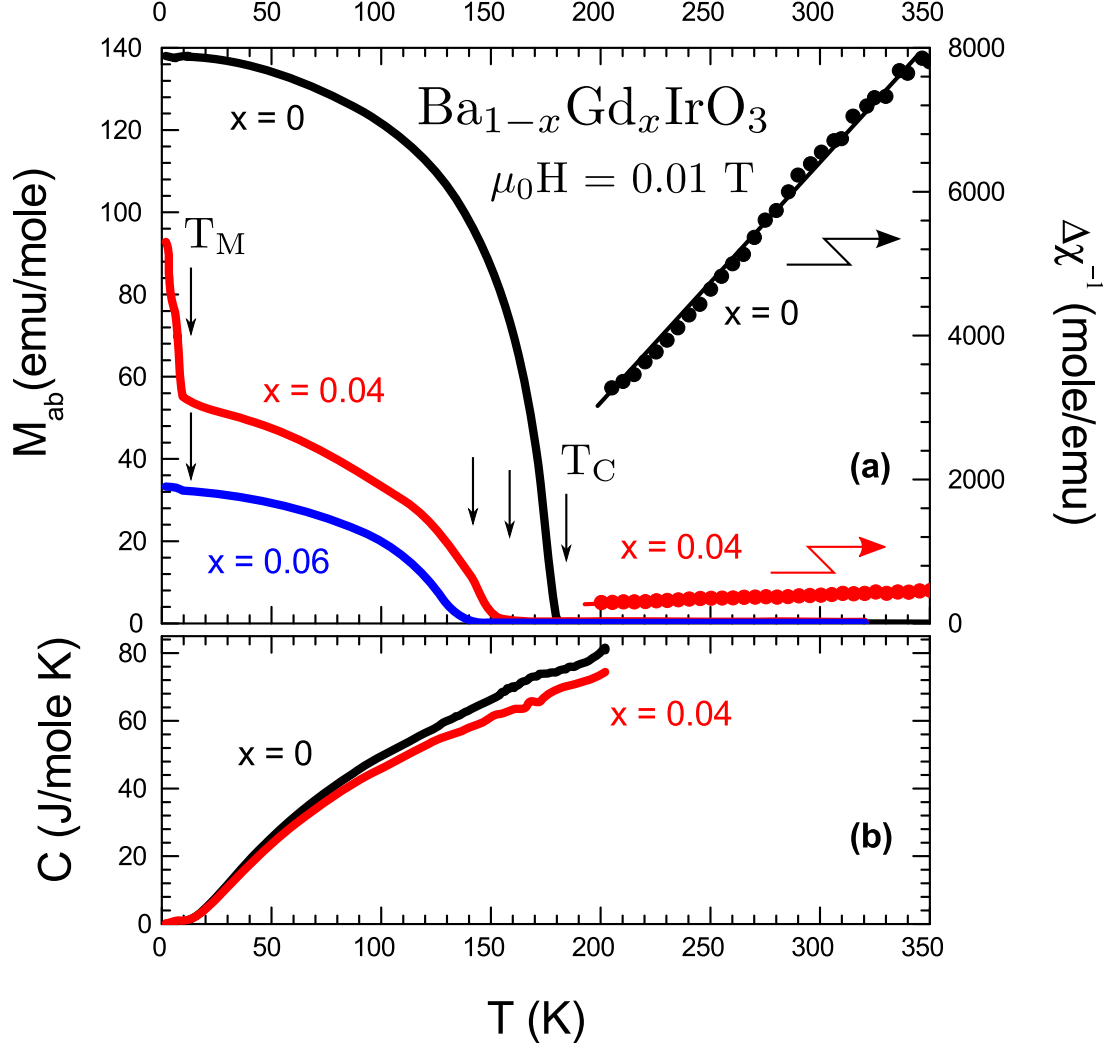


Figure 4.3: The temperature dependence of (a) the magnetization $M(T)$ and $1/\Delta\chi$ (right scale, data points and Curie-Weiss fit), (b) specific heat $C(T)$ of Gd-doped BaIrO_3 .

exhibits complex thermodynamic behavior, with an anomaly evident at $T_M = 9.5$ K followed by two additional features at $T_{M2} = 6.5$ K and $T_{M3} = 3$ K, which can be observed on both magnetization $M_{ab}(T)$ and specific heat $C(T)$ data. The latter obviously confirms the bulk effect of transformation. Using the specific heat dependence for parent compound BaIrO_3 $C(T < 15$ K) as a background, we have determined ΔC_M – the magnetic contribution to specific heat (figure 4.4 (b)). This dependence allows to calculate the magnetic entropy removal $S_M = 0.70$ J/mole K by integration of $\Delta C_M/T$ vs T . Assuming

$$S_M = R \ln(2S + 1) \quad (4.2)$$

where R – universal gas constant and $S = 7/2$ for $4f$ -orbital, the result reasonably

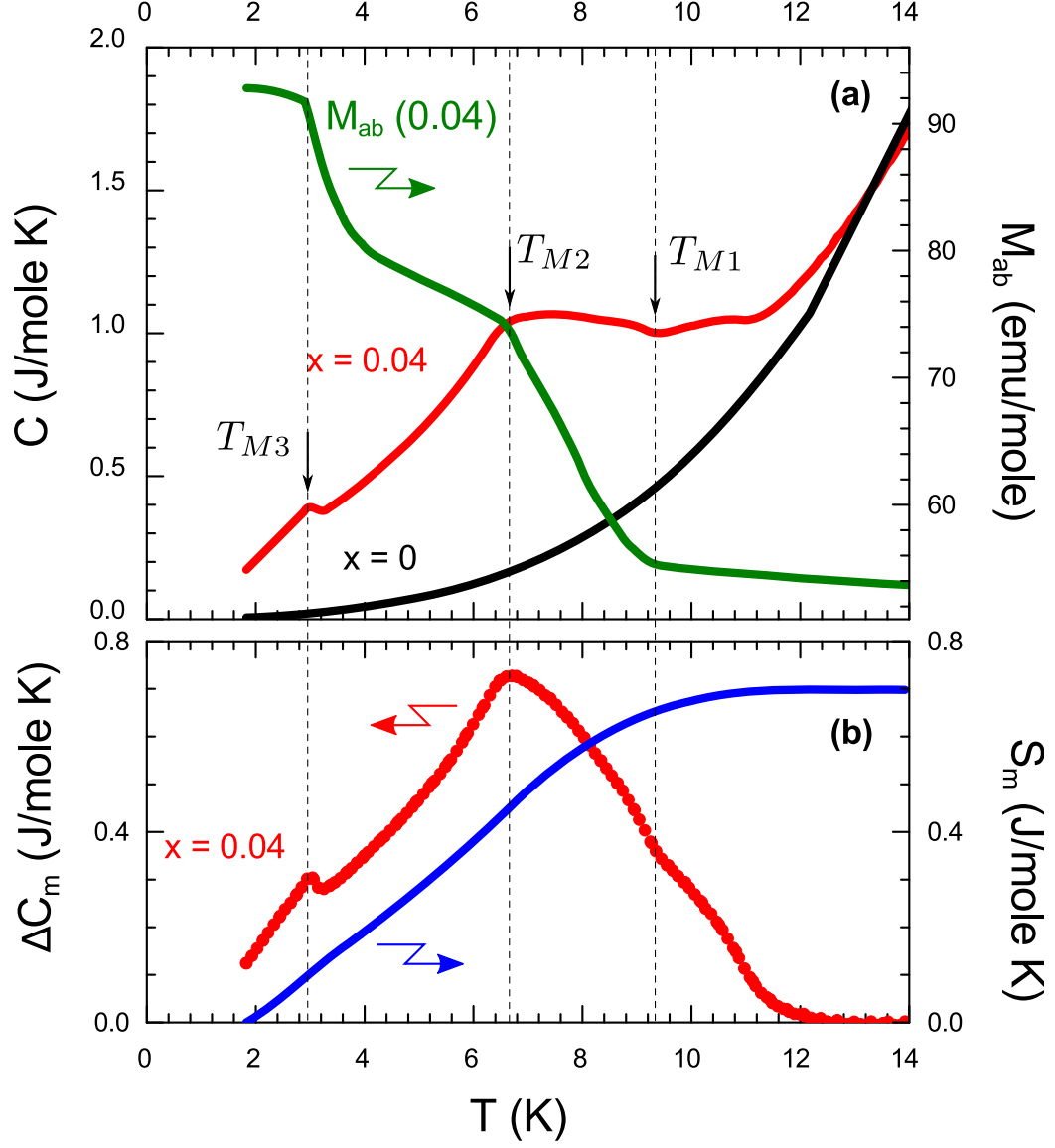


Figure 4.4: The low-temperature dependence for $\text{Ba}_{1-x}\text{Gd}_x\text{IrO}_3$ of (a) $C(T)$ for $x = 0, 0.04$ and $M_{ab}(T)$ for $x = 0.04$ (right scale), and (b) magnetic contribution to specific heat $\Delta C_M(T)$ and magnetic entropy removal S_M (right scale).

agrees with approximately 5% doping of Gd^{3+} ions. This is well consistent with the sample composition, measured by energy dispersion X-ray spectroscopy method (EDX). The result allows us to attribute the low-temperature magnetic transitions mainly to the ordering of Gd moments.

Using the expression for specific heat

$$C = \gamma T + \beta T^3 \quad (4.3)$$

we determine the Sommerfeld coefficient – the electronic contribution to heat

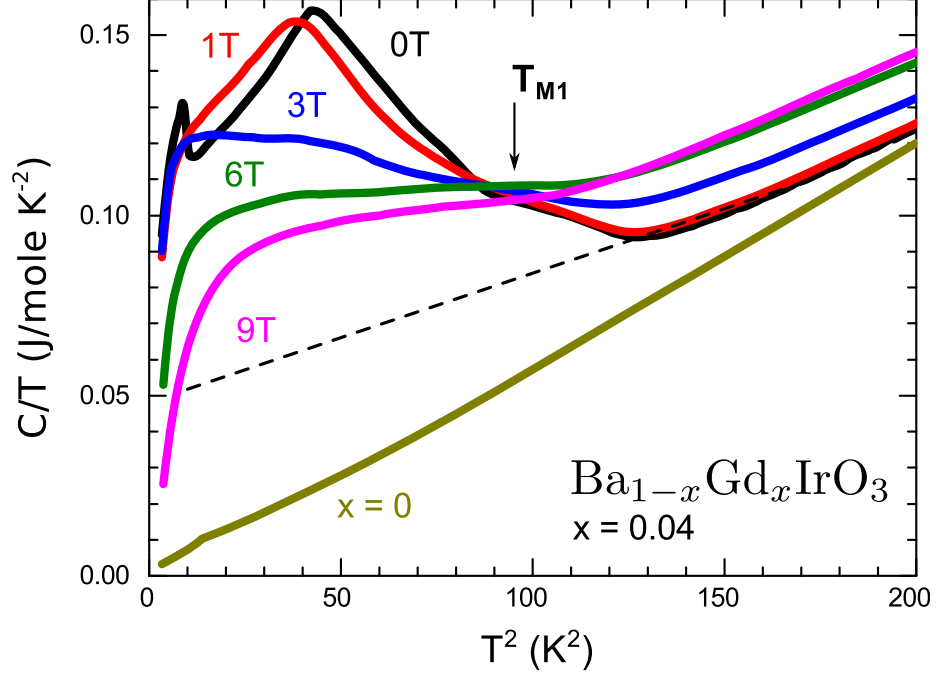


Figure 4.5: The low-temperature dependence for $\text{Ba}_{1-x}\text{Gd}_x\text{IrO}_3$ of $C(T)/T$ vs T^2 for $x = 0$ and $x = 0.04$ at various magnetic fields H up to 9 T.

capacity from our data. The notable feature is a drastic enhancement of the Sommerfeld γ above T_{M1} from $\gamma = 1$ mJ/mole K^2 for $x = 0$, to an extrapolated value of $\gamma = 50$ mJ/mole K^2 for $x = 0.04$ (figure 4.5, dash line). Such a major enhancement signals about substantial increase of the density of states at the Fermi level $N(E_F)$. The application of magnetic field H to the compound with $x = 0.04$ leads to overall gradual decrease of low temperature heat capacity, while the transitions temperatures T_{M1} , T_{M2} and T_{M3} become less and less defined (figure 4.6 (a)). This could indicate a gradual polarization of the spin structure, which is supported by isothermal magnetization data $M_C(B)$ (figure 4.6 (a)), demonstrating two consecutive metamagnetic transitions at $H_{C1} = 0.2$ T and $H_{C2} = 1.8$ T at $T = 1.7$ K. Extrapolating the isothermal magnetization on $\mu_0 H = 0$ T the saturation moment has been determined $\approx 0.3 \mu_B/\text{f.u.}$ – the value is over ten times larger than that observed for $x = 0$ compound [158]. The result correlates very well with expected contribution of $S = 7/2$ magnetic moment or $7 \mu_B/\text{Gd}^{3+}$ for 4.3% of Gd doping. Remarkably, doping by other rare-earth such as Pr, Sm, Eu and Lu does not induce nearly as high magnetic moment as the one in case of Gd substitution, and no low-temperature magnetic anomalies have been observed (see figure 4.6 (a) and (b) respectively). The rare-earths element we have tried for doping span a significant range of $4f$ -electron crystal-field schemes, localizations and ionic radius. One known feature that makes the Gd to stand out of the list is its maximal value of the de Gennes factor of the RE^{3+} Hund's rule of the

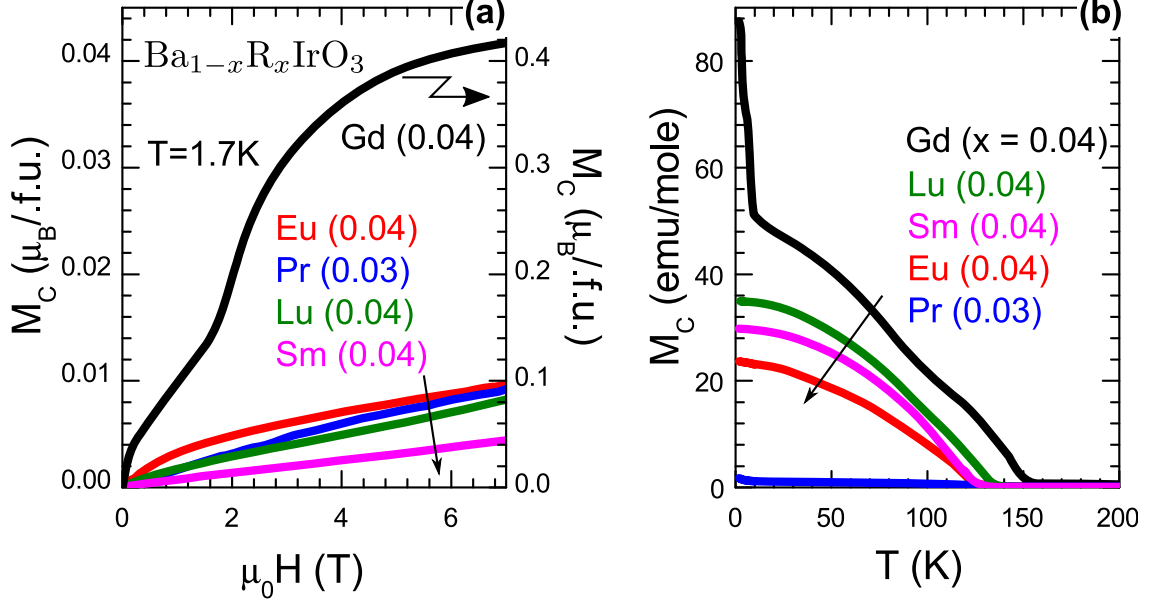


Figure 4.6: The c -axis magnetization data M_C for $\text{Ba}_{1-x}\text{R}_x\text{IrO}_3$ with $\text{Gd}(x = 0.04)$ and other rare earth doping as indicated. (a) isothermal magnetization $M_C(B)$ up to 7 Tesla at $T = 1.7 \text{ K}$, (b) temperature dependence of magnetization M_T up to 200 K.

ground state [233].

$$DG = (g_L - 1)^2 J(J + 1) \quad (4.4)$$

Here g_L is the Landé g -factor and J is the total angular momentum. Essentially the de Gennes scaling describes the dependence of antiferromagnetic T_N and superconducting T_C for various isostructural RE -based metallic compounds and originates from the exchange interaction of conduction electrons with $4f$ electrons of rare-earths. In a rough approximation both T_N and ΔT_C (a difference of the critical temperature compared with that of nonmagnetic material $DG = 0$) can be written as

$$T_N \sim -\Delta T_C \sim I^2 N(E_F) DG. \quad (4.5)$$

Where I is the strength of exchange coupling between $4f$ -electrons and the conduction electrons, $N(E_F)$ is the density of states at Fermi level [234]. Moreover, because of zero-orbital momentum contribution to magnetic moment ($L = 0$), the Gd^{3+} does not exhibit anisotropic orbital exchanges, as do the other rare earth from the pool, which also may give a rise to unique effect of Gd doping.

4.6 Transport properties

The sharp kink on temperature dependence of resistivity $\rho(T)$ in pure compound was associated with opening of an insulating gap, earlier attributed to formation of charge density wave in this material (CDW) [158, 37], resulting in an insulating low

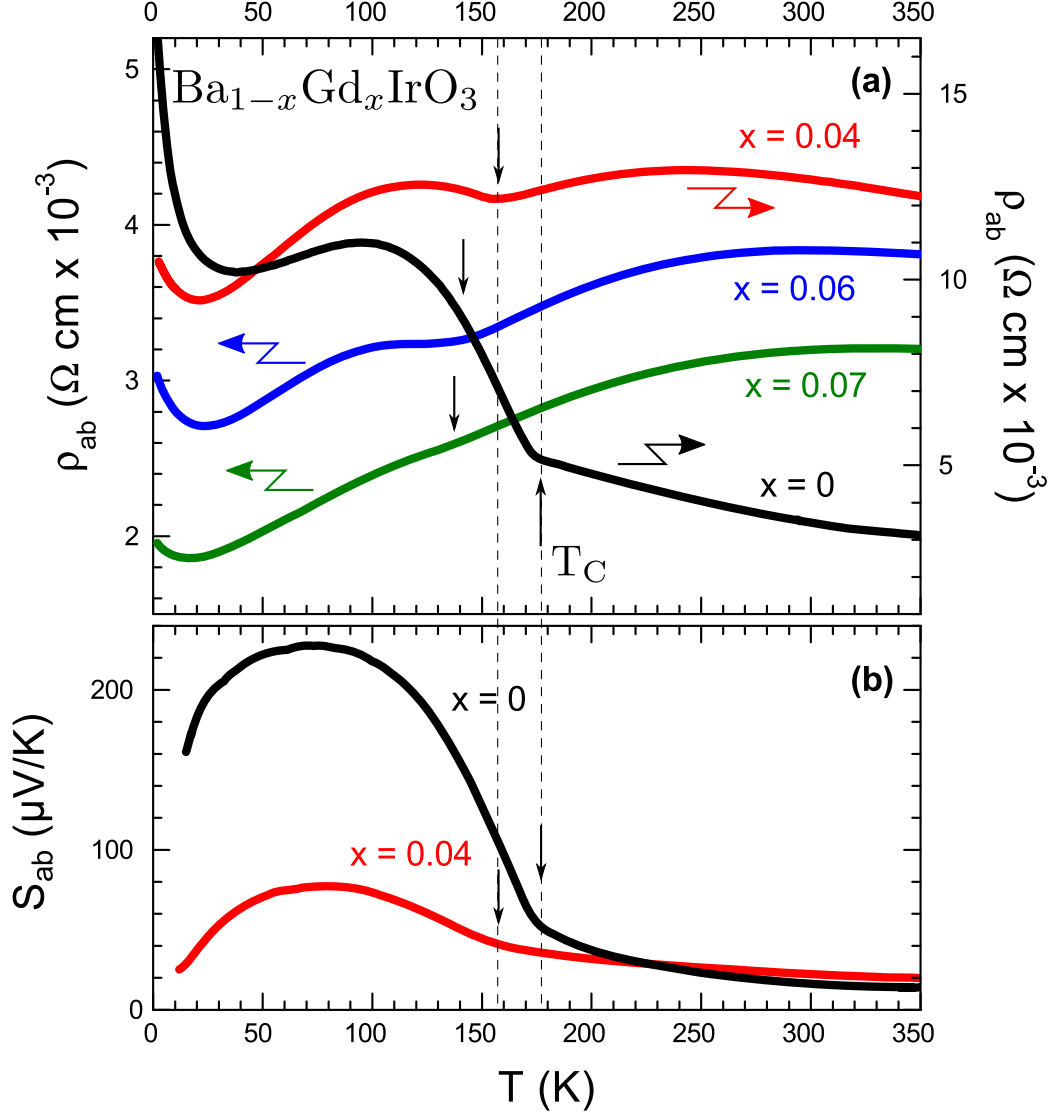


Figure 4.7: The temperature dependence of (a) $\rho_{ab}(T)$ (left scale for $x = 0.06$ and 0.07), (b) Seebeck coefficient $S_{ab}(T)$ for Gd-doped BaIrO_3 .

temperature state of BaIrO_3 . Gd doping was found to strongly impact the transport properties of BaIrO_3 , gradually changing the overall behavior from weakly-localized metallic to well-defined metallic (see figure 4.7 (a)).

As seen, the insulating gap can be readily reduced by merely a few percent of rare-earth doping. And it is worth noting that Gd and other attempted rare-earths such as Eu, Sm, Lu and Pr all produce similar effect on transport properties of the compound, in contrast to effect on magnetic properties. In this discussion I will mainly focus on the effect from Gd and Eu doping. Gradual increase of concentration till the level where the material still retains the original crystal structure configuration of a parent compound, leads to metal-insulator transition as a function of x as seen

on figure 4.7 (a). The data for $\rho_{ab}(T)$ for $x = 0.04, 0.06$ and 0.07 show that the gap energy and T_C systematically decrease with x . An additional feature in form of a broad hump in the high-temperature region, where resistivity increases at first and then decreases rapidly is attributed to electron doping of the compound (Gd^{3+} vs Ba^{2+}). At $x = 0.04$ it peaks near $T^* = 250$ K and corresponds to no magnetic anomaly on figure 4.4 (a) and in our studies it turned out to be completely insensitive to applied magnetic field. Typically this indicates that scattering of charge carriers is most likely due to phonon modes (electron-lattice coupling) rather than spin scattering. An additional feature in the resistivity data is the minimum observed near the temperature 20 K. The fact that it diminishes with an increase of doping concentration indicates that the increase of scattering in that region is not due to a lattice disorder introduced by doping. The exact nature of this is not clear to us, however we do not rule out the possibility that it could be related to additional anomaly observed on low-temperature heat capacity $C(T)$ near 11.5 K (see figure 4.4 (a)), which has no reflection on magnetization data. The thermoelectric power measurements (Seebeck coefficient) results are consistent with resistivity behavior in $\text{Ba}_{1-x}\text{Gd}_x\text{IrO}_3$. A sharp transition near $T_C = 183$ K for $x = 0$ is followed by 5-fold increase of $S_{ab}(T)$, which peaks near 75 K, signaling the strong decrease of carrier concentration and opening of the insulating at T_C . The magnitude of thermoelectric power of BaIrO_3 was found to be comparable to those reported on this compound by other groups [235, 227] and on other insulating iridates [23]. As can be seen the $S_{ab}(T)$ for $x = 0.04$ exhibits a similar temperature dependence, with a broadened transition at $T_C = 154$ K. A substantially lower peak magnitude (70 $\mu\text{V/K}$ is about 1/3 of that for pure compound) is consistent with a robust metallic state since $S_{ab} \propto N(E_F)$ at low temperatures in metals [236, 62]. Even though the parent compound exhibits a non-metallic behavior the transition to metallic state can be understood in analogy with ordinary semiconductors – the overlapping donor states are eventually forming a conduction impurity band. Since at the given level of doping with Gd^{3+} the system should already behave like a bad metal, we are allowed to employ the last argument. The positive sign of S_{ab} indicates that the dominant charge carriers in BaIrO_3 are holes, therefore the reduction of the magnitude of thermoelectric power on $\text{Ba}_{0.96}\text{Gd}_{0.04}\text{IrO}_3$ is consistent with electron doping. As mentioned above, another successful and interesting results were obtained in attempt to substitute Ba for Eu in BaIrO_3 . In overall, the effect on magnetization and transport properties is very similar to what has been observed in $\text{Ba}_{1-x}\text{Gd}_x\text{IrO}_3$, however at $x = 0.04$ of Eu content the resistivity dependence on temperature $\rho_C(T)$ demonstrates a sharp downturn at low temperature (figure 4.8 (a)) in contrast to Gd-doping where we observe an upturn on both $\rho_{ab}(T)$ and $\rho_c(T)$. The magnetic ordering temperature T_C also decreases quite substantially, down to 130 K (figure 4.8 (b)). From the field dependence of magnetization (figure 4.6 (a)) Eu is expected to be trivalent, or possess an intermediate valent state since it does not have a moment as Eu^{2+} , the phenomena further highlights the exotic ground state of this iridate.

According to band-structure calculations for BaIrO_3 [39], the Fermi energy level lies in the vicinity of a sharp peak in the density of states (DOS), which is originat-

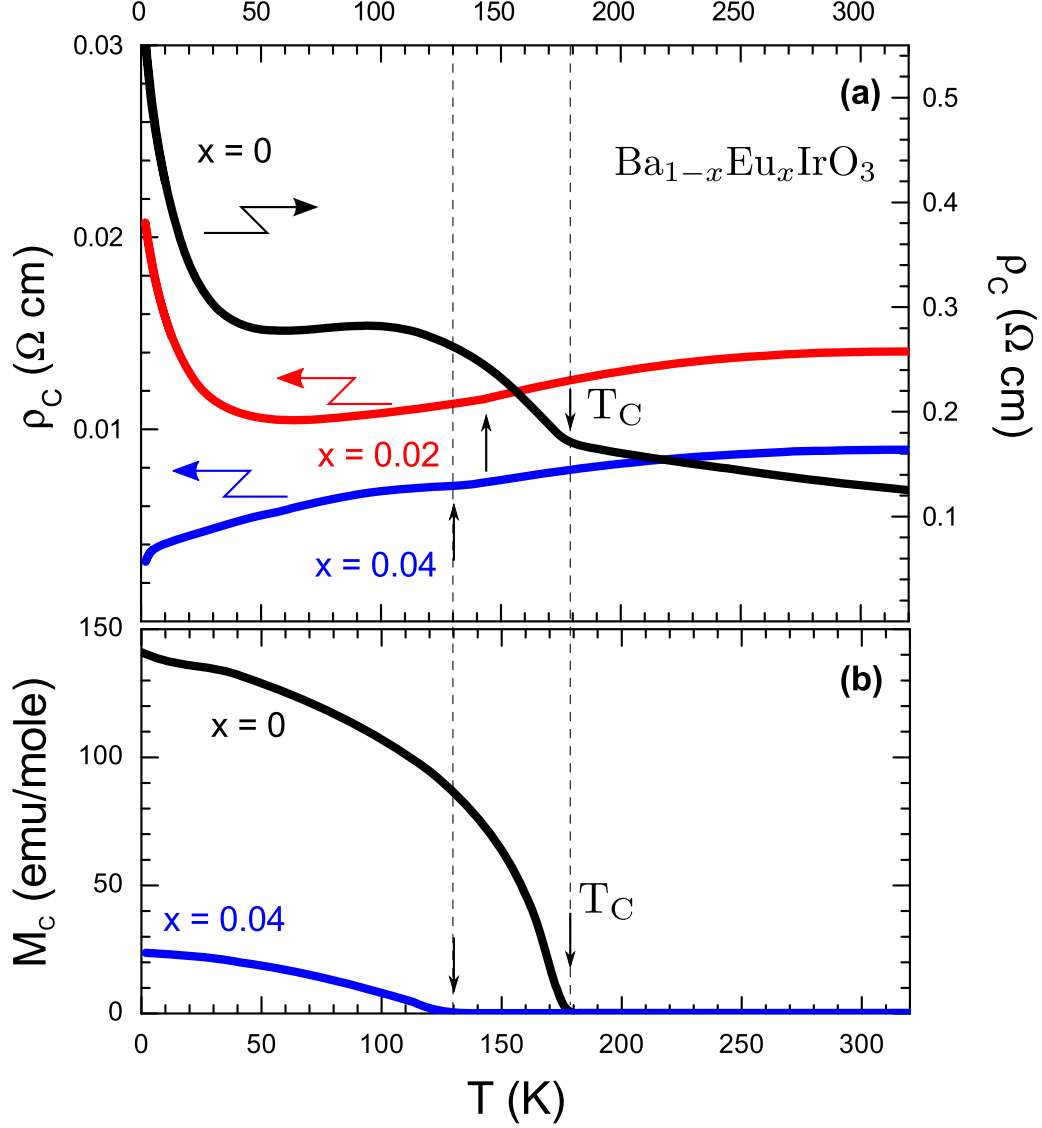


Figure 4.8: The temperature dependence of (a) $\rho_C(T)$ for $\text{Ba}_{1-x}\text{Eu}_x\text{IrO}_3$ $x = 0$ (right scale) and $x = 0.02, 0.04$ (left scale); (b) magnetization $M_C(T)$ for $x = 0$ and $x = 0.04$.

ing from t_{2g} orbitals of Ir1 and Ir3 ions. Thus by all means this should make the system metallic like the isostructural 9R-BaRuO₃, which exhibits a robust metallic state demonstrating quantum oscillations. However, the latter suffers no monoclinic distortion or octahedral buckling observed in BaIrO₃, therefore the authors claim BaIrO₃ a weakly-localized metal, where the localization would be due to low-energy vibrations associated with twisting and bending of Ir1-O2-Ir2 bonds. Here Ir1 and Ir3 are the sites in the center of corner-sharing octahedra (see figure 4.2). Thus, having a material which is in a close proximity to metallic state and is susceptible to lattice contractions it is expected that a metallic state can be recovered through the electron-lattice effect.

4.7 Pressure effect studies

Chemical substitution of the smaller rare-earth ions (Gd, Eu) into the bigger (Ba^{2+}) sites relaxes the crystal structure reducing internal strains as is evident from the bond angle increase. Moreover, using structural refinement, we have determined a partial decrease of the lattice parameters (a and b constants decrease while c – increases at 300 K) and overall change of their temperature dependence character, see tables 4.1 and 4.2. In general, it is expected that by its effect on crystal structure of a material such substitution is qualitatively equivalent to an applied external pressure, causing so called *chemical pressure*. Our structural measurements certainly confirm that, and therefore the application of a hydrostatic pressure to the doped compound $\text{Ba}_{1-x}\text{Gd}_x\text{IrO}_3$ is expected to continue a established trend, as to improve the metallic behavior in electrical transport properties. This comes from the fact that the essential effect of pressure on transport properties of a compound is to increase the overlap of adjacent electronic orbitals, which can broaden energy bands in a way that supports a metallic state. In the case of a metallic compound ($d\rho/dT > 0$) this should improve the metallicity, while in case of insulating or semiconducting material ($d\rho/dT < 0$) an insulator-to-metal transition is expected or at least an overall increase of electrical conductivity if the pressure is not sufficiently high to induce the MIT (see section 2.5.4). This is a typical result observed in a wide variety of materials, particularly in 3d-transition-metal oxides such as perovskite manganites [103, 237, 238]. There, applied pressure primarily leads to an increase of Mn-O-Mn bond angle but decrease of the Mn-O-Mn bond length, thus broadening the band and stabilizing FM metallic state. Another effect of high interest is the pressure dependence of magnetic ordering temperature T_C . Since the ordering temperature is coupled with an opening of the insulating gap in BaIrO_3 , we can track the change of dT_C/dP by measuring the electrical resistivity under pressure. Our previous pressure studies of magnetization and resistivity on this compound revealed a monotonic decrease of T_C with pressure with a rate $dT_C/dP \approx -1.7$ K/kbar and $d\ln T_C/dP \approx 0.013$ kbar⁻¹ [222]. Since negative dJ_{FM}/dP is typically expected for itinerant ferromagnets (see section 2.4.5), this once again confirms the model of a band ferromagnetism in this compound in contrary to previous reports where FM ordering is suggested to originate from canted localized moments [28].

The astonishing result is that application of modest pressures readily drives both $\text{Ba}_{1-x}\text{Gd}_x\text{IrO}_3$ and $\text{Ba}_{1-x}\text{Eu}_x\text{IrO}_3$ back into an insulating state with as much as three orders of magnitude increase in ρ_C at $T = 1.8$ K and $P \leq 12.1$ kbar (figures 4.9 and 4.10). On the other hand the results are consistent with our early pressure studies on the parent compound BaIrO_3 , where ρ_C rises by a factor of 30 at $T = 1.8$ K and pressure $P_{\text{max}} = 12.8$ kbar [222]. The pressure coefficient of critical temperature on $\text{Ba}_{1-x}\text{Eu}_x\text{IrO}_3$ is $dT_C/dP \approx -1.5$ K/kbar and its logarithmic value $d\ln T_C/dP \approx -0.12$ kbar⁻¹, which is very close to that reported by us for BaIrO_3 (see figure 4.11). Similar but weaker pressure effect on ρ has been reported recently for polycrystalline BaIrO_3 in pressure measurements up to 10 kbar [223]. However, this observation is very surprising, considering that according to Curie-Weiss fitting, the 4 % Gd

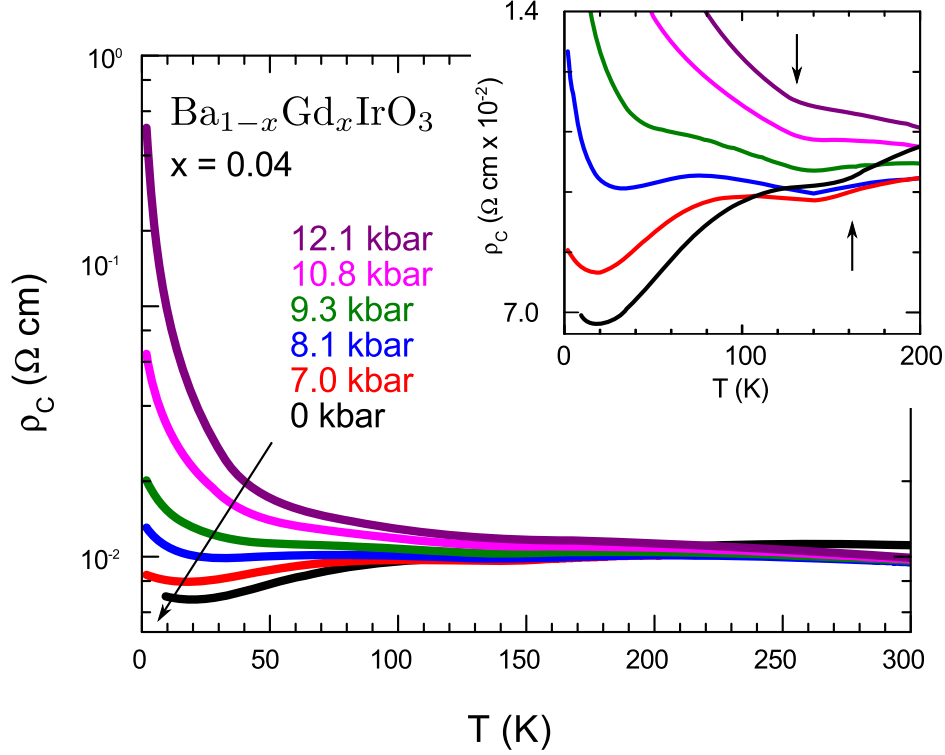


Figure 4.9: The c -axis resistivity $\rho_C(T)$ for $\text{Ba}_{1-x}\text{Gd}_x\text{IrO}_3$ ($x = 0.04$) under a hydrostatic pressure up to 12.1 kbar. Inset: enlarged $\rho_C(T)$, highlighting changes near T_C .

doping has radically changed the type of magnetic ordering in this compound from ferromagnetic to antiferromagnetic (see figure 4.3).

It is worth mentioning, that pressure-induced insulating or semiconducting states have been observed and reported in the literature before. In fact, in an attempt to promote a band insulator or semiconductor to a metallic state under an applied external pressure, several materials have demonstrated completely opposite behavior, becoming much stronger insulators instead (see discussion on pressure effect on MIT, section 2.5.4). For instance, Yb compounds, where pressure up to 50 kbar reduces the hybridization of $4f$ hole with the ligand states and leads to an increased localization [142]. The more recent examples include Li at $P = 950$ kbar (after undergoing several phase transitions to low-symmetry structures) [145] and $(\text{La,Sr})\text{CoO}_3$, which becomes an insulator near $P \approx 140$ kbar due to a spin-state change of the Co^{3+} ion [239]. However, in all these cases the pressure is much higher than the maximum pressure $P \approx 12$ kbar applied in this work. Therefore, the pressure-induced insulating state we observe in $\text{Ba}_{1-x}\text{R}_x\text{IrO}_3$ ($\text{R} = \text{Gd}, \text{Eu}$) is a fundamentally distinct phenomenon, as it happens in a material with extended $5d$ -orbitals and at a relatively low pressures. Recalling the effect of Gd ($x = 0.04$) doping on crystal structure changes (see section 4.3), we conclude that the lattice stability has been significantly altered and the buckling of the corner-sharing Ir_2O_{12} trimers is considerably weak-

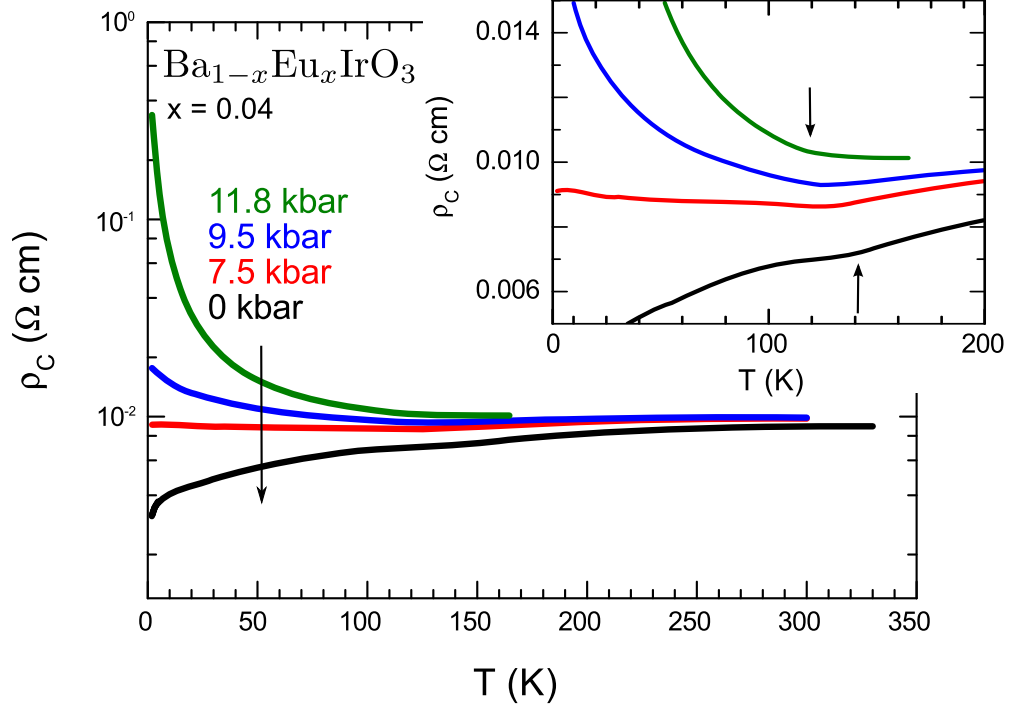


Figure 4.10: The c -axis resistivity $\rho_C(T)$ for $\text{Ba}_{1-x}\text{Eu}_x\text{IrO}_3$ ($x = 0.04$) under a hydrostatic pressure up to 12.1 kbar. Inset: enlarged $\rho_C(T)$, highlighting changes near T_C .

ened. As mentioned above, the band-structure calculations for BaIrO_3 [39] show that a sharp peak in the density of states (DOS) near the Fermi energy is due to t_{2g} orbitals of Ir1 and Ir3 ions, and is therefore governed by corner-sharing IrO_6 octahedra. Thus we propose that any reduction in the twisting and tilting of these octahedra should lead to the enhancement of the density of states near the Fermi surface, which we apparently observe in the change of the Sommerfeld γ coefficient. Obviously, increase of Ir1-O2-Ir3 bond closer to an ideal value of 180° favors the metallic state below T_C . In an ideal case, an application of hydrostatic pressure to a material causes a uniform compression of its unit cell and is not expected to affect the bond angles significantly. In cases when the material under test experiences a shear stress in the high-pressure experiments (sudden crystallization of the pressure medium) or possesses a strongly anisotropic compressibility, one would expect the bond angles to be affected. This possibility was a major concern for us and was paid extra attention. Considering the known properties of the pressure medium used in our hydrostatic pressure cell ("Daphney 7373" oil, see section 3.8) and the fact that the same results have been confirmed in other pressure cells of different types using a pressure medium with different characteristics (helium gas) allows us to reject the shear stress option. The structural integrity of samples was also tested and no difference has been found between the data of the measurements in different pressure variation modes (pressure increase versus pressure decrease). Recalling the anomalous changes in the thermal expansion behavior of the different crystallographic axes due to dilute doping

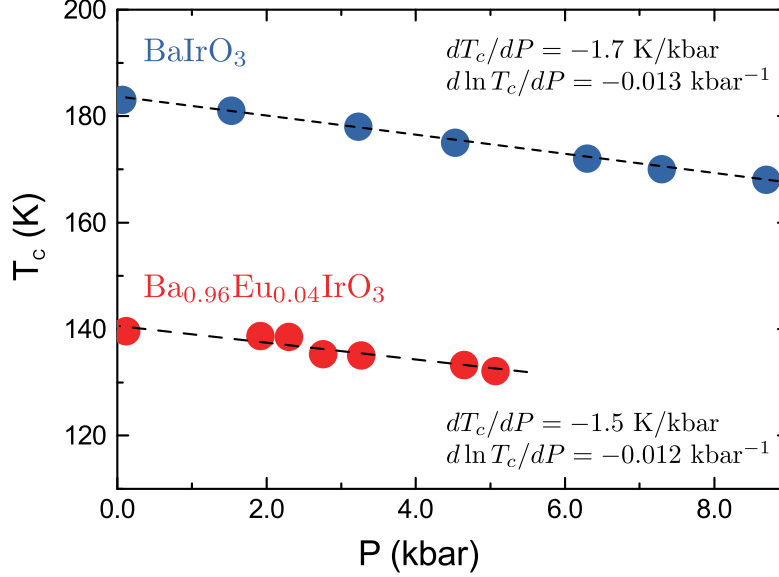


Figure 4.11: Pressure dependence of critical temperature $T_C(P)$ for BaIrO_3 and $\text{Ba}_{0.96}\text{Eu}_{0.04}\text{IrO}_3$ obtained from resistivity data. The critical temperature of the transition cannot be reliably established above $P \approx 5$ kbar as the transition is shadowed by the overall insulating behavior the compound, even though the measurements continue up to $P \approx 12$ kbar.

of Gd (see table 4.2) we suggest that under pressure the three t_{2g} orbitals are affected significantly differently. Consequently, the effect of hydrostatic pressure on the t_{2g} orbitals may appear to be paradoxically anisotropic or even uniaxial. Therefore it is reasonable to expect that with increasing pressure the crucial Ir1–O2–Ir3 bond angle is severely bent, causing the electronic structure to revert back to insulating state, which is even stronger than that of the parent compound (composition $x = 0$).

As known, the t_{2g} -block bands of d -orbitals in BaIrO_3 are not completely filled, which should make this compound metallic. However, a weak localization associated with twisting and bending of Ir_3O_{12} essentially renders the system into an insulating-like state [39]. Analyzing the data of the changes to the crystal structure caused by dilute Gd doping (see table 4.2), we conclude that the lattice stability is significantly altered in this compound as is signaled by the increase of the Ir1–O2–Ir3 bond angle. The buckling of the Ir_3O_{12} trimers is considerably weakened and the structure seems to be more relaxed. This inevitably leads to enhancement of the density of states near the Fermi surface as evident from the enhancement of the Sommerfeld coefficient (see figure 4.5). This enhancement together with the impurity band drive the metallic state below T_C . The behavior is schematically illustrated on the right panel of the figure 4.12 (a). Using the exaggerated pictograms of the trimers at $T = 90$ K, we indicate that a bond angle closer to 180° favors a metallic state. A negative linear

thermal expansion along c -axis and positive thermal expansion with the ab -plane are associated with a relaxed Ir1–O2–Ir3 bond. It is plausible that under an external hydrostatic pressure the three t_{2g} orbitals will be affected significantly differently.

Chemical substitution of the smaller rare-earth ions (Gd, Eu) into the bigger (Ba^{2+}) sites is expected to be qualitatively equivalent to an applied external pressure by its effect on crystal structure. Therefore we allow ourselves to plot a pressure dependence (right panel of the figure 4.12 (a)) as an extension of the doping dependence diagram. Considering the correlation between the transport properties of BaIrO_3 and the vertex angle between the trimers, we reasonably expect the structure to be severely distorted and the bond angle to decrease with increase of the external pressure. As an outcome of such situation the system can revert to an insulating state, which is possibly even stronger than that for the parent compound with $x = 0$. Thus the behavior of the rare-earth BaIrO_3 system would be described by a conventional impurity band formation in semiconductor, which reinstates the expected metallic behavior. However the observed effect of applied external pressure does not fit within that picture. Invoking the structural changes, such as initial relaxation of the lattice followed by severe distortion of Ir–O–Ir bonds could help to explain the observed pressure-induced metal–non-metal transition. The described effects of chemical doping and applied pressure on the electronic ground state can be summarized on a diagram mapping various phases of BaIrO_3 (figure 4.12 (b)). There the left-hand side reflects the evolution of the materials through various phases, illustrating the suppression of the ferromagnetic insulating state as a Gd content increases, and an emergence of a non-metallic behavior above T^* . The right panel of figure 4.12 (b) extends the phase diagram to an external pressure-induced transformations at a constant value of Gd concentration and depicts the recovery of the anomalous magnetic insulating state at low temperature, much stronger than in stoichiometric BaIrO_3 compound.

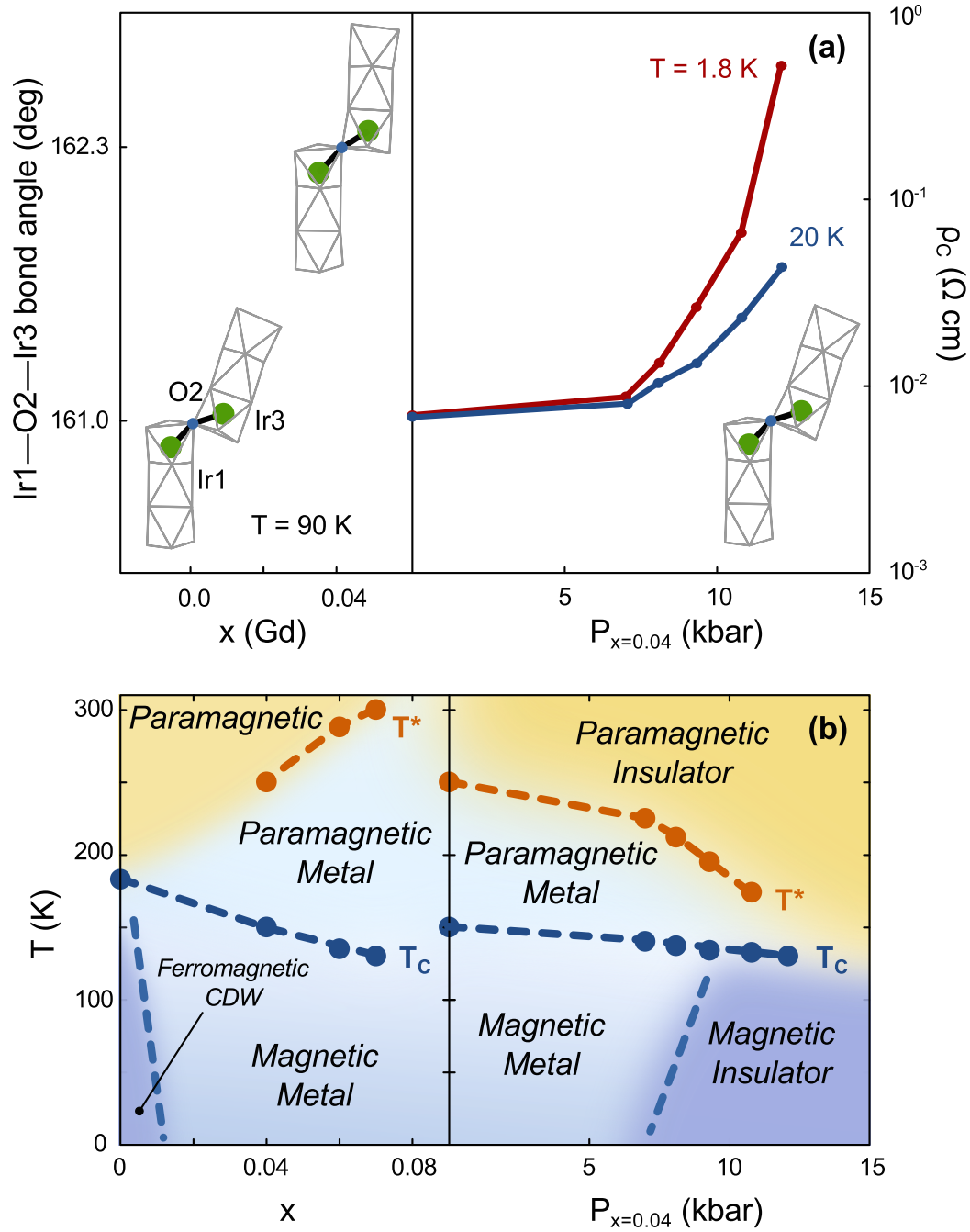


Figure 4.12: (a) Left panel: the schematic of the Ir1–O2–Ir3 bond angle (vertex link between the trimers) at $T = 90$ K as a function of doping content x . The respective values of the bond angle are labeled on the left axis. Right panel: pressure dependence of resistivity $\rho_C(P)$ for the Gd content $x = 0.04$ at $T = 1.8$ K and $T = 20$ K. Inset: projected schematic of the Ir1–O2–Ir3 bond angle at high pressure. (b) The $T-x$ (left panel) and $T-P$ (right panel) phase diagrams for $\text{Ba}_{1-x}\text{Gd}_x\text{IrO}_3$.

4.8 Summary

BaIrO₃ is an end member of the Ruddlesden-Popper series of iridium oxides under a general formula $A_{n+1}\text{Ir}_n\text{O}_{3n+1}$ ($A = \text{Ba}, \text{Sr}$) with $n = \infty$. Because of the significant size mismatch between the Ba²⁺ and Ir⁴⁺ cations (perovskite tolerance factor is $t \approx 1.051$) the stoichiometric compound can form several polytypes of hexagonal perovskites with various ratio of face-sharing to corner-sharing octahedra. The 9R phase of BaIrO₃ is stable at ambient pressure and the structural, transport and magnetic properties of its doped derivatives are the in the focus of this work. Intuitively, oxides of the 5d-element Ir should be more metallic and less magnetic than their 3d-element counterparts due to reduced Coulomb interaction and broadened W — the consequences of spatially extended 5d-orbitals. However, contrary to expectations the compound is a weak ferromagnetic ($\mu_S = 0.03 \mu_B/\text{Ir}$) non-metal (within a wide temperature range $1.7 \div 900$ K) which is considered to be a manifestation of the competition between strong spin-orbit coupling, $d - p$ hybridization and other interactions. Despite the insulating properties of BaIrO₃, the first principle band structure calculations predict a substantial density of states near Fermi level and conclude that the electrons are localized by structural distortions in this compound, while the ground state is in proximity to a metallic state. Due to peculiar crystal structure of BaIrO₃ both the magnetic and the transport properties appear to be extremely sensitive to structural modifications. The previous attempt to tune the ground state by modification of lattice parameters was implemented by dilute isovalent substitution of Sr²⁺ ($r_{\text{Sr}} = 1.18$ Å) on the Ba²⁺ ($r_{\text{Ba}} = 1.35$ Å) ionic sites, inducing a *negative chemical pressure*. The successful recovery of paramagnetic metallic state at $x \approx 0.20$ in Ba_{1-x}Sr_xIrO₃, would suggest a typical bandwidth-driven metal-insulator transition. In this work we report the results of effective dilute rare-earth doping on Ba²⁺ site in BaIrO₃, resulting in induced lattice strains due to ionic size difference and formation of an impurity band in this compound due to introduction of the donor states. Among the wide range of attempted rare-earth elements (Sm $r = 0.96$ Å, Lu $r = 0.86$ Å, Pr $r = 1.03$ Å, Eu $r = 0.95$ Å and Gd $r = 0.94$ Å) the emphasis in this work is on results obtained on Ba_{1-x}Gd_xIrO₃ and Ba_{1-x}Eu_xIrO₃, as demonstrating the most pronounced changes compared to the parent compound. A mere 4% of Gd substitution affects the temperature-dependent crystal lattice parameters while preserving the overall crystal structure, as evident from single crystal X-ray measurements. Significant changes are observed in magnetic properties including reduced ordering temperature, reduced effective magnetic moment and an overall change of the exchange coupling from FM to AFM. A new sharply defined magnetic phase transition is observed at low temperature, attributed to the ordering of the Gd magnetic moments. The magnetic phase transitions are consistently reflected in thermoelectric power and specific heat capacity data, including the complex low temperature structure, demonstrating multiple anomalies ($T_{M1} = 9.5$ K, $T_{M2} = 6.5$ K, $T_{M1} = 3$ K). Remarkably, the doping with the other attempted rare-earths (Sm, Lu, Pr and Eu), fails to induce these strong magnetic anomalies. The measurements of thermodynamic properties confirms the overall bulk effect of the induced changes. The main result of the doping is evident from the electrical resistivity measurements,

which reveals a robust metallic state established in $\text{Ba}_{1-x}\text{Gd}_x\text{IrO}_3$ at $x = 0.04$ (an effect of all other rare-earth doping on transport properties is essentially the same) along the in-plane and inter-plane directions, progressing with increase of doping concentration. Despite the not-activated semiconductor-like behavior of resistivity at low temperature in BaIrO_3 , the ground state in this compound is a complex interplay of different order parameters (CDW, SDW and magnetic order). Nevertheless one could try to interpret the transition to metallic state via analogy with behavior of ordinary semiconductors — conductivity impurity band formed by overlapping donor states. However, the previous results of isovalent doping [40] and the known properties of isostructural $9R\text{-BaIrO}_3$ [240] suggest that the strong coupling of the ground state to the lattice degrees of freedom should be considered as the primary mechanism. Nevertheless, regardless on the model, according to conventional knowledge, the applied external pressure effect on the properties this material should complement the negative chemical pressure effect induced by smaller size ionic substitution. That is to say, the external hydrostatic pressure is expected to increase the bandwidth W through increase of overlap of electronic orbitals, which in turn should result in better support of metallic state. The presented experimental observations of pressure dependence of resistivity on doped compounds destroy this picture. Astonishingly, the application of a modest pressure drives both $\text{Ba}_{1-x}\text{Gd}_x\text{IrO}_3$ and $\text{Ba}_{1-x}\text{Eu}_x\text{IrO}_3$ back into the insulating state with as much as three order of magnitude increase of resistivity. We compare the results with similar known results on other compounds ((La,Sr) CO_3 [239] and simple metals like Li [145], Sr [142], Yb [143]) and conclude that the observed phenomenon is fundamentally distinct as it happens in a material with extended $5d$ -orbitals and at relatively low applied pressure. Examining the result of the structural refinement data on the doped compounds reported in this work reveals the important changes in crystal lattice stability of the material. Evidently, the RE doping considerably weakens the twisting and buckling of IrO_{12} trimers, leading to relaxation of the Ir1-O2-Ir3 bond angle, which favors the metallic state. Simultaneously, the thermal expansion along a , b and c axes is affected significantly differently, which signals about increasing the anisotropy of the compressibility of BaIrO_3 single crystals. Thus, despite the sample being subjected to a hydrostatic pressure, the resulting effect on each of three t_{2g} orbitals could be significantly different, leading to severe distortion of the Ir1-O2-Ir3 bond. Due to experimentally established intimate correlation between this bond and the transport properties of doped BaIrO_3 , we observe the electronic structure reverting back to insulating state, significantly stronger than that of the parent compound. Summarizing the data from magnetic and transport properties measurements with its pressure dependence, we have constructed a rich phase diagrams aimed to illustrates the extraordinary delicacy of the balancing ground state of BaIrO_3 , due to the strong coupling between the orbital electronic and lattice degrees of freedom.

Chapter 5 TRANSPORT AND THERMODYNAMIC PROPERTIES OF SPIN-ORBIT INDUCED MOTT INSULATOR Sr_2IrO_4

5.1 Introduction

Transition metal oxides display a wide variety of structural and physical properties and continue to be of great interest to researchers. Oxides with a K_2NiF_4 -type structure have been intensively studied following the discovery of superconductivity in $\text{La}_{2-x}\text{Ba}_x\text{CuO}_4$ family of compounds [241]. After the discovery of unconventional spin-triplet superconductivity in Sr_2RuO_4 by Maeno *et al.* [242] the Sr_2IrO_4 has been identified as another candidate, mainly due to its structural and electronic similarities with La_2CuO_4 — the parent compound of superconducting cuprates [243, 244]. It has been discovered that Sr_2IrO_4 is an archetype for the novel, spin-orbit interaction induced Mott insulator (on which I elaborate further in this section), where the half-filled $J_{\text{eff}} = 1/2$ band is so narrow that even a reduced U can open an insulating gap. This high temperature Mott insulating state and the half-filled d -bands are the similar properties of these two compounds which have led some researchers to suggest that doped Sr_2IrO_4 compounds can potentially exhibit a high temperature superconductivity, similar to the doped cuprates [245]. In addition, the recent discovery of superconductivity in Re and Os-based pyrochlores-type oxides [246, 247] has shifted a great deal of attention to the $5d$ -based transition metal oxides. Notably, superconductivity is one of the properties of Sr_2IrO_4 which yet remains to be found.

The first reported synthesis of Sr_2IrO_4 was performed by Randall *et al.* in 1956, although the structure was mistakenly assigned to the highly symmetric tetragonal $I4/mmm$ space group. The real lattice parameters and the proper space group have been identified much later from electron diffraction [248] and confirmed by neutron diffraction data [249]. It turned out that Sr_2IrO_4 forms a less symmetric crystal structure than La_2CuO_4 — due to an alternating rotation and elongation of IrO_6 octahedra the modified unit cell is four times larger (expanded by $\sqrt{2} \times \sqrt{2} \times 2$) and belongs to the tetragonal space group $I4_1/acd$ (illustrated in details in the section 5.2). Considering the crystal field configuration of most of the $5d$ compounds, the Ir^{4+} ions are expected to be in the $[\text{Xe}]4f^{14}5d^5$ electronic configuration and the low spin state $t_{2g}^5 e_g^0$. Structurally, the IrO_6 octahedra are elongated along the c -axis (attributed to a Jahn–Teller distortion [243]), suggesting the existence of degeneracy in the d_{xz} and d_{yz} orbitals. Thus the unpaired electron is occupying a half-filled d_{xy} orbital [229]. Considering 5 electrons per Ir site, a half-filled d -band, significantly spatially-extended $5d$ orbitals and smaller than in Ir metal interatomic distance (Ir metal forms on FCC structure with $a = 3.8466 \text{ \AA}$ [231]), in a conventional band picture Sr_2IrO_4 is expected to exhibit metallic properties ($d\rho/dT > 0$) and very weak magnetism. However, stoichiometric Sr_2IrO_4 exhibits an insulating behavior at all temperatures, as can be seen in figure 5.2 (a) and is a weak ferromagnet below $T_M = 240 \text{ K}$ (figure 5.2 (b)). This behavior has been puzzling the researchers

for quite some time, since neutron diffraction patterns did not reveal any superlattice pattern which would indicate a charge order or a CDW states, which could be responsible for insulating behavior [249]. Moreover, according to band structure calculations, in order to open the insulating gap in Sr_2IrO_4 one would need $U \approx 10$ eV, which is unrealistically large for $4d$ or $5d$ based compounds.

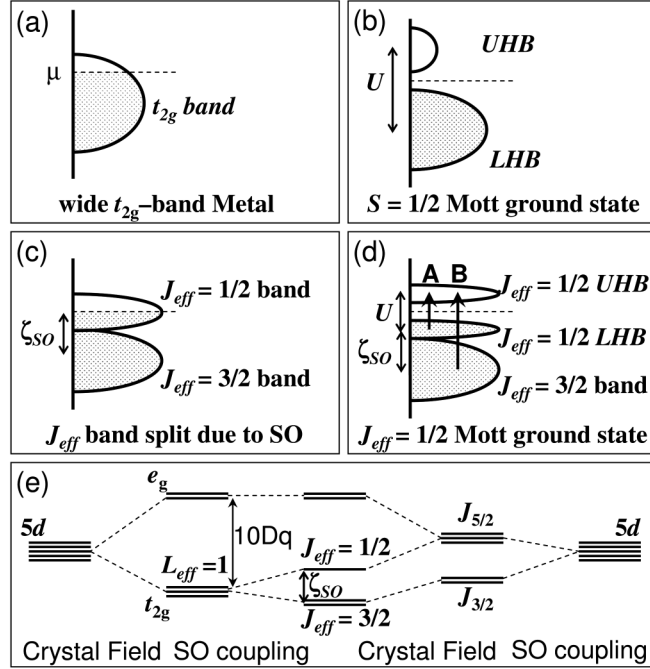


Figure 5.1: Schematic energy diagrams for the $5d^5$ (t_5^2) configuration: (a) without SO and U , (b) with unrealistically large U and no SO, (c) with SO but no U , (d) with SO and U included. Possible optical transitions **A** and **B** are indicated by arrows. (e) $5d$ level splitting by the crystal field and SO coupling. Courtesy of B.J. Kim *et al.* [33].

It is known however, that the relativistic spin-orbit (SO) interaction, which is proportional to Z^4 (Z is the nuclear charge, see section 2.1.4) can no longer be treated as a perturbation in $5d$ based compounds, as it was in $3d$ ones. Instead, its magnitude ($0.4 \div 1$ eV) allows it to compete with the substantially reduced Coulomb repulsion U ($0.4 \div 2.5$ eV) and other interactions. In the study reported by B.J. Kim *et al.* in collaboration with G. Cao's group [33] the unusual behavior in Sr_2IrO_4 was found to be well described taking into account the relativistic SO coupling under a large crystal field. It is demonstrated that a novel $J_{\text{eff}} = 1/2$ Mott ground state is realized in this compound. According to the proposed picture of this SO-induced Mott insulator, the spin-orbit coupling splits the t_{2g} orbitals into $J_{\text{eff}} = 1/2$ states (two-fold degenerate) and $J_{\text{eff}} = 3/2$ states (four-fold degenerate), where J_{eff} denotes the *effective* total angular momentum derived from the large SO coupling with the large crystal field (see figure 5.1). When the SO coupling is large enough, the lower $J_{\text{eff}} = 3/2$ state is fully filled and the upper $J_{\text{eff}} = 1/2$ state forms a half-filled energy band where the

Fermi level resides. The bandwidth of this $J_{\text{eff}} = 1/2$ band (≈ 0.4 eV) is much smaller compared to the one without the SO coupling, therefore even a reduced U is strong enough to open a gap, thus supporting an insulating state. This is a new mechanism driving the Mott state, therefore interesting and important. This picture is qualitatively well supported by data from the resonant X-ray scattering measurements, angle resolved photoemission spectroscopy and optical conductivity [33, 34, 250]. The results of the most recent XAS and XMCD experiment suggest a significant mixing of $J_{\text{eff}} = 1/2$ and $J_{\text{eff}} = 3/2$ bands [153].

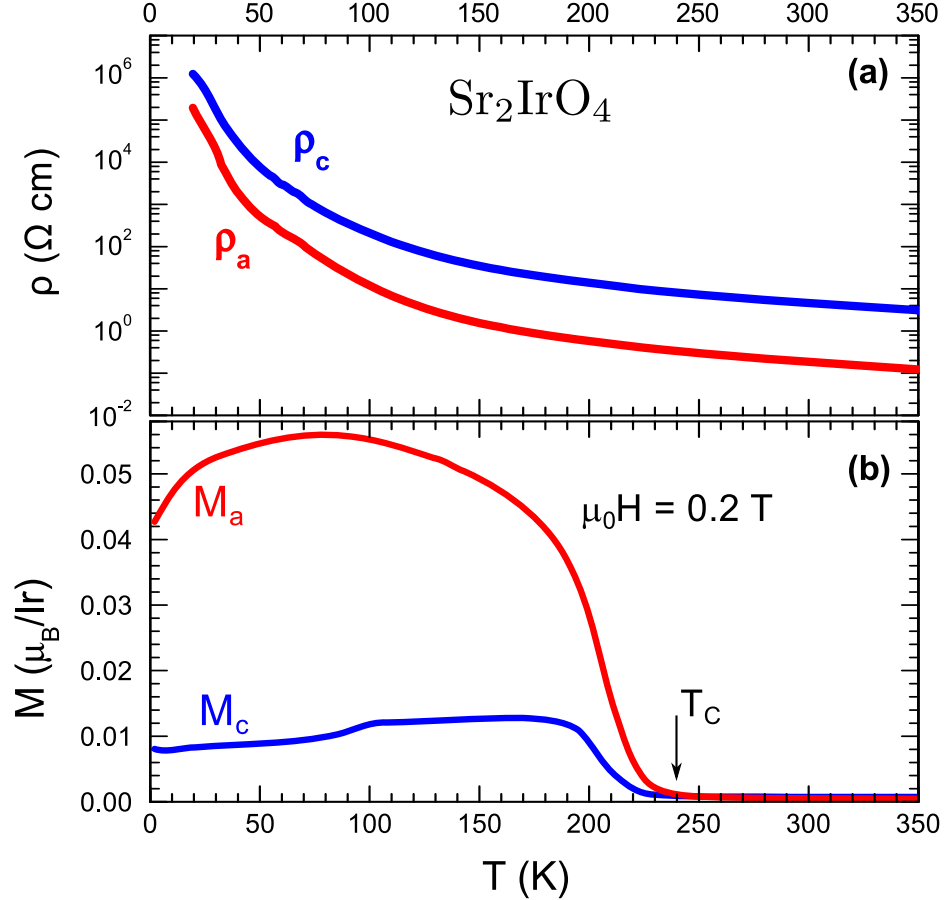


Figure 5.2: Temperature dependence of (a) a - and c -axis resistivity ρ_a , ρ_c and (b) magnetization c -axis and ab -plane M_a , M_c for Sr_2IrO_4 .

The magnetic properties of Sr_2IrO_4 are determined by the extended character of the $5d$ orbitals. Since the electron repulsion effects are small, the exchange terms favoring parallel spin configurations are negligible, while the conventional superexchange bonding contribution is dominant. Therefore, an antiferromagnetic ordering of Ir–O–Ir spins is expected. Experimentally, below the ordering temperature $T_M = 240$ K this compound exhibits the properties of a weak ferromagnet (figure 5.2 (b)), where a Curie-Weiss fit yields $\theta_{CW} = 251$ K, effective paramagnetic moment $\mu_{\text{eff}} = 0.50 \mu_B/\text{Ir}$ and a saturation magnetic moment of only

$\mu_S = 0.14 \mu_B/\text{Ir}$ [229]. Both μ_{eff} and μ_S are only a fraction of what is expected for spin $S = \frac{1}{2}$. The weak ferromagnetic properties of this compound are known to be produced from spin canting, either as a result of the Dzialoshinsky–Moriya interaction mechanism [243, 82] or due to the crystal lattice distortion by the rotation of IrO_6 octahedra [33]. The magnetic properties are strongly anisotropic, with the easy axis parallel to crystallographic a -axis, thus the magnetic moments are confined within the ab -plane. However, as recently reported in the work by M. Ge *et al.* [251], the low temperature anomalies on magnetization data observed near 100 K and 20 K in this compound could be an indication of magnetic moment reorientation, which actually reduces the magnetic anisotropy in this material and results in anomalous magnetoresistance behavior. Similar anisotropy is observed on the electronic transport measurements on this compound, with the in-plane direction being substantially more conductive than inter-plane ($\rho_c/\rho_a = 10^2 - 10^3$). Nonetheless, the qualitative behavior of the resistivity in Sr_2IrO_4 is almost identical in both directions (figure 5.2 (a)). Notably, no anomalies corresponding to magnetic ordering are ever observed in the resistivity or thermodynamic data (presented further in this chapter). In an attempt to explain this phenomena D. Hsieh *et al.* reported the results of a time-resolved photocarrier dynamics on Sr_2IrO_4 single crystals from G. Cao’s group, [252]. They claim to be able to detect a metallic phase high above the Néel temperature T_N and argue that Sr_2IrO_4 undergoes a metal-to-insulator transition across T_N . Therefore, unlike isostructural $3d$ counterparts, this $5d$ system is not pure Mott-type insulator but rather can be described as a mix of Slater-type and Mott–Hubbard-type insulator with some key characteristics from both of those models. This argument is also supported by the theoretical work of R. Arita *et al.* based on first principle calculations [253]. The argument is that the metal-insulator transition in this material spans over a wide temperature window compared to T_N , which should explain an absence of sharp anomalies on the data from other measurements performed on this compound.

As evident, Sr_2IrO_4 is another end member of the Ruddlesden–Popper series of layered iridates $A_{n+1}\text{Ir}_n\text{O}_{3n+1}$ (where $A = \text{Sr}, \text{Ba}$) with $n = 1$ (see section 1.2). The formation of ordered anionic vacancies in the host lattices of layer-structured materials can lead to new mixed frameworks where the cations are able to adopt several coordinations and to exhibit mixed valence states. Numerous novel physical properties emerging on materials with induced oxygen deficiency have been observed in close packed ABO_3 perovskites and layered cuprates [1]. As evident from the discussion above, in the case of Sr_2IrO_4 it is the competing energies and strong spin-orbit coupling (thus strong spin-lattice coupling) that make the system susceptible to any small perturbations such as chemical doping. A post-growth introduction of very dilute oxygen vacancies in $\text{Sr}_2\text{IrO}_{4-\delta}$, performed in this work, readily drives a number of intriguing phenomena in this compound, including (1) an insulator-to metal-transition with a drastic change in resistivity by a factor of $\sim 10^9$, (2) highly non-linear current-voltage characteristics and (3) an abrupt current-induced transition, separating the regions with different $I-V$ curve behavior. To our knowledge, no previous attempts have been made to characterize the physical properties of the novel

ground state in $\text{Sr}_2\text{IrO}_{4-\delta}$ induced by an introduction of oxygen non-stoichiometry.

5.2 Crystal structure and basic properties

As mentioned previously, Sr_2IrO_4 crystallizes in the K_2NiF_4 structure as La_2CuO_4 and its $4d$ counterpart Sr_2RuO_4 , however it adopts a reduced tetragonal structure of $I4_1/acd$ space group (figure 5.3 (a)), with the lattice parameters $a \approx 5.5 \text{ \AA}$ and $c \approx 25.8 \text{ \AA}$ (see table 5.1). Comparing to the reference structure a $\sqrt{2} \times \sqrt{2}$ superlattice is formed within the plane, associated with the staggered rotation of IrO_6 octahedra by $\approx 11^\circ$ about the c -axis clockwise and anticlockwise (see panel (b) of figure 5.3). The rotation removes the $I4/mmm$ inversion center existing between the Ir ions along the (100) and (010) directions [243], hence $a = \sqrt{2}a_0$ ($a_0 \approx 3.9 \text{ \AA}$, the in-plane nearest Ir-Ir distance) and $c = 4c_0$ ($c_0 \approx 6.5 \text{ \AA}$ is the inter-layer distance). The rotation angle of the octahedra is temperature dependent, increasing from 11.36° at room temperature to 11.72° at 10 K [249, 244] and corresponds to the distorted in-plane Ir1-O2-Ir1 bond angle θ , which in stoichiometric compound ($\delta = 0$) decreases with temperature from 157.28° to 156.56° . This rotation of the octahedra is also accompanied by the elongation of c -axis while the temperature decreases, mainly due to elongation of the IrO_6 octahedra. The latter is thought to occur either due to Jahn-Telles distortion or as a result of anisotropic crystal structure [254].

Table 5.1: Lattice parameters, Ir1-O2-Ir1 bond length and bond angle at 90 K for $\text{Sr}_2\text{IrO}_{4-\delta}$.

δ ($T = 90 \text{ K}$)	a (\AA)	c (\AA)	V (\AA^3)	Ir1-O2-Ir1 bond angle θ (deg)
0	5.4836(8)	25.8270(5)	776.61(22)	156.28
0.04	5.4812(3)	25.8146(16)	775.56(8)	157.072

The post-growth oxygen reduction process significantly alters the crystal structure parameters in the $\text{Sr}_2\text{IrO}_{4-\delta}$ samples ($0 \leq \delta \leq 0.04$). As revealed by our single crystal X-ray diffraction data (see table 5.1) the bond angle dependence on temperature is reversed in oxygen deficient samples ($\delta = 0.04$). This time θ increases from 157.028° to 157.072° while the temperature decreases from 295 K to 90 K. In fact, even the room temperature angle is significantly larger than that for $\delta = 0$, and the difference is rather appreciable for such a small oxygen depletion. Moreover, the volume of the unit cell contracts by 0.14 % compared to that for stoichiometric compound. This data indicates a significant reduction of structural distortions at low temperature as a result of introduction of dilute oxygen vacancies. Even though the changes in Ir1-O2-Ir1 angle θ alone cannot completely define the observed electronic structure changes I will present further, it certainly plays an important role in controlling the hopping of the $5d$ electrons and superexchange interaction between the Ir atoms via

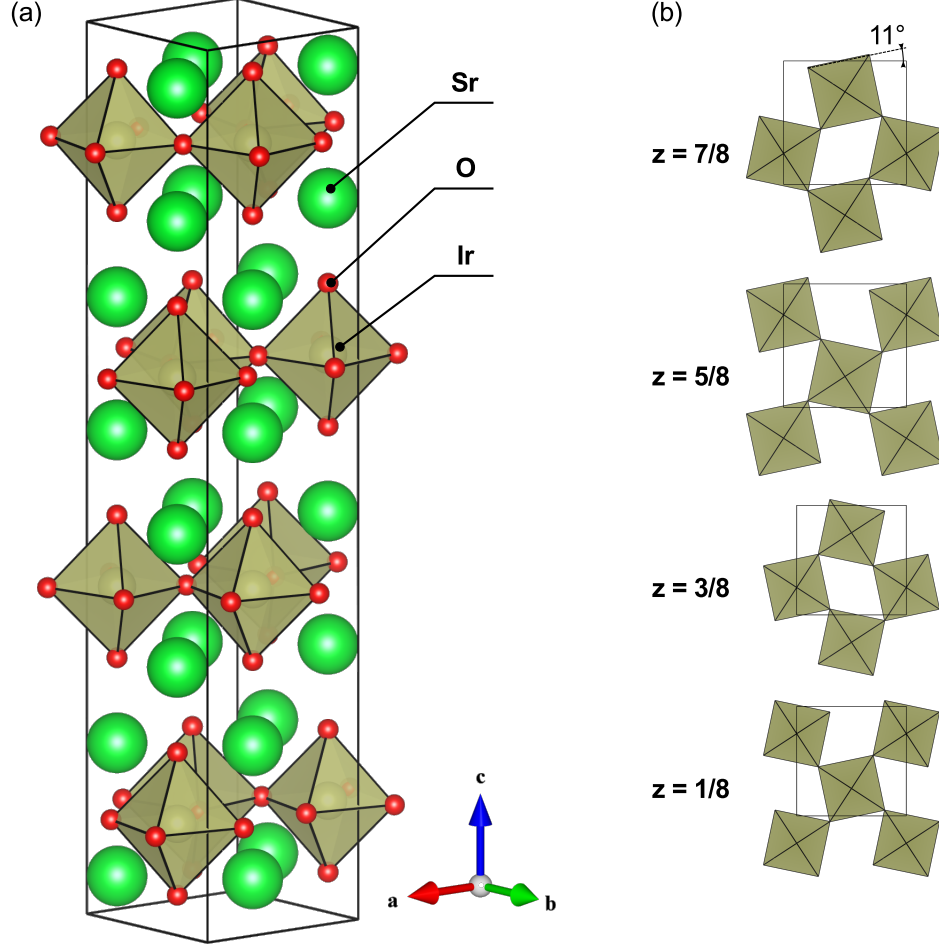


Figure 5.3: Polyhedral representation of the crystal structure of Sr_2IrO_4 : (a) crystal structure unit cell, corresponding ions are indicated; (b) IrO_6 octahedra rotation pattern in each layer of the unit cell as seen along c -axis direction, the z coordinate for each layer is indicated, the unit cell boundaries are superimposed. Model produced from original measurements using *VESTA 3* software [9].

the bridging O sites [35] and therefore is an important focus of this work. The fact that we observe these changes using single crystal X-ray diffraction supports the claim that the oxygen vacancies are uniformly distributed through the bulk of the material and are not confined to the surface of the crystals. In the latter case no such changes in the lattice parameters would be observable.

5.3 Oxygen depleted Sr_2IrO_4

The first result of oxygen depletion in $\text{Sr}_2\text{IrO}_{1-\delta}$ is a gradual decrease of resistivity as δ increases. As illustrated on figure 5.4, the a -axis resistivity $\rho_a(T = 1.8 \text{ K})$ of five representative single crystal samples is reduced by a factor of 10^9 as δ changes within the range from 0 to ≈ 0.04 . Simultaneously, the c -axis resistivity ρ_c decreases

by a factor of 10^7 , which is evidence of a rapid increase of the density of states at the Fermi level $N(E_F)$. A sharp insulator-to-metal transition occurs near the temperature $T_{MI} = 105$ K for $\delta \approx 0.04$, resulting in a reduction of ρ_a by a factor of 10^4 and ρ_c by one order of magnitude on the temperature range from T_{MI} to $T = 1.8$ K (figure 5.5 (a)). Despite the reduction of the resistivity, the oxygen deficient compound still retains the anisotropy in transport properties inherited from the parent compound even at the lowest temperature which is consistent with a nearly two-dimensional, strongly correlated electron system. The resistivity for both ρ_a and ρ_c demonstrate a linear low temperature dependence without saturation to a residual resistivity limit. For a -axis this can be observed below 20 K, and for c -axis the plateau below 35 K is followed by a sudden downturn at $T = 5$ K, indicating a rapid decrease in inelastic scattering. Application of a magnetic field tends to destabilize the low-temperature metallic state as illustrated on figure 5.5 panel (a). At $\mu H_0 = 7$ T we observe a positive magnetoresistance of about 10 % along c -axis and a ≈ 6 K shift of T_{MI} to lower temperatures. The last observation indicates a possible tendency for destabilization of low-temperature metallic state by the high magnetic field. Remarkably, the distinct low-temperature downturn on $\rho_c(T)$ is insensitive to the magnetic field.

Thermoelectric power $S(T)$ measures a potential difference induced by a temperature gradient through the bulk of a material, and its change is a good indicator of the changes in electronic density of states in a material with metallic behavior, since $S \propto N(E_F)^{-1}$ [62]. As seen from our data, the peak value of the Seebeck coefficient along c -axis $S_c(T)$ for the oxygen depleted $\text{Sr}_2\text{IrO}_{1-\delta}$ ($\delta = 0.04$) is only $\simeq 1/3$ of the value observed for stoichiometric compound ($\delta = 0$) (figure 5.5 (b)), further confirming the effect we observe on the resistivity data. Moreover, the result of thermoelectric power measurements is another strong indication (in addition to uniform changes of lattice parameters) that oxygen depletion in this material is a bulk effect.

The $J_{\text{eff}} = 1/2$ bandwidth in stoichiometric Sr_2IrO_4 is very narrow, $W = 0.48$ eV, so even a modest U (~ 0.5 eV) would be sufficient to induce a Mott gap in this band [33]. According to first-principle calculations W in this compound is very sensitive to structural modifications, such that an increase of the Ir–O–Ir bond angle θ from 157° to 170° should cause a broadening of the $J_{\text{eff}} = 1/2$ band and consequent decrease of the Mott gap by ≈ 0.13 eV [35]. Obviously, the measured change of $\Delta\theta = 0.792^\circ$ is way below the theoretically required value of 13° and does not appear to be sufficient to produce the observed changes in transport properties. Apparently a simple lattice distortion could not explain the large required changes in bandwidth, therefore we are looking for other possible mechanisms responsible for the metal–insulator transition. Creation of oxygen vacancies in Sr_2IrO_4 inevitably results in electron doping of the insulating state. According to LDA+SO+U band structure calculations for this compound, additional electrons will occupy states in four symmetric pockets located near the M point of the basal plane of the Brillouin zone, with the estimated filling of ~ 2 % for each pocket at $\delta = 0.04$ [35]. The process appears to be similar to the doping of strongly correlated $\text{La}_2\text{CuO}_{4+\delta}$ — the isostructural parent compound for high-temperature superconductors [36]. However, there are fundamental differences in the magnetic properties of these compounds (La_2CuO_4

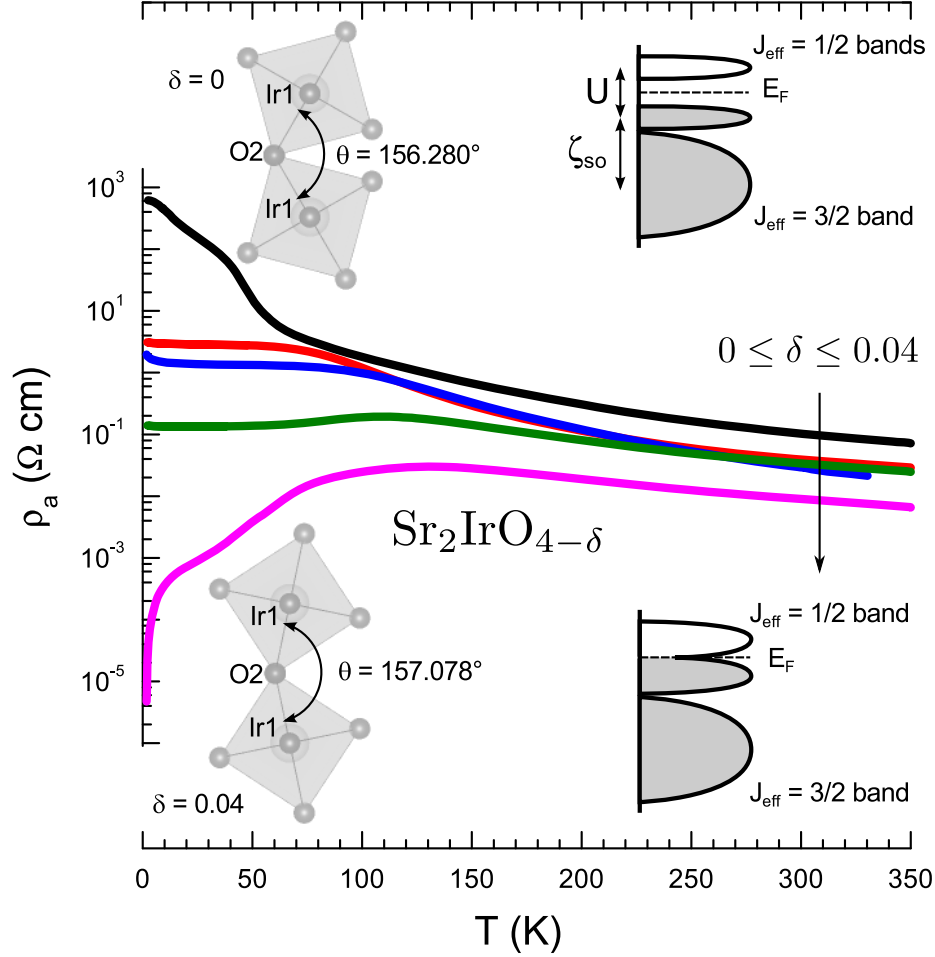


Figure 5.4: Temperature dependence of ρ_a for several representative values of δ in $\text{Sr}_2\text{IrO}_{4-\delta}$. Inset: a schematics of the Ir1-O2-Ir1 bond angle θ and schematic of corresponding band structure at $T = 90$ K for $\delta = 0$ (top panel) and $\delta \simeq 0.04$ (bottom panel). The changes in angle θ are exaggerated for clarity. Note that θ decreases for $\delta = 0$, but slightly increases for $\delta \simeq 0.04$.

is a simple antiferromagnet versus weakly ferromagnetic Sr_2IrO_4) and the sign of the doped carriers (holes in La_2CuO_4 versus the electrons in Sr_2IrO_4). Another important outcome of the oxygen non-stoichiometry in a solid, single crystal compound is a structural disorder. In a quasi-2D system like Sr_2IrO_4 this factor is expected to lead to localization of states close to the band edge. Taking into account both of these factors, the following scenario could take place. Assuming that the Fermi level lies below the mobility edge for $\delta > 0$, the occupied states should be localized at high temperature. As the temperature decreases the compound develops an increasing ferromagnetic polarization below T_C and the intersection of the Fermi level with the majority spin band is being gradually pushed towards the mobility edge, while the exchange splitting of the band increases below T_C . Eventually the Fermi crosses the

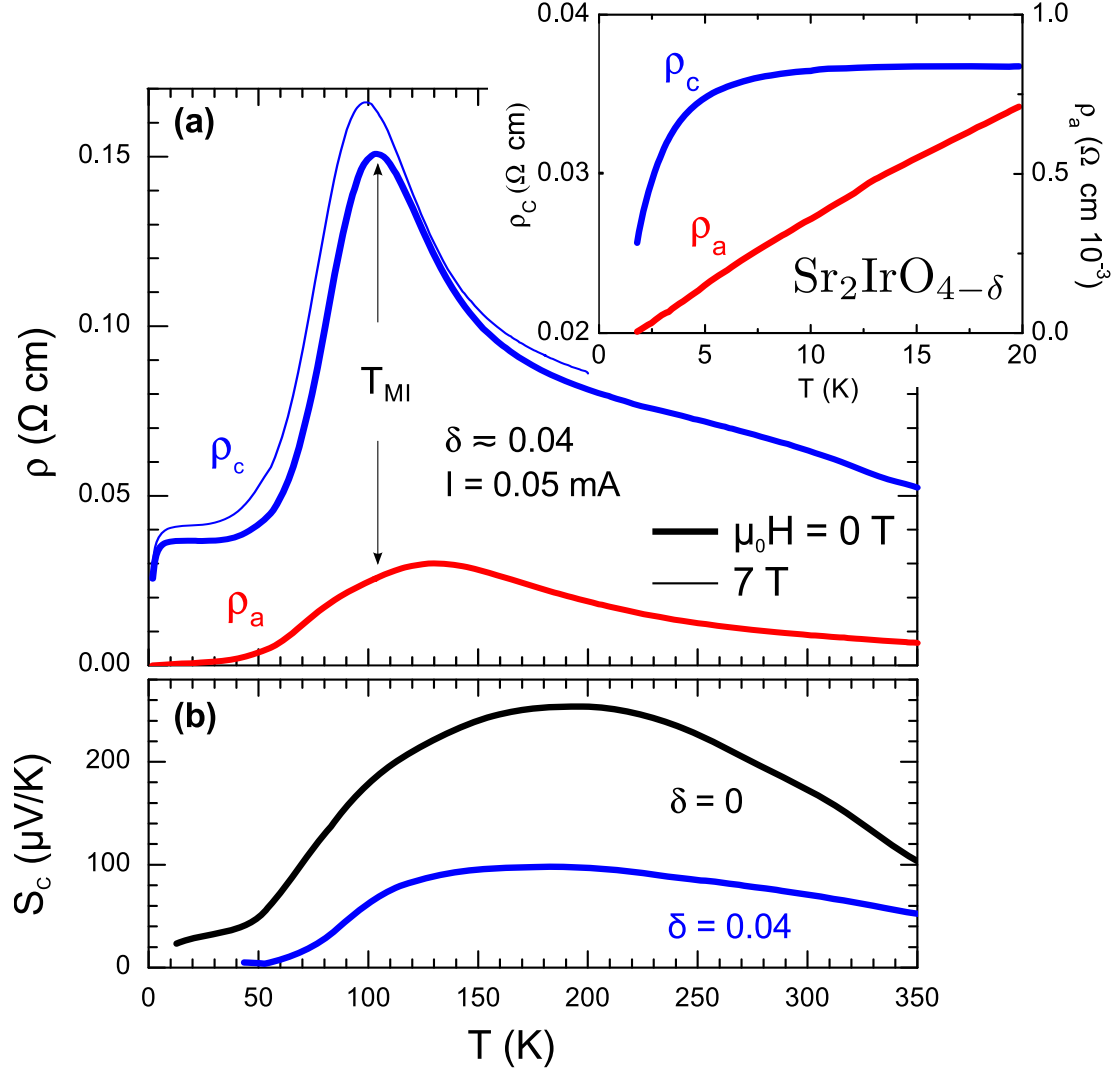


Figure 5.5: Temperature dependence of (a) a - and c -axis resistivities $\rho_a(T)$, $\rho_c(T)$ for $\delta = 0.04$ in $\text{Sr}_2\text{IrO}_{4-\delta}$. (b) thermoelectric power along c -axis $S_c(T)$ for $\delta = 0$ and $\delta = 0.04$. Note a downturn near 5 K in ρ_c and the linear low-temperature dependence in $\rho_a(T)$ on inset in (a).

mobility edge resulting in metallic behavior below T_{MI} , however the minority-spin carriers remain always localized. Because we can observe a clearly defined T_{MI} only for $\delta \approx 0.04$ (see figure 5.4) it must be that the electron density is insufficient for mobility edge crossing at lower doping values. Obviously, in order for this scenario to work the electrons in the M pockets have to be polarized first, therefore T_{MI} needs to be considerably lower than the magnetic ordering temperature T_C . The importance of disorder in physical properties of $\text{Sr}_2\text{IrO}_{4-\delta}$ is corroborated by resistivity fits using

a variable range hopping (VRH) relation

$$\rho(T) = Ae^{(\frac{T_0}{T})^\nu} \quad (5.1)$$

where A is a proportionality constant, T_0 is characteristic temperature and $\nu = 1/2$ for VRH or $\nu = 1/4$ for VRH with negligible long-range Coulomb repulsion. The figure 5.6 illustrates a decent quality fit for the temperature range from 187 K up to 350 K. It is worth mentioning that a similar behavior is observed for the insulating samples as well [229]. Thus, the metallic state is expected to be inhomogeneous and conductivity increases from the growth and percolation of metallic patches, when the metallic state develops from the phase separation of competing states. The changes in Ir–O–Ir bond angle, like the reversed trend of the temperature dependence and increase of θ with doping, could be a consequence of increased screening in the metallic state.

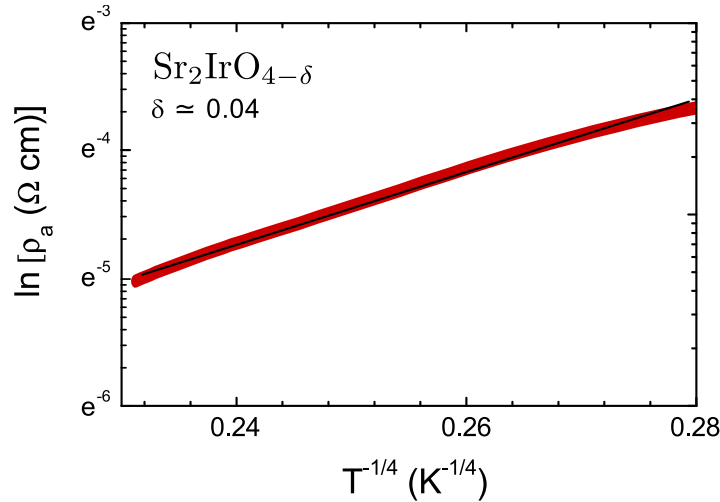


Figure 5.6: Temperature dependence of resistivity $\rho(T)$ fit for variable range hopping (VRH) relation on a range $T = 187 \div 350$ K. Straight line is a guide for an eye.

5.4 Magnetic properties of $\text{Sr}_2\text{IrO}_{4-\delta}$

The changes in magnetization with increasing oxygen deficiency concentration δ are modest comparing to those in resistivity and thermoelectric power, but remarkable nonetheless. Illustrated in figure 5.7, are magnetization curves $M(T)$ measured for stoichiometric and the oxygen-deficient compounds ($\delta = 0.04$) in applied magnetic field $\mu_0 H = 0.2$ Tesla. As can be seen, the anisotropy of the magnetic moment is preserved in the oxygen deficient compound. The FM ordering temperature T_C increases by approximately 10 K for $\delta = 0.04$ compared to $\delta = 0$, also the magnetic anomaly on $M_c(T)$ near 100 K for $\delta = 0$ shifts upward to ≈ 160 K for the

oxygen deficient sample. Moreover, both M_a and M_c exhibit a weak but noticeable feature near $T = 100$ K, which closely correlates with the metal-insulator transition temperature T_{MI} on resistivity data, see figure 5.5 (a). This is quite a contrasting behavior comparing to that of the stoichiometric parent compound, where none of the magnetic anomalies are reflected on resistivity $\rho(T)$ or thermoelectric power $S(T)$ data [248, 229, 33], despite the fact that magnetic correlations drive the material into a weak FM state below 240 K. Hence, the overall behavior is that ferromagnetic order is stabilized with of oxygen deficiency δ , judging by increase of T_c , the appreciable increase of magnetization is definitely observed at low temperatures.

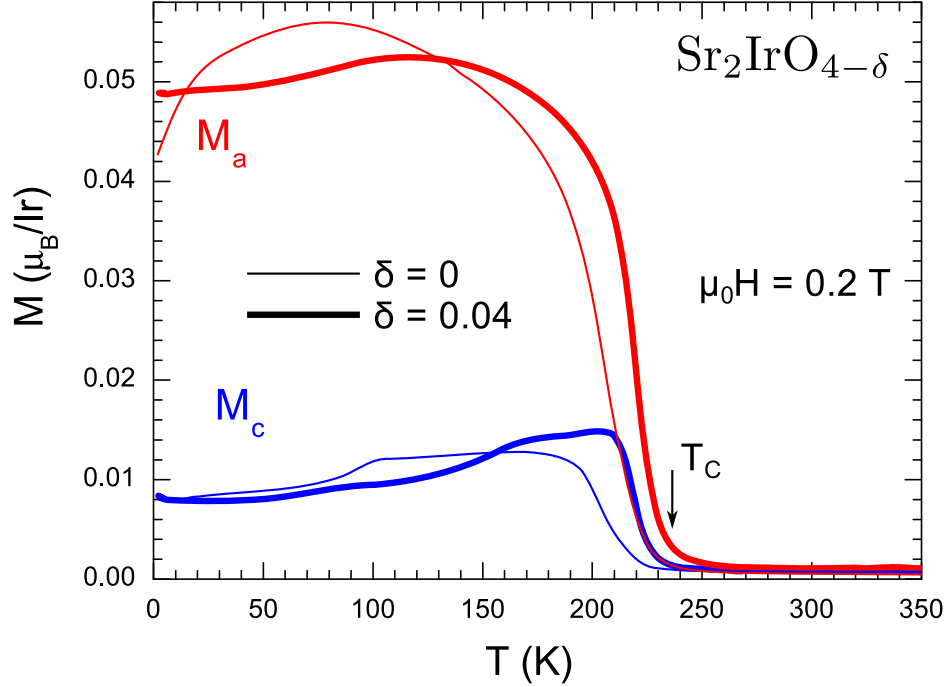


Figure 5.7: Temperature dependence of a - and c -axis magnetization M_a , M_c for $\text{Sr}_2\text{IrO}_{4-\delta}$, $\delta = 0$ (thin lines) and $\delta \approx 0.04$ (thick line).

5.5 Non-Ohmic behavior of $\text{Sr}_2\text{IrO}_{4-\delta}$

Another major feature in this system is the non-Ohmic behavior which exhibits current-controlled negative differential resistivity (NDR) for both the a - and c -axis crystallographic directions. Figure 5.8 illustrates the temperature dependence of $\rho_c(T)$ for several representative values of excitation current. The dependence is almost negligible when the current density $J \leq 0.6$ A/cm², but when $J \geq 3.3$ A/cm² the behavior changes dramatically. The characteristic temperature $T^* \approx 52$ K marks the contrasting behavior for low- and high-current modes of $\rho(T)$ dependence. As one can see ρ_c drops sharply at T^* for $J \approx 3.3$ A/cm², but rapidly rises for $J = 3.27$ A/cm², indicating apparent current-induced phase transition. Notably, the distinct low-

temperature behavior on resistivity below 5 K disappears already at $J \geq 0.64 \text{ A/cm}^2$, although we are observing this feature preserved under the application of high magnetic field, as illustrated in magnetoresistance data in figure 5.7.

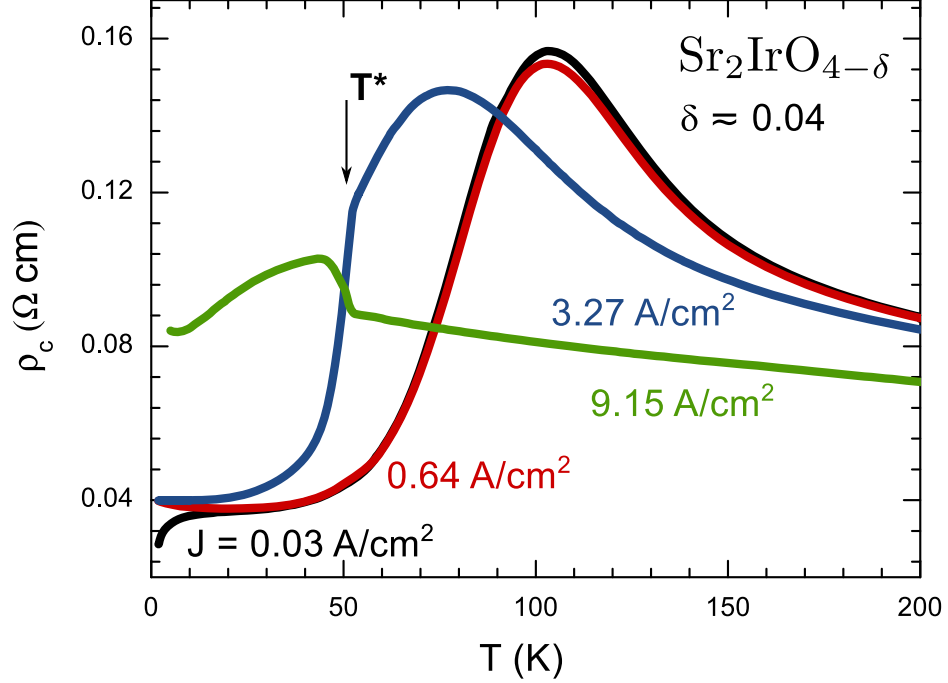


Figure 5.8: Temperature dependence of c -axis resistivity ρ_c at several representative values of excitation current I for $\text{Sr}_2\text{IrO}_{4-\delta}$ ($\delta = 0.04$).

The nonlinear characteristic behavior persists over the T_{MI} and higher and is more dramatically demonstrated on normalized $I - V$ curves, where one can observe mode switching occurring at multiple threshold potentials (E_{T1} , E_{T2} and E_{T3}) as the current density varies from $65 \mu\text{A/cm}^2$ up to 33 A/cm^2 (see figure 5.9). The initial linearity in the $I - V$ curve persists up to $J \approx 2.5 \text{ A/cm}^2$ for electric field below the first threshold potential E_{T1} ($E_{\text{T1}} \approx 0.4 \text{ V/cm}$ at $T = 5 \text{ K}$) where the change of slope occurs, however the dependence remains linear up to the second threshold potential $E_{\text{T2}} \approx 1.2 \text{ V/cm}$. As the electric current density increases further the $I - V$ curve exhibits a third threshold E_{T3} , marking the onset of the current-controlled negative differential resistivity potential drop across the sample decreases as the excitation current increases. All three threshold potentials clearly exhibit a strong temperature dependence, and when mapped on a separate plot reveal a qualitative difference between the two regions separated by temperature T^* (figure 5.10). Notably, for the temperature region $T < T^*$ the threshold potentials E_{T2} and E_{T3} increase as the temperature increases, while for temperatures above T^* the trend for E_{T2} and E_{T3} is reversed and E_{T1} rapidly tends to zero. The characteristic temperature T^* remains sharply defined at 52 K on resistivity data independent on excitation current density J value.

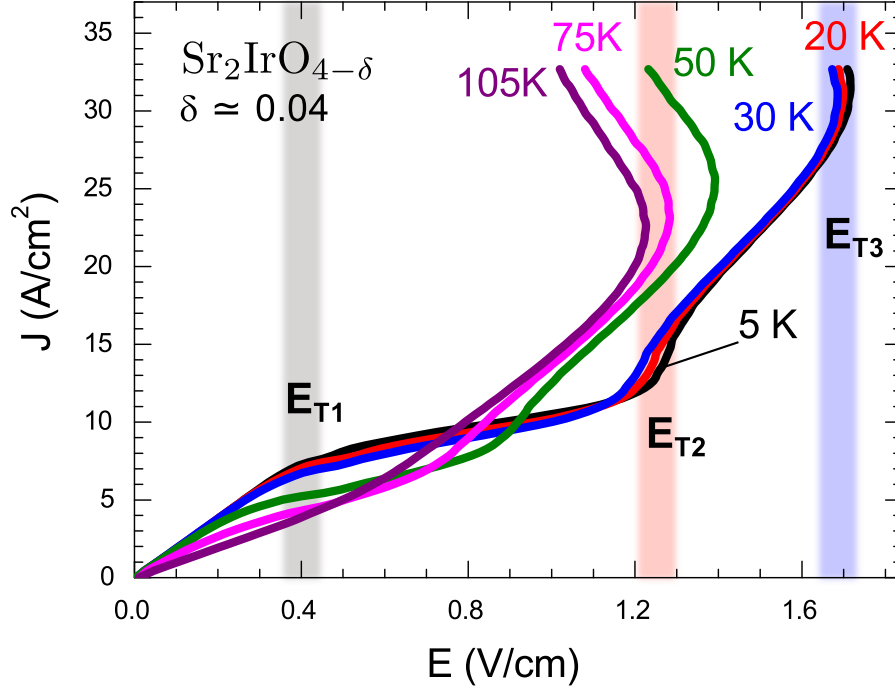


Figure 5.9: Normalized I-V curves for Sr_2IrO_4 with $\delta = 0.04$ at several representative temperatures. The threshold electric potentials E_{T1} , E_{T2} and E_{T3} are labeled.

When observing the current-dependent non-linear effect like this, it is very important to exclude the possibility of self-heating playing a dominant role in this behavior. One of the options is to refine the experimental approach utilizing a pulsed excitation current source, as have been done previously [227] and study the dependence of the behavior on the pulse width. However, to the first approximation there are indirect factors indicating whether the observed behavior is indeed intrinsic property of this compound. The sharply defined temperature T^* , which is independent of J , is in this case one of the factors strongly ruling out the self-heating possibility. Moreover, using the measured temperature dependence of resistance of the sample for low currents and the specific heat dependence on temperature, we have estimated the worst-case scenario Joule heat output for the duration of the single $I - V$ curve measurements cycle, and found it on the level of few degrees near the characteristic temperature. In the real case, the sample is thermalized by thermally anchoring it to sample holder in form of a copper plate of appreciable weight using a thermoconducting varnish VGE-7031, which helps to stabilize the temperature and maintain an efficient heat exchange with the thermal bath (see section 3.5.1 for detailed description of resistivity measurements). Hence, the parasitic temperature change ΔT is expected to be about an order of magnitude lower.

The non-Ohmic behavior of $I - V$ characteristics and the NDR are not exactly new phenomena observed in the study of layered iridates with an insulating state. Similar effects have been previously reported by our group on the parent compounds stoi-

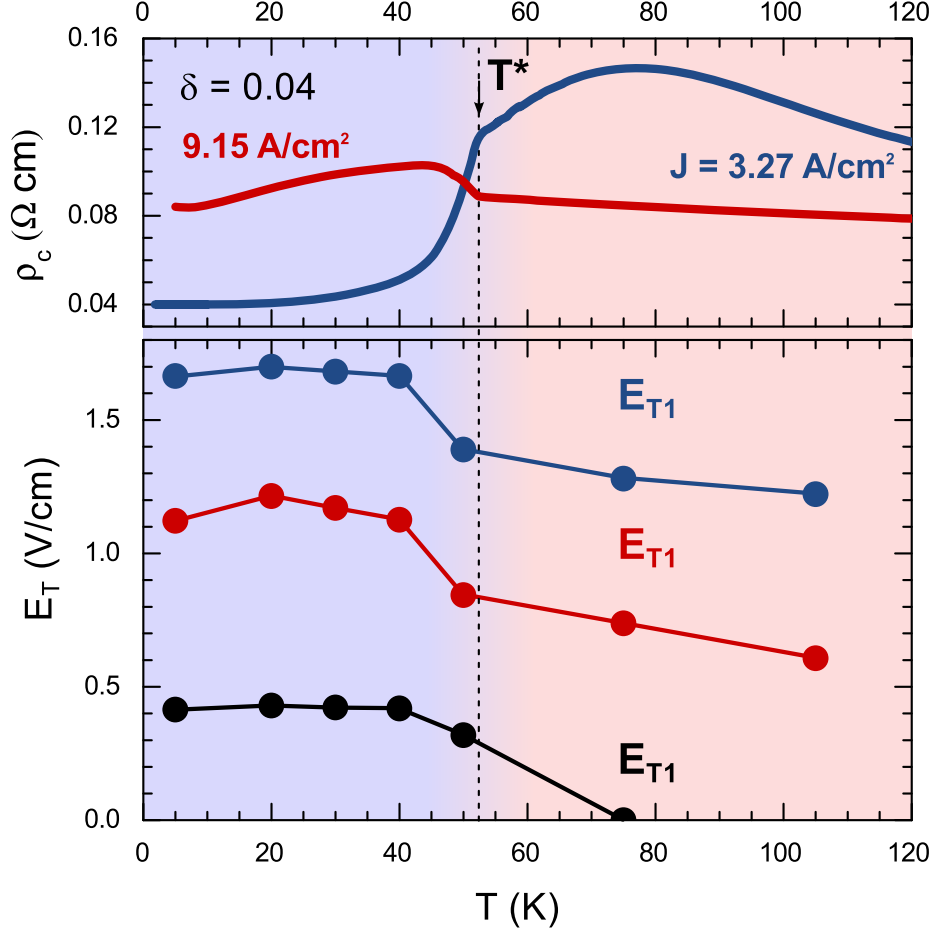


Figure 5.10: Temperature dependence of (a) c -axis resistivity ρ_c measured at representative excitation current values, (b) threshold potentials E_T of negative differential resistivity.

chometric Sr_2IrO_4 [229] and hexagonal perovskite BaIrO_3 [158], and have been later confirmed by other groups [227]. The temperature-dependent switching behavior observed on BaIrO_3 is characterized by a single threshold potential E_T , comparable by magnitude with the maximum value of the upper threshold $E_{T3} \approx 1.7 \text{ V/cm}$ for the oxygen deficient $\text{Sr}_2\text{IrO}_{4-\delta}$ ($\delta \simeq 0.04$). In this compound the observed behavior was attributed to a collective charge-density wave (CDW) dynamics in the presence of disorder. Indeed, the depinning of the density waves from the oxygen vacancies by an applied potential is one of possible mechanisms for non-Ohmic behavior of resistivity [132, 130]. However, the non-Ohmic behavior observed on oxygen deficient samples of $\text{Sr}_2\text{IrO}_{4-\delta}$ takes place in metallic phase, therefore the question concerning its origin is quite intriguing. It would be quite surprising if the observed non-Ohmic behavior for both metallic and insulating states of this compound originated from the same CDW state, especially considering that the highest threshold potential E_{T3} observed for $\delta = 0.04$ is still about an order of magnitude lower than that one observed

in the stoichiometric ($\delta = 0$) parent compound [229]. This would either suggest much weaker CDW depinning potential in oxygen deficient sample, or a novel metallic state with non-Ohmic behavior, where the resistivity of the material can be manipulated with modest applied current.

5.6 Summary

To summarize, the aim of this work was to study structural, thermodynamic and transport properties of the anomalous metallic state induced by oxygen deficiency in $\text{Sr}_2\text{IrO}_{4-\delta}$. The stoichiometric Sr_2IrO_4 is an end member of the Ruddlesden-Popper series of iridium oxides, with a general formula $A_{n+1}\text{Ir}_n\text{O}_{3n+1}$ ($A = \text{Ba}, \text{Sr}$) with $n = 1$. Similar to many recently studied iridates, it was expected that due to spatially extended $5d$ orbitals the Coulomb interaction is reduced such that electronic correlation effects are insignificant. The compounds were anticipated to exhibit more metallic and less magnetic ground state than their $3d$ and $4d$ counterparts. However, apart from limited exceptions, most of the iridates from R-P series are found in a magnetic, insulating ground state. As demonstrated in previous studies [33, 153, 250] the uniqueness of this class of materials is that these unusual physical properties are driven by a vigorous competition between the strong spin-orbit coupling λ_{SO} , the reduced Coulomb interaction U and other types of interaction. The strong spin-lattice coupling, caused by strong SO interaction [82] makes a perturbative approach a very effective tool in the study of these iridium-based compounds. In this work we report the results of resistivity measurements on $\text{Sr}_2\text{IrO}_{4-\delta}$, demonstrating the evolution of electronic transport properties as function of very dilute oxygen vacancies. In overall, as δ increases from 0 to 0.04 the electrical resistivity is reduced by a factor of 10^9 and 10^7 for a -axis direction ρ_a and c -axis direction ρ_c respectively. For sample with $\delta \approx 0.04$ a strong metal-insulator transition is observed at $T_{MI} = 105$ K for both crystallographic directions, with highly distinct anisotropy. The linear temperature dependence of resistivity without saturation to a residual limit below 20 K is quite intriguing. However, it demonstrates no dependence on high magnetic field, which unfortunately rules out the case of possible developing superconductivity. The results of the thermoelectric power (strong reduction of Seebeck coefficient) indicated an increase of density of states at the Fermi level $g(E_F)$ and confirm the bulk effect of post-growth oxygen depletion. The slight increase of magnetic ordering temperature in $\text{Sr}_2\text{IrO}_{4-\delta}$ ($\delta \approx 0.04$) seems a modest change comparing to the changes in resistivity, nonetheless indicates the further stabilization of ferromagnetic order. The non-Ohmic behavior and *negative differential resistivity* has been previously observed on several other layered iridates in their insulating state [158, 229]. However, the effect observed on oxygen depleted samples is observed in metallic phase and is more complex, exhibiting several threshold potentials, which are an orders of magnitude lower than that for the stoichiometric parent compound Sr_2IrO_4 ($\delta = 0$). The behavior is still not understood, but potentially constitutes a new paradigm for current-controlled NDR electronic memory devices, which have attracted attention over the past years [255, 256, 257]. The analysis of the crystal structure data obtained on the stoichiometric and oxygen deficient samples indicates that the intro-

duction of dilute oxygen vacancies increases the bond angle between the rotated IrO_6 octahedra (Ir-O2-Ir1 angle) and reverses its temperature dependence, significantly reducing the structural distortion. It is known that this angle controls the hopping of the $5d$ electrons and superexchange interaction via the bridging oxygen site, therefore its modification is expected to influence physical properties. However, the observed structural modification in $\text{Sr}_2\text{IrO}_{4-\delta}$ are substantially lower than those theoretically predicted, required to close the $J_{\text{eff}} = 1/2$ Mott gap [35]. We conclude that another mechanism must be responsible for the induced metal-insulator transition and propose that the combination of the electron doping and the disorder introduced by oxygen vacancies might play a role similar to the case of superconducting cuprates.

Chapter 6 CONCLUDING REMARKS AND OUTLOOK

For many years the material researchers enjoyed studying the rich physics of electron correlation in transition metal oxides. For a long time the main fruitful playground for studying such strong correlations effects was the family of $3d$ TMOs due to a large on-site Coulomb repulsion U ($2 - 10$ eV). This was a celebrated class of materials for which an independent electron description fails, therefore the properties cannot be understood from a framework of weakly-interacting electrons. The Coulomb repulsion of the elements with $5d$ -electrons was estimated to be less than 1 eV, and was reasonably expected to be simply too low to drive the electronic correlation effects. The realization of the fact that spin orbit coupling λ_{SO} in these compounds is strong enough to compete with other interactions like crystal field, sparked a great interest of condensed matter physicist to this new area. In the Ruddlesden-Popper series of iridium oxides $A_{n+1}\text{Ir}_n\text{O}_{3n+1}$ ($A = \text{Ba}, \text{Sr}$), both magnetic and the transport properties were always expected to be extremely sensitive to structural modifications, particularly on the relative orientation of the building block of these compounds — IrO_6 octahedra. However, complemented by the strong spin-orbital interaction effects, the physical properties of compounds of this family exhibit even stronger coupling to lattice, charge, orbital and spin degrees of freedom. Hence a perturbative approach, particularly chemical doping, in these strongly correlated electron materials has been found very fruitful and the its results formed the keynote of this thesis. In this work I have concentrated on the transport, magnetic and thermodynamic properties of structurally and electronically modified two end members of the series of iridium-based oxides, namely BaIrO_3 and Sr_2IrO_4 . The major findings of this work include:

- a robust metallic state introduced in BaIrO_3 , doped with low amount of wide range of rare-earth elements.
- an insulating state reinstated by applied hydrostatic pressure in metallic compounds $\text{Ba}_{1-x}\text{Eu}_x\text{IrO}_3$ and $\text{Ba}_{1-x}\text{Gd}_x\text{IrO}_3$,
- illustration of an intrinsically unstable ground state of Sr_2IrO_4 , which readily changes between highly insulating ($10^5 \Omega \text{ cm}$) and metallic ($10^{-5} \Omega \text{ cm}$) behavior via slight change of oxygen stoichiometry;
- non-Ohmic conductivity behavior of unknown origin in $\text{Sr}_2\text{IrO}_{4-\delta}$, which potentially constitutes a paradigm for current-controlled switching devices of a new type.

As for now the study of iridium based oxides is still rather young and actively developing field. Understandably, the situation of delicate interplay of orbital and lattice degrees of freedom is always of high interest for material researchers, therefore at the time of finishing this work numerous other cases of ionic substitution on different sites in these compounds have been attempted our lab as well as by some

Table 6.1: A list of studied single crystal iridates of various crystal structure and their respective properties. (*Oxide compound exhibits metallic ground state).

Structure	Compound	Physical Properties
Layered perovskite	$\text{Sr}_3\text{Ir}_2\text{O}_7$ Sr_2IrO_4	$J_{\text{eff}} = 1/2$ Mott insulator, complex magnetism, lattice magnetoresistance, giant magnetoelectric effect, anomalous magnetism, non-Ohmic behavior
Hexagonal perovskite	BaIrO_3 SrIrO_3^* $\text{Ca}_5\text{Ir}_3\text{O}_{12}$ Ca_4IrO_6	$J_{\text{eff}} = 1/2$ Mott insulator, coexistence of FM and CDW, QCP, geometrically frustrated system
Pyrochlore	$\text{RE}_2\text{Ir}_2\text{O}_7$ $\text{Y}_2\text{Ir}_2\text{O}_7$ $\text{Bi}_2\text{Ir}_2\text{O}_7^*$ $\text{Pb}_2\text{Ir}_2\text{O}_7^*$	Possible topological insulator, strong magnetic instability
Honeycomb	Na_2IrO_3	Zig-zag magnetic order, possible topological insulator
Double Perovskite ($\text{Ir}^{5+} 5d^5$)	Sr_2YIrO_6 $\text{Sr}_2\text{GdIrO}_6$	Correlated insulator
Kagome	$\text{Na}_4\text{Ir}_3\text{O}_8$	Spin liquid

other groups. With an idea to independently tune the crystal field or spin-orbit coupling, the samples of Sr_2IrO_4 chemically doped with K, La and Rh elements have been successfully synthesized recently, and some are reported to demonstrate very remarkable physical properties [251, 258]. However, some other theoretically predicted cooperative phenomena such as anisotropic superconductivity in Sr_2IrO_4 compound (or its derivatives) [245] yet remains to be found. Another option of high interest for the theorists working in this area is a Ba-doped Sr_2IrO_4 , which is anticipated to reduce dimensionality of this compound even further and remove rotational distortion between the octahedra, but the synthesis of the good samples so far has been unsuccessful. Although recent report about a successful synthesis of Ba_2IrO_4 under high pressure of ≈ 6 GPa [29, 30] should help the studies to advance. In our preliminary studies, the introduction of dilute oxygen vacancies into the structure of some other members of R-P series (like double layer iridate and hexagonal perovskite) are also found to result in drastic changes of their physical properties, which outlines some prospects for our future research in this area.

Besides the R-P series the list of iridium-based transition metal oxides, studied by our and other research groups, include the representatives from such structural families as pyrochlores, kagome-type lattices, honeycomb-type structures and double perovskites (see table 6.1). Very few of these materials exhibit simple metallic

ground states, instead demonstrating a great variety of interesting physical properties, many of which are considered to be the result of vigorous competitions between the spin-orbit coupling, Coulomb repulsion and other types of interaction. The properties reported so far include charge-density waves coexisting with ferromagnetic order, negative differential resistivity, lattice-driven magnetoresistance, giant magnetoelectric effect, quantum critical points, geometrically frustrated magnetism, possible topological insulator states and strong magnetic instabilities. The more exotic anticipated examples are a topological Mott insulator [259, 260], a Weyl semimetal [261] and a possible realization of the long-sought Kitaev model [82, 262]. Thus, the quest is far from complete and many more systems remain to be unveiled and studied. In overall, the area of $5d$ transition metal oxides, and iridium-based compounds in particular, still remains largely unexplored and promises a great deal of exciting discoveries.

Copyright© Oleksandr Korneta, 2012.

Bibliography

- [1] C. N. R. Rao and B. Raveau, *Transition Metal Oxides: Structure, Properties, and Synthesis of Ceramic Oxides*. John Wiley & Sons, 2nd ed., 1998.
- [2] T. H. Geballe and J. K. Hulm, "Superconductivity – the state that came in from the cold," *Science*, vol. 239, no. 4838, pp. 367–375, 1988.
- [3] E. Dagotto, T. Hotta, and A. Moreo, "Colossal magnetoresistant materials: the key role of phase separation," *Physics Reports*, vol. 344, no. 1-3, pp. 1 – 153, 2001.
- [4] S. G. Ovchinnikov, "Exotic superconductivity and magnetism in ruthenates," *Physics-Uspekhi*, vol. 46, no. 1, p. 21, 2003.
- [5] B. Raveau, "Transition metal oxides: Promising functional materials," *J. Eur. Ceram. Soc.*, vol. 25, no. 12, pp. 1965 – 1969, 2005.
- [6] S. Ramanathan, *Thin Film Metal-Oxides: Fundamentals and Applications in Electronics and Energy*. Springer, 2009.
- [7] S. N. Ruddlesden and P. Popper, "New compounds of the K_2NiF_4 type," *Acta Crystallographica*, vol. 10, pp. 538–539, Aug 1957.
- [8] S. N. Ruddlesden and P. Popper, "The compound $Sr_3Ti_2O_7$ and its structure," *Acta Crystallographica*, vol. 11, pp. 54–55, Jan 1958.
- [9] K. Momma and F. Izumi, "VESTA 3 for three-dimensional visualization of crystal, volumetric and morphology data," *J. Appl. Crystallogr.*, vol. 44, pp. 1272–1276, Dec 2011.
- [10] M. Vračar, A. Kuzmin, R. Merkle, J. Purans, E. A. Kotomin, J. Maier, and O. Mathon, "Jahn-teller distortion around Fe^{4+} in $Sr(Fe_xTi_{1-x})O_{3-\delta}$ from x-ray absorption spectroscopy, x-ray diffraction, and vibrational spectroscopy," *Phys. Rev. B*, vol. 76, p. 174107, Nov 2007.
- [11] V. M. Goldschmidt, "Die gesetze der krystallochemie," *Naturwissenschaften*, vol. 14, pp. 477–485, 1926.
- [12] B. Dabrowski, O. Chmaissem, J. Mais, S. Kolesnik, J. Jorgensen, and S. Short, "Tolerance factor rules for $Sr_{1-x-y}Ca_xBa_yMnO_3$ perovskites," *J. Solid State Chem.*, vol. 170, no. 1, pp. 154 – 164, 2003.
- [13] Y. Takeda, F. Kanamura, M. Shimada, and M. Koizumi, "The crystal structure of $banio_3$," *Acta Cryst. B*, vol. 32, pp. 2464–2466, Aug 1976.
- [14] J. J. Adkin and M. A. Hayward, " $BaMnO_{3-x}$ revisited: A structural and magnetic study," *ChemInform*, vol. 38, no. 19, pp. 755 – 762, 2007.

- [15] B. Chamberland, "A study on the BaIrO_3 system," *Journal of the Less Common Metals*, vol. 171, no. 2, pp. 377 – 394, 1991.
- [16] J.-G. Cheng, J. A. Alonso, E. Suard, J.-S. Zhou, and J. B. Goodenough, "A new perovskite polytype in the high-pressure sequence of BaIrO_3 ," *J. Am. Chem. Soc.*, vol. 131, no. 21, pp. 7461–7469, 2009.
- [17] B.-H. Chen, "Introduction of a tolerance factor for the $\text{Nd}_2\text{CuO}_4(1t')$ -type structure," *J. Solid State Chem.*, vol. 125, no. 1, pp. 63 – 66, 1996.
- [18] I. Sharma and D. Singh, "Solid state chemistry of Ruddlesden-Popper type complex oxides," *Bull. Mater. Sci.*, vol. 21, pp. 363–374, 1998.
- [19] B. Beznosikov and K. Aleksandrov, "Perovskite-like crystals of the Ruddlesden-Popper series," *Crystallogr. Rep.*, vol. 45, pp. 792–798, 2000.
- [20] C. Lang and H. Müller-Buschbaum, "Über ein neues oxoiridat(IV): $\text{Ba}_7\text{Ir}_6\text{O}_{19}$," *Monatshefte für Chemie*, vol. 120, pp. 705–710, 1989. 10.1007/BF00809961.
- [21] Y. Moritomo, A. Asamitsu, H. Kuwahara, and Y. Tokura, "Giant magnetoresistance of manganese oxides with a layered perovskite structure," *Nature*, vol. 380, pp. 141–144, Mar. 1996.
- [22] G. Cao, O. Korneta, S. Chikara, L. DeLong, and P. Schlottmann, "Non-fermi-liquid behavior in single-crystal CaRuO_3 : Comparison to ferromagnetic SrRuO_3 ," *Solid State Commun.*, vol. 148, no. 7-8, pp. 305 – 309, 2008.
- [23] S. Chikara, O. Korneta, W. P. Crummett, L. E. DeLong, P. Schlottmann, and G. Cao, "Giant magnetoelectric effect in the $J_{\text{eff}} = \frac{1}{2}$ Mott insulator Sr_2IrO_4 ," *Phys. Rev. B*, vol. 80, p. 140407, Oct 2009.
- [24] G. Cao, Y. Xin, C. S. Alexander, J. E. Crow, P. Schlottmann, M. K. Crawford, R. L. Harlow, and W. Marshall, "Anomalous magnetic and transport behavior in the magnetic insulator $\text{Sr}_3\text{Ir}_2\text{O}_7$," *Phys. Rev. B*, vol. 66, p. 214412, Dec 2002.
- [25] J. Kafalas and J. Longo, "High pressure synthesis of $(\text{ABX}_3)(\text{AX})_n$ compounds," *J. Solid State Chem.*, vol. 4, no. 1, pp. 55 – 59, 1972.
- [26] G. Cao, V. Durairaj, S. Chikara, L. E. DeLong, S. Parkin, and P. Schlottmann, "Non-fermi-liquid behavior in nearly ferromagnetic SrIrO_3 single crystals," *Phys. Rev. B*, vol. 76, p. 100402, Sep 2007.
- [27] T. Siegrist and B. Chamberland, "The crystal structure of BaIrO_3 ," *Journal of the Less Common Metals*, vol. 170, no. 1, pp. 93 – 99, 1991.
- [28] R. Lindsay, W. Strange, B. Chamberland, and R. M. Jr., "Weak ferromagnetism in BaIrO_3 ," *Solid State Commun.*, vol. 86, no. 11, pp. 759 – 763, 1993.

- [29] H. Okabe, M. Isobe, E. Takayama-Muromachi, A. Koda, S. Takeshita, M. Hiraishi, M. Miyazaki, R. Kadono, Y. Miyake, and J. Akimitsu, “Ba₂IrO₄: A spin-orbit Mott insulating quasi-two-dimensional antiferromagnet,” *Phys. Rev. B*, vol. 83, p. 155118, Apr 2011.
- [30] H. Okabe, N. Takeshita, M. Isobe, E. Takayama-Muromachi, T. Muranaka, and J. Akimitsu, “Pressure-induced metal-insulator transition in the spin-orbit Mott insulator Ba₂IrO₄,” *Phys. Rev. B*, vol. 84, p. 115127, Sep 2011.
- [31] M. Imada, A. Fujimori, and Y. Tokura, “Metal-insulator transitions,” *Rev. Mod. Phys.*, vol. 70, pp. 1039–1263, Oct 1998.
- [32] Y. S. Lee, J. S. Lee, T. W. Noh, D. Y. Byun, K. S. Yoo, K. Yamaura, and E. Takayama-Muromachi, “Systematic trends in the electronic structure parameters of the 4d transition-metal oxides SrMO₃ ($M = \text{Zr, Mo, Ru, and Rh}$),” *Phys. Rev. B*, vol. 67, p. 113101, Mar 2003.
- [33] B. J. Kim, H. Jin, S. J. Moon, J.-Y. Kim, B.-G. Park, C. S. Leem, J. Yu, T. W. Noh, C. Kim, S.-J. Oh, J.-H. Park, V. Durairaj, G. Cao, and E. Rotenberg, “Novel $J_{\text{eff}} = 1/2$ Mott state induced by relativistic spin-orbit coupling in Sr₂IrO₄,” *Phys. Rev. Lett.*, vol. 101, p. 076402, Aug 2008.
- [34] B. J. Kim, H. Ohsumi, T. Komesu, S. Sakai, T. Morita, H. Takagi, and T. Arima, “Phase-sensitive observation of a spin-orbital Mott state in Sr₂IrO₄,” *Science*, vol. 323, p. 1329, Mar. 2009.
- [35] S. J. Moon, H. Jin, W. S. Choi, J. S. Lee, S. S. A. Seo, J. Yu, G. Cao, T. W. Noh, and Y. S. Lee, “Temperature dependence of the electronic structure of the $J_{\text{eff}} = \frac{1}{2}$ Mott insulator Sr₂IrO₄ studied by optical spectroscopy,” *Phys. Rev. B*, vol. 80, p. 195110, Nov 2009.
- [36] J. D. Jorgensen, B. Dabrowski, S. Pei, D. G. Hinks, L. Soderholm, B. Morosin, J. E. Schirber, E. L. Venturini, and D. S. Ginley, “Superconducting phase of La₂CuO_{4- δ} : A superconducting composition resulting from phase separation,” *Phys. Rev. B*, vol. 38, pp. 11337–11345, Dec 1988.
- [37] K. Maiti, R. S. Singh, V. R. R. Medicherla, S. Rayaprol, and E. V. Sampathkumaran, “Origin of charge density wave formation in insulators from a high resolution photoemission study of BaIrO₃,” *Phys. Rev. Lett.*, vol. 95, p. 016404, Jun 2005.
- [38] M. L. Brooks, S. J. Blundell, T. Lancaster, W. Hayes, F. L. Pratt, P. P. C. Frampton, and P. D. Battle, “Unconventional magnetic properties of the weakly ferromagnetic metal BaIO₃,” *Phys. Rev. B*, vol. 71, p. 220411, Jun 2005.
- [39] M.-H. Whangbo and H.-J. Koo, “Structural and electronic features of BaIrO₃ causing the simultaneous occurrence of weak ferromagnetism and charge density wave formation,” *Solid State Commun.*, vol. 118, no. 10, pp. 491 – 495, 2001.

- [40] G. Cao, X. N. Lin, S. Chikara, V. Durairaj, and E. Elhami, “High-temperature weak ferromagnetism on the verge of a metallic state: Impact of dilute Sr doping on BaIrO_3 ,” *Phys. Rev. B*, vol. 69, p. 174418, May 2004.
- [41] L. Lévy, *Magnetism and superconductivity*. Texts and monographs in physics, Springer, 2000.
- [42] S. Blundell, *Magnetism in Condensed Matter*, vol. 4 of *Oxford master series in condensed matter physics*. Oxford University Press, Dec. 2001.
- [43] C. M. Hurd, “Varieties of magnetic order in solids,” *Contemporary Physics*, vol. 23, no. 5, pp. 469–493, 1982.
- [44] J. B. Goodenough, *Magnetism and the chemical bond*, vol. 1 of *Interscience monographs on chemistry: Inorganic chemistry section*. Interscience Publishers, 1963.
- [45] B. Halperin and R. Engelman, “Cooperative dynamic Jahn-Teller Effect. II. crystal distortion in perovskites,” *Phys. Rev. B*, vol. 3, pp. 1698–1708, Mar 1971.
- [46] D. Griffiths, *Introduction to quantum mechanics*. Prentice Hall, 1995.
- [47] Y. Tokura and N. Nagaosa, “Orbital physics in transition-metal oxides,” *Science*, vol. 288, no. 5465, pp. 462–468, 2000.
- [48] F. Mancini, ed., *Lectures on the physics of highly correlated electron systems IV: Fourth Training Course in the Physics of Correlated Electron Systems and High- T_C Superconductors: Salerno, Italy, 11-22 October 1999*. No. v. 1999 in AIP conference proceedings, American Institute of Physics, 2000.
- [49] G. Kalvius, D. Noakes, and O. Hartmann, “Chapter 206 μSR studies of rare-earth and actinide magnetic materials,” in *Handbook on the Physics and Chemistry of Rare Earths* (L. E. Karl A. Gschneidner, Jr. and G. H. Lander, eds.), vol. 32 of *Handbook on the Physics and Chemistry of Rare Earths*, pp. 55 – 451, Elsevier, 2001.
- [50] G. Cao, X. N. Lin, L. Balicas, S. Chikara, J. E. Crow, and P. Schlottmann, “Orbitally driven behaviour: Mott transition, quantum oscillations and colossal magnetoresistance in bilayered $\text{Ca}_3\text{Ru}_2\text{O}_7$,” *New Journal of Physics*, vol. 6, no. 1, p. 159, 2004.
- [51] V. Durairaj, *A systematic study of thermodynamic and transport properties of layered $\text{Ca}_{n+1}(\text{Ru}_{1-x}\text{Cr}_x)_n\text{O}_{3n+1}$* . PhD thesis, University of Kentucky, Lexington, KY, 2008.
- [52] Z. Fang, K. Terakura, and N. Nagaosa, “Orbital physics in ruthenates: first-principles studies,” *New Journal of Physics*, vol. 7, no. 1, p. 66, 2005.
- [53] J. Kanamori, “Superexchange interaction and symmetry properties of electron orbitals,” *J. Phys. Chem. Solids*, vol. 10, pp. 87–98, July 1959.

- [54] R. Stuart and W. Marshall, “Direct exchange in ferromagnets,” *Phys. Rev.*, vol. 120, pp. 353–357, Oct 1960.
- [55] K. W. Bae, M. A. Mohamed, D. W. Jung, and N. Otsuka, “Direct exchange interaction of localized spins associated with unpaired sp electrons in be-doped low-temperature-grown GaAs layers,” *J. Appl. Phys.*, vol. 109, no. 7, p. 073918, 2011.
- [56] H. Kramers, “L’interaction entre les atomes magnétogènes dans un cristal paramagnétique,” *Physica*, vol. 1, pp. 182 – 192, 1934.
- [57] J. B. Goodenough and A. L. Loeb, “Theory of ionic ordering, crystal distortion, and magnetic exchange due to covalent forces in spinels,” *Phys. Rev.*, vol. 98, pp. 391–408, Apr. 1955.
- [58] T. N. Casselman and F. Keffer, “Right-angled superexchange,” *Phys. Rev. Lett.*, vol. 4, pp. 498–500, May 1960.
- [59] J. B. Goodenough, “Theory of the role of covalence in the perovskite-type manganites [LaM(II)]MnO₃,” *Phys. Rev.*, vol. 100, pp. 564–573, Oct 1955.
- [60] C. Zener, “Interaction between the *d*-shells in the transition metals II. Ferromagnetic compounds of manganese with perovskite structure,” *Phys. Rev.*, vol. 82, pp. 403–405, May 1951.
- [61] C. N. R. Rao and A. K. Cheetham, “Materials science: Charge ordering in manganates,” *Science*, vol. 276, no. 5314, pp. 911–912, 1997.
- [62] P. A. Cox, *Transition Metal Oxides: An Introduction to their Electronic Structure and Properties*. International Series of Monographs on Chemistry, Oxford University Press, reprint ed., June 1995.
- [63] M. A. Ruderman and C. Kittel, “Indirect exchange coupling of nuclear magnetic moments by conduction electrons,” *Phys. Rev.*, vol. 96, p. 99, Oct. 1954.
- [64] T. Kasuya, “A theory of metallic ferro- and antiferromagnetism on Zener’s model,” *Progress of Theoretical Physics*, vol. 16, pp. 45–57, 1956.
- [65] K. Yosida, “Magnetic properties of Cu-Mn alloys,” *Phys. Rev.*, vol. 106, pp. 893–898, June 1957.
- [66] D. N. Aristov, “Indirect RKKY interaction in any dimensionality,” *Phys. Rev. B*, vol. 55, pp. 8064–8066, Apr. 1997.
- [67] T. Dietl and H. Ohno, “Ferromagnetic III–V and II–VI semiconductors,” *MRS Bulletin*, vol. 28, pp. 714–719, Oct. 2003.
- [68] Y. Zhao, T. Shishidou, and A. J. Freeman, “Ruderman-Kittel-Kasuya-Yosida-like ferromagnetism in Mn_xGe_{1-x},” *Phys. Rev. Lett.*, vol. 90, no. 4, p. 047204, 2003.

- [69] R. Skomski, J. Zhou, J. Zhang, and D. J. Sellmyer, "Indirect exchange in dilute magnetic semiconductors," *J. Appl. Phys.*, vol. 99, no. 8, p. 08D504, 2006.
- [70] U. Hardebusch, W. Gerhardt, and J. S. Schilling, "Effect of hydrostatic pressure on the magnetic susceptibility of a Ag:Mn spin-glass," *Phys. Rev. Lett.*, vol. 44, pp. 352–355, Feb. 1980.
- [71] U. Larsen, "Characteristic temperatures in the spin-glass AuFe," *Phys. Rev. B*, vol. 18, pp. 5014–5032, Nov. 1978.
- [72] J. Schilling, "Pressure as a parameter in the study of dilute magnetic alloys," *Advances in Physics*, vol. 281, pp. 657–715, Sept. 1979.
- [73] Jose Jesus Rodríguez-Nuñez, H. Beck, J. Konior, A. M. Oleś, and B. Coqblin, "Effective RKKY interaction in high- T_c cuprates," *Phys. Lett. A*, vol. 197, no. 2, pp. 173 – 178, 1995.
- [74] I. Dzyaloshinsky, "A thermodynamic theory of "weak" ferromagnetism of anti-ferromagnetics," *J. Phys. Chem. Solids*, vol. 4, no. 4, pp. 241 – 255, 1958.
- [75] T. Moriya, "New mechanism of anisotropic superexchange interaction," *Phys. Rev. Lett.*, vol. 4, pp. 228–230, Mar 1960.
- [76] T. Moriya, "Anisotropic superexchange interaction and weak ferromagnetism," *Phys. Rev.*, vol. 120, pp. 91–98, Oct 1960.
- [77] P. M. Levy and A. Fert, "Origin of magnetic anisotropy in transition metal spin-glass alloys," *J. Appl. Phys.*, vol. 52, no. 3, pp. 1718–1719, 1981.
- [78] F. Keffer, "Moriya interaction and the problem of the spin arrangements in β -MnS," *Phys. Rev.*, vol. 126, pp. 896–900, May 1962.
- [79] T. Thio, T. R. Thurston, N. W. Preyer, P. J. Picone, M. A. Kastner, H. P. Jenssen, D. R. Gabbe, C. Y. Chen, R. J. Birgeneau, and A. Aharony, "Antisymmetric exchange and its influence on the magnetic structure and conductivity of La_2CuO_4 ," *Phys. Rev. B*, vol. 38, pp. 905–908, Jul 1988.
- [80] S.-W. Cheong, J. D. Thompson, and Z. Fisk, "Metamagnetism in La_2CuO_4 ," *Phys. Rev. B*, vol. 39, pp. 4395–4398, Mar 1989.
- [81] S. Cheong and M. Mostovoy, "Multiferroics: a magnetic twist for ferroelectricity," *Nat. Mater.*, vol. 6, pp. 13–20, Jan. 2007.
- [82] G. Jackeli and G. Khaliullin, "Mott insulators in the strong spin-orbit coupling limit: From Heisenberg to a Quantum Compass and Kitaev models," *Phys. Rev. Lett.*, vol. 102, p. 017205, Jan 2009.
- [83] J. Singleton, *Band theory and electronic properties of solids*, vol. 2 of *Oxford master series in condensed matter physics*. Oxford University Press, 2001.

- [84] C. Kittel, *Introduction to solid state physics*. Wiley, 7th ed., 1996.
- [85] R. H. Fowler and P. Kapitza, “Magnetostriction and the phenomena of the curie point,” *Proceedings of the Royal Society of London. Series A*, vol. 124, no. 793, pp. 1–15, 1929.
- [86] J. B. Goodenough, “Localized versus collective d electrons and Néel temperatures in perovskite and perovskite-related structures,” *Phys. Rev.*, vol. 164, pp. 785–789, Dec. 1967.
- [87] J.-S. Zhou and J. B. Goodenough, “Pressure-induced transition from localized electron toward band antiferromagnetism in LaMnO_3 ,” *Phys. Rev. Lett.*, vol. 89, p. 087201, Aug. 2002.
- [88] P. W. Anderson, *Solid State Physics*, vol. 14. New York: Academic Press, 1963.
- [89] P. W. Anderson, “New approach to the theory of superexchange interactions,” *Phys. Rev.*, vol. 115, p. 2, July 1959.
- [90] N. Menyuk, J. A. Kafalas, K. Dwight, and J. B. Goodenough, “Pressure-effect measurements using a vibrating-coil magnetometer,” *J. Appl. Phys.*, vol. 40, pp. 1324–1326, Mar. 1969.
- [91] V. C. Srivastava, “Effect of pressure on the Néel temperature of MnCO_3 , CoCO_3 , and FeCO_3 ,” *J. Appl. Phys.*, vol. 41, no. 3, pp. 1190–1191, 1970.
- [92] D. Bloch, F. Chaisse, and R. Pauthenet, “Effects of hydrostatic pressure on the compensation temperatures of iron garnets,” *J. Appl. Phys.*, vol. 38, pp. 1029–1030, Mar. 1967.
- [93] D. Bloch, “The 10/3 law for the volume dependence of superexchange,” *J. Phys. Chem. Solids*, vol. 27, pp. 881–885, May 1966.
- [94] G. K. White, “Thermal expansion at low temperatures– V. Dilute alloys of manganese in copper,” *J. Phys. Chem. Solids*, vol. 23, no. 1-2, pp. 169–171, 1962.
- [95] G. K. White, “Thermal expansion of magnetic metals at low temperatures,” *Proceedings of the Physical Society*, vol. 86, no. 1, pp. 159–169, 1965.
- [96] N. W. Ashcroft and N. D. Mermin, *Solid State Physics*. Science: Physics, Brooks Cole, 1 ed., January 1976.
- [97] R. H. Carr, R. D. McCammon, and G. K. White, “The thermal expansion of copper at low temperatures,” *Proceedings of the Royal Society of London. Series A, Mathematical and Physical Sciences*, vol. 280, pp. 72–84, July 1964.
- [98] K. C. Johnson and A. J. Sievers, “Hydrostatic-pressure studies of magnetic modes in the far infrared,” *Phys. Rev. B*, vol. 10, pp. 1027–1038, Aug. 1974.

- [99] M. T. Hutchings, R. J. Birgeneau, and W. P. Wolf, “Magnetic interactions between rare-earth ions in insulators. i. accurate electron-paramagnetic-resonance determination of Gd^{3+} pair-interaction constants in LaCl_3 ,” *Phys. Rev.*, vol. 168, pp. 1026–1044, Apr. 1968.
- [100] K. N. Shrivastava and V. Jaccarino, “Variation of superexchange with interatomic distance. i. the t_{2g} system $\text{V}^{++}-\text{F}^--\text{V}^{++}$,” *Phys. Rev. B*, vol. 13, pp. 299–303, Jan. 1976.
- [101] J.-S. Zhou and J. B. Goodenough, “Exchange interactions in the perovskites $\text{Ca}_{1-x}\text{Sr}_x\text{MnO}_3$ and RMnO_3 ($\text{R} = \text{La}, \text{Pr}, \text{Sm}$),” *Phys. Rev. B*, vol. 68, p. 054403, Aug 2003.
- [102] J. J. Neumeier, M. F. Hundley, J. D. Thompson, and R. H. Heffner, “Substantial pressure effects on the electrical resistivity and ferromagnetic transition temperature of $\text{La}_{1-x}\text{Ca}_x\text{MnO}_3$,” *Phys. Rev. B*, vol. 52, pp. R7006–R7009, Sept. 1995.
- [103] H. Y. Hwang, T. T. M. Palstra, S.-W. Cheong, and B. Batlogg, “Pressure effects on the magnetoresistance in doped manganese perovskites,” *Phys. Rev. B*, vol. 52, pp. 15046–15049, Dec 1995.
- [104] Y. Moritomo, A. Asamitsu, and Y. Tokura, “Pressure effect on the double-exchange ferromagnet $\text{La}_{1-x}\text{Sr}_x\text{MnO}_3$ ($0.15 \leq x \leq 0.5$),” *Phys. Rev. B*, vol. 51, pp. 16491–16494, June 1995.
- [105] P. W. Anderson and H. Hasegawa, “Considerations on double exchange,” *Phys. Rev.*, vol. 100, pp. 675–681, Oct. 1955.
- [106] V. Laukhin, J. Fontcuberta, J. L. García-Muñoz, and X. Obradors, “Pressure effects on the metal-insulator transition in magnetoresistive manganese perovskites,” *Phys. Rev. B*, vol. 56, pp. R10009–R10012, Oct. 1997.
- [107] J. L. García-Muñoz, J. Fontcuberta, M. Suaaidi, and X. Obradors, “Bandwidth narrowing in bulk $\text{L}_{2/3}\text{A}_{1/3}\text{MnO}_3$ magnetoresistive oxides,” *J. Phys.: Condens. Matter*, vol. 8, pp. L787–L793, Dec. 1996.
- [108] A. Mang, K. Reimann, and S. Rübenacke, “Band gaps, crystal-field splitting, spin-orbit coupling, and exciton binding energies in ZnO under hydrostatic pressure,” *Solid State Commun.*, vol. 94, no. 4, pp. 251 – 254, 1995.
- [109] D. M. Wilson and S. Broersma, “Magnetization of FeBO_3 under pressure near the critical temperature,” *Phys. Rev. B*, vol. 14, pp. 1977–1982, Sep 1976.
- [110] V. Sarkisyan, I. Troyan, I. Lyubutin, A. Gavriluk, and A. Kashuba, “Magnetic collapse and the change of electronic structure of FeBO_3 antiferromagnet under high pressure,” *JETP Letters*, vol. 76, pp. 664–669, 2002. 10.1134/1.1545580.

- [111] L. Patrick, “The change of ferromagnetic curie points with hydrostatic pressure,” *Phys. Rev.*, vol. 93, pp. 384–392, Feb 1954.
- [112] J. B. MacChesney, H. J. Williams, J. F. Potter, and R. C. Sherwood, “Magnetic study of the manganate phases: CaMnO_3 , $\text{Ca}_4\text{Mn}_3\text{O}_{10}$, $\text{Ca}_3\text{Mn}_2\text{O}_7$, Ca_2MnO_4 ,” *Phys. Rev.*, vol. 164, pp. 779–785, Dec 1967.
- [113] J. Neumeier, A. Cornelius, and K. Andres, “Thermodynamic investigation of the magnetic phase transitions of CaMnO_3 and SrRuO_3 ,” *Phys. Rev. B*, vol. 64, p. 172406, Oct 2001.
- [114] D. Bloch and R. Pauthenet, “Magnetic properties under pressure of some transition metal alloys,” *J. Appl. Phys.*, vol. 36, no. 3, pp. 1229–1231, 1965.
- [115] V. Heine, “ $s-d$ interaction in transition metals,” *Phys. Rev.*, vol. 153, pp. 673–682, Jan 1967.
- [116] N. D. Lang and H. Ehrenreich, “Itinerant-electron theory of pressure effects on ferromagnetic transition temperatures: Ni and ni-cu alloys,” *Phys. Rev.*, vol. 168, pp. 605–622, Apr 1968.
- [117] E. P. Wohlfarth, “Forced magnetostriction in the band model of magnetism,” *Journal of Physics C: Solid State Physics*, vol. 2, no. 1, p. 68, 1969.
- [118] L. R. Edwards and L. C. Bartel, “Effect of pressure on the ferromagnetic transition of $\text{MnAs}_{1-x}\text{Sb}_x$ solid solutions,” *Phys. Rev. B*, vol. 5, pp. 1064–1072, Feb 1972.
- [119] H. Hasegawa, “A theory of magneto-volume effects of itinerant-electron magnets. ii. pressure dependence of the critical temperature,” *J. Phys. Soc. Jpn.*, vol. 51, no. 3, pp. 767–775, 1982.
- [120] N. F. Mott, “The basis of the electron theory of metals, with special reference to the transition metals,” *Proceedings of the Physical Society. Section A*, vol. 62, no. 7, p. 416, 1949.
- [121] K. M. Shen and J. S. Davis, “Cuprate high- T_C superconductors,” *Materials Today*, vol. 11, no. 9, pp. 14 – 21, 2008.
- [122] G. Baskaran, “Impurity band Mott insulators: a new route to high T_C superconductivity,” *Science and Technology of Advanced Materials*, vol. 9, no. 4, p. 044104, 2008.
- [123] G. Kotliar and D. Vollhardt, “Strongly correlated materials: Insights from dynamical mean-field theory,” *Physics Today*, vol. 57, no. 3, pp. 53 – 59, 2004.
- [124] P. W. Anderson, “Absence of diffusion in certain random lattices,” *Phys. Rev.*, vol. 109, pp. 1492–1505, Mar 1958.

- [125] N. F. Mott, *Festkörperprobleme 9*, vol. 9 of *Advances in Solid State Physics*, ch. Charge transport in non-crystalline semiconductors, pp. 22–45. Springer, 1969.
- [126] J. C. Slater, “Magnetic effects and the hartree-fock equation,” *Phys. Rev.*, vol. 82, pp. 538–541, May 1951.
- [127] F. Gebhard, *The Mott metal-insulator transition: models and methods*, vol. 137 of *Springer Tracts in Modern Physics*. Springer, illustrated ed., 1997.
- [128] A. W. Overhauser, “Giant spin density waves,” *Phys. Rev. Lett.*, vol. 4, pp. 462–465, May 1960.
- [129] A. W. Overhauser, “Exchange and correlation instabilities of simple metals,” *Phys. Rev.*, vol. 167, pp. 691–698, Mar 1968.
- [130] G. Grüner, *Density waves in solids*. Frontiers in Physics, Westview Press, revised, reprint ed., 2000.
- [131] C. Schlenker, J. Dumas, M. Greenblatt, and S. van Smaalen, eds., *Physics and Chemistry of Low-Dimensional Inorganic Conductors*. NATO ASI series: Physics, Plenum Press, 1996.
- [132] G. Grüner, “The dynamics of charge-density waves,” *Rev. Mod. Phys.*, vol. 60, pp. 1129–1181, Oct 1988.
- [133] J. Hubbard, “Electron correlations in narrow energy bands,” *Proceedings of the Royal Society of London. Series A. Mathematical and Physical Sciences*, vol. 276, no. 1365, pp. 238–257, 1963.
- [134] A. Sutton, *Electronic Structure of Materials*. Oxford Science Publications, Clarendon Press, illustrated, reprint ed., 1993.
- [135] S. J. Moon, H. Jin, K. W. Kim, W. S. Choi, Y. S. Lee, J. Yu, G. Cao, A. Sumi, H. Funakubo, C. Bernhard, and T. W. Noh, “Dimensionality-controlled insulator-metal transition and correlated metallic state in 5d transition metal oxides $\text{Sr}_{n+1}\text{Ir}_n\text{O}_{3n+1}$ ($n=1, 2$, and ∞),” *Phys. Rev. Lett.*, vol. 101, p. 226402, Nov. 2008.
- [136] A. Shitade, H. Katsura, J. Kuneš, X.-L. Qi, S.-C. Zhang, and N. Nagaosa, “Quantum spin hall effect in a transition metal oxide Na_2IrO_3 ,” *Phys. Rev. Lett.*, vol. 102, p. 256403, Jun 2009.
- [137] F. Ye, S. Chi, H. Cao, B. C. Chakoumakos, J. A. Fernandez-Baca, R. Custelcean, T. F. Qi, O. B. Korneta, and G. Cao, “Direct evidence of a zigzag spin-chain structure in the honeycomb lattice: A neutron and x-ray diffraction investigation of single-crystal Na_2IrO_3 ,” *Phys. Rev. B*, vol. 85, p. 180403, May 2012.

- [138] P. P. Edwards and M. J. Sienko, "Phase separation in metal solutions and expanded fluid metals," *J. Am. Chem. Soc.*, vol. 103, no. 11, pp. 2967–2971, 1981.
- [139] P. P. Edwards and M. J. Sienko, "The transition to the metallic state," *Acc. Chem. Res.*, vol. 15, no. 3, pp. 87–93, 1982.
- [140] S. Minomura and H. Drickamer, "Pressure induced phase transitions in silicon, germanium and some III-V compounds," *J. Phys. Chem. Solids*, vol. 23, no. 5, pp. 451 – 456, 1962.
- [141] H. Olijnyk and W. B. Holzapfel, "Phase transitions in Si, Ge and Sn under pressure," *J. Phys. Colloques*, vol. 45, no. C8, pp. 153–156, 1984.
- [142] D. B. McWhan, T. M. Rice, and P. H. Schmidt, "Metal-semiconductor transition in ytterbium and strontium at high pressure," *Phys. Rev.*, vol. 177, pp. 1063–1071, Jan 1969.
- [143] E. G. Maksimov, M. V. Magnitskaya, and V. E. Fortov, "Non-simple behavior of simple metals at high pressure," *Uspekhi Fizicheskikh Nauk*, vol. 175, no. 8, pp. 793–813, 2005.
- [144] H. Okamura, K. Senoo, M. Matsunami, and T. Nanba, "Pressure-tuning of the c - f hybridization in Yb metal detected by infrared spectroscopy up to 18 GPa," *J. Phys. Soc. Jpn.*, vol. 76SA, no. Supplement A, pp. 9–10, 2007.
- [145] T. Matsuoka and K. Shimizu, "Direct observation of a pressure-induced metal-to-semiconductor transition in lithium," *Nature*, vol. 458, pp. 186–189, Mar. 2009.
- [146] D. B. McWhan, A. Menth, J. P. Remeika, W. F. Brinkman, and T. M. Rice, "Metal-insulator transitions in pure and doped V_2O_3 ," *Phys. Rev. B*, vol. 7, pp. 1920–1931, Mar 1973.
- [147] M. S. Laad, L. Craco, and E. Müller-Hartmann, "Orbital-selective insulator-metal transition in V_2O_3 under external pressure," *Phys. Rev. B*, vol. 73, p. 045109, Jan 2006.
- [148] E. Knittle and R. Jeanloz, "High-pressure electrical resistivity measurements of Fe_2O_3 : Comparison of static-compression and shock-wave experiments to 61 gpa," *Solid State Commun.*, vol. 58, no. 2, pp. 129 – 131, 1986.
- [149] M. P. Pasternak, G. K. Rozenberg, G. Y. Machavariani, O. Naaman, R. D. Taylor, and R. Jeanloz, "Breakdown of the Mott-Hubbard state in Fe_2O_3 : A first-order insulator-metal transition with collapse of magnetism at 50 GPa," *Phys. Rev. Lett.*, vol. 82, pp. 4663–4666, Jun 1999.
- [150] I. S. Lyubutin and A. G. Gavriluk, "Sovremennye dostizheniya v issledovanii fazovykh prevrashchenii v oksidakh 3d-metallov pri vysokikh i sverkhvysokikh davleniyakh," *Uspekhi Fizicheskikh Nauk*, vol. 179, no. 10, pp. 1047–1078, 2009.

- [151] F. Nakamura, T. Goko, M. Ito, T. Fujita, S. Nakatsuji, H. Fukazawa, Y. Maeno, P. Alireza, D. Forsythe, and S. R. Julian, “From Mott insulator to ferromagnetic metal: A pressure study of Ca_2RuO_4 ,” *Phys. Rev. B*, vol. 65, p. 220402, May 2002.
- [152] C. S. Snow, S. L. Cooper, G. Cao, J. E. Crow, H. Fukazawa, S. Nakatsuji, and Y. Maeno, “Pressure-tuned collapse of the Mott-like state in $\text{Ca}_{n+1}\text{Ru}_n\text{O}_{3n+1}$ ($n=1, 2$): Raman spectroscopic studies,” *Phys. Rev. Lett.*, vol. 89, p. 226401, Nov 2002.
- [153] D. Haskel, G. Fabbris, M. Zhernenkov, P. P. Kong, C. Q. Jin, G. Cao, and M. van Veenendaal, “Pressure tuning of the spin-orbit coupled ground state in Sr_2IrO_4 ,” *Phys. Rev. Lett.*, vol. 109, p. 027204, Jul 2012.
- [154] B. Pamplin, *Crystal growth*, vol. 16 of *International series on the science of the solid state*. Pergamon Press, 2nd ed., 1980.
- [155] T. Massalski and H. Okamoto, *Binary alloy phase diagrams*. ASM International, 2nd ed., 1990.
- [156] H. Okamoto, *Desk handbook: phase diagrams for binary alloys*. ASM International, 2000.
- [157] H. Dabkowska and A. Dabkowski, “Crystal growth of oxides by optical floating zone technique,” in *Springer Handbook of Crystal Growth* (G. Dhanaraj, K. Byrappa, V. Prasad, and M. Dudley, eds.), pp. 367–391, Springer Berlin Heidelberg, 2010.
- [158] G. Cao, J. Crow, R. Guertin, P. Henning, C. Homes, M. Strongin, D. Basov, and E. Lochner, “Charge density wave formation accompanying ferromagnetic ordering in quasi-one-dimensional BaIrO_3 ,” *Solid State Commun.*, vol. 113, no. 11, pp. 657 – 662, 2000.
- [159] B. Raveau, *Crystal chemistry of high T_C superconducting copper oxides*, vol. 15 of *Springer series in materials science*. Springer-Verlag, 1991.
- [160] A. Colombo, “Systematic errors in vacuum and inert gas fusion analysis for oxygen in metals,” *Anal. Chim. Acta*, vol. 81, no. 2, pp. 397 – 402, 1976.
- [161] R. Dinnebier and S. Billinge, *Powder Diffraction: Theory and Practice*. Royal Society of Chemistry, 2008.
- [162] C. Hammond, *The basics of crystallography and diffraction*. IUCr texts on crystallography, Oxford University Press, 3 ed., June 2009.
- [163] D. Brandon and W. Kaplan, *Microstructural Characterization of Materials*. Quantitative software engineering series, John Wiley & Sons, 2008.
- [164] Scintag Inc. USA, Cupertino, CA 95014, *Scintag X1. Technical Manual*, 1999.

- [165] H. Czichos, T. Saito, and L. Smith, eds., *Springer Handbook of Materials Measurement Methods*. No. v. 978, nos. 3-20786 in Springer Handbook of Materials Measurement Methods, Springer, 1st ed., 2006.
- [166] D. Smith and R. Jenkins, "The powder diffraction file: Past, present, and future," *J. Res. Natl. Inst. Stand. Technol.*, vol. 101, pp. 259–271, May 1996.
- [167] S. Parkin and H. Hope, "Macromolecular cryocrystallography: Cooling, mounting, storage and transportation of crystals," *J. Appl. Crystallogr.*, vol. 31, pp. 945–953, Dec 1998.
- [168] Hampton Research, Aliso Viejo, CA 92656-3317 U.S.A., *Paratone-N User Guide/Certificate of Analysis*, 2008.
- [169] G. M. Sheldrick, "A short history of SHELX," *Acta Cryst. A*, vol. 64, pp. 112–122, Jan 2008.
- [170] G. M. Sheldrick, "SADABS. version 2.03," 1996. University of Göttingen, Germany.
- [171] K. Tsuji, J. Injuk, and R. Grieken, *X-ray spectrometry: recent technological advances*. John Wiley and Sons, 1st ed., 2004.
- [172] J. Goldstein, ed., *Scanning electron microscopy and X-ray microanalysis: a text for biologists, materials scientists, and geologists*. New York: Plenum Press, 2nd ed., 1981.
- [173] E. Gatti and P. Rehak, "Semiconductor drift chamber – an application of a novel charge transport scheme," *Nuclear Instruments and Methods in Physics Research*, vol. 225, no. 3, pp. 608 – 614, 1984.
- [174] E. Lifshin, ed., *X-ray Characterization of Materials*. John Wiley & Sons, 2008.
- [175] R. P. W. Scott, *Thermal Analysis*. Physical Chemistry Resources, Library4science LLC, 2003. <http://physicalchemistryresources.com>.
- [176] C. Duval, *Inorganic thermogravimetric analysis*. Amsterdam: Elsevier Pub. Co., 2 ed., 1963.
- [177] M. Brown and P. Gallagher, *Handbook of Thermal Analysis and Calorimetry: Recent Advances, Techniques and Applications*, vol. 5 of *Handbook of Thermal Analysis and Calorimetry*. Elsevier, 2007.
- [178] J. Goworek and W. Stefaniak, "Application of thermogravimetric analysis to the estimation of the porosity of silica gels," *Colloids and Surfaces*, vol. 60, no. 0, pp. 341 – 349, 1991.
- [179] C. D. Doyle, "Kinetic analysis of thermogravimetric data," *J. Appl. Polym. Sci.*, vol. 5, no. 15, pp. 285–292, 1961.

- [180] C. D. Doyle, “Estimating thermal stability of experimental polymers by empirical thermogravimetric analysis,” *Anal. Chem.*, vol. 33, no. 1, pp. 77–79, 1961.
- [181] K. Marthi, M. Ács, G. Pokol, K. Tomor, and K. Eröss-Kiss, “DSC studies on the polymorphism and pseudopolymorphism of pharmaceutical substances,” *J. Therm. Anal. Calorim.*, vol. 38, pp. 1017–1025, Apr. 1992.
- [182] D. Bom, R. Andrews, D. Jacques, J. Anthony, B. Chen, M. S. Meier, and J. P. Selegue, “Thermogravimetric analysis of the oxidation of multiwalled carbon nanotubes: Evidence for the role of defect sites in carbon nanotube chemistry,” *Nano Lett.*, vol. 2, no. 6, pp. 615–619, 2002.
- [183] “TGA/DSC 1. product brochure,” Mettler-Toledo AG, Analytical, Schwerzenbach, Switzerland, July 2007.
- [184] *Gas controller. Option of the STARe thermal analysis system. Appendix to the operating instructions.* Mettler-Toledo AG, Schwerzenbach, Switzerland, 2007.
- [185] Quantum Design, San Diego, CA, *Magnetic Property Measurement System MPMS XL. Hardware Reference Manual.*, 2000.
- [186] M. Tinkham, *Introduction to Superconductivity.* Krieger Pub Co, 1975.
- [187] F. Bassani, G. L. Liedl, and P. Wyder, eds., *Encyclopedia Dictionary of Condensed Matter Physic*, vol. I. Academic Press, September 2005.
- [188] E. du Trémolet de Lacheisserie, D. Gignoux, and M. Schlenker, eds., *Magnetism: Materials and applications*, vol. II. Springer, 1st ed., October 2004.
- [189] K. H. J. Buschow, ed., *Concise Encyclopedia of Magnetic and Superconducting Materials.* Elsevier Science, 2nd ed., March 2006.
- [190] J. Clarke and A. I. Braginski, eds., *The SQUID Handbook: Applications of SQUIDS and SQUID Systems*, vol. II. Wiley-VCH, 1st ed., August 2006.
- [191] M. McElfresh, “Fundamentals of magnetism and magnetic measurements featuring quantum design’s magnetic property measurement system,” tech. rep., Quantum Design, 1994.
- [192] D. R. Lide, ed., *CRC handbook of chemistry and physics: a ready-reference book of chemical and physical data.* CRC Handbook of Chemistry and Physics, CRC Press, 85th ed., 2004.
- [193] “7031 varnish (phenolic butvar resin).” Material Safety Data Sheet, General Electric Co. Schenectady, NY, 1985.
- [194] “EPO-TEK[®] H20E.” Material Safety Data Sheet, Epoxy Technology Inc., Billerica, MA, September 2010.

- [195] “Dotite XC-12 (carbon containing conductive paste).” Material Safety Data Sheet, Fujikura Kasei Co. Ltd., Tokyo, Japan, 2010.
- [196] “Ceramabond™ 865 (high-temperature ceramic adhesive).” Aremco Products Inc., Valley Cottage, NY. Material Safety Data Sheet, February 2009.
- [197] Linear Research Inc., San Diego, CA, *LR-700 AC Resistance Bridge User’s Manual*, v1.3 ed., 1996.
- [198] Keithley Instruments, Inc., Cleveland, OH, *Model 6220 DC Current Source. Reference Manual*, June 2005.
- [199] Advanced Research Systems, Allentown, PA, *DE202 Technical manual*, 2003.
- [200] Quantum Design, San Diego, CA, *Physical Property Measurement System PPMS. Hardware Reference Manual.*, 3rd ed., 2000.
- [201] J. S. Hwang, K. J. Lin, and C. Tien, “Measurement of heat capacity by fitting the whole temperature response of a heat-pulse calorimeter,” *Rev. Sci. Instrum.*, vol. 68, pp. 94 – 101, June 1997.
- [202] “Apiezon® N, cryogenic high vacuum grease.” Technical Data Sheet, M&I Materials, Manchester, United Kingdom, August 2005.
- [203] “Apiezon® H, high temperature vacuum grease.” Technical Data Sheet, M&I Materials, Manchester, United Kingdom, August 2005.
- [204] P. Limelette, S. Hébert, V. Hardy, R. Frésard, C. Simon, and A. Maignan, “Scaling behavior in thermoelectric misfit cobalt oxides,” *Phys. Rev. Lett.*, vol. 97, p. 046601, Jul 2006.
- [205] M. Hatami, G. E. W. Bauer, Q. Zhang, and P. J. Kelly, “Thermoelectric effects in magnetic nanostructures,” *Phys. Rev. B*, vol. 79, p. 174426, May 2009.
- [206] Y. Klein, S. Hébert, D. Pelloquin, V. Hardy, and A. Maignan, “Magnetoresistance and magnetothermopower in the rhodium misfit oxide $[\text{Bi}_{1.95}\text{Ba}_{1.95}\text{Rh}_{0.1}\text{O}_4][\text{RhO}_2]_{1.8}$,” *Phys. Rev. B*, vol. 73, p. 165121, Apr 2006.
- [207] Lake Shore Cryotronics, Inc., Westerville, Ohio, USA, *Lake Shore Model 331 temperature controller. Users manual.*, 1.9 ed., May 2009.
- [208] W. Holzapfel and N. Isaacs, *High-pressure techniques in chemistry and physics: a practical approach*. Practical approach in chemistry series, Oxford University Press, 1997.
- [209] M. Eremets, V. Struzhkin, and A. Utjuzh, “Miniature high pressure cells for high magnetic field applications,” *Physica B: Condensed Matter*, vol. 211, no. 1-4, pp. 369 – 371, 1995.

- [210] M. Konczykowski, M. Baj, E. Szafarkiewicz, L. Konczewicz, and S. Porowski, "Narrow gap semiconductors as low temperature pressure gages," in *High-Pressure and Low-Temperature Physics* (C. W. Chu and J. Woollam, eds.), (New York), pp. 523–528, Plenum Press, 1978.
- [211] E. M. Ivanova and E. E. Chaputovich, "Application of InSb as a material for pressure measurement transducers," *Measurement Techniques*, vol. 15, pp. 1311–1312, 1972.
- [212] R. Wisniewski and G. Molinar, "Pressure standards and sensors up to 3.0 GPa, actual state and development trends," *Physica B: Condensed Matter*, vol. 265, no. 1-4, pp. 246 – 253, 1999.
- [213] High Pressure Research Center, Polish Academy of Sciences, Warsaw, Poland, *LC10 Liquid pressure cell. Instruction Manual*, October 2000.
- [214] I. R. Walker, "Nonmagnetic piston-cylinder pressure cell for use at 35 kbar and above," *Rev. Sci. Instrum.*, vol. 70, no. 8, pp. 3402–3412, 1999.
- [215] Y. Uwatoko, S. Todo, K. Ueda, A. Uchida, M. Kosaka, N. Mori, and T. Matsumoto, "Material properties of Ni–Cr–Al alloy and design of a 4 GPa class non-magnetic high-pressure cell," *J. Phys.: Condens. Matter*, vol. 14, no. 44, p. 11291, 2002.
- [216] K. Yokogawa, K. Murata, H. Yoshino, and S. Aoyama, "Solidification of high-pressure medium Daphne 7373," *Japanese Journal of Applied Physics*, vol. 46, no. 6A, pp. 3636–3639, 2007.
- [217] P. L. B. Walling and J. R. Ferraro, "New method for measuring electrical conductivities of solids in a diamond anvil cell," *Rev. Sci. Instrum.*, vol. 49, no. 11, pp. 1557–1558, 1978.
- [218] K. Murata, H. Yoshino, H. O. Yadav, Y. Honda, and N. Shirakawa, "Pt resistor thermometry and pressure calibration in a clamped pressure cell with the medium, Daphne 7373," *Rev. Sci. Instrum.*, vol. 68, no. 6, pp. 2490–2493, 1997.
- [219] J. J. Randall and R. Ward, "The preparation of some ternary oxides of the platinum metals," *J. Am. Chem. Soc.*, vol. 81, no. 11, pp. 2629–2631, 1959.
- [220] J. G. Dickson, L. Katz, and R. Ward, "Compounds with the hexagonal barium titanate structure," *J. Am. Chem. Soc.*, vol. 83, no. 14, pp. 3026–3029, 1961.
- [221] P. Donohue, L. Katz, and R. Ward, "The modification of structures of ternary oxides by cation substitution. ii. substitution of various cations for ruthenium in barium ruthenium oxide," *Inorg. Chem.*, vol. 5, no. 3, pp. 339–342, 1966.
- [222] S. O. Leontsev, O. B. Korneta, Y. V. Sushko, S. Chikara, and G. Cao, "High-pressure effects on magnetic and electrical properties of BaIrO₃," in *Workshop on Novel Electronic Materials*, (University of Kentucky, Lexington, Kentucky, USA), April 2005.

- [223] J. Zhao, L. Yang, K. Mydeen, F. Li, R. Yu, and C. Jin, "Effects of pressure on electrical property of BaIrO_3 ," *Solid State Commun.*, vol. 148, no. 9-10, pp. 361 – 364, 2008.
- [224] M. A. Laguna-Marco, D. Haskel, N. Souza-Neto, J. C. Lang, V. V. Krishnamurthy, S. Chikara, G. Cao, and M. van Veenendaal, "Orbital magnetism and spin-orbit effects in the electronic structure of BaIrO_3 ," *Phys. Rev. Lett.*, vol. 105, p. 216407, Nov 2010.
- [225] H. E. Stanley, *Introduction to Phase Transitions and Critical Phenomena*. International Series of Monographs on Physics, Oxford University Press, 1987.
- [226] T. Kida, A. Senda, S. Yoshii, M. Hagiwara, T. Takeuchi, T. Nakano, and I. Terasaki, "Unconventional critical behavior in the weak ferromagnet BaIrO_3 ," *Europhys. Lett.*, vol. 84, no. 2, p. 27004, 2008.
- [227] T. Nakano and I. Terasaki, "Giant nonlinear conduction and thyristor-like negative differential resistance in BaIrO_3 single crystals," *Phys. Rev. B*, vol. 73, p. 195106, May 2006.
- [228] J. Zhao, L. Yang, Y. Yu, F. Li, R. Yu, and C. Jin, "Structural and physical properties of the 6M BaIrO_3 : A new metallic iridate synthesized under high pressure," *Inorg. Chem.*, vol. 48, no. 10, pp. 4290–4294, 2009.
- [229] G. Cao, J. Bolivar, S. McCall, J. E. Crow, and R. P. Guertin, "Weak ferromagnetism, metal-to-nonmetal transition, and negative differential resistivity in single-crystal Sr_2IrO_4 ," *Phys. Rev. B*, vol. 57, pp. R11039–R11042, May 1998.
- [230] A. Powell and P. Battle, "A time-of-flight powder neutron diffraction study of non-stoichiometry in barium iridate $\text{BaIrO}_{3-\delta}$," *J. Alloys Compd.*, vol. 232, no. 1-2, pp. 147 – 153, 1996.
- [231] H. P. Singh, "Determination of thermal expansion of germanium, rhodium and iridium by x-rays," *Acta Cryst. A*, vol. 24, pp. 469–471, Jul 1968.
- [232] G. Cao, G. Shaw, and J.W. Brill, "Quasi-one-dimensional BaIrO_3 : On the verge of a weak ferromagnetic metallic state," *J. Phys. IV France*, vol. 12, pp. 91–92, Nov 2002.
- [233] K. Gschneidner and L. Eyring, *Handbook on the Physics and Chemistry of Rare Earths*. No. v. 34 in Handbook on the Physics and Chemistry of Rare Earths, Elsevier, 2005.
- [234] K.-H. Müller and V. N. Narozhnyi, "Interaction of superconductivity and magnetism in borocarbide superconductors," *Reports on Progress in Physics*, vol. 64, no. 8, p. 943, 2001.
- [235] N. Kini, A. Bentien, S. Ramakrishnan, and C. Geibel, "Specific heat and transport study of the co-existence of charge-density-wave and weak ferromagnetism in BaIrO_3 ," *Physica B: Condensed Matter*, vol. 359–361, pp. 1264 – 1266, 2005.

- [236] N. Mott, *Metal-insulator transitions*. Taylor & Francis, 1990.
- [237] C. Meneghini, D. Levy, S. Mobilio, M. Ortolani, M. Nuñez Reguero, A. Kumar, and D. D. Sarma, “High-pressure structure and electronic transport in hole-doped $\text{La}_{3/4}\text{Ca}_{1/4}\text{MnO}_3$ perovskites,” *Phys. Rev. B*, vol. 65, p. 012111, Dec 2001.
- [238] T. Kawakami, S. Nasu, T. Sasaki, K. Kuzushita, S. Morimoto, S. Endo, T. Yamada, S. Kawasaki, and M. Takano, “Pressure-induced transition from a charge-disproportionated antiferromagnetic state to a charge-uniform ferromagnetic state in $\text{Sr}_{2/3}\text{La}_{1/3}\text{FeO}_3$,” *Phys. Rev. Lett.*, vol. 88, p. 037602, Jan 2002.
- [239] R. Lengsdorf, M. Ait-Tahar, S. S. Saxena, M. Ellerby, D. I. Khomskii, H. Micklitz, T. Lorenz, and M. M. Abd-Elmeguid, “Pressure-induced insulating state in $(\text{La},\text{Sr})\text{CoO}_3$,” *Phys. Rev. B*, vol. 69, p. 140403, Apr 2004.
- [240] C. S. Alexander, Y. Xin, Z. X. Zhou, S. McCall, G. Cao, and J. E. Crow, “Observation of quantum oscillations in four-layer BaRuO_3 ,” in *Physical Phenomena at High Magnetic Fields-IV* (G. Boebinger, A. Lacerda, Z. Fisk, L. P. Gor’kov, and J. R. Schrieffer, eds.), pp. 393–396, July 2002.
- [241] J. G. Bednorz and K. A. Müller, “Possible high T_C superconductivity in the Ba–La–Cu–O system,” *Zeitschrift für Physik B*, vol. 64, pp. 189–193, 1986.
- [242] Y. Maeno, H. Hashimoto, K. Yoshida, S. Nishizaki, T. Fujita, J. G. Bednorz, and F. Lichtenberg, “Superconductivity in a layered perovskite without copper,” *Nature*, vol. 372, pp. 532–534, Dec. 1994.
- [243] M. K. Crawford, M. A. Subramanian, R. L. Harlow, J. A. Fernandez-Baca, Z. R. Wang, and D. C. Johnston, “Structural and magnetic studies of Sr_2IrO_4 ,” *Phys. Rev. B*, vol. 49, pp. 9198–9201, Apr 1994.
- [244] M. Subramanian, M. Crawford, R. Harlow, T. Ami, J. Fernandez-Baca, Z. Wang, and D. Johnston, “ Sr_2RhO_4 and Sr_2IrO_4 : Structural and magnetic studies of 4d and 5d transition metal analogs of La_2CuO_4 ,” *Physica C: Superconductivity*, vol. 235-240, pp. 743 – 744, 1994.
- [245] F. Wang and T. Senthil, “Twisted Hubbard model for Sr_2IrO_4 : Magnetism and possible high temperature superconductivity,” *Phys. Rev. Lett.*, vol. 106, p. 136402, Mar 2011.
- [246] M. Hanawa, Y. Muraoka, T. Tayama, T. Sakakibara, J. Yamaura, and Z. Hiroi, “Superconductivity at 1 k in $\text{Cd}_2\text{Re}_2\text{O}_7$,” *Phys. Rev. Lett.*, vol. 87, p. 187001, Oct 2001.
- [247] S. Yonezawa, Y. Muraoka, Y. Matsushita, and Z. Hiroi, “Superconductivity in a pyrochlore-related oxide KOs_2O_6 ,” *J. Phys.: Condens. Matter*, vol. 16, no. 3, p. L9, 2004.

- [248] R. J. Cava, B. Batlogg, K. Kiyono, H. Takagi, J. J. Krajewski, W. F. Peck, L. W. Rupp, and C. H. Chen, “Localized-to-itinerant electron transition in $\text{Sr}_2\text{Ir}_{1-x}\text{Ru}_x\text{O}_4$,” *Phys. Rev. B*, vol. 49, pp. 11890–11894, May 1994.
- [249] Q. Huang, J. Soubeyroux, O. Chmaissem, I. Sora, A. Santoro, R. Cava, J. Krajewski, and W. P. Jr., “Neutron powder diffraction study of the crystal structures of Sr_2RuO_4 and Sr_2IrO_4 at room temperature and at 10 K,” *J. Solid State Chem.*, vol. 112, no. 2, pp. 355 – 361, 1994.
- [250] Q. Wang, Y. Cao, J. A. Waugh, T. F. Qi, O. B. Korneta, G. Cao, and D. S. Dessau, “Dimensionality-controlled Mott transition in single- and bi-layer perovskite iridates.” submitted to *Phys. Rev. Lett.*, 2012.
- [251] M. Ge, T. F. Qi, O. B. Korneta, D. E. De Long, P. Schlottmann, W. P. Crummett, and G. Cao, “Lattice-driven magnetoresistivity and metal-insulator transition in single-layered iridates,” *Phys. Rev. B*, vol. 84, p. 100402, Sep 2011.
- [252] D. Hsieh, F. Mahmood, D. H. Torchinsky, G. Cao, and N. Gedik, “Observation of a metal-to-insulator transition with both Mott-Hubbard and Slater characteristics in Sr_2IrO_4 from time-resolved photocarrier dynamics,” *Phys. Rev. B*, vol. 86, p. 035128, Jul 2012.
- [253] R. Arita, J. Kuneš, A. V. Kozhevnikov, A. G. Eguiluz, and M. Imada, “*Ab initio* studies on the interplay between spin-orbit interaction and coulomb correlation in Sr_2IrO_4 and Ba_2IrO_4 ,” *Phys. Rev. Lett.*, vol. 108, p. 086403, Feb 2012.
- [254] K. W. H. Stevens, “On the magnetic properties of covalent XY_6 complexes,” *Proceedings of the Royal Society of London. Series A. Mathematical and Physical Sciences*, vol. 219, no. 1139, pp. 542–555, 1953.
- [255] T. Yamamoto and M. Morimoto, “Thin-MIS-structure Si negative-resistance diode,” *Applied Physics Letters*, vol. 20, no. 8, pp. 269–270, 1972.
- [256] A. Kastalsky, S. Luryi, A. Gossard, and R. Hendel, “A field-effect transistor with a negative differential resistance,” *Electron Device Letters, IEEE*, vol. 5, pp. 57 – 60, feb 1984.
- [257] J. N. Baillargeon, K. Y. Cheng, J. Laskar, and J. Kolodzey, “Three-terminal delta-doped barrier switching device with S-shaped negative differential resistance,” *Applied Physics Letters*, vol. 55, no. 7, pp. 663–665, 1989.
- [258] T. F. Qi, O. B. Korneta, L. Li, K. Butrouna, V. S. Cao, Xiangang Wan, P. Schlottmann, R. Kaul, and G. Cao, “Tuning the ground state of Sr_2IrO_4 via reducing spin-orbit interaction: an investigation of single-crystal $\text{Sr}_2\text{Ir}_{1-x}\text{Rh}_x\text{O}_4$ ($0 \leq x \leq 1$).” to be published, 2012.
- [259] D. Pesin and L. Balents, “Mott physics and band topology in materials with strong spin-orbit interaction,” *Nature Physics*, vol. 6, pp. 376–381, May 2010.

- [260] B.-J. Yang and Y. B. Kim, “Topological insulators and metal-insulator transition in the pyrochlore iridates,” *Phys. Rev. B*, vol. 82, p. 085111, Aug 2010.
- [261] X. Wan, A. M. Turner, A. Vishwanath, and S. Y. Savrasov, “Topological semimetal and Fermi-arc surface states in the electronic structure of pyrochlore iridates,” *Phys. Rev. B*, vol. 83, p. 205101, May 2011.
- [262] J. Reuther, R. Thomale, and S. Trebst, “Finite-temperature phase diagram of the Heisenberg-Kitaev model,” *Phys. Rev. B*, vol. 84, p. 100406, Sep 2011.

VITA

Oleksandr Korneta

Date and place of birth

May 22, 1978, Velykyi Bereznyi, Transcarpathian Region, Ukraine

Educational institutions attended and degrees awarded

2001-2002 Doctoral student, left the program to pursue a study in the USA

[Kyiv National Taras Shevchenko University](#)

[Institute of Semiconductor Physics](#)

Kyiv, Ukraine

1999-2001 M.Sc., Solid State Physics,

[Kyiv National Taras Shevchenko University](#)

Kyiv, Ukraine

1995-1999 B.Sc., Mechanical Engineering and Instrument Design,

[Uzhgorod National University](#)

Uzhgorod, Ukraine

Professional positions held

2007-2012 Research Assistant

University of Kentucky

2003-2007 Teaching Assistant

University of Kentucky

2001-2002 Research Assistant

Institute of Semiconductor Physics, Kyiv, Ukraine

2001-2002 Graphics designer

“Land Polygraph”, Graphics Design and Publishing Company, Kyiv, Ukraine

2000-2001 Computer network administrator

Youth Center for Development of Education, Science and Culture “Planeta”,
Kyiv Taras Shevchenko University, Kyiv, Ukraine

1997-1999 Laboratory technician

West division of State Enterprise “Scientific-Research Institute for Metrology of Measurement and Control Systems” (DP NDI “Systema”), Uzhgorod, Ukraine

Scholastic and professional honors

- University of Kentucky Linda and Jack Gill Eminent Research Assistant, 2012
- University of Kentucky Domestic Travel Student Support Award, 2007-2012
- University of Kentucky Huffaker Travel Scholarships, 2007-2012
- University of Kentucky Outstanding Teaching Assistant Award, 2005

List of publications

1. N. I. Klyui, V. G. Litovchenko, A. B. Korneta, V. P. Kostylev, U. K. Gaziev, M. U. Dzhanklych, V. G. Dyskin, R. A. Muminov, Z. S. Settarova, and M. N. Tursunov, "Characteristics of polycrystalline silicon solar cells with antireflecting and protective coatings of different types," *Applied Solar Energy* **38** no. 4, (2002) 1018.
2. N. I. Klyui, O. B. Korneta, V. P. Kostilyov, V. G. Litovchenko, A. V. Makarov, V. N. Dikusha, L. V. Neselevska, and V. I. Gorbulik, "High efficient solar cells and modules based on diamond-like carbon film - multicrystalline Si structures," *Semiconductor Physics, Quantum Electronics & Optoelectronics* **6** no. 2, (Jun, 2003) 197–201.
3. A. A. Evtukh, N. I. Klyui, V. G. Litovchenko, Y. M. Litvin, O. B. Korneta, V. M. Puzikov, and A. V. Semenov, "Peculiarities of field emission from silicon carbide films," *Appl. Surf. Sci.* **215** no. 1-4, (Jun, 2003) 237–241.
4. V. A. Makara, N. I. Klyui, A. G. Rozhin, V. G. Litovchenko, Y. P. Piryatinskii, and O. B. Korneta, "Porous silicon photoluminescence modification by surface treatments and impregnation of carbon based nanoclusters," *Phys. Status Solidi A* **197** no. 2, (May, 2003) 355–359.
5. Y. V. Sushko, O. B. Korneta, S. O. Leontsev, R. Jin, B. C. Sales, and D. Mandrus, "Pressure effects on superconducting and magnetic transitions in layered sodium cobalt oxides, Na_xCoO_2 ," *J. Low Temp. Phys.* **142** no. 3-4, (Feb, 2006) 573–576.
6. Y. V. Sushko, S. O. Leontsev, O. B. Korneta, and A. Kawamoto, "SQUID-magnetometry study of the P–T phase diagram of κ -[(BEDT-TTF) $_{1-x}$ (BEDSe-TTF) $_x$] $_2\text{Cu}[\text{N}(\text{CN})_2\text{Br}]$," *J. Low Temp. Phys.* **142** no. 3-4, (Feb, 2006) 563–566.
7. G. Cao, O. Korneta, S. Chikara, L. E. DeLong, and P. Schlottmann, "Non-Fermi-liquid behavior in single-crystal CaRuO_3 : Comparison to ferromagnetic SrRuO_3 ," *Solid State Commun.* **148** no. 7-8, (Nov, 2008) 305–309.
8. S. Chikara, O. Korneta, W. P. Crummett, L. E. DeLong, P. Schlottmann, and G. Cao, "Giant magnetoelectric effect in the $J_{eff} = \frac{1}{2}$ Mott insulator Sr_2IrO_4 ," *Phys. Rev. B* **80** no. 14, (Oct, 2009) 140407.
9. G. Cao, O. Korneta, S. Chikara, L. E. DeLong, and P. Schlottmann, "Ca $_3$ (Ru $_{1-x}$ Cr $_x$) $_2\text{O}_7$: A new paradigm for spin valves," *J. Appl. Phys.* **107** no. 9, (May, 2010) 09D718.
10. S. Chikara, O. Korneta, W. P. Crummett, L. E. DeLong, P. Schlottmann, and G. Cao, "Giant magnetoelectric effect in the $J_{eff} = \frac{1}{2}$ Mott insulator Sr_2IrO_4 ," *J. Appl. Phys.* **107** no. 9, (May, 2010) 09D910.

11. O. B. Korneta, S. Chikara, S. Parkin, L. E. DeLong, P. Schlottmann, and G. Cao, "Pressure-induced insulating state in $\text{Ba}_{1-x}\text{R}_x\text{IrO}_3$ ($\text{R}=\text{Gd}, \text{Eu}$) single crystals," *Phys. Rev. B* **81** no. 4, (Jan, 2010) 045101.
12. O. B. Korneta, T. Qi, S. Chikara, S. Parkin, L. E. De Long, P. Schlottmann, and G. Cao, "Electron-doped $\text{Sr}_2\text{IrO}_{4-\delta}$ ($0 \leq \delta \leq 0.04$): evolution of a disordered $J_{eff} = \frac{1}{2}$ Mott insulator into an exotic metallic state," *Phys. Rev. B* **82** no. 11, (Sep, 2010) 115117.
13. T. F. Qi, O. B. Korneta, S. Parkin, L. E. De Long, P. Schlottmann, and G. Cao, "Negative volume thermal expansion via orbital and magnetic orders in $\text{Ca}_2\text{Ru}_{1-x}\text{Cr}_x\text{O}_4$ ($0 < x < 0.13$)," *Phys. Rev. Lett.* **105** no. 17, (Oct, 2010) 177203.
14. O. B. Korneta, T. F. Qi, M. Ge, S. Parkin, L. E. De Long, P. Schlottmann, and G. Cao, "Correlated giant dielectric peaks and antiferromagnetic transitions near room temperature in pure and alkali-doped $\text{BaMnO}_{3-\delta}$," *Journal of Physics: Condensed Matter* **23** no. 43, (Oct, 2011) 435901.
15. M. Ge, O. B. Korneta, T. F. Qi, S. Parkin, P. Schlottmann, and G. Cao, "Magnetic anisotropy and geometrical frustration in the Ising spin-chain system $\text{Sr}_5\text{Rh}_4\text{O}_{12}$," *J. Appl. Phys.* **109** no. 7, (Apr, 2011) 07E164.
16. M. Ge, T. F. Qi, O. B. Korneta, D. E. De Long, P. Schlottmann, W. P. Crummett, and G. Cao, "Lattice-driven magnetoresistivity and metal-insulator transition in single-layered iridates," *Phys. Rev. B* **84** (Sep, 2011) 100402.
17. T. Qi, M. Ge, O. Korneta, S. Parkin, L. D. Long, and G. Cao, "Structurally-driven metal-insulator transition in $\text{Ca}_2\text{Ru}_{1-x}\text{Cr}_x\text{O}_4$ ($0 \leq x < 0.14$): A single crystal X-ray diffraction study," *J. Solid State Chem.* **184** no. 4, (Apr, 2011) 893 – 898.
18. T. F. Qi, O. B. Korneta, S. Chikara, M. Ge, S. Parkin, L. E. De Long, P. Schlottmann, and G. Cao, "Electron doped $\text{Sr}_2\text{IrO}_{4-\delta}$ ($0 \leq \delta < 0.04$): Evolution of a disordered $J_{eff} = \frac{1}{2}$ Mott insulator into an exotic metallic state," *J. Appl. Phys.* **109** no. 7, (Apr, 2011) 3.
19. T. F. Qi, O. B. Korneta, S. Parkin, J. Hu, and G. Cao, "Magnetic and orbital orders coupled to negative thermal expansion in Mott insulators $\text{Ca}_2\text{Ru}_{1-x}\text{M}_x\text{O}_4$ ($M = \text{Mn}$ and Fe)," *Phys. Rev. B* **85** (Apr, 2012) 165143.
20. F. Ye, S. Chi, H. Cao, B. C. Chakoumakos, J. A. Fernandez-Baca, R. Custelcean, T. F. Qi, O. B. Korneta, and G. Cao, "Direct evidence of a zigzag spin-chain structure in the honeycomb lattice: A neutron and x-ray diffraction investigation of single-crystal Na_2IrO_3 ," *Phys. Rev. B* **85** (May, 2012) 180403.
21. T. F. Qi, O. B. Korneta, X. Wan, L. E. DeLong, P. Schlottmann, and G. Cao, "Strong magnetic instability in correlated metallic $\text{Bi}_2\text{Ir}_2\text{O}_7$," *J. Phys.: Condens. Matter* **24** no. 34, (Jul, 2012) 345601.